# Strongly Correlated Ultracold Gases in Disordered Optical Lattices

DISSERTATION

zur Erlangung des Doktorgrades

der Naturwissenschaften

vorgelegt beim Fachbereich Physik

der Johann Wolfgang Goethe-Universität

in Frankfurt am Main

von
Dipl.-Phys. Denis Semmler
aus Fulda

Frankfurt 2011

vom Fachbereich Physik

der Johann Wolfgang Goethe-Univerität als Dissertation angenommen.

# Contents

CONTENTS

# 1. Introduction

Since the very beginning of solid state physics the question why some materials are insulating whereas others are conductors lies at the very heart of solid state theory. A first explanation was achieved by band theory in the early days of quantum mechanics [23, 44]. The ions of the solid give rise to a periodic potential, which the electrons are exposed to. A consequence is the formation of energy bands, and the filling of the bands determines whether the material is a conductor or not. In many experiments, it was observed that solids can undergo a transition from an insulating state to a conducting state, if external parameters like temperature or pressure are changed [151, 206]. Such transitions are called metal-insulator transitions. A central purpose of solid state theory is to gain a comprehensive understanding of the underlying mechanisms of these macroscopic phenomena [120, 151, 205].

Two types of metal-insulator transitions are known [120]. Firstly, thermodynamic phase transitions, which result from the competition between the internal energy of the system and the entropy [264, 304]. Secondly, quantum phase transitions due to opposing energy contributions in the system [280]. Concerning the latter, two instances of completely different nature gained outstanding attention: the Anderson transition [17, 172, 204, 270] occurring in disordered solids and the Mott transition [151, 206] due to strong correlations between the electrons. Whereas the prior can be understood in a single-particle theory, the latter mechanism arises by reason of mutual interactions in the many-body problem.

Historically, the field of correlation-induced metal-insulator transitions originates from the experimental observation of insulating materials, which were in conflict with band theory predictions [79]. Theoretical efforts came to the conclusion that interactions between the electrons are responsible for the insulating behavior [203, 205, 206, 295]. In the course of the theoretical research, the famous Hubbard model was introduced as a generic model for electron correlations in solids [139, 147, 162]. Although the Hubbard model incorporates strong correlations on the level of pure on-site interactions, an exact solution has not been achieved up to day, except in one dimension [186]. First, rough approximations far from a realistic picture [147, 149] show that the Hubbard model can successfully describe the Mott transition. The discovery of high-temperature

superconductivity [31] and the evidence for its electronic origin boosted the interest in the Hubbard model [21]. Subsequently, the discovery of crucial - but not trivial - simplifications in infinite dimensions [193] paved the way towards the dynamical mean-field theory [122, 123, 171] in which on-site interactions are treated non-perturbatively. Within this method, the Mott transition can be understood to be driven by local quantum fluctuations [55, 57, 121, 236, 305].

On the other hand, disorder in solids - such as impurities or vacancies - was found to strongly modify band theory predictions, even in absence of many-particle physics [172, 204, 270]. In 1958, Anderson showed in his analysis of a disordered tight binding model - the Anderson model - that a sufficient amount of disorder hinders the diffusion of particles [17]. Coherent backscattering processes cause a localization of the particle, i.e. it is confined to a finite region of the lattice. In particular, the localization of states at the Fermi level induces a metal-insulator transition, the Anderson transition. Although the disorder physics is described on a single particle-level, the randomness impedes exact solutions. Therefore, numerical investigations are indispensable.

Albeit each fundamental phenomenon - correlations and disorder - on its own gives rise to challenges to both experimental and theoretical research and is still subject of current investigations, the realistic modeling of materials requires the simultaneous consideration of both effects. This interplay is of central interest within present day's solid state physics [32, 174, 182, 196].

Theoretical investigations, e.g. of the Anderson-Hubbard model combining the Hubbard model and the Anderson model are notoriously difficult. The most intriguing effects, such as the Mott transition and the Anderson transition, take place at intermediate interaction and disorder strength requiring a non-perturbative approach. Extensions of the dynamical mean-field theory to disordered systems are especially promising in this respect, since local correlations are incorporated non-perturbatively. Such extensions were performed on a level of the coherent potential approximation [275, 279] and on an effective level of typical medium theory incorporating localization effects [5, 58, 60–62, 82]. Both approaches neglect disorder-induced fluctuations. Dobrosavljević and Kotliar extended the dynamical mean-field theory to include disorder fluctuations on a fully stochastic level, which is referred to as statistical dynamical mean-field theory [85, 86]. This theory is capable of describing Mott and Anderson-Mott transitions non-perturbatively and on equal footing. However, the theory is numerically very demanding, which might explain the lack of comprehensive statistical dynamical mean-field theory studies on the Anderson-Hubbard model to date.

From the solid state point of view, precise experimental investigations are difficult, since the disorder is hard to control, both in its nature and intensity. It

is also not possible to tune the interaction strength in a precise and controlled way and in particular, it is not possible to isolate one single effect. Here, the recently developed experiments with ultracold atoms in optical lattices [45, 183, 202] are very promising to overcome these problems.

Experiments with ultracold atoms were enabled by the invention of laser cooling [24, 71, 225, 298, 299] and further developments in that field which allowed for the realization of quantum degenerate Bose, Fermi and Bose-Fermi gases [16, 78, 81]. Interestingly, it is possible to load these degenerate quantum gases into optical lattices [45, 132, 138, 159, 166, 220, 229], systems to be used as quantum simulators for quantum many-body models [108, 145, 154, 155, 183]. Bosons in an optical lattice, for example, constitute a realization of the Bose-Hubbard model up to a very high degree of accuracy [154] which was first achieved by Greiner *et al.* in 2002 [132]. Characteristic for these experiments is the possibility to tune the experimental parameters, like the interaction strength very precisely and independently [45]. Remarkably from the solid state point of view, the fermionic Hubbard model was also realized [166] and the fermionic Mott insulator has been observed recently [160, 242]. Furthermore, ultracold atoms were exposed to disordered potentials within different setups [25, 199, 239]. For instance, a speckle disorder can be created by scattering a coherent laser beam from a diffusor plate leading to a random intensity field for the atoms through the AC Stark effect [39, 73, 191]. Such random speckle patterns were successfully superimposed onto optical lattices [223, 293] realizing a disordered periodic potential for the atoms. In a further approach, laser beams with incommensurate frequencies are superimposed, resulting in a quasi-periodic potential [76, 101, 235]. Remarkably, clear observation of localized matter waves was achieved recently within both approaches [39, 233]. In a further approach, it is also aimed to realize binary disorder in optical lattices. Here, the strategy is to load two species of atoms into an optical lattices, of which one is immobile on the relevant time scale. Consequently, the mobile species is exposed to a impurity disorder potential mediated by the interspecies interaction. First experiments in that direction have been performed [138, 220].

These new experimental developments enable the quantum simulation of strongly correlated systems in disordered potentials [25, 199, 239]. In particular, it is possible to investigate the Anderson-Hubbard model with unprecedented experimental control. The prospect to tune the disorder, as well as the inter-particle interaction strength over several orders of magnitude is especially appealing.

The theoretical investigation of degenerate ultracold quantum gases in disordered optical lattices is subject of this thesis. The main focus lies on the study of fermionic quantum gases within the statistical dynamical mean-field theory.

## 1.1.  Outline of the thesis

As starting point the Hubbard model and the notion of many-particle Green's functions are introduced, followed by the derivation of dynamical mean-field theory and discussion of the Mott insulator transition in chapter 2. In chapter 3, non-interacting, disordered systems are considered with an emphasis on localization signatures within the Green's function formalism. The findings are numerically checked with the local distribution method [2, 13, 14], the discussion of which facilitates the subsequent introduction of the statistical dynamical mean-field theory. This in turn is carried out in detail within chapter 4, which is dedicated to strongly-correlated fermions in disordered lattices and the various extensions of dynamical mean-field theory to disordered systems. Hereafter in chapter 5, a brief overview on ultracold atoms in optical lattices is presented, with a special emphasis on the disordered case. After having set the stage, the statistical dynamical mean-field theory is established for the Anderson-Hubbard model by application to the commonly used box disorder distribution in chapter 6.

Subsequently, two disorder types are investigated for fermionic systems, which are of fundamental interest regarding experiments with ultracold atoms. As a first instance, the binary distribution of on-site energies is considered in chapter 7. This type of disorder cannot only be realized in optical lattices, but it is also of fundamental interest in solid state physics, where it serves as primary model of alloys or doped semiconductors. The purpose of the investigation is to significantly extend the theoretical picture achieved so far. Interestingly, a novel Mott transition at non-integer filling has been predicted recently [59], but localization effects have not been incorporated. It is our goal to complete the picture by describing correlation-induced and localization-induced metal-insulator transitions on equal footing within the statistical dynamical mean-field theory. The underlying intention of the investigation is to test whether the mentioned novel kind of Mott transition persists in presence of disorder.

Chapter 8 is dedicated to the investigation of fermions in speckle disordered optical lattices. This type of disorder is specific to ultracold atoms. A fundamental difference to disorder prototypes in solid state theory is that the distribution function of the on-site energies for speckle disorder is unbounded. An accurate description is accomplished by considering realistic parameter regimes close to experimental realizations. Therefore, an extension of the statistical dynamical mean-field theory is developed to include off-diagonal disorder which allows for additionally taking probability distribution functions for the hopping amplitude into account. The major goal is to determine the paramagnetic ground state phase diagram for the first time. The question of the consequences arising

from the specific nature of speckle disorder is addressed, which is of particular interest in the context of simulating disordered solids state systems with cold atoms.

Finally, Bose-Fermi mixtures in disordered optical lattices are studied in chapter 9. Based on the recently developed generalized dynamical mean-field theory [272, 273], the typical medium theory is extended to incorporate localization effects for the bosons. This allows for a non-perturbative investigation of the disordered system with mixed quantum statistics. In particular, two kinds of Bose-Fermi mixtures are considered. On the one hand, mixtures of bosons and spin-polarized fermions, on the other hand mixtures of bosons and two-component fermions. The competition of correlation-induced and disorder-induced localized phases is of interest. Furthermore, the purpose is to gain a fundamental insight into the intricate interplay between the bosonic and the fermionic subsystem.

# 2. Strongly correlated fermions in high dimensions

Solid state theory classifies metals and insulators as distinct and separate states of matter. Electrons in a crystal are exposed to the periodic potential which gives rise to a band structure (cf. appendix A). In band theory metals exhibit partially filled bands, whereas for insulators the highest occupied band is completely filled. Accordingly, insulators are characterized by a Fermi level that lies in a band gap.

However, some elements and compounds such as NiO do not obey this basic band theory, as first pointed out by de Boer and Verwey [79]. Although some compounds are predicted to be metals by band theory, experiments show them to be insulators. Shortly after these observations Wigner [295] argued that the Coulomb interaction between the electrons might be the origin of the insulating behavior. Thereby, the research field of strong correlations[1] was opened.

During the following decades, significant progress was achieved and many more physical behaviors have been explained through strong correlations [151, 206]. In particular, it was Mott who gave first explanations[2] how interactions between the electrons might give rise to insulating behavior [203, 205, 206]. By considering single orbitals on each lattice site, which can be doubly occupied by electrons with opposite spin, he argued that the repulsion between electrons gives rise to a the formation of an upper band. Hence, if the Fermi level lies between the two states an insulator is obtained.

Further progress was obtained by the introduction of the Hubbard model [139, 147, 162] which describes electrons in a lattice in a simple fashion by the hopping from one site to adjacent lattice sites and by a purely local repulsive interaction. This plain model is able to capture a metal insulator phase transition already on a level of basic approximations [149]. However, except the one-

---

[1] The notion of strong correlations in many-particle systems refers to the fact, that correlation functions like density-density correlations in general can not be factorized into a simple product of the single expectation values due to interactions between the particles. Nowadays the notion is acclimated as a synonym of non-trivial effects in strongly interacting many-particle systems.

[2] Therefore, the metal-insulator transition due to interaction is commonly known as Mott transition.

dimensional case [186] no explicit analytical solutions have been obtained for higher dimensions so far. In 1986, after the discovery of high-temperature superconductivity [31] the Hubbard model attracted even greater attention as experimental data indicated an electronic nature behind the basic mechanism, and Anderson argued that the Hubbard model should constitute an appropriate model to explain its behavior [21].

Due to the lack of explicit solutions, theoretical investigations have been restricted to weak-coupling or strong-coupling perturbative approaches in higher dimensions. In order to explain the most intriguing phenomena like the Mott transition, which take place at intermediate couplings [151], non-perturbative methods were much-needed. Besides other approximative treatments[3] the limit of infinite dimensions turned out to become especially useful [193, 210], as the theory becomes significantly simplified by a local self-energy. This observation cleared the way towards the development of the so-called dynamical mean-field theory (DMFT) [122, 123, 170, 171], which is non-perturbative in the interaction strength and features a well-defined limit of infinite dimensions.

## 2.1. Hubbard model

One of the most successful models of strongly correlated fermions was introduced independently by Hubbard [147], Kanamori [162] and Gutzwiller [139] in 1963. Nowadays, this model is commonly known as the Hubbard model, since Hubbard published several important works consecutively [148, 149]. In principle, the model consists of a hopping contribution and a simple on-site interaction between two fermions, which is motivated by the screening of the charge for large distances. In general, the model is suitable for materials with narrow energy bands. It is widely used in the theory of high-temperature superconductivity, band magnetism, metal-insulator transitions as well as for the description of transition metals. Due to its structural simplicity and its wide range of applications, it nowadays represents the standard model of strong correlations. In second quantization (see e.g. [215]) the single-orbital Hubbard model reads in the Wannier representation (see appendix A)

$$H = \sum_{ij\sigma} t_{ij} c_{i\sigma}^\dagger c_{j\sigma} - \mu \sum_{i\sigma} c_{i\sigma}^\dagger c_{i\sigma} + U \sum_i n_{i\uparrow} n_{i\downarrow} \,, \tag{2.1}$$

where $c_{i\sigma}^\dagger$ ($c_{i\sigma}$) denotes fermionic creation (annihilation) operators at a lattice site $i$ with spin $\sigma = \pm 1/2$. The fermionic number operator is given by $n_{i\sigma} = c_{i\sigma}^\dagger c_{i\sigma}$.

---

[3]For a comprehensive review see e.g. [120, 151].
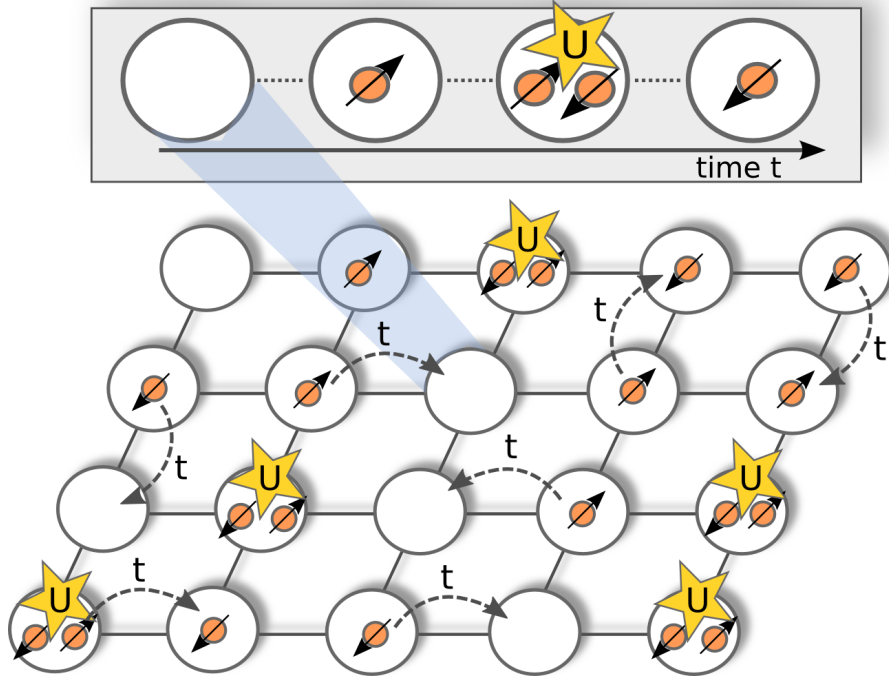
**Figure 2.1.:** Illustration of the Hubbard model on the square lattice. Particles are hopping with amplitude $t$ between nearest neighboring sites. If on a lattice site both spin components are present, they interact repulsively with strength $U$. Under time evolution the state on a single site might change from unoccupied, singly occupied to doubly occupied.

The hopping amplitude between the sites $i$ and $j$ is denoted by $t_{ij}$, the local interaction amplitude is represented by $U$, and the chemical potential is given by $\mu$. In the simplest case, just nearest neighbor hopping is considered, i.e. $t_{ij} = -t$ for site $i$ and site $j$ nearest neighbors and zero otherwise.

The Hubbard model is given on a lattice of dimensionality $d$ and number of nearest neighbors $z$. An illustration of the Hubbard model on the square lattice is given in figure 2.1.

Of course, the goal of all theoretical investigations is to estimate the eigenvalues of physical observables $A$, their expectation values $\langle A \rangle$ or the correlation functions between two observables $\langle AB \rangle$. If it would be possible to solve the many-body system (2.1) analytically, all physical quantities of interest – e.g. density of states, conductivity or the responses to the change of external parameters – would be accessible. Despite its structural simplicity, the Hubbard model is notoriously hard to solve and many important questions about its

physics are unknown up to day. This can easily be seen from the fact, that while the interaction part is diagonal in real space, the hopping part is not and vice versa in momentum space.

In the limit $U = 0$ the Hubbard model describes Bloch electrons, which are extended and give rise to a finite conductivity. Hence this limit describes a metal. In the limit of zero hopping, the so-called atomic limit, the Hamiltonian is decomposed to the direct sum of local operators, whose highly degenerate eigenfunctions are direct products of atomic states on each lattice site [148]. In this limit, the system describes an insulating state.

A third limit is given by $U \gg t$, the limit of strong interactions. Here, the system evolves exclusively in the subsystem of lowest possible number of double occupancies [120] and a first order perturbation approach in the hopping amplitude is well suited and usually termed the Nagaoka problem. Although this problem still cannot be solved in general, some parameter configurations allow for an explicit solution, as for example, a single hole in arbitrary dimensions [212], which was shown to feature a ferromagnetic ground state. Furthermore, the case of half-filling, i.e. number of electrons equal to number of lattice sites, is special in the large $U$ limit, as the Hubbard model can be mapped onto the anti-ferromagnetic Heisenberg model [18]. Hence, at half filling the Hubbard model on a bipartite lattice[4] possesses an anti-ferromagnetic insulator as a ground state.

From the above limits, we can already conclude that the Hubbard model exhibits a quantum phase transition[5] from a metal to an insulator. In particular, the well-known Fermi-liquid theory [180, 217], which substitutes the interacting fermions by non-interacting quasi-particles as elementary excitations does not give a comprehensive picture as it is not able to describe incoherent excitations, which drive the metal-insulator transition as it is known nowadays.

As unfortunately no analytical solution exists at the time of writing, except in one dimension for zero temperature [186], investigations of the Hubbard model rely on numerical solutions or approximation schemes. The development of a very powerful method – the DMFT – was triggered by the observation, that the self-energy becomes local in infinite dimensions, which was shown in a ground breaking paper by Metzner and Vollhardt [193]. The assumption of a local self-energy is known to be a good approximation for high dimensional lattices such as three-dimensional lattices [123], on which this work focuses on. The DMFT will be introduced in detail in section 2.3 after the introduction of

---

[4]A lattice is called bipartite, if the lattice can be divided into two sublattices $A$ and $B$, so that all nearest neighbors of a member site of sublattice $A$ are part of the sublattice $B$ and vice versa.

[5]For a review see e.g. [280].

the appropriate theoretical terminology for many particle systems in section 2.2.

## 2.2. Green's functions of many-particle systems

The introduction of Green's function is useful for theoretical investigations of many-particle systems. Given two operators $A(t)$ and $B(t)$ in the Heisenberg picture the retarded, advanced and the causal two-time Green's functions are defined as [309]:

$$G_{AB}^{\mathrm{r}}(t,t') \equiv \langle\langle A(t); B(t')\rangle\rangle^{\mathrm{r}} := -i\theta(t-t')\langle[A(t),B(t')]_{-\epsilon}\rangle \tag{2.2}$$

$$G_{AB}^{\mathrm{a}}(t,t') \equiv \langle\langle A(t); B(t')\rangle\rangle^{\mathrm{a}} := i\theta(t'-t)\langle[A(t),B(t')]_{-\epsilon}\rangle \tag{2.3}$$

$$G_{AB}^{\mathrm{c}}(t,t') \equiv \langle\langle A(t); B(t')\rangle\rangle^{\mathrm{c}} := -i\langle T_{\epsilon}(A(t)B(t'))\rangle . \tag{2.4}$$

Here, the expression $[..,..]_{-\epsilon}$ denotes the commutator $[..]_{-}$ for $\epsilon = +$ and the anticommutator $[..]_{+}$ for $\epsilon = -$ and $\theta(x)$ denotes the Heaviside function. It is customary to use the commutator for bosonic operators and the anticommutator for fermionic, although this choice is not mandatory. The Wick time ordering operator is defined as

$$T_{\epsilon}(A(t)B(t')) := \theta(t-t')A(t)B(t') + \epsilon\theta(t'-t)B(t')A(t) . \tag{2.5}$$

The brackets $\langle..\rangle$ denote the grand canonical thermal average

$$\langle X\rangle = \frac{1}{Z}\mathrm{Tr}(Xe^{-\beta(H-\mu N)}) \tag{2.6}$$

of the quantity $X$ at finite temperature, where $\beta = 1/k_B T$ the inverse temperature and the grand canonical partition function $Z := \mathrm{Tr}\exp(-\beta(H-\mu N))$. For zero temperature the brackets denote the expectation value of the quantity $X$ in the ground state $|\mathrm{gs}\rangle$:

$$\langle X\rangle = \langle\mathrm{gs}|X|\mathrm{gs}\rangle . \tag{2.7}$$

The retarded and the advanced Green's function can be continued analytically in the upper and lower complex half-plane respectively [309], which is not true for the causal Green's function. Therefore, in practical calculations one usually deals with only the retarded Green's function or the advanced Green's function. The retarded and the advanced Green's functions are closely connected to one

another. From the definitions given above, we can derive the relation

$$G^{\mathrm{r}}_{AB}(t,t') = \epsilon G^{\mathrm{a}}_{BA}(t',t) \,. \tag{2.8}$$

Furthermore, the real part and the imaginary part of the Green's functions are not independent, but connected via the Kramers-Kronig relations [215].

Henceforth we will focus on the retarded two-time Green's function and suppress the index $r$. By differentiating the Green's function with respect to $t$ we obtain

$$\begin{aligned} i\frac{d}{dt}G_{AB}(t,t') &=& \frac{d\theta(t-t')}{dt}\langle[A(t),B(t')]_{-\epsilon}\rangle + \langle\langle\frac{dA(t)}{dt};B(t')\rangle\rangle \tag{2.9} \\ &=& \delta(t-t')\langle[A(t),B(t')]_{-\epsilon}\rangle + \langle\langle[A(t),H];B(t')\rangle\rangle \,, \tag{2.10}\end{aligned}$$

in which the Heisenberg equation of motion was used and we set $\hbar = 1$ as used throughout the entirety of this work. Equation (2.10) represents an equation of motion for the Green's function, which allows the determination of the two-time Green's function in principle. However, we note the occurrence of a higher-oder Green's function on the right hand side of equation (2.10). An analogous equation of motion can be constructed for this higher-order Green's function, which will again result in general in the occurrence of another higher-order Green's function. Hence, the equation of motion leads to an infinite hierarchy of coupled differential equations, which necessitates a truncation so that a solution may be found.

If the Hamilton operator does not explicitly depend on time, i.e. $\partial H/\partial t = 0$, which is true in general for all subsequent considerations in this work, the two-time Green's function depends only on the difference of times

$$G_{AB}(t,t') = G_{AB}(t-t') \,. \tag{2.11}$$

In order to obtain an algebraic set of equations one performs a Fourier transformation

$$G_{AB}(\omega) \equiv \langle\langle A(t);B(t')\rangle\rangle_\omega := \frac{1}{2\pi}\int d(t-t')\,G_{AB}(t-t')e^{i\omega(t-t')} \tag{2.12}$$

so that the equation of motion (2.10) becomes

$$\omega\langle\langle A;B\rangle\rangle_\omega = \langle[A,B]_{-\epsilon}\rangle + \langle\langle[A,H];B\rangle\rangle_\omega \,. \tag{2.13}$$

The Green's functions is conveniently expressed in the spectral representation.

For this purpose one defines the spectral function as

$$S_{AB}(t,t') := \frac{1}{2\pi}\langle [A(t),B(t')]_{-\epsilon}\rangle . \tag{2.14}$$

By substitution of the complete basis set of eigenfunctions $|E_n\rangle$ of the grand canonical Hamiltonian $\mathcal{H} = H - \mu N$ and subsequent Fourier transformation, the spectral representation

$$S_{AB}(\omega) = \frac{1}{Z}\sum_{n,m}\langle E_n|B|E_m\rangle\langle E_m|A|E_n\rangle e^{-\beta E_n}(e^{\beta(E_n-E_m)}-\epsilon)\delta(\omega-(E_n-E_m)) \tag{2.15}$$

is obtained. The connection between the retarded Green's function and the spectral function reads

$$G_{AB}(\omega) = \int d\epsilon \frac{S_{AB}(\epsilon)}{\omega - \epsilon + i\eta} \tag{2.16}$$

and by inserting (2.15) the spectral representation of the retarded Green's function is derived

$$G_{AB}(\omega) = \frac{1}{Z}\sum_{n,m}\langle E_n|B|E_m\rangle\langle E_m|A|E_n\rangle e^{-\beta E_n}\frac{e^{\beta(E_n-E_m)}-\epsilon}{\omega-(E_n-E_m)+i\eta} , \tag{2.17}$$

from which we conclude that the Green's function has poles at the excitation energies of the interacting system and moreover the relation

$$S_{AB}(\omega) = -\frac{1}{\pi}\mathrm{Im}G_{AB}(\omega) , \tag{2.18}$$

to which we will refer many times during this work. An analogous consideration for the advanced Green's function gives the remarkable relation

$$S_{AB}(\omega) = \frac{i}{2\pi}(G^{\mathrm{r}}_{AB}(\omega + i\eta) - G^{\mathrm{a}}_{AB}(\omega - i\eta)) , \tag{2.19}$$

which states that the spectral density results from a discontinuity of the advanced and retarded Green's function in the limit $\eta \to 0$.

Regarding the Hubbard model 2.1 an important quantity of interest is the retarded single-particle Green's function, defined as

$$G_{ij\sigma}(t) \equiv G_{c_{i\sigma}(t)c^{\dagger}_{j\sigma}(0)}(t) = -i\theta(t)\langle [c_{i\sigma}(t),c^{\dagger}_{j\sigma}(0)]_{+}\rangle , \tag{2.20}$$

## 2. Strongly correlated fermions in high dimensions

By knowing the single-particle Green's function of an interacting many-body problem, all single-particle physical observables are accessible. In particular, the spectral function of the site-diagonal single-particle Green's function

$$\rho_i(\omega) \equiv S_{c_{i\sigma}c_{i\sigma}^\dagger}(\omega) := -\frac{1}{\pi}\mathrm{Im}G_{ii\sigma}(\omega) \tag{2.21}$$

gives the local density of states (LDOS).

Consider the Hubbard model in Bloch representation (see appendix A)

$$H = \sum_{\mathbf{k},\sigma}(\epsilon_\mathbf{k} - \mu)c_{\mathbf{k}\sigma}^\dagger c_{\mathbf{k}\sigma} + \frac{U}{N}\sum_{\mathbf{k_1 k_2 q}}c_{\mathbf{k_1}\uparrow}^\dagger c_{\mathbf{k_1+q}\uparrow}c_{\mathbf{k_2}\downarrow}^\dagger c_{\mathbf{k_2-q}\downarrow}\,, \tag{2.22}$$

where the dispersion relation

$$\epsilon_\mathbf{k} = \frac{1}{N}\sum_{ij}t_{ij}e^{-i\mathbf{k}(\mathbf{R_i}-\mathbf{R_j})} \tag{2.23}$$

contains the lattice structure. The Green's function in Bloch representation reads

$$G_{c_{\mathbf{k}\sigma}c_{\mathbf{k}\sigma}^\dagger}(\omega) \equiv G_{k\sigma}(\omega) = \langle\langle c_{\mathbf{k}\sigma}; c_{\mathbf{k}\sigma}^\dagger\rangle\rangle_\omega\,. \tag{2.24}$$

The non-trivial part in the equation of motion for the single-particle Green's function (2.13) involves the commutator $[c_{\mathbf{k}\sigma},H]$ which we split into two parts by defining $H_0$ by the single-particle part of the Hubbard model. We evaluate the commutator

$$[c_{\mathbf{k}\sigma},H_0]_- = [c_{\mathbf{k}\sigma}, \sum_{\mathbf{k_1},\sigma}(\epsilon_{\mathbf{k_1}} - \mu)c_{\mathbf{k_1}\sigma}^\dagger c_{\mathbf{k_1}\sigma}]_- \tag{2.25}$$

$$= (\epsilon_\mathbf{k} - \mu)c_{\mathbf{k}\sigma}\,. \tag{2.26}$$

We require the commutator

$$[c_{\mathbf{k}\sigma}, c_{\mathbf{k_1}\uparrow}^\dagger c_{\mathbf{k_1+q}\uparrow}c_{\mathbf{k_2}\downarrow}^\dagger c_{\mathbf{k_2-q}\downarrow}]_- = \delta_{\mathbf{k,k_1}}\delta_{\sigma,\uparrow}c_{\mathbf{k_1+q}\uparrow}c_{\mathbf{k_2}\downarrow}^\dagger c_{\mathbf{k_2-q}\downarrow}$$
$$+\delta_{\mathbf{k,k_2}}\delta_{\sigma,\downarrow}c_{\mathbf{k_1}\uparrow}^\dagger c_{\mathbf{k_1+q}\uparrow}c_{\mathbf{k_2-q}\downarrow} \tag{2.27}$$

from which we find

$$[c_{\mathbf{k}\sigma},H - H_0] = \frac{U}{N}\sum_{\mathbf{k_1,k_2,q}}(\delta_{\mathbf{k,k_1}}\delta_{\sigma,\uparrow}c_{\mathbf{k_2}\downarrow}^\dagger c_{\mathbf{k_2-q}\downarrow}c_{\mathbf{k_1+q}\uparrow}$$
$$+\delta_{\mathbf{k,k_2}}\delta_{\sigma,\downarrow}c_{\mathbf{k_1}\uparrow}^\dagger c_{\mathbf{k_1+q}\uparrow}c_{\mathbf{k_2-q}\downarrow}) \tag{2.28}$$

$$[c_{\mathbf{k}\sigma}, H - H_0] = \frac{U}{N} \sum_{\mathbf{k_1},\mathbf{q}} (\delta_{\sigma,\uparrow} c^{\dagger}_{\mathbf{k_1}\downarrow} c_{\mathbf{k_1}-\mathbf{q}\downarrow} c_{\mathbf{k}+\mathbf{q}\uparrow} + \delta_{\sigma,\downarrow} c^{\dagger}_{\mathbf{k_1}\uparrow} c_{\mathbf{k_1}+\mathbf{q}\uparrow} c_{\mathbf{k}-\mathbf{q}\downarrow})$$

$$\tag{2.29}$$

$$= \frac{U}{N} \sum_{\mathbf{k_1},\mathbf{q}} (c^{\dagger}_{\mathbf{k_1}\bar{\sigma}} c_{\mathbf{k_1}+\mathbf{q}\bar{\sigma}} c_{\mathbf{k}-\mathbf{q}\sigma}) . \tag{2.30}$$

Here, $\bar{\sigma}$ refers to the opposite spin of $\sigma$. When these expressions are substituted into the equation of motion (2.13) we obtain

$$(\omega + \mu - \epsilon_{\mathbf{k}}) G_{\mathbf{k}\sigma}(\omega) = 1 + \frac{U}{N} \sum_{\mathbf{k_1},\mathbf{q}} \langle\langle c^{\dagger}_{\mathbf{k_1}\bar{\sigma}} c_{\mathbf{k_1}+\mathbf{q}\bar{\sigma}} c_{\mathbf{k}-\mathbf{q}\sigma}; c^{\dagger}_{\mathbf{k}\sigma} \rangle\rangle_{\omega} , \tag{2.31}$$

where we note the previously mentioned occurrence of higher order Green's functions. By postulating the decomposition

$$\langle\langle [c_{\mathbf{k}\sigma}, H - H_0]; c^{\dagger}_{\mathbf{k}\sigma} \rangle\rangle_{\omega} = \frac{U}{N} \sum_{\mathbf{k_1},\mathbf{q}} \langle\langle c^{\dagger}_{\mathbf{k_1}\bar{\sigma}} c_{\mathbf{k_1}+\mathbf{q}\bar{\sigma}} c_{\mathbf{k}-\mathbf{q}\sigma}; c^{\dagger}_{\mathbf{k}\sigma} \rangle\rangle_{\omega} \tag{2.32}$$

$$=: \Sigma_{\mathbf{k}\sigma}(\omega) G_{\mathbf{k}\sigma}(\omega) \tag{2.33}$$

we introduce the self-energy, $\Sigma_{\mathbf{k}\sigma}(\omega)$. Therefore the solution of the equation of motion for the single-particle Green's function is formally given by

$$G_{\mathbf{k}\sigma}(\omega) = (\omega + \mu - \epsilon_{\mathbf{k}} - \Sigma_{\mathbf{k}\sigma}(\omega))^{-1} . \tag{2.34}$$

Remarkably, the influence of the particle interactions is contained solely in the self-energy. The real part of the self-energy corresponds to the energy of the system's quasi-particles, and their lifetime is given by the imaginary part [215].

## 2.3. Dynamical mean-field theory

A theoretical breakthrough in understanding the physics of the Hubbard model was achieved with the development of the DMFT [123, 171]. The theory was pioneered by the work of Metzner and Vollhardt, who showed that the self-energy becomes local in infinite dimensions [193]. Further progress was achieved by – among others – the remarkable works of Müller-Hartmann [209, 210], Brandt and Mielsch [49–51], Janis [157], Jarrell [158], and Georges and Kotliar [122]. A detailed and comprehensive review is given by Georges et al. [123]. In this section we will briefly outline the main ideas of the method and derive the self-consistent equations within the framework of the cavity method [123].

A convenient starting point of the calculation is the grand canonical partition

function of the fermionic Hubbard model, given as a functional integral over Grassmann variables [214]. From statistical mechanics we know that the partition function reads,

$$Z = \mathrm{Tr}(e^{-\beta H}) = \lim_{n \to \infty} \mathrm{Tr}((1 - \beta\frac{H}{n})^n) \tag{2.35}$$

One proceeds by inserting $n$ unity identities constituted by the completeness of the coherent states in Fock space [214]. Subsequently, the eigenvalue equation of the annihilation operator acting on coherent states and its conjugate equation for the creation operator are used for the second-quantized, normal-ordered Hamiltonian, such that the Hamiltonian becomes a function of the grassmann variables. Finally, a Wick rotation is performed such that $t = i\tau$, where the imaginary time $\tau = \beta l/n$ with $l = 1, \ldots, n$ is introduced. The limit $n \to \infty$ is taken, resulting in the partition function [214]

$$Z = \int \prod_i Dc_{i\sigma}^{\dagger} Dc_{i\sigma} e^{-S}, \tag{2.36}$$

with the action $S$ given by

$$S = \int_0^{\beta} d\tau \left( \sum_{i\sigma} c_{i\sigma}^{\dagger}(\tau)(\partial_{\tau} - \mu)c_{i\sigma}(\tau) - \sum_{\langle i,j \rangle \sigma} t_{ij} c_{i\sigma}^{\dagger}(\tau)c_{j\sigma}(\tau) + U \sum_i n_{i\uparrow}(\tau)n_{i\downarrow}(\tau) \right). \tag{2.37}$$

In a manner analogous to static mean field theories, an effective action is formally defined by focusing on one single site $i = 0$ and tracing out all other degrees of freedom of the system:

$$\frac{1}{Z_{\mathrm{eff}}} e^{-S_{\mathrm{eff}}} := \frac{1}{Z} \int \prod_{i \neq 0, \sigma} Dc_{i\sigma}^{\dagger} Dc_{i\sigma} e^{-S}. \tag{2.38}$$

In order to proceed, the action is split into three parts, the pure local contribution $S_0$ of site $i = 0$, the contribution $\Delta S$ corresponding to the coupling from site $i = 0$ to the other lattice degrees of freedom and the cavity action $S^{(0)}$, so that

$$S = S_0 + \Delta S + S^{(0)} \tag{2.39}$$

with the definitions

$$
S_0 = \int_0^\beta d\tau \left( \sum_\sigma c_{0\sigma}^\dagger(\tau)(\partial_\tau - \mu)c_{0\sigma}(\tau) + U n_{0\uparrow}(\tau)n_{0\downarrow}(\tau) \right) \tag{2.40}
$$

$$
\Delta S = -\int_0^\beta d\tau \sum_{i\sigma} t_{i0}(c_{i\sigma}^\dagger(\tau)c_{0\sigma}(\tau) + c_{0\sigma}^\dagger(\tau)c_{i\sigma}(\tau)). \tag{2.41}
$$

With these definitions the partition function reads

$$
Z = \int Dc_{0\sigma}^\dagger Dc_{0\sigma} e^{-S_0} \int \prod_{i\neq 0} Dc_{i\sigma}^\dagger Dc_{i\sigma} \exp\left( -S^{(0)} - \int_0^\beta d\tau \Delta S(\tau) \right), \tag{2.42}
$$

with $\Delta S = \int_0^\beta d\tau \Delta S(\tau)$. Expanding (2.42) results in

$$
\begin{aligned}
Z = {} & \int Dc_{0\sigma}^\dagger Dc_{0\sigma} e^{-S_0} \int \prod_{i\neq 0} Dc_{i\sigma}^\dagger Dc_{i\sigma} e^{-S^{(0)}} \\
& \times \left( 1 - \int_0^\beta d\tau \Delta S(\tau) + \frac{1}{2} \int_0^\beta d\tau_1 \int_0^\beta d\tau_2 T_\tau \Delta S(\tau_1)\Delta S(\tau_2) + \dots \right).
\end{aligned} \tag{2.43}
$$

By noting that expectation values of the cavity system,

$$
\langle A \rangle^{(0)} = \frac{1}{Z^{(0)}} \int \prod_{i\neq 0} Dc_{i\sigma}^\dagger Dc_{i\sigma} \, A \, e^{-S^{(0)}} \tag{2.44}
$$

occur in (2.43), we obtain

$$
\begin{aligned}
Z = {} & \int Dc_{0\sigma}^\dagger Dc_{0\sigma} \, e^{-S_0} Z^{(0)} \Big( 1 - \int_0^\beta d\tau \langle \Delta S(\tau) \rangle^{(0)} \\
& + \frac{1}{2} \int_0^\beta d\tau_1 \int_0^\beta d\tau_2 \langle T_\tau \Delta S(\tau_1)\Delta S(\tau_2) \rangle^{(0)} + \dots \Big),
\end{aligned} \tag{2.45}
$$

where $T_\tau$ is the imaginary time ordering operator. In case of fermions, which we consider here, the odd terms of the expansion vanish, which however is not true for bosons [65, 150]. Therefore, by substituting definition (2.41) the leading

*2. Strongly correlated fermions in high dimensions*

order contribution is given by

$$\frac{1}{2}\int_0^\beta d\tau_1 \int_0^\beta d\tau_2 \sum_\sigma c_{0\sigma}^\dagger(\tau_1) \sum_{ij} t_{i0}t_{0j}\langle T_\tau c_{i\sigma}(\tau_1)c_{j\sigma}^\dagger(\tau_2)\rangle^{(0)} c_{0\sigma}(\tau_2)$$

$$= -\frac{1}{2}\int_0^\beta d\tau_1 \int_0^\beta d\tau_2 \sum_\sigma c_{0\sigma}^\dagger(\tau_1) \sum_{ij} t_{i0}t_{0j}G_{ij}^{(0)}(\tau_1-\tau_2)c_{0\sigma}(\tau_2) \qquad (2.46)$$

in which the cavity Green's function $G_{ij}^{(0)}(\tau_1-\tau_2)$ is identified. The higher order contributions consist of n-particle cavity Green's functions where, according to the linked cluster theorem, all unconnected Green's functions can be written as a sum of only connected Green's functions. Returning back to the definition of the effective action (2.38) we find

$$S_{\text{eff}} = \ln Z - \ln Z_{\text{eff}} - \ln \left( \int \prod_{i\neq 0,\sigma} Dc_{i\sigma}^\dagger Dc_{i\sigma} e^{-S} \right)$$

$$= \text{const} + S_0 + \sum_{n=1}^\infty \sum_{i_1,\cdots,j_n} \int d\tau_{i_1}\ldots d\tau_{j_n} c_{0\sigma}^\dagger(\tau_{i_1})\ldots c_{0\sigma}^\dagger(\tau_{i_n})$$

$$G_{i_1\cdots j_n}^{(0)}(\tau_{i_1}\ldots\tau_{j_n})c_{0\sigma}(\tau_{j_1})\ldots c_{0\sigma}(\tau_{j_n}) . \qquad (2.47)$$

This expression simplifies considerably in the limit of infinite dimensions, as will be shown in the subsequent discussion.

To obtain a meaningful limit in infinite dimensions, the kinetic energy must remain of the same order of magnitude as the interaction energy. For zero temperature, the kinetic energy is given as

$$E_{\text{kin}} = -t\sum_{ij,\sigma}\langle c_{i\sigma}^\dagger c_{j\sigma}\rangle , \qquad (2.48)$$

where the square of the element $\langle c_{i\sigma}^\dagger c_{j\sigma}\rangle$ of single-particle density matrix can be interpreted as the probability for a particle to hope from lattice site $j$ to lattice site $i$. For nearest neighbors we conclude that the probability scales accordingly to $|\langle c_{i\sigma}^\dagger c_{j\sigma}\rangle|^2 \sim 1/z \sim 1/d$ [193]. Hence, $\langle c_{i\sigma}^\dagger c_{j\sigma}\rangle \sim 1/\sqrt{z} \sim 1/\sqrt{d}$ and the single-particle Green's function scales in the same manner. Therefore the hopping amplitude must be scaled as [193]

$$t = \frac{t^*}{\sqrt{z}} \qquad (2.49)$$

with dimension independent $t^*$ in order to keep the kinetic energy finite in the limit of infinite dimensions. For general sites $i$ and $j$ the single-particle Green's function scales as [88, 193]

$$G_{ij,\sigma} \sim d^{-\frac{1}{2}\|\mathbf{R_i}-\mathbf{R_j}\|} \ . \tag{2.50}$$

Due to this property, all connected irreducible diagrams of a diagrammatic perturbation theory in the local interaction $U$ collapse to their local contributions in position space [193]. In particular, the self-energy becomes local

$$\Sigma_{ij,\sigma}(\omega) \to \delta_{i,j}\Sigma_i(\omega) \ . \tag{2.51}$$

In order to evaluate the summation involving the connected n-particle cavity Green's functions in equation (2.47), we have to determine the overall scaling factor of each term in the order $n$ contribution. For the single-particle term we find a contribution $d^2$ from the summation over $i$ and $j$, a contribution of $d^{-1}$ from both the factor $t^2$ as well as from $G_{ij}$, resulting in a net constant scaling factor. The second term is composed of a contribution $d^4$ from the summation over $i_1, i_2, j_1$ and $j_2$, a contribution $d^{-2}$ from the hopping amplitude to the forth power and a contribution of $d^{-3}$ from $G_{i_1,i_2,j_1,j_2}$ if $i_1, i_2, j_1$ and $j_2$ are all different, giving a total scaling $1/d$ [123]. If the summation indices take the same value then a total scaling $1/d$ is also obtained [123]. Therefore, it can be seen that all higher order terms vanish if the dimension is scaled to infinity [123] and we finally obtain the effective action

$$S_{\text{eff}} = -\int_0^\beta d\tau_1 \int_0^\beta d\tau_2 \, c_{0\sigma}^\dagger(\tau_1)\mathcal{G}_0^{-1}(\tau_1-\tau_2)c_{0\sigma}(\tau_2) + U\int_0^\beta d\tau \, n_{0\uparrow}(\tau)n_{0\downarrow}(\tau) \tag{2.52}$$

where $\mathcal{G}_0$ denotes the so-called Weiss function. The Fourier transformed Weiss function is given as

$$\mathcal{G}_0^{-1}(i\omega_n) = i\omega_n + \mu - \Gamma(i\omega_n) \tag{2.53}$$

with Matsubara frequencies $\omega_n = (2n+1)\pi/\beta$ [215]. The so-called hybridization function

$$\Gamma(i\omega_n) = \sum_{i,j} t_{0i}t_{0j}G_{ij}^{(0)}(i\omega_n) \ , \tag{2.54}$$

where $j,k$ are summed over nearest neighbors, relates the Weiss function to the cavity Greens function $G_{ij}^{(0)}$. The cavity Greens function in turn can be

*2. Strongly correlated fermions in high dimensions*

expressed through the Greens function of the original lattice [149]

$$G_{ij}^{(0)} = G_{ij} - \frac{G_{i0}G_{0j}}{G_{00}} \, , \tag{2.55}$$

enabling the construction of a self-consistent closed set of equations. The effective action (2.52) is exact in infinite dimensions under appropriate scaling (2.49) of the hopping amplitude. In finite dimensions the effective action corresponds to an approximate action with small control parameter $1/z$.

By using the Fourier transform of the Greens function $G_{ij}(i\omega_n)$

$$G_{ij}(i\omega_n) = \sum_{\mathbf{k}} e^{i\mathbf{k}\cdot(\mathbf{R_i}-\mathbf{R_j})} G_{\mathbf{k}}(i\omega_n) \, , \tag{2.56}$$

we find that

$$
\begin{aligned}
\sum_{i,j} t_{0i}t_{0j} G_{ij}(i\omega_n) &= \sum_{i,j} t_{0i}t_{0j} \sum_{\mathbf{k}} e^{i\mathbf{k}\cdot(\mathbf{R}_i-\mathbf{R}_j)} G_{\mathbf{k}}(i\omega_n) \\
&= \sum_{i,j} \sum_{\mathbf{k}} t_{0i}t_{0j} e^{i\mathbf{k}\cdot(\mathbf{R}_i-\mathbf{R}_j)} \frac{1}{i\omega_n + \mu - \Sigma(i\omega_n) - \epsilon_{\mathbf{k}}}
\end{aligned}
\tag{2.57}
$$

under the assumption of a local self-energy [193]. We can identify the sum $\sum_i t_{0i} \exp{(i\mathbf{k}\cdot\mathbf{R}_i)}$ gives the dispersion relation $\epsilon_k$ and therefore the hybridization can be written as

$$\Gamma(i\omega_n) = I_2 - \frac{(I_1)^2}{I_0} \, , \tag{2.58}$$

where

$$I_0(\xi) \quad := \quad \int_{-\infty}^{\infty} d\epsilon \, \rho^{\mathrm{lat}}(\epsilon) \frac{1}{\xi - \epsilon} \tag{2.59}$$

$$I_1(\xi) \quad := \quad \int_{-\infty}^{\infty} d\epsilon \, \rho^{\mathrm{lat}}(\epsilon) \frac{\epsilon}{\xi - \epsilon} \tag{2.60}$$

$$I_2(\xi) \quad := \quad \int_{-\infty}^{\infty} d\epsilon \, \rho^{\mathrm{lat}}(\epsilon) \frac{\epsilon^2}{\xi - \epsilon} \, . \tag{2.61}$$

Here, $\rho^{\mathrm{lat}}(\epsilon)$ is the non-interacting density of states of the original lattice and $\xi := i\omega_n + \mu - \Sigma(i\omega_n)$.

From equations (2.59 - 2.61) we can identify the relations $I_1 = -1 + \xi I_0$ and $I_2 = \xi I_1$, from which equation (2.54) may be reduced to a simpler form:

$$
\begin{aligned}
\Gamma(i\omega_n) &= \xi I_1 - \frac{(-1 + \xi I_0)^2}{I_0} \\
&= \xi(-1 + \xi I_0) - I_0^{-1} + 2\xi - \xi^2 I_0 \\
&= \xi - \frac{1}{I_0}.
\end{aligned}
\tag{2.62}
$$

Hence, the Weiss function finally reads

$$
\begin{aligned}
\mathcal{G}_0^{-1}(i\omega_n) &= \Sigma(i\omega_n) + \left( \int_{-\infty}^{\infty} d\epsilon\, \rho(\epsilon) \frac{1}{\xi - \epsilon} \right)^{-1} \\
&= \Sigma(i\omega_n) + G_{00}^{-1}(i\omega_n).
\end{aligned}
\tag{2.63}
$$

Here in the second step, the k-summed Dyson equation

$$
G_{ii}(i\omega_n) = \sum_{\mathbf{k}} G(\mathbf{k}, i\omega_n)
\tag{2.64}
$$

$$
= \sum_{\mathbf{k}} \frac{1}{i\omega_n + \mu - \epsilon_{\mathbf{k}} - \Sigma(i\omega)}
\tag{2.65}
$$

$$
= \int d\epsilon\, \frac{\rho(\epsilon)}{i\omega_n + \mu - \Sigma(i\omega_n) - \epsilon}
\tag{2.66}
$$

was used, which presumes a local self-energy. In equation (2.65) we exploit the fact, that in infinite dimensions, the momentum dependence of the Green's function is only present in the dispersion [210]. By using the short-hand notation $G_{00} \equiv G$ we arrive at the Dyson equation

$$
G^{-1} = \mathcal{G}_0^{-1} - \Sigma .
\tag{2.67}
$$

To summarize, by focusing on a single lattice site, integrating out the degrees of freedom of the remaining lattice and taking the limit of infinite dimensions we have obtained a set of self-consistent equations

$$
S_{\text{eff}} = -\int_0^{\beta} d\tau_1 \int_0^{\beta} d\tau_2\, c_{0\sigma}^{\dagger}(\tau_1) \mathcal{G}_0^{-1}(\tau_1 - \tau_2) c_{0\sigma}(\tau_2) + U \int_0^{\beta} d\tau\, n_{0\uparrow}(\tau) n_{0\downarrow}(\tau)
\tag{2.68}
$$

$$
G(i\omega_n) = \int d\epsilon\, \frac{\rho^{\text{lat}}(\epsilon)}{i\omega_n + \mu - \Sigma(i\omega_n) - \epsilon}
\tag{2.69}
$$
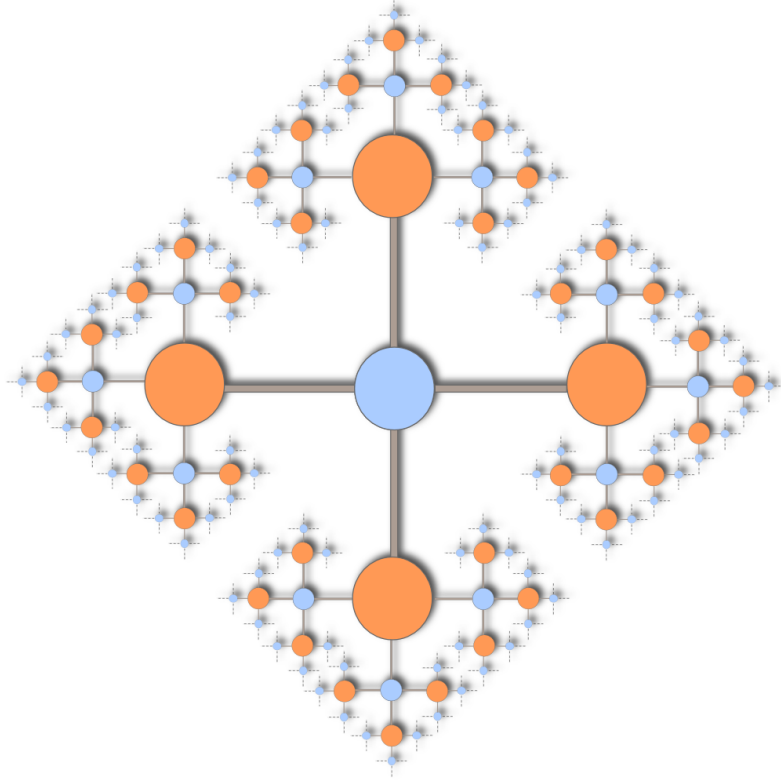
**Figure 2.2.:** Illustration of the Bethe lattice with coordination number $z = 4$ and accordingly connectivity $K = 3$.

$$\mathcal{G}_0^{-1}(i\omega_n) \quad = \quad G^{-1}(i\omega_n) + \Sigma(i\omega_n) \,. \tag{2.70}$$

These equations define a single-site quantum impurity system embedded in an effective medium, which has to be determined self-consistently and can be interpreted as a mean-field theory in the sense that spatial fluctuations are frozen. However, quantum fluctuations are still present, which can be seen from the energy dependence of the self-consistency equations. The impurity quantum state will fluctuate in time, driven by the bath Weiss function $\mathcal{G}_0$, which represents the influence of the remaining lattice[6], and the local interaction.

Equation (2.69) is simplified enormously if the Bethe lattice [90, 123, 168] is considered. The Bethe lattice is not a Bravais lattice – as it does not possess the usual point symmetry – but a tree-like, loop-free Graph (as depicted in figure 2.2)

---

[6]In particular, the Weiss function should not be mistaken as the non-interacting lattice Green's function.

with fixed coordination number $z$, related to the connectivity $K$ via $K = z - 1$. It exhibits a semi-elliptical density of states and is bipartite. For a finite lattice, the number of sites increases exponentially with the distances to the central site, such that the number of boundary sites is as numerous as the number of sites in the bulk. Nevertheless, it often gives valuable insight into statistical physics and condensed matter problems, since these problems often become simpler and may be even able to be solved analytically (e.g. in case of Ising physics [146], percolation physics [99] or disorder physics [2, 100]). In the context of DMFT and the limit of infinite dimensions it becomes especially valuable, as the density of states of a hypercubic lattice is given by a Gaussian [193], which is well approximated by the semi-elliptical density of states of the Bethe lattice [283]. Furthermore, it is interesting to note that the influence of the lattice structure is only present in the calculations due to the corresponding density of states in equation (2.69). A detailed comparison between the hypercubic lattice and the Bethe lattice with respect to the Mott transition is given e.g. in [55] and remarkable agreement was found. The Hilbert transform appearing in equation (2.69) can be performed explicitly in case of the Bethe lattice, i.e. the semi-elliptical density of states together with the Dyson equation produce a simple self-consistency relation of the form

$$\mathcal{G}_0^{-1}(i\omega_n) = i\omega_n + \mu - t^2 G(i\omega_n) . \tag{2.71}$$

## 2.4. Impurity model mean-field picture of DMFT

Georges and Kotliar [122] described a mean-field picture, which has become very convenient to use in practical calculations. They related the effective action (2.68) to the action given by the single impurity Anderson Hamiltonian [19]

$$H_{\text{AIM}} = \sum_{\mathbf{k}\sigma} \varsigma_{\mathbf{k}} a_{\mathbf{k}\sigma}^\dagger a_{\mathbf{k}\sigma} + \sum_{\mathbf{k}\sigma} (V_{\mathbf{k}} a_{\mathbf{k}\sigma}^\dagger c_\sigma + V_{\mathbf{k}}^* c_\sigma^\dagger a_{\mathbf{k}\sigma}) - \mu \sum_\sigma c_\sigma^\dagger c_\sigma + U n_\uparrow n_\downarrow , \tag{2.72}$$

where $a_{\mathbf{k}\sigma}^\dagger$ is the fermionic creation operator of a conduction electron, $c_\sigma^\dagger$ is the fermionic impurity creation operator, $n_\sigma = c_\sigma^\dagger c_\sigma$ is the impurity number operator, $\varsigma_{\mathbf{k}}$ the bath band energies and coupling constants $V_{\mathbf{k}}$. The corresponding action is quadratic in the corresponding conduction band Grassmann variables $a_{\mathbf{k}\sigma}$.

*2. Strongly correlated fermions in high dimensions*

Thus, these can be integrated out, giving rise to the action

$$
S_{\text{AIM}} \quad = \quad - \int_0^\beta d\tau_1 \int_0^\beta d\tau_2 \, c_\sigma^\dagger(\tau_1) \mathcal{G}_{\text{AIM}}^{-1}(\tau_1 - \tau_2) c_\sigma(\tau_2) + U \int_0^\beta d\tau \, n_\uparrow(\tau) n_\downarrow(\tau) \, ,
$$

(2.73)

where $\mathcal{G}_{\text{AIM}}$ after Fourier transformation is given as

$$
\mathcal{G}_{\text{AIM}}^{-1}(i\omega_n) = i\omega_n + \mu - \int_{-\infty}^\infty d\omega \, \frac{\gamma(\omega)}{i\omega_n - \omega}
$$

(2.74)

and

$$
\gamma(\omega) = \sum_{\mathbf{k}} |V_{\mathbf{k}}|^2 \delta(\omega - \varsigma_{\mathbf{k}}) \, .
$$

(2.75)

By comparison to equation (2.54) we find that, if

$$
\Gamma(i\omega_n) = \int_{-\infty}^\infty d\omega \, \frac{\gamma(\omega)}{i\omega_n - \omega} \, ,
$$

(2.76)

then the Anderson impurity Hamiltonian (2.72) constitutes a Hamiltonian representation of the effective action given in equation (2.52). For a given hybridization function $\Gamma$ there are many possible sets of Anderson impurity model parameters $V_{\mathbf{k}}$ and $\varsigma_{\mathbf{k}}$. The connection of the single-site quantum impurity system embedded in an effective medium to that of the Anderson impurity problem is finally made by requiring that the impurity self-energy corresponds to the local self-energy of the lattice problem in high dimensions [122], i.e.

$$
\Sigma_{\text{imp}}(i\omega_n) \equiv \Sigma(i\omega_n) \, .
$$

(2.77)

We have finally derived a practical and convenient self-consistent calculation scheme[7], which is depicted in figure 2.3. The scheme is begun by assuming a particular hybridization function or likewise a Weiss function $\mathcal{G}_{\text{AIM}}$, which constitutes the impurity problem. Afterwards the impurity problem (2.72) has to be solved, which results in an impurity self-energy $\Sigma_{\text{imp}}$. Then the local lattice self-energy is identified as the impurity self-energy and the lattice Green's function is obtained by the Hilbert transform (2.69). Subsequent application of

---

[7]It should be mentioned that there exist more than one way of implementing a self-consistent DMFT calculation scheme.
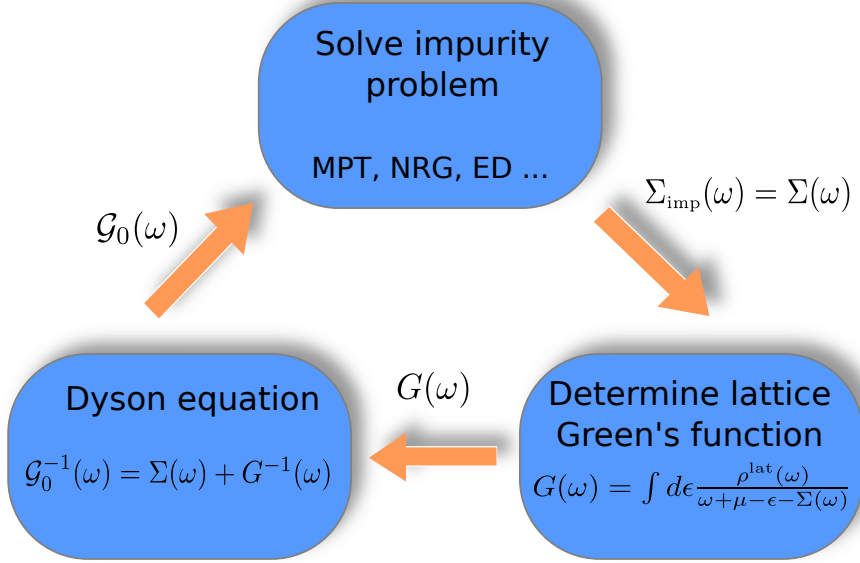
**Figure 2.3.:** Illustration of the DMFT self-consistent calculation scheme.

the Dyson equation (2.70) yields a new hybridization function. The scheme is iterated until self-consistency is obtained.

The difficult step in the self-consistency loop is the solution of the single-impurity Anderson model. However, during the last four decades a number of different solution or approximative solution methods have been established. In the next section the impurity solver that is used later in this work will be introduced. A literature review of various impurity solvers, as well as a brief introduction to their use can be found e.g. in [123].

## 2.5. Iterated and modified perturbation theory

In order to realize a DMFT computation we have to solve the single impurity Anderson model (2.72), a non-trivial many-body problem. A method that determines the self-energy for a given hybridization is called impurity solver. In the following we will shortly introduce the impurity solver, which will be used in the following chapters of this thesis.

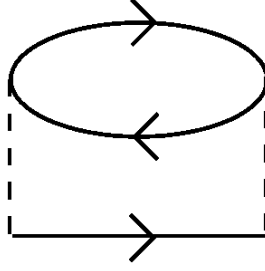An approximate analytical solution of the Anderson impurity problem can

**Figure 2.4.:** Second order contribution to the self-energy in perturbation theory.

be obtained by perturbation theory (see e.g. [301]) in the interaction strength $U$. The self-energy is given by series expansion

$$\Sigma(\omega) = \Sigma^{(1)}(\omega) + \Sigma^{(2)}(\omega) + O(U^3) \,, \tag{2.78}$$

where the constant first order contribution, also called the Hartree-Fock contribution is $\Sigma^{(1)}(\omega) = U\langle n \rangle$, where $n$ denotes the number operator. The second order contribution (see figure 2.4) is given by a three-fold integrals

$$\begin{aligned}
\Sigma^{(2)}(\omega) &= U^2 \int\limits_{-\infty}^{0} d\epsilon_1 \int\limits_{0}^{\infty} d\epsilon_2 \int\limits_{0}^{\infty} d\epsilon_3 \, \frac{\rho^{(0)}(\epsilon_1)\rho^{(0)}(\epsilon_2)\rho^{(0)}(\epsilon_3)}{\omega + \epsilon_1 - \epsilon_2 - \epsilon_3 + i\eta} \\
&+ U^2 \int\limits_{0}^{\infty} d\epsilon_1 \int\limits_{-\infty}^{0} d\epsilon_2 \int\limits_{-\infty}^{0} d\epsilon_3 \, \frac{\rho^{(0)}(\epsilon_1)\rho^{(0)}(\epsilon_2)\rho^{(0)}(\epsilon_3)}{\omega + \epsilon_1 - \epsilon_2 - \epsilon_3 + i\eta} \,.
\end{aligned} \tag{2.79}$$

Here, $\rho^{(0)}$ denotes the Hartree-Fock spectral function

$$\rho^{(0)}(\omega) := -\frac{1}{\pi}\text{Im}\left(\frac{1}{\omega + \tilde{\mu} - \epsilon - U\langle n \rangle - \Gamma(\omega) + i\eta}\right) \tag{2.80}$$

with the parameter $\tilde{\mu}$, which will be fixed later. This means, that the perturbation theory chosen here is performed with respect to the Hartree-Fock solution. Besides other applications the expansion was used to investigate the periodic Anderson model [245, 246, 302], where it is usually termed second order perturbation theory. In context of DMFT, it is usually called iterated perturbation theory (IPT), as the solution has to be determined self-consistently [121–123, 237, 247, 305].

Of course, a three-fold integral is numerically expensive to evaluate. In order

to reduce the effort, the identity

$$-i \int_0^\infty dt \, e^{it(z+\epsilon_1-\epsilon_2-\epsilon_3)} = \frac{1}{z + \epsilon_1 - \epsilon_2 - \epsilon_3} \tag{2.81}$$

is used, which is valid for a complex $z$ with a small positive imaginary part. After performing the Fourier transforms

$$\tilde{\rho}_\pm(t) = \int_0^\infty d\omega \, e^{-i\omega t} \rho^{(0)}(\pm\omega) \tag{2.82}$$

the second contribution to the self-energy becomes

$$\Sigma^{(2)}(\omega) = \frac{U^2}{i} \int_0^\infty dt \, e^{i\omega t} \left( \tilde{\rho}_-(t)\tilde{\rho}_+(t)\tilde{\rho}_+(t) + \tilde{\rho}_+(-t)\tilde{\rho}_-(-t)\tilde{\rho}_-(-t) \right). \tag{2.83}$$

Hence, the original three-fold integral has been substituted by simple single integrals, which can be numerically implemented efficiently by the fast Fourier transform algorithm.

One may be tempted to ask, how a perturbation theory would be a useful impurity solver within a DMFT scheme at all, as the most intriguing feature of DMFT is that it treats local correlations non-perturbatively. However, it turns out, that the second order perturbation theory reproduces the atomic limit in the half-filled case [305] and combined with the intrinsic good description at weak interactions, IPT represents a reliable interpolation scheme between the weakly and the strongly interacting limits. Comparison to exact diagonalization and quantum Monte-Carlo calculations showed convincing agreement in the paramagnetic case [121].

The original formulation of the IPT was restricted to the half-filled case. Later the method was extended to work with densities away from half-filling and this extension is commonly referred to as modified perturbation theory (MPT) [161, 228]. The self-energy within MPT is given by a interpolation formula [161]

$$\Sigma(\omega) = Un + \frac{a\Sigma^{(2)}(\omega)}{1 - b\Sigma^{(2)}(\omega)}. \tag{2.84}$$

Therefore three parameters, namely $a$, $b$ and $\tilde{\mu}$ have to be fixed. For $a = 1$ and $b = 0$, IPT is reproduced.

## 2. Strongly correlated fermions in high dimensions

Kajueter and Kotliar used a $1/\omega$ expansion of the self-energy and chose $a$ such that the high-energy behavior is reproduced exactly for the first two coefficients of the expansion [161], giving

$$a = \frac{\langle n \rangle (1 - \langle n \rangle)}{\langle n \rangle^{(0)} (1 - \langle n \rangle^{(0)})} \,, \tag{2.85}$$

with $\langle n \rangle^{(0)}$ being the occupation corresponding to the Hartree-Fock solution. Afterwards, the parameter $b$ was fixed to reproduce the atomic limit. Potthoff *et al.* [228] improved the ansatz by fixing the first three ($m = 0,1,2,3$) spectral moments resulting from a equation of motion analysis,

$$M^{(m)} = \int\limits_{-\infty}^{\infty} d\omega \rho(\omega) \omega^m \,, \tag{2.86}$$

as performed in the spectral density approach (SDA) [216], which constitutes a strong coupling approach to the Hubbard model, by assuming a two-pole structure of the Green's function. For the parameter $b$ it has been shown [228] that the choice

$$b = \frac{B - B^{(0)} - \mu + \tilde{\mu} + U(1 - 2\langle n \rangle)}{U^2 \, n^{(0)} (1 - \langle n \rangle^{(0)})} \,, \tag{2.87}$$

ensures the correct high-energy behavior of the spectral function up to $m = 3$, with higher order correlation function $B^{(0)}$ and $B$. Furthermore, this choice delivers the correct behavior in the atomic limit. Both higher order correlation functions are determined self-consistently,

$$B^{(0)} = \epsilon + \frac{1 - 2\langle n \rangle^{(0)}}{\pi \langle n \rangle^{(0)} (1 - \langle n \rangle^{(0)})} \text{Im} \int\limits_{-\infty}^{0} d\omega \, \Gamma(\omega) G^{(0)}(\omega) \,.$$

The correlation function $B$ is given by

$$B = \epsilon - \frac{1}{\pi \langle n \rangle (1 - \langle n \rangle)} \text{Im} \int\limits_{-\infty}^{0} d\omega \, \Gamma(\omega) \big( \frac{2}{U} \Sigma(\omega) - 1 \big) G(\omega) \,. \tag{2.88}$$

Finally, the parameter $\tilde{\mu}$ has to be fixed. According to Ref. [228] there are three approaches for fixing $\tilde{\mu}$. The first is to require $\mu = \tilde{\mu}$. Secondly, one imposes the Friedel sum rule to ensure the low energy Fermi liquid behavior as done by Kajueter and Kotliar [161]. The last possibility requires that $n^{(0)} = n$. All three

possibilities do not affect the validity of the MPT in the weakly interacting limit as all methods guarantee that $\tilde{\mu} \to \mu_{U=0}$ as $U \to 0$ [228]. Furthermore, all three approaches have been compared carefully and checked against exact diagonalization (ED) calculations [228]. In conclusion, the second and the third approach show very good agreement whereas the first one differs considerably from ED results. In the work presented here we choose the third possibility.

In summary, the MPT self-energy shows by construction the correct behavior in the weakly interacting regime and by fixing the first three spectral moments also incorporates the correct high-energy behavior as given by the strong coupling SDA. Moreover, as it is also exact in the atomic limit, it represents a reliable interpolation scheme between the weakly and strongly interacting regimes.

## 2.6. Mott metal-insulator transition

An *insulator* is conventionally defined by a vanishing static electrical conductivity at zero temperature [120]. The conductivity in turn is given as current-current correlation function and therefore describes the propagation of a particle-hole pair. Hence, for a finite conductivity there exists a requirement that states of particle-hole excitation must be available at energies immediately above the Fermi-level and these states must be delocalized, so that they can contribute to transport over a macroscopic sample size.

This basic definition results in the gap criterion if the motion of the particle and the hole are uncorrelated. Since in this case the particle-hole motion can be decomposed into the superposition of two individual single-particle excitations and the conductivity is directly related to the single-particle excitation spectrum; then the single-particle spectral function in the insulating phase exhibits a gap.

In contrast, the relation between the single-particle spectral function and the conductivity is invalid if, for example, the electrons form bound states as in case of superconductivity. However, throughout this work, we will use the zero-temperature gap of single-particle excitations to macroscopically extended states as definition of an insulator.

In figure 2.5 the spectral functions resulting from a DMFT calculation using MPT as an impurity solver are compared between the Bethe lattice and the cubic lattice for increasing on-site interaction strength $U$ at half-filling. We note the formation of the two Hubbard subbands, constituting incoherent single-particle excitations. Furthermore, coherent excitations are present for weak and intermediate interaction strength. As soon as the critical interaction strength $U_c$ is reached, the system becomes a *Mott insulator* as is signaled by the opening
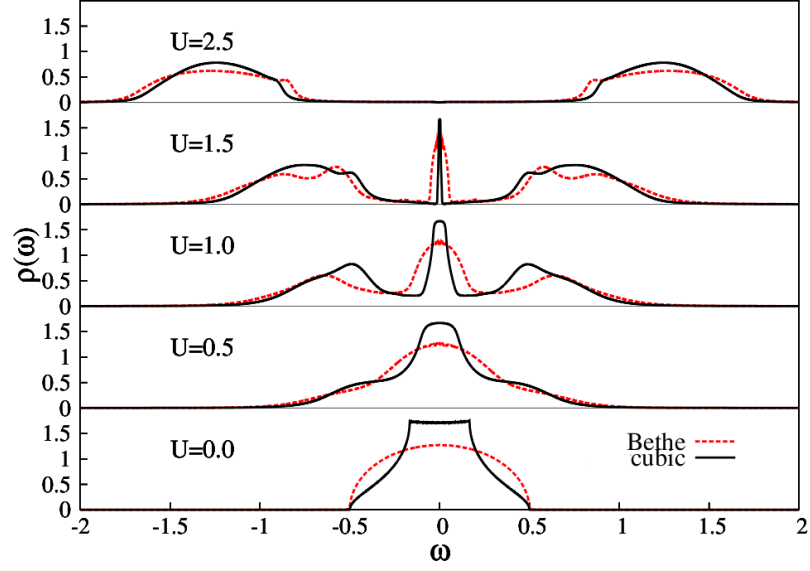
**Figure 2.5.:** Evolution of the spectral function with increasing interaction strength $U$ obtained within a DMFT+MPT calculation for the Bethe lattice and the cubic lattice at half-filling. In units of the non-interacting bandwidth $W_0$.

of the gap in the single-particle excitation spectrum. Here, we see explicitly one of the breakthroughs of DMFT mentioned previously, as it is capable of describing the *Mott transition* in the Hubbard model. Detailed DMFT studies of the Mott metal-insulator transition can be found in [55, 57, 121, 236, 305].

# 3. Localization in disordered lattices

A further route to the understanding of a different class of metal-insulator transitions was triggered by electron spin resonance experiments [104, 105]. Extraordinary large relaxation times of impurity spins in doped silicon were found in comparison to Golden Rule predictions. These results were interpreted as the absence of spin diffusion [20, 106].

In 1958, Anderson examined quantum transport in random lattices to give an explanation, and thereby set up the research field of disordered materials [17]. By investigating the diffusion process of a single particle in a random potential he showed that the particle localizes, if the disorder strength exceeds a critical value. In the first place, localization was understood as the 'absence of diffusion'. That is, the localization manifests itself in a finite return probability to the lattice site of the infinite system where the particle was initially located. Later, the equivalent, well-known interpretation was elaborated that a localized particle is exponentially localized in space [47, 204, 207].

Anderson's findings stimulated extensive theoretical and experimental research[1]. Mott gave reasoning for the existence of a sharp transition in the spectrum from extended states in the interior of the band to localized states in the outer parts [204]. Such energies are commonly referred to as mobility edges [93]. The early considerations cumulated in the picture that under an increase of the disorder strength, the mobility edges move from the band tails to the band center [93]. As soon as the band center is reached, all states are localized which is named Anderson transition [92, 185, 204, 307]. To be more precise, the Anderson transition is characterized by a change of the states at the Fermi level from being macroscopically extended to exponentially localized, thus giving rise to a metal-insulator transition.

Valuable progress has been achieved by the single-parameter scaling theory [3, 289], from which it is concluded that an arbitrarily small amount of disorder excludes extended states in one dimension[2] and two dimensions. In contrast, an Anderson transition takes place in three dimensions. The analysis showed that

---

[1]Comprehensive reviews on disorder physics are e.g. given by Elliot, Krumhansl and Leath [96], Thouless [270], Lee and Ramakrishnan [182], Phillips [224] or Kramer and MacKinnon [172].

[2]For one dimension this result was already obtained earlier by Mott and Twose [207].

the dimension two is marginal, which was taken as starting point by Schäfer and Wegner [241, 290] for further analysis. They performed a dimensional expansion around the marginal dimension and constructed by the non-linear sigma model an effective field-theoretical approach for weak disorder. Although being inherently phenomenological, the scaling theory received wide theoretical confirmation, besides others by the weak-disorder diagrammatic self-consistent theory [284–286] or by numerical studies (e.g. [259]).

The theory of weak localization was established in the course of investigating effects due to the presence of weak disorder in the metallic regime [3, 33, 128, 181, 182, 284, 285]. It is basically understood as coherent backscattering processes [181] and self-interference of a propagating quantum particle. Thereby, corrections to transport properties arise, such as the famous logarithmic correction to the temperature dependence of the conductivity [128]. Weak localization is often considered as a precursor to the Anderson localization[3] and the theoretical predictions were extensively tested within experiments on thin metal films [33].

However, all analytic investigations involve in one or more aspects approximations or inhere limitations, such as describing only weak disorder. Therefore, numerical methods serve as veritable tools for testing predictions of the analytic statements and for quantitative calculations of the critical disorder strength, the mobility edges, or the critical exponents. Commonly used methods are, for example, the transfer matrix method [192, 260], the kernel polynomial method [291] or the local distribution approach [2, 13–15]. The latter is of special interest within this work as it corresponds to the non-interacting limit of the statistical DMFT, which in turn is a generalization of DMFT to disordered systems and is discussed in section 4.4.

Nowadays, it is known that localization effects are not restricted to solids but a common phenomenon in wave physics [179, 294]. In this work, we focus on matter waves, in particular on cold atoms in optical lattices. These experimental setups are introduced in chapter 5.

## 3.1. Anderson Hamiltonian and localization

Anderson introduced a minimal tight binding Hamiltonian

$$H = \sum_{i\sigma} \epsilon_i c_{i\sigma}^\dagger c_{i\sigma} + \sum_{\langle i,j \rangle \sigma} t_{ij} c_{i\sigma}^\dagger c_{j\sigma} \, , \tag{3.1}$$

---

[3]In order to distinguish clearly between weak localization and Anderson localization, the latter is also referred to as strong localization.

known as the Anderson model. It consists of the tight-binding hopping term already introduced in the Hubbard model 2.1 and random on-site energies $\epsilon_i$. In general, the correlated probability distribution function (PDF) of all on-site energies $p_{\{\epsilon\}}(\epsilon_1, \ldots, \epsilon_N)$ has to be considered, but typically uncorrelated disorder is assumed given by[4]

$$p_{\{\epsilon\}}(\epsilon_1, \ldots, \epsilon_N) = \prod_{i=1}^{N} p_\epsilon(\epsilon) . \tag{3.2}$$

Therein the on-site energies $\epsilon_i$ are random quantities distributed identically and independently by a PDF $p_\epsilon(\epsilon)$. Its strength is subsequently denoted by a capital $\Delta$, which is proportional to the standard deviation of the PDF. Moreover, one often requires that the PDF is time independent, termed quenched disorder, which should be distinguished from thermally fluctuating disorder called annealed.

A first rough grasp of the physics of the Anderson model can be gained by looking at two limits. First, considering the strong disorder limit and treating the hopping as perturbation. It becomes apparent, that in zeroth order we will have disconnected lattice sites and the eigenstates are bound states. Moreover, a small perturbation is unlikely to give extended states over the entire lattice, as orbitals which are nearby in space will in general differ energetically strongly [17]. On the other hand, for zero disorder we are left with a tight-binding hopping Hamiltonian giving rise to extended Bloch waves as eigenstates. This heuristic reasoning indicates a transition from extended to localized states triggered by an increase of the ratio of disorder strength to the homogeneous, non-interacting bandwidth $\Delta/W_0$, where $W_0$ is given as function of the hopping amplitude.

To gain more insight into the phenomenon of localization and to obtain a criterion of localization at hand for our latter investigations, we consider a particle initially given at site 0. Under time evolution, the particle starts propagating through the infinite disordered lattice (cf. figure 3.1). The simple question, that Anderson brought forward is whether the particle is confined to a finite region of the lattice, i.e. it is localized or not. A natural and intuitive definition of being localized or extended is given via the return probability to the initial lattice site $p_{0 \to 0}(t)$ for time $t$ goes to infinity. If the return probability is finite, the particle is said to be localized. On the other hand, if the return

---

[4]This is quite often a reasonable assumption as e.g. within the theoretical description of doped semiconductors.
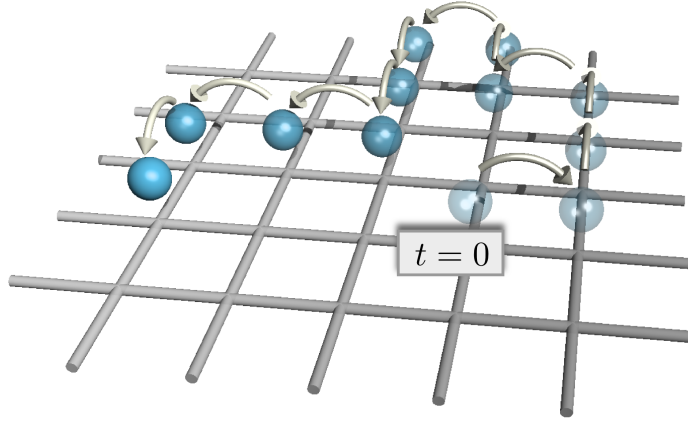
**Figure 3.1.:** Illustration of a particle diffusing from an initial lattice site.

probability is zero, the particle's wave function is extended:

$$\lim_{t \to \infty} p_{0 \to 0}(t) \begin{cases} > 0 & \text{localized} \\ = 0 & \text{extended} \end{cases} . \tag{3.3}$$

In the following, our aim is to infer analytical properties of the local Green's function $G_{ii}(\omega)$ from this definition of localization. The local Green's function is given as matrix element of the resolvent operator

$$G(z) = \frac{1}{z - H} , \tag{3.4}$$

in Wannier basis. For $z = \omega \pm i\eta$ the greater and lesser Green's function is obtained, corresponding to the retarded and advanced single-particle Green's function for non-interacting particles respectively [91]. The aimed connection is established below and follows the lines given by Thouless [269], Economou and Cohen [92] and Licciardello and Economou [185].

Returning to our particle initially in the Wannier state $|0\rangle$, the state at later times can be expanded in Wannier states

$$|\Psi(t)\rangle = \sum_n c_n(t)|n\rangle . \tag{3.5}$$

As already explained, the quantity of interest is the return probability to site zero [189, 270]

$$p_{0 \to 0}(t) := |c_0(t)|^2 = |G_{00}(t)|^2 \tag{3.6}$$

as time $t$ goes to infinity. Applying the final value theorem of the Laplace transform $\lim_{t\to\infty} f(t) = \lim_{u\to 0} uF(u)$ with the Laplace transform

$$F(u) = \int_0^\infty dt e^{-ut} f(t) \;, \tag{3.7}$$

we obtain

$$\lim_{t\to\infty} p_{0\to 0}(t) = \lim_{u\to 0} u \int_0^\infty dt |G_{00}(t)|^2 e^{-ut} \;. \tag{3.8}$$

By inserting the Fourier transforms of the time-dependent Green's functions, performing the integral over $t$ and finally using the Dirac identity, the return probability reads [92, 185, 270]

$$p_{0\to 0}(t \to \infty) = \lim_{u\to 0^+} \frac{u}{\pi} \int_{-\infty}^\infty d\omega G_{00}(\omega + iu) G_{00}(\omega - iu) \;. \tag{3.9}$$

Similar, the probability of our particle to be on lattice site $n$ is found to be

$$p_{0\to n}(t \to \infty) = \lim_{u\to 0^+} \frac{u}{\pi} \int_{-\infty}^\infty d\omega G_{0n}(\omega + iu) G_{n0}(\omega - iu) \tag{3.10}$$

and it can be shown that the sum of all probabilities $p_{0\to n}(t \to \infty)$ over all lattice sites equals one [92], as it should. Analogously to interacting many-body problems a 'self-energy'[5] $\Gamma_0(\omega)$ can be defined for the disorder problem [91, 92] (for more details see appendix B)

$$G_{00}(z) = \frac{1}{z - \epsilon_0 - \Gamma_0(z)} \;. \tag{3.11}$$

leading to [92]

$$p_{0\to 0}(t \to \infty) = \lim_{u\to 0^+} \frac{u}{\pi} \int_{-\infty}^\infty d\omega \frac{\mathrm{Im} G_{00}(\omega - iu)}{2iu - (\Gamma_0(\omega + iu) - \Gamma_0(\omega - iu))} \;. \tag{3.12}$$

---

[5]The terminus self-energy will be used only throughout this section for historical reasons, but should not be confused with the correlation-induced self-energy defined in section 2.2. Later, we refer to it as hybridization function (cf. sections 2.3 and 2.4).

*3. Localization in disordered lattices*

From equation (3.9), we can already see that the question, if a state is localized or not, is directly related to the analytic structure of the Green's function. A branch cut of the Green's function on the real $\omega$-axis will not give any contribution to the returning probability, as the limit $u \to 0$ gives well-defined finite values and the factor $u$ will lead to a total zero. Hence, branch cuts do not correspond to localized states but to extended states [91, 92]. On the other hand localized states are characterized by the non-existence of the limits $u \to 0$ and thus by poles on the real axis [92, 269]. By inserting the complete set of the eigenfunctions of the system $|\psi_n\rangle$ into equation (3.4), we find the local Green's function

$$G_{00}(\omega) = \sum_n \frac{f_n}{\omega - E_n} \ . \tag{3.13}$$

with the overlap $f_n = \langle 0|\psi_n\rangle\langle\psi_n|0\rangle$ of the eigenstate $n$ with the Wannier function on site 0 and the return probability is given by $p_{0\to 0}(t \to \infty) = \sum_n f_n^2$ [185]. An analogue expression can be found for the 'self-energy', except that here the poles correspond to the eigenenergies of the lattice with site 0 removed [92]. Random on-site energies lead to random eigenenergies $E_n$ and random residues $f_n$. Consequently, the local Green's function and the 'self-energy' are random variables as well. A random variable is generally described via a PDF, and the significance of studying PDFs was emphasized by Anderson from the very beginning [17].

In case of an extended eigenstate, the residue $f_n$ is proportional to the inverse number of lattice sites $N^{-1}$ and the return probability approaches zero in the limit of an infinite system. In contrast, for a localized state there is a distribution of poles in the allowed energy interval on the real $\omega$-axis. The distribution becomes dense in the limit $N \to \infty$ and the residues approach finite values. Since the residues are given by the overlap of the localized eigenstate with a single Wannier state, some residues will dominate the sum in equation (3.13). If the residues were sorted by value, their contribution would decrease exponentially for spatially localized states. In particular, if we consider a contour which encloses a small energy interval $\delta E$, then the *most probable* value of the sum of the residues of poles enclosed by the contour is of the order $\exp(-\Delta/\delta E)$. Accordingly, at a small distance $\eta$ from the real axis, the *most probable* value of the imaginary part of the Green's function is proportional to $\eta$ [269]. Hence, the local spectrum will be highly fragmented in case of localized eigenstates, characterized by dominating well-separated resonances. This fragmentation is impressively visualized, in a recent scanning tunneling microscope experiment [232]. In contrast, the averaged spectral function, i.e. the density of states of

the system, does not show these high fragmentation, since the spectral weight must be located somewhere in the lattice for each energy. We will use these specific analytic characteristics of the local Green's function throughout this work to study localization effects. How this is accomplished is explained in section 3.3.

In order to gain consolidated findings about the disorder physics, the 'self-energy' $\Gamma_0(\omega)$ has to be calculated at least in an approximative fashion. For that purpose the renormalized perturbation expansion [91] was used to a great deal [2, 17, 53, 92, 185]. The renormalized perturbation expansion (see appendix B) is based on ordinary perturbation expansion in the hopping, but only self-avoiding paths are summed up, which are decorated by factors accounting for the omitted loops. Within this approach the 'self-energy' reads [185] (see appendix B for the derivation)

$$
\begin{aligned}
\Gamma_0(\omega) \quad = \quad & \sum_{n \neq 0} t_{0n} \frac{1}{\omega - \epsilon_n - \Gamma_n^{(0)}} t_{n0} \\
& + \sum_{n \neq 0; n' \neq n,0} t_{0n'} \frac{1}{\omega - \epsilon_{n'} - \Gamma_{n'}^{(0,n)}} t_{n'n} \frac{1}{\omega - \epsilon_n - \Gamma_n^{(0)}} t_{n0} + \dots
\end{aligned}
$$

(3.14)

with $\Gamma_k^{(a,b,\dots)}$ the 'self-energy' at site $k$ of a lattice with sites $a, b, \dots$ removed. The appearing 'self-energies' can be expressed in a similar way and reinserting gives a continued-fraction expression for $\Gamma_0$, which terminates for a finite system. This expression in turn can be rewritten as a series [185]. In the infinite system the convergence of the series corresponds to a localized state, which was basically used by Anderson to study the diffusion process. He concentrated on the first term appearing in (3.14) and studied the convergence of the PDF of $\Gamma_0$ in the infinite system. By showing that higher order terms do not change the probabilistic convergence, he finally succeeded to show the existence of a critical disorder strength above which the series converges accounting for a localized state. For our purposes it is furthermore interesting to note that Abou-Chacra *et al.* [2] also took the first term into account, but solved the iterative procedure necessary for the continued-fraction expression self-consistently. This procedure paved the way to the method nowadays named local distribution approach.

The to date cumulated picture of localization in high-dimensional systems may be summarized roughly as follows [96, 172, 182, 224, 270]: The presence of disorder causes repeating scattering processes, leading to interference of the particle with itself. At weak disorder these processes give rise to corrections to transport properties of the system, known as weak localization. If the disorder

strength is high enough, the scattering processes finally lead to exponential localization [47, 204, 207] of the state with energy $\omega$ and the particle is confined to a finite region of the infinite lattice. The lattice Green's function is characterized by branch cuts and dense distributions of poles on the real axis, corresponding to an extended and localized spectrum respectively. Intermixing of extended states and localized states at the same energy is not possible, since the energetic degeneracy would delocalize the latter by hybridization. Thus, localized and extended states are well separated energetically [204]. One refers to these separation energies as mobility edges. In the spectrum, band tails emerge at the band edges due to the disorder, which fall off in an exponential manner [187]. With an increase of the disorder strength, the band tails extend and the states within localize first. A further increase causes the mobility edges to move to the core of the band until a critical strength is exceeded, corresponding to the localization of all states. Localized states have been shown to be not able to contribute to DC conductivity [118, 204, 205]. In fact, Mott originally defined localized states as states, which do not contribute to the DC conductivity [205, 208], which is equivalent to absence of diffusion in infinite systems [118]. This means that as soon as all states near the Fermi level become localized, a metal-insulator transition occurs at zero temperature known as *Anderson transition.*

## 3.2. Criteria of Localization

Besides the above discussed absence of diffusion, which might be judged by the finite return probability, several other quantities are used to define localization. In this section we will shortly introduce the most frequently used.

Of course, one way to distinguish extended states from localized states is given by direct calculation of the wave function in real space. The absolute value of the wave function of a localized state is characterized by a spatially exponentially declining envelope [47, 204, 207]

$$|\Psi(\mathbf{r})| \sim e^{-\frac{r}{\lambda}} \tag{3.15}$$

where $\lambda$ denotes the localization length. However, the explicit calculation of the wave function is a difficult task, since in general disorder models are hard to solve exactly. Strongly connected to the wave function, the participation ratio [270]

$$p := \left( \frac{\sum_i |\Psi(\mathbf{R_i})|^4}{(\sum_i |\Psi(\mathbf{R_i})|^2)^2} \right)^{-1} \tag{3.16}$$

and its inverse, the inverse participation ratio [287], represent further quantities, which allow for the distinction between localized and extended states. A localized state exhibits a ratio of order unity, whereas the inverse participation ratio scales like $L^{-d}$ for an extended state, where d denotes the dimension of the system and $L^d$ the volume of the system. These quantities are often used in numerical investigations on finite lattices and a proper finite size scaling is necessary to allow for a distinction between extended and localized states. Within finite-size scaling approaches, it is further possible to distinguish between the localized and extended regime by the level statistics on both sides of the metal-insulator transition [12, 143, 197, 254]. In the extended regime the distribution of the energy level spacing $P(s)$ corresponds to a Gaussian orthogonal ensemble, whereas a Poisson ensemble is given in the localized phase.

In finite systems, it can also be investigated, how the energy eigenvalues change when the boundary conditions are switched from periodic to anti-periodic [94]. While the eigenvalues of localized states are clearly unaffected, the eigenvalues of extended states are shifted by a value much larger than the typical energy spacing.

As we will see in detail in the next section 3.3, the analytic properties of the Green's function, which are strongly connected to the return probability as discussed above, can be used as a criterion for localization. Similar properties are of course also present in the analytic structure of the 'self-energy' $\Gamma$, which might be used to characterize localized states as well [185]. Remarkably, this criterion has been recently generalized to many-body localization for finite temperatures [29].

## 3.3. Local distribution method

From the discussion above, we already understand the validity of Anderson's early point of view [17], that the investigation of disordered system should naturally focus on PDFs and the use of averaged quantities is in general not sufficient. In Anderson's words [20]:

> "No real atom is an average atom, nor is an experiment ever done on an ensemble of samples."

The local distribution approach represents a self-consistent computational scheme for determining the PDF of the local single-particle Green's functions, i.e. $p\left[G_{ii\sigma}(\omega)\right]$. It was invented and analytically used by Abou-Chacra, Anderson and Thouless [2] and recently implemented numerically [13–15].

In the absence of interactions the renormalized perturbation expansion [91] shows that the local Green's function can always be expressed as [91, 92] (see

also appendix B)

$$G_{ii}(\omega) = \frac{1}{\omega + \mu - \epsilon_i - \Gamma_i(\omega) + i\eta}, \qquad (3.17)$$

where the hybridization function $\Gamma_i(\omega)$ – which we named in the discussion above as 'self-energy' for historical reasons – describes all effects of the coupling of site $i$ with other nearest neighbor lattice sites. The chemical potential is given by $\mu$. In order to study localization effects, the limit $\eta \to 0$ has to be performed as we will understand later in detail. Physically, the broadening $\eta$ represents a small coupling to a dissipative bath.

The hybridization function $\Gamma_i(\omega)$ can be expressed by an infinite, renormalized series of the form (see appendix B)

$$\Gamma_i(\omega) = \sum_{j \neq i} t_{ij} G_{jj}^{(i)}(\omega) t_{ji} + \sum_{j \neq i; k \neq j,i} t_{ij} G_{jj}^{(i)}(\omega) t_{jk} G_{kk}^{(j,i)}(\omega) t_{ki} + \dots, \quad (3.18)$$

where $G_{qq}^{(n,m,\dots)}(\omega)$ is the diagonal cavity Green's function of the system when the sites $n,m,\dots$ are removed. The corresponding diagonal cavity Green's functions are determined by similar series on cavity lattices and a hierarchy of equations is obtained.

On the Bethe lattice with connectivity $K = z - 1$ this series is exactly truncated after the first term (see appendix B) and the hybridization functions are exactly given by [2, 90, 168]

$$\Gamma_i(\omega) = \sum_{n \text{ N.N. of } i} t_{in} \frac{1}{z - \epsilon_n - \Gamma_n^{(i)}(\omega)} t_{ni} \qquad (3.19)$$

$$\Gamma_n^{(i)}(\omega) = \sum_{m \text{ N.N. of } n} t_{nm} \frac{1}{z - \epsilon_m - \Gamma_m^{(i,n)}(\omega)} t_{mn} \qquad (3.20)$$

$$\Gamma_m^{(i,n)}(\omega) = \sum_{o \text{ N.N. of } m} t_{mo} \frac{1}{z - \epsilon_o - \Gamma_o^{(i,n,m)}(\omega)} t_{om} \qquad (3.21)$$

$$\dots$$

Additionally we use the fact, that the cavity hybridization functions of lattices with several sites removed are also simplified due to the absence of loops on the Bethe lattice. The corresponding equations reproduce their structure from the second equation on (see appendix B) and therefore there are only two classes of hybridization functions - and corresponding Green's functions - governed by

the equations

$$
\begin{aligned}
\Gamma_i(\omega) &= \sum_{n=1}^{z} t_{in}^2 G_{nn}^{(i)}(\omega) & (3.22) \\
\Gamma_n^{(i)}(\omega) &= \sum_{m=1}^{K} t_{mn}^2 G_{mm}^{(n)}(\omega) \; . & (3.23)
\end{aligned}
$$

Here, both sums extend over the nearest neighbors and the second one is defined on the cavity lattice.

Next, we will include the further approximation that was introduced and successfully used by Abou-Chacra *et al.* [1, 2]. Therein, the structural differences in the equations (3.22) and (3.23) are neglected and replaced by a single equation

$$
\Gamma_i(\omega) = \sum_{j=1}^{K} t_{ij}^2 G_{jj}(\omega) \; . \tag{3.24}
$$

This basically means, that the cavity hybridization function is approximated by the hybridization function. Surely, the approximation gets better the higher the connectivity is, since then the difference between $z$ and $K$ becomes smaller. Furthermore, we note that all equations in the hierarchy incorporate the sum over $K$ diagonal Green's Functions except the first. Even on a real Bravais lattice restricted to the leading contribution, the first equation would extend over $z$ neighbors, but all subsequent equations would incorporate $z - 1$ or less summands. Thus, $K$ can be considered as a typical number of summands in the equations of the hierarchy [2].

Equation 3.24 is of central significance for the local distribution method and our later implementation of the statistical DMFT in chapter 4.4. It is interpreted as a self-consistent stochastic equation for the hybridization function $\Gamma$. $K$ random variables $\epsilon_j$ and $K$ random hybridization functions are generating a PDF for the hybridization function $\Gamma_i$, which is required to be identical to the PDF of the $\Gamma_j$ [2]. The last-mentioned defines the self-consistency. We note, that in contrast to the self-consistency on a level of a function discussed in the framework of DMFT (cf. section 2.3) we are considering here a self-consistency on a level of PDFs, appropriate for disordered systems. Moreover, equation 3.24 enables an efficient numerical sampling procedure, called the local distribution approach [13–15] for the solution of the self-consistent problem, which is described in the following.

The numerical implementation of the local distribution method simulates the PDF of the local single-particle Green's functions $p\left[G_{ii\sigma}(\omega)\right]$ by an ensemble

of single-particle Green's functions of size $N$. Of course, high values of the ensemble size $N$ are desired, as it determines the accuracy of the simulation and the resolution of the later described distinction between localized and extended states.

Given an initial PDF $p\,[G_{ii}(\omega)]$ the computational scheme of the local distribution method is the following:

1. For each ensemble member we draw a random on-site energy $\epsilon_i$ out of the PDF $p_\epsilon(\epsilon_i)$.

2. The hybridization function $\Gamma_i(\omega)$ is determined via Eq. (3.24), in which the nearest neighbor cavity Green's functions $G_{jj}^{(i)}(\omega)$ are randomly sampled from the PDF $p\,[G_{ii}(\omega)]$.

3. The local single-particle Green's function $G_{ii}(\omega)$ is calculated using Eq. (3.17).

4. Having calculated all new $G_{ii}(\omega)$ a new PDF $p\,[G_{ii}(\omega)]$ is obtained and we return to step 1.

The algorithm is repeated until self-consistency for $p\,[G_{ii}(\omega)]$ is achieved. We note that this method incorporates spatial fluctuations, i.e. quantum interference effects, caused by the disorder via equation 3.24. For the non-interacting disordered systems considered in this chapter, ensemble sizes up to $N = 10^5$ with complete frequency resolution are computationally feasible. As the single frequencies decouple without interactions single frequencies can be investigated. In this case, even ensemble sizes up to $N = 10^8$ can be used.

The above described approximations that lead from equations (3.22) and (3.23) to equation (3.24) can be relaxed, if both the PDF of the full and the PDF of the cavity Green's function are calculated. Then the procedure would be exact up to numerical restrictions on the Bethe lattice. On the other hand, significant differences in the results are not expected and the numerical procedure becomes much more involved. Hence, in this work we will always incorporate the approximation of equation 3.24.

One relevant physical observable is the LDOS $\rho_i(\omega)$, defined in (2.21), which is a random quantity in disordered systems. The corresponding distribution $p[\rho_i(\omega)]$ is obtained by counting all values of the LDOS for each frequency and constructing a histogram. The construction of the histogram incorporates a logarithmic discretization of the $\rho$ axis. Therewith, several orders of magnitude of the LDOS are accessible, which is essential for the discussion of localization physics as we will see below. In this work typically a range $10^{-12} < \rho < 10^3$

is considered and a typical resolution is given by 60 bins per decade. In order to minimize the statistical fluctuations, we artificially increase the size of our ensemble after having reached the self-consistency. This is done by constructing the histogram on basis of typically $50 - 100$ successional update iterations.

From the calculated PDF we can extract all moments of the PDF, here e.g. for the PDF of the LDOS

$$M_{\rho(\omega)}^{(k)} := \int\limits_0^\infty d\rho' \, p[\rho'(\omega)] \rho'^k \tag{3.25}$$

In particular, the first ($k = 1$) moment corresponds to the arithmetic average of the LDOS. Later, we will also consider the cumulative PDFs

$$P[\rho(\omega)] = \int\limits_0^{\rho(\omega)} p[\rho'(\omega)] \, d\rho'(\omega) \tag{3.26}$$

which turned out to be useful to characterize the disordered system.

In order to see how localization effects can be studied within the local distribution method, the procedure is now applied to the Anderson model (3.1). Parts of this section have been published [249]. The gained insights will be useful for the later generalization to strongly correlated systems. For the PDF of the on-site energies we consider the box distribution (cf. illustration in figure 3.2)

$$p_\epsilon(\epsilon_i) = \frac{1}{\Delta} \Theta\left(\frac{\Delta}{2} - |\epsilon_i|\right) , \tag{3.27}$$

which is used widely in theoretical investigations. The expectation value is given by $\langle\epsilon\rangle = \int d\epsilon \, p_\epsilon(\epsilon)\epsilon = 0$ and the expectation value of the on-site energy squared is given as

$$\langle\epsilon^2\rangle = \int d\epsilon \, p_\epsilon(\epsilon)\epsilon^2 = \frac{1}{12}\Delta^2 , \tag{3.28}$$

from which the standard deviation follows to equal $\frac{1}{2\sqrt{3}}\Delta$.

We work in energy units of the non-interacting bandwidth $W_0 = 1$ in the following. In figure 3.3 two resulting local spectra of one random sample out of the ensemble resulting from the local distribution method are displayed. Panel (a) shows a typical spectrum for small disorder strengths, namely $\Delta = 1$. The spectrum is smooth and furthermore broadened in comparison to $W_0$ due to
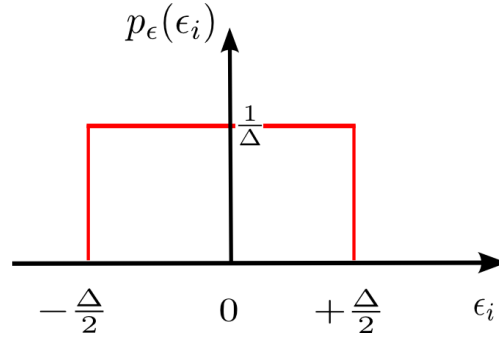
47

**Figure 3.2.:** Illustration of the probability distribution function of the on-site energies in case of box disorder. $\Delta$ denotes the disorder strength.

the disorder. In contrast, the spectrum at higher disorder strength $\Delta = 6$ in panel (b) is highly fragmented and consists of various delta peaks, which are broadened by the artificial value $\eta$. This can be seen more clearly in the inset. In fact, this is exactly what we expect from the analytical considerations in section 3.1: Extended states of the system are characterized by a branch cut on the real axis of the local Green's function, whereas localized states are given by poles.
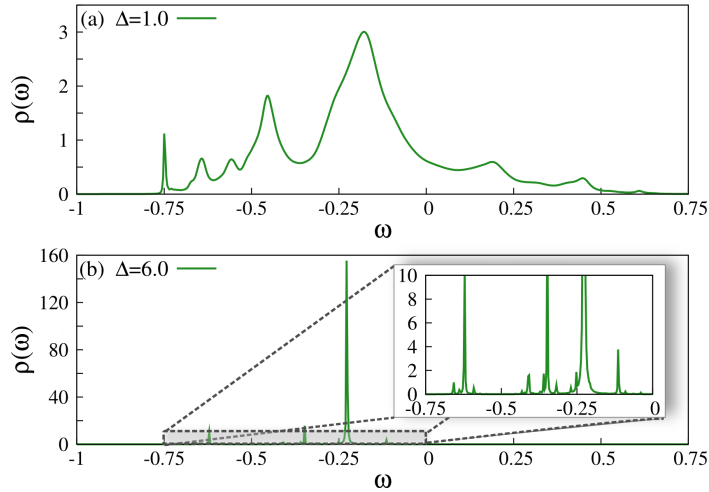


**Figure 3.3.:** Local density of states $\rho(\omega)$ of one random sample out of the ensemble for two different box disorder strengths $\Delta$: (a) $\Delta = 1$ and (b) $\Delta = 6$. The broadening $\eta = 10^{-4}$, connectivity $K = 6$ and $W_0 = 1$

So far, the spectrum of a single sample was considered and we face the question how the overall PDF of the LDOS is affected by disorder. In figure 3.4 the PDF of the LDOS at the Fermi level is displayed for several disorder strengths. The initial delta function for the homogeneous system located at $\rho = 1.265$ (not displayed) is broadened by a small amount of disorder ($\Delta = 0.5$) due to the disorder-induced fluctuations. By increasing the disorder strength the PDF spreads more and more, long tails develop and more weight is shifted to smaller values. This becomes evident, if we focus on the most probable value of the PDF, also called the *typical value*, which approaches zero with increasing disorder strength.
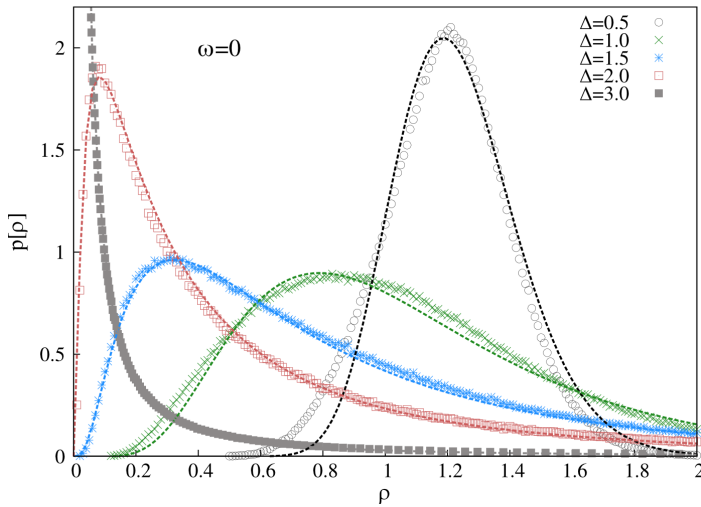


**Figure 3.4.:** Evolution of the probability distribution function $p[\rho(\omega)]$ obtained within the local distribution method with increasing disorder strength $\Delta$ for frequency $\omega = 0$ in case of box disorder. The dashed lines correspond to least square fits with log-normal distributions. The ensemble size is given by $N = 10^6$, the broadening by $\eta = 10^{-6}$, connectivity $K = 6$ and $W_0 = 1$. No averaging over successional iterations was used to minimize the statistical fluctuations.

In fact, regarding the explicit shape of the PDF of the LDOS, it is analytically predicted [197, 198] that the PDF close to the transition corresponds to a log-normal distribution

$$p^{\text{ln}}[\rho_i(\omega)] = \frac{1}{\sqrt{2\pi\sigma^2}\rho_i(\omega)} \exp\left(-\frac{\ln\rho_i(\omega) - \mu}{2\sigma^2}\right). \tag{3.29}$$

Recently, this analytic prediction has been inspected numerically in detail for two-dimensional and three-dimensional systems and various lattice types by the kernel polynomial method [243]. Log-normal PDFs have been found to a high degree of accuracy, as well as a present Anderson transition in various three-dimensional systems and the localization of all states at arbitrary disorder strength in two dimensions. In figure 3.4 least square fits with log-normal distributions to the numerically obtained PDFs. We note that the data is only roughly approximated by log-normal distribution function for small disorder strengths. However, the agreement gets better the stronger the disorder is. Please note, that for $\Delta = 3$ a logarithmic grid was used for the LDOS to obtain a reasonable resolution for the relevant small values of the LDOS. From now on the use of a logarithmic grid is the standard choice.

In the localized phase the Green's function is given by a distribution of poles. Hence, an arbitrarily chosen frequency $\omega$ lies with probability one between the poles resulting in a value of the LDOS equal to zero. If it hits exactly a $\delta$-peak, the resulting value would be infinity. However, the probability for this event is zero. The artificially introduced coupling to a dissipative bath via the small factor $\eta$ broadens the $\delta$-peaks to Lorentzians with width $\eta$ and generates a finite probability to obtain a finite value of the LDOS. Moreover, let us consider an energy in the vicinity of a pole present in the considered sample. The corresponding value of the LDOS is proportional to $\eta$, since the LDOS is given by the imaginary part of the single-particle Green's function. Now the observed features of the PDF can be understood: In the localized phase most ensemble samples will exhibit a nearly zero ($\sim \eta$) value of the LDOS states for a given frequency $\omega$. On the other hand, a small fraction will contribute high values of the LDOS, corresponding to the broadened $\delta$-peaks.

This enables a numerical distinction between localized and extended states. Clearly, the PDF of the LDOS of an extended state will not be affected upon lowering of $\eta$ from some value of $\eta$ on. In contrast, in the localized phase, the PDF will be affected dramatically: With decreasing broadening $\eta$ an increasing amount of the PDF's weight is shifted to smaller values, the tail of the PDF will extend to higher values and the most probable value will shift to zero. Figure 3.5 displays the evolution of the PDF of the LDOS at frequency $\omega = 0$ on a log-log scale when the broadening is decreased. In panel (a) the disorder strength $\Delta$ is equal to one and the PDF is found to saturate. We conclude that the state is extended. For $\Delta = 6$ in panel (b) the PDF exhibits the above described behavior. We conclude that the state is localized.

When the analysis is performed with a complete frequency resolution, the mobility edges of the system can be identified. For example this is done in figure 3.6, where the natural logarithm of the PDF $p[\rho(\omega)]$ is plotted color coded for
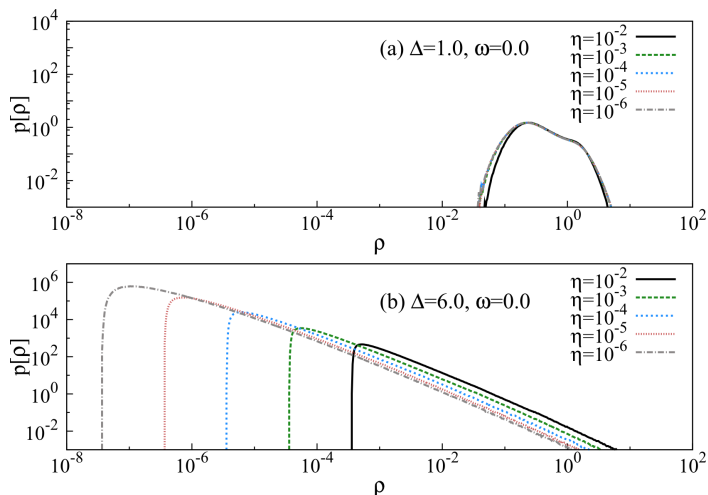
**Figure 3.5.:** Evolution of the probability distribution function $p[\rho(\omega)]$ obtained within the local distribution method with decreasing broadening $\eta$ for frequency $\omega = 0$ and two different disorder strengths $\Delta$: (a) $\Delta = 1$ and (b) $\Delta = 6$. The ensemble size is given by $N = 5 \times 10^4$, connectivity $K = 6$ and $W_0 = 1$.

fixed disorder strength $\Delta = 4$ in the $\omega$-$\rho$-plane. The broadening factor $\eta$ is lowered from $10^{-3}$ in panel (a) to $10^{-6}$ in panel (d). When the broadening is decreased, we notice clearly a low-energy core of the band, where the PDFs are unaffected under further lowering of the broadening. On the other hand, outside of the core the PDF show the explained behavior for localized states. The separating energy represents the mobility edge we look for. It is important to note, that the resolution of this procedure is determined by the lowest possible value of $\eta$, which is basically determined by the finite bath size. In any case, the procedure will give the lower bound of the critical disorder strength for the transition from extended to localized states, since an extended state will never be mistaken as a localized state. This resolution issue was examined in more detail in [13].

When the mobility edges cross the Fermi level in the band center all states become localized corresponding to the Anderson insulator. Since localized states do not contribute to the DC conductivity, a metal-insulator transition is obtained, caused by the disorder. For the determination of the transition, we can apply the extended gap criterion as discussed in section 2.6. The gap might be defined as energy necessary to create a macroscopically extended charge excitation. If the spectrum exhibits such a gap, it is in the insulating state.
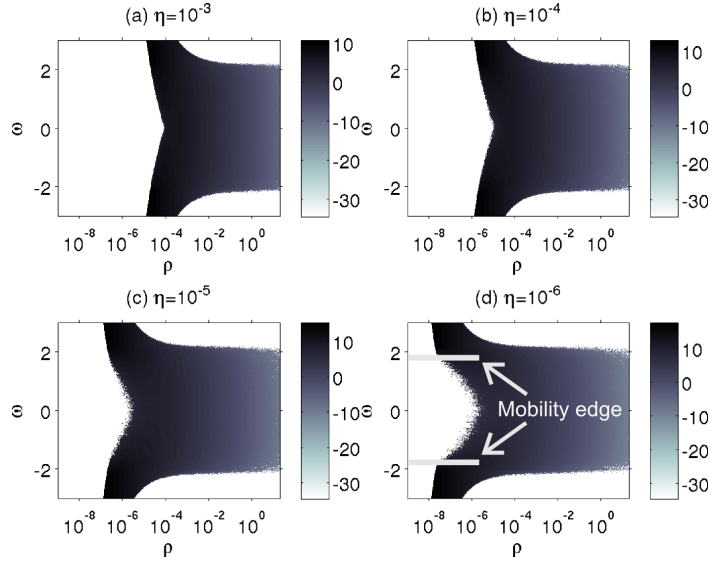
**Figure 3.6.:** Natural logarithm of the probability distribution function $p[\rho(\omega)]$ obtained within the local distribution method for fixed box disorder strength $\Delta = 4$ and several broadenings $\eta$: (a) $\eta = 10^{-3}$, (b) $\eta = 10^{-4}$, (c) $\eta = 10^{-5}$ and (d) $\eta = 10^{-6}$. The ensemble size is given by $N = 10^4$, the connectivity by $K = 6$ and $W_0 = 1$

The extended gap criterion can be used for correlation and disorder-induced metal insulator transitions at the same time and therefore it paves the way to a simultaneous description of Mott- and Anderson-Mott transitions in strongly correlated, disordered systems.

Comprehensive results for the Anderson model (3.1) obtained by means of the local distribution approach are given in the works by Alvermann and Fehske in case of box disorder [14] and in case of binary disorder [13]. Both disorder types are investigated for strongly correlated systems in chapter 6 and chapter 7 respectively.

# 4. Strongly correlated fermions in disordered lattices

So far the discussion focused on strongly correlated systems on the one hand, and on single particle disorder physics on the other hand. Although both phenomena are still subject to current investigations, the fundamental mechanisms are well-understood. However, both phenomena play a key role in the description and physics of real materials. To gain a fundamental understanding of the interplay between these two phenomena is of crucial significance in today's research on solid states. Major progress in understanding systems that combine both effects has been achieved in the past [32, 174, 182], but many central questions are left to be answered and these systems are far from being completely understood [32, 174, 182, 221].

From the solid state point of view, this can be partially traced back to the missing possibility of fine tuning the strength of the interaction and disorder strength in real materials, nor is it possible to isolate one effect in a clear fashion. This handicaps the interplay between theory and experiment that is useful to verify the validity of the indispensable theoretical approximations. These are necessary, since even the most rudimentary theoretical models of disordered and interacting systems cannot be solved exactly in general. Therefore, there is a huge need for further effort on both the experimental side as well as on the theoretical side in order to gain a better understanding.

Theoretical approaches were initially developed in the regime of weak disorder [182], by e.g. extending the Fermi liquid theory to disordered systems [10, 112, 113]. A further approach consisted of mapping the problem onto a field-theoretical model which was then investigated by a renormalization group technique [66, 109, 110]. This approach can also be understood as an effective Fermi liquid description [67]. The Fermi liquid parameters evolve under an increase of the disorder strength and their instability signals a metal-insulator transition.

These works focus on perturbative corrections to the Fermi liquid theory and are consequently inappropriate in the regime of strong correlations. Moreover, disorder is incorporated perturbatively, for which reason these approaches fail to give a comprehensive picture. In particular, diverging magnetic susceptibilities

and specific heat coefficients in the metallic phase of doped semiconductors could not be explained within the effective Fermi liquid picture[1] [37, 84, 221]. The discovery of a metal-insulator transition in two-dimensional electron gases, e.g. in a silicon MOSFET [173–175], caused enhanced interest in strong correlation effects within disordered solids, since this observation is not in agreement with scaling theory.

Such experimental findings strongly motivated the need for further theoretical models and understanding of strongly correlated, disordered systems. Such a theory must be non-perturbative in both, the interaction and the disorder. As DMFT (described in section 2.3) already treats local correlations non-perturbatively, the extension of DMFT to disordered systems is a promising approach in this regard. Three different extensions were found to give much insight into the interplay. One extension was performed in analogy to the well-known coherent potential approximation (CPA) [275, 279], and another extension is given as a fully stochastic approach to contain effects of Anderson localization, called statistical DMFT [85, 86, 196]. If one treats correlation effects on a rigorous level within statistical DMFT and keeps sufficiently large ensembles of disorder realizations, this approach is computationally very expensive. For this reason, the typical medium theory (TMT) was developed [87], which is computational less demanding and superior to CPA. Therein, the geometrically averaged LDOS is used as an order parameter for Anderson localization [87]. The TMT was recently successfully applied to strongly correlated systems with disorder [5, 58, 60–62, 82].

In this chapter we will introduce the 'Drosophila model' of disordered, strongly correlated systems, the Anderson-Hubbard model. Afterwards, we will turn to the various extensions of DMFT to disordered systems by shortly introducing the CPA extension in section 4.2. As this extension is not capable of describing localization physics, we will proceed by introducing the TMT which overcomes this shortcoming (see section 4.3). Finally, we will introduce the statistical DMFT in section 4.4 which enables the self-consistent calculation of PDFs of local single-particle observables. Since the statistical DMFT contains both disorder fluctuations, as well as treating local correlations non-perturbatively, it is superior to many other theoretical approaches and the method of choice for the investigation of high-dimensional strongly-correlated, disordered systems.

---

[1]Such properties are generally referred to as non-Fermi liquid behavior, for a review see [196].

## 4.1. Anderson-Hubbard Hamiltonian and many-body localization

Strongly correlated fermions in disordered lattices are well described by the Anderson-Hubbard Hamiltonian

$$H = -\sum_{ij\sigma} t_{ij} c_{i\sigma}^\dagger c_{j\sigma} - \sum_{i\sigma} (\mu - \epsilon_i) c_{i\sigma}^\dagger c_{i\sigma} + U \sum_i n_{i\uparrow} n_{i\downarrow} \,, \tag{4.1}$$

which conatins the strong correlations physics of the Hubbard model (2.1) and the disorder effects of the Anderson model (3.1).

From a first naive consideration one might expect that the localization tendencies due to both correlations and disorder are enhanced when both are present, leading to an insulator transition at smaller values of the disorder strength and the interaction strength. However, this is incorrect and more careful considerations are necessary. For instance, the on-site interaction gives rise to incoherent excitations in the single-particle spectrum, which increase the effective bandwidth. Due to the enlarged bandwidth, the Anderson transition is shifted to higher values of the disorder strength, since the transition is triggered by the ratio of disorder strength to bandwidth. On the other hand, if the system is Mott insulating and characterized by an energy gap in the excitation spectrum, the additional disorder generally redistributes states into the gap, eventually closing it. Therefore, additional disorder drives the system into the metallic phase. From this basic reasoning, we see that the presence of both phenomena gives rise to delocalization effects. It was also shown that two particles in a random potential can propagate coherently through the lattice due to their repulsive interaction [251]. Another aspect arises in solids from the well known fact, that for finite temperatures the coupling to phonons gives rise to a phenomenon called hopping conductivity [205]: electrons can hop from a localized state to another localized stated due to the interaction with phonons, which leads to a finite DC conductivity. The obvious question arises if interactions among the electrons lead to a similar effect [112, 213].

Basko *et al.* [29] recently addressed this question and worked out that inelastic electron-electron interactions alone cannot produce a finite DC conductivity for small enough temperatures. Consequently, the DC conductivity is exactly zero below some critical temperature in the absence of extended single-particle states. Already on the level of the above simple considerations and these recent results, we can conclude that the interplay of interactions and disorder is quite involved and subtle.

In a first step we have to define what is understood by localization in

interacting many-particle systems. Many different criteria of localization have already been introduced for the non-interacting disordered systems (see section 3.1) and it is not to be expected that the situation is less complex in the presence of many-particle correlations. In case of interacting systems, one speaks of *many-body localization* and there is no consensus on its exact definition so far. Unfortunately, a rigorous connection between the different definitions of many-body localization has also not been established either.

Localization is in first place a pure single-particle phenomenon and therefore its description bases on single-particle properties only, whereas the extension to many-particle systems is not unique and clear. There is no natural approach given for defining localization in a many-particle system. Typically, one considers many-body localization as localization of excitations. But here also a variety of possibilities exists and single-particle excitations or many-particle excitations may be considered. There is no fundamental connection of these concepts so far. A useful definition of many-body localization requires the following properties: it should be well-defined for any many-particle state, be reducible to a definition of single-particle localization in the non-interacting limit and fulfill the physical picture of all single particle states being localized.

Most approaches and investigations use the localization of single-particle excitations as definition for many-body localization (see e.g. [29, 97, 258, 281, 282]). Instead of an exponential decaying envelope of single-particle wave functions in real space, the single-particle density matrix or the single-particle Green's function in coordinate representation $G_{ij}$ are used. In case of localized single-particle excitations, these quantities approach zero in the limit of large $|\mathbf{R}_i - \mathbf{R}_j|$.

A generalization of the localization criterion given by the analytic structure of the Green's function as discussed for the non-interacting system (see section 3.1) is self-evident. Here, many-body localization is understood within the singular analytic properties of the single-particle Green's function of the many-body system, which corresponds to localized single-particle excitations. This is exactly what we will employ throughout the following chapters.

The analytic structure of the single-particle self-energy, the imaginary part of which represents the single-particle quasi-particle relaxation is a closely connected concept. The quasi-particles are defined to be localized if the quasi-particle relaxation is given by an infinite number of narrow $\delta$-peaks [29]. This is contrasted by the single-particle quasi-particle relaxation, given as a smooth function of the energy in the metallic phase [29]. The question of localization can be determined from the full PDF of the random single-particle quasi-particle relaxation, similar to the discussion of the PDF of the LDOS in section 3.3.

The recently considered generalized inverse participation ratio [211, 258]

$$I_2(\omega) = \frac{\sum_i (\rho_i(\omega))^2}{(\sum_i \rho_i(\omega))^2} \tag{4.2}$$

reduces to the inverse participation ratio in absence of interactions, and was shown to reproduce established results in this case [211]. Furthermore, the generalized single-particle return probability [97, 281, 282]

$$R(\omega) = \frac{1}{N} \sum_i \lim_{s \to 0} \frac{s}{\pi} G_{ii}(\omega + is) G_{ii}(\omega - is) \tag{4.3}$$

has been discussed, which reduces to the averaged inverse of the participation ratio in the non-interacting limit [282].

An useful definition of many-body localization was introduced by the concept of Fock space localization for finite lattices [11]. The distance of two Fock states is defined as the number of positions in which the occupation of the single-particle states differ. This concept was first used to connect the lifetime of quasi-particles to an Anderson localization problem on an abstract Bethe lattice. The sites of the abstract Bethe lattice correspond to all possible many-particle states connected to each other by the two-particle interaction term. The notion of Fock space localization is a general concept for Hamiltonians consisting of single-particle and two-particle contributions. A picture similar to the spatial localization of non-interacting particles is obtained when the Fock space states are given in the basis of single-particle states in coordinate representation. In this context, a typical measure of localization is the inverse of the Fock-space participation number [34, 282]

$$p_F^{-1}(\nu) = \sum_\alpha |\langle \alpha | \nu \rangle|^4 \ . \tag{4.4}$$

Here, $|\nu\rangle$ denotes a Fock state and $\{|\alpha\rangle\}$ is a basis set of the complete Fock space. A completely localized state results in $p_F = 1$ and an extended state corresponds to $p_F > 1$ [282]. Also the level spacing statistics (cf. section 3.1) have been discussed as distinguishing mark for Fock space localization [34].

From a experimental point of view, the most convenient quantity to measure is the conductivity. This quantity is related to two-particle observables, like the density-density correlation functions. From a physical educated guess, one might expect that localized single-particle excitations at the Fermi level may induce a vanishing DC conductivity, as in the non-interacting case. However, such a statement has not been rigorously proven and is a topic of current debate

[29, 129, 218]. In particular, Basko *et al.* [29] predicted that the DC conductivity identically vanishes in absence of extended single-particle states and of any external continuous bath, like given by a coupling to phonons. This even holds for sufficiently low, but finite temperatures. Their prediction is based on the concept of Fock-space localization and on an effective low-energy Hamiltonian for weak local interactions. Furthermore, it was shown that the quasi-particle relaxation – that means localization on the single-particle excitation level – is closely connected to Fock space localization in infinite systems [29]. This is attributed to the two-particle interaction coupling the single-particle excitation with three-particle excitations, these in turn with five-particle excitations and so on. The single-particle excitation may thus decay into all possible many-body states. In terms of Fock-space localization, this means that the many-body eigenstate becomes Fock delocalized. If, on the other hand, the quasi-particles do not decay the single-particle excitation is localized in Fock space [29].

If we assume this correspondence between localized single-particle excitations and a vanishing DC conductivity – which is assumed or suggested in most works to date – a metal-insulator transition is obtained in analogy to the non-interacting case as soon as the single-particle excitations at the Fermi level are localized. This transition is usually referred to as *Anderson-Mott transition.*

## 4.2. Coherent potential approximation extension of DMFT

The first route to an extension of DMFT to disordered systems was given by an approach analogous to the CPA [96, 263] of non-interacting systems. Focusing on the limit of large coordination numbers, a self-consistent theory was formulated [84, 156, 275, 279], that maps the Anderson-Hubbard Hamiltonian (4.1) onto an ensemble of Anderson impurity problems, supplemented by a self-consistency relation. The theory treats interactions on a DMFT level, where local correlations are treated exactly, and the disorder is included on a CPA level.

By means of the cavity method, as performed in the homogeneous case (cf. section 2.3), a local effective action [84]

$$S_{\text{eff},\epsilon_i} = - \int_0^\beta d\tau \int_0^\beta d\tau' c_{i\sigma}^\dagger(\tau) \mathcal{G}_{0,\epsilon_i}^{-1}(\tau,\tau') c_{j\sigma}(\tau') + \int_0^\beta d\tau U n_\uparrow n_\downarrow \qquad (4.5)$$

is derived in the limit of infinite dimensions. Here, the Weiss function takes on

the form

$$\mathcal{G}_{0,\epsilon_i}^{-1}(\tau,\tau') = -(\partial_\tau - \mu + \epsilon_i)\delta(\tau - \tau') - \Gamma_i(\tau,\tau') \ . \tag{4.6}$$

As already discussed in the homogeneous case, the effective action (4.5) corresponds to a single impurity Anderson model for each lattice site. In case of disorder, each lattice site will have a different, independent random on-site energy, effectively giving rise to an ensemble of impurity models. The hybridization function is site-dependent and given as an intricate functional of the Green's function $G_{jk}(\omega)$ [86], incorporating local and non-local terms. Within the CPA approximation, one assumes a *dynamical* coherent potential, manifesting itself in a site-independent hybridization function, as will be explained in the following. Consequently, one deals with an ensemble of impurity problems with a parametric dependence on the on-site energy $\epsilon$, distributed according to the PDF $p_\epsilon(\epsilon)$.

Changing to the real frequency representation, the calculation starts with a given dynamical coherent potential $\Gamma(\omega)$. In combination with the on-site energies, an ensemble of impurity models is obtained. Their solution results in an on-site dependent Green's function $G_\epsilon(\omega)$ for each member in the ensemble. By calculating the arithmetical disorder average over the Green's functions

$$\langle G(\omega)\rangle_{\text{dis}} = \int\limits_{-\infty}^{\infty} d\epsilon \, p_\epsilon(\epsilon) G_\epsilon(\omega) \tag{4.7}$$

the Green's function within CPA approximation is obtained. The averaging restores the translational invariance. In order to perform the disorder average, we have to integrate over the product of the PDF $p_\epsilon(\epsilon)$ and the on-site energy dependent Green's function. In practice, this can be done exactly for discrete disorder, but for the case of continuous disorder, we have to discretize the PDF. Assuming a local self-energy in the DMFT spirit, the self-energy can be extracted by using the the Dyson equation

$$\langle G(\omega)\rangle_{\text{dis}}^{-1} = \omega + \mu - \Sigma(\omega) - \Gamma(\omega) \ . \tag{4.8}$$

Now, one is able to calculate the Green's function for the given lattice with the non-interaction density of states $\rho^{(0)}(\omega)$ via the Hilbert transform

$$G(\omega) = \int d\varepsilon \, \frac{\rho^{(0)}(\varepsilon)}{\omega + \mu - \Sigma(\omega) - \varepsilon}. \tag{4.9}$$

Finally, by reapplying the Dyson-equation for the lattice Green's function, a new

hybridization function is obtained, which corresponds to the updated dynamical coherent potential. In combination with the possible realizations of the on-site energies, a new ensemble of impurity problems is defined. The procedure is repeated until self-consistency for the lattice Green's function is obtained.

The approach is unable to describe spatial fluctuation effects associated with Anderson localization. Therefore it is not able to describe Anderson localization like it is known for CPA in the non-interacting case [189, 270, 288]. However, several nontrivial disorder-induced effects can be described, as for example the metal-insulator transitions due to disorder-induced band splitting [59, 178]. Moreover, CPA combined with DMFT is exact in infinite dimensions [84, 275, 279]. For these reasons, it provides a valuable method to investigate strongly correlated fermions in high-dimensional disordered lattices despite its shortcomings.

## 4.3. Typical medium theory

As already pointed out in the previous chapter 3, an investigation of localization effects in disordered systems should incorporate full distributions of physical observables. Such approaches provide the most natural description of localization physics. Nevertheless, due to the complexity of systems that are both disordered and strongly correlated, such theoretical investigations require the use of perturbative approaches, rough approximations or an infeasible amount of numerical effort. Therefore, it is desirable, to develop a simpler theory that is superior to CPA in the sense that it is sensitive towards localization. The recently developed TMT [60–62, 82, 87] represents such a theory. The general idea of the TMT is to avoid the laborious explicit calculation of the full PDFs, but to consider specific single moments of the PDFs instead, that are informative regarding the localization of particles.

Adopting Anderson's local point of view once again, we are interested in the diffusive rate of a particle from a given lattice site. According to Fermi's golden rule, the escape rate $\tau_{\text{esc}}^{-1}$ is proportional to the LDOS of its immediate neighborhood

$$\tau_{\text{esc}}^{-1} \sim t^2 \rho \,. \tag{4.10}$$

In the considered case of disordered systems, the escape rate is distributed by a PDF which is directly connected to the PDF of the observable LDOS. A natural question is thus, if there is a single moment of the PDF of the LDOS that might be informative regarding localization phenomena.

The crucial value determining the escape rate of our particle is the *typical*,

i.e the most probable value. In figure 4.1 the PDFs of the LDOS at the Fermi
level are given for (a) $\Delta = 1.0$ and (b) $\Delta = 6.0$ calculated by means of the local
distribution method for the non-interacting, box-disordered system. As the
disorder strength increases, the PDF of the LDOS at a given frequency $p[\rho(\omega)]$
transforms from a $\delta$-peak distribution into a log-normal distribution [198, 243].
As described in section 3.3 we note that in case of a localized state the typical
value of the LDOS, is close to zero. That the typical value is non-zero is due to
the finite broadening. Of course, without knowledge of the full PDF, we are
not able to determine the most probable value. But our original question can
now be reformulated as: does a moment of the PDF exist, that approximates
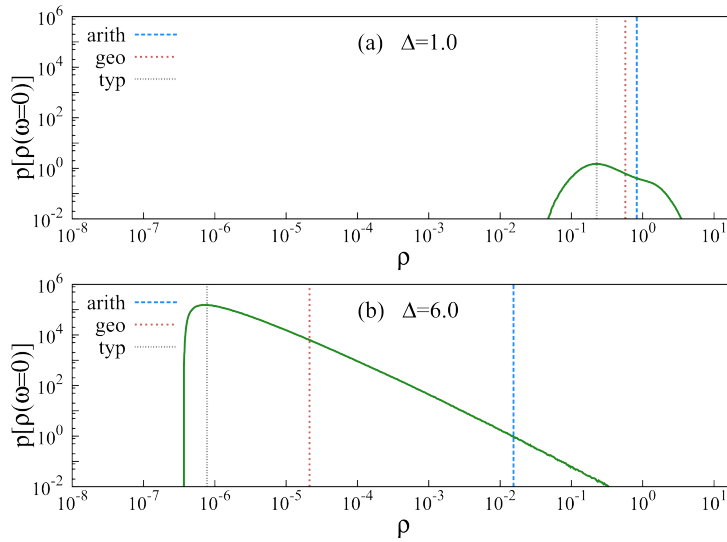the typical value?



**Figure 4.1.:** Probability distribution function $p[\rho(\omega)]$ at $\omega = 0.0$ for two different
box disorder strengths $\Delta$: (a) $\Delta = 1.0$ and (b) $\Delta = 6.0$. The arith-
metic average, geometric average and the typical value of the probability
distribution are marked. The PDFs were calculated within the local
distribution method and parameters are $K = 6$ and $\eta = 10^{-5}$.

In figure 4.1 the arithmetic average, as well as the geometric average of the
PDFs are marked. The geometric average of the PDF of the LDOS is defined
as

$$\langle \rho(\omega) \rangle_{\text{geo}} := \exp \int d\rho'(\omega) \, p[\rho'(\omega)] \ln \rho'(\omega) \, . \tag{4.11}$$

It can be seen that the arithmetic average is well separated from the typical

value. From here we conclude, that the arithmetic average is not an useful quantity to indicate localization. Hence, the LDOS in disordered systems is not a *self-averaging* quantity[2]. However, the geometric average can serve as an crude approximation of the typical value. Most importantly, if the typical value of a log-normal distribution declines to zero for increasing disorder strength, the geometric average follows in a similar fashion, which is not true for the arithmetic average.

To substantiate the reasoning, numerical data obtained by the local distribution approach is given in figure 4.2. The geometric and the arithmetic average of the PDF of the LDOS, as well as the typical values of the PDFs are plotted as a function of the disorder strength. For weak disorder, all quantities are approximately equal. We note that the typical value does not exactly reproduce the arithmetic average in homogeneous case. This discrepancy is due to the binning procedure necessary for the construction of the PDF as a histogram. The typical value does exactly correspond to one bin, whereas the calculation of the averages incorporates the information of the whole histogram. All quantities decay to zero for increasing disorder strength, but in very different fashions. This is clearly recognized if the logarithmic scale on the *y*-axis is taken into account. Of course, the arithmetic average also declines due to the disorder induced broadening of the bandwidth. The spectral weight is distributed over a larger energy interval, but it is of order $\mathcal{O}(10^{-1})$ even for strong disorder of five times the homogeneous non-interacting bandwidth. In contrast, the geometric average declines much faster, following the typical value of the PDFs. The observed behavior is in agreement with our above expectation.

Returning to the question of localization we summarize: as the typical value of the LDOS, which can be approximated by the geometric average vanishes the escape rate also vanishes and the corresponding state is said to be localized. Therefore, by incorporating the typical value of the LDOS in the DMFT calculation scheme, a description of particle localization is possible [60, 62, 82, 87].

Technically, this is achieved by considering an ensemble of impurity problems as in the CPA, but using the geometric average instead of the arithmetic average in equation (4.7). Since our physical reasoning was based on the typical value of the LDOS, the geometric disorder average of the LDOS,

$$\langle\rho(\omega)\rangle_{\text{geo-dis}} = \exp\langle\ln\rho(\omega)\rangle_{\text{dis}} = \exp\big(\int\limits_{-\infty}^{\infty} d\epsilon\, p_\epsilon(\epsilon)\ln(\rho_\epsilon(\omega))\big) \tag{4.12}$$

---

[2]A random variable $X$ with a PDF P(X) is defined to be self-averaging if the relative variance $R_X := (\langle X^2\rangle - \langle X\rangle^2)/(\langle X\rangle^2)$ vanishes when the system size goes to infinity [300].
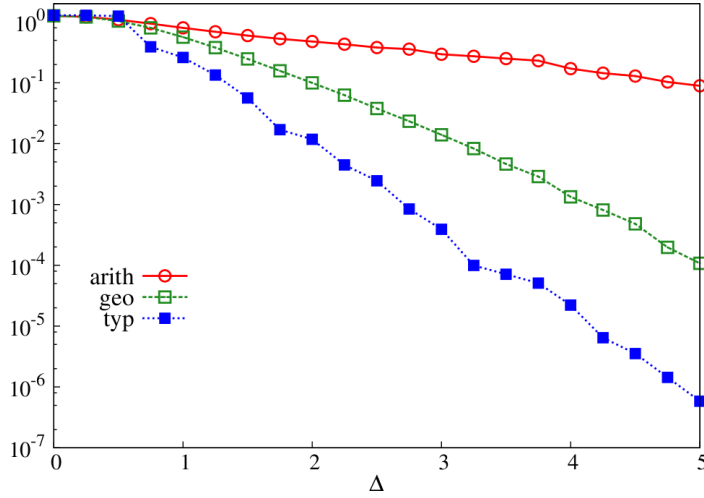
**Figure 4.2.:** The arithmetic average, geometric average and the typical value of the PDF $p[\rho(\omega = 0.0)]$ for the Anderson model with box disorder as a function of the disorder strength. The PDFs were calculated within the local distribution method and parameters are $K = 6$, $W_0 = 1.0$ and $\eta = 10^{-6}$.

is used. This is not to be mistaken for the geometric average of equation (4.11), which requires the knowledge of the full PDF. Here, the on-site energy dependent LDOS $\rho_\epsilon(\omega) = -\mathrm{Im}G_\epsilon(\omega)/\pi$ corresponds to one impurity problem out of the ensemble. The full Green's function is obtained by analytic continuation via the Hilbert transform

$$\langle G(\omega)\rangle_{\text{geo-dis}} = \int\limits_{-\infty}^{\infty} dz\, \frac{\langle\rho(z)\rangle_{\text{geo-dis}}}{\omega - z}\ . \tag{4.13}$$

A local self-energy can be extracted like in the CPA by using the Dyson equation

$$\langle G(\omega)\rangle_{\text{geo-dis}}^{-1} = \omega + \mu - \Sigma(\omega) - \Gamma(\omega)\ . \tag{4.14}$$

and the subsequent steps are identical to those used in CPA. Finally, a typical hybridization function $\Gamma_{\text{typ}}(\omega)$ is obtained, which together with the PDF of the on-site energies defines a new set of impurity problems and closes the self-consistent loop.

Like in the CPA extension, taking the average restores translational invariance, which means that the hybridization function becomes site-independent. However, using the geometric average accounts for localization effects and the

hybridization function can thus be regarded as a typical dynamical coherent potential. In particular, it was shown, that the geometrically averaged LDOS can serve as an order parameter for the Anderson transition in the non-interacting case [87], as well as in the interacting case [60]. The TMT treats disorder and interaction on equal footing, in the whole range from weak to strong interactions and also incorporates localization effects. It can be regarded as a minimal extension of DMFT to disordered systems, which accounts for localization in the thermodynamic limit.

The TMT was successfully used to determine the paramagnetic ground state phase diagram [60] consisting of the disordered metallic, the Mott insulating, and the Anderson-Mott insulating phases. Recently, it was successfully employed to study the critical behavior of the Anderson-Mott transition. It was found that the Anderson-Mott transition is driven by a formation of two fluids [4, 5, 82]. A fraction of the particles form localized magnetic moments, whereas the remaining system is described by coherent quasi-particle excitations which are Anderson localized. On physical grounds, this corresponds to a spatially inhomogeneous system consisting of regions of Mott droplets and regions of Anderson localized quasi-particles. Furthermore, TMT was also used to study the magnetic ground state phase diagram of the Anderson-Hubbard model [61], where, in particular, the existence of an antiferromagnetic metal has been predicted. It becomes apparent by the above reasoning and mentioned results, that the TMT has been proven to be a powerful and valuable tool for investigating strongly correlated, disordered systems [62, 82].

A word of caution should be mentioned at this point: it was shown that the decline of the geometric average to zero cannot uniquely be attributed to the Anderson localization, nor is it independent of the energy discretization [256]. Also the translational invariant hybridization function restricts the analysis of the localization effects to quite an extent, as it does not account for spatial fluctuations. We conclude that an approach focusing on PDFs of physical observables is desirable and such an approach will be discussed in the next section. Furthermore, it is interesting to note that, although most studies so far made use of the geometric average, there is no principle stating that the geometric mean is the most suitable and most informative. In fact, the more general mean, called the Hölder mean

$$M_q(x) = \left( \frac{1}{n} \sum_{i=1}^{n} x_i^q \right)^{1/q} \tag{4.15}$$

has been suggested and applied to the Anderson-Falicov-Kimball model [58, 262].

Besides other means, the geometric average $(q \to 0)$ and arithmetic average $(q \to 1)$ are contained as special cases. It was shown, that for $q < 0.5$, the mean is critical towards localization and also that the extent of the metallic phase in the phase diagram depends on the mean used within TMT.

In this work, we will use a generalized version of the TMT to investigate Bose-Fermi mixtures in disordered optical lattices in chapter 9.

## 4.4. Statistical dynamical mean-field theory

The statistical DMFT [85, 86] represents a theoretical description of interacting fermions in high-dimensional, disordered lattices, which permits the explicit calculation of the full PDFs of local observables. The method is based on a purely local point of view and, therefore, disorder-induced localization is investigated in a natural and adequate manner, as has been discussed in the preceding chapter 3 and preceding section 4.3. In combination with the unmatched properties of the DMFT to study local correlations, it constitutes a state-of-the-art tool for strongly correlated, disordered fermionic systems.

Starting with the general effective action already given in (4.5) with the Weiss field for the disordered case (4.6), the site-dependent hybridization function becomes

$$\Gamma_i(\omega) = \sum_{j,k} t_{ij} t_{ik} G_{jk}^{(i)}(\omega) \; . \tag{4.16}$$

This is given in the real-frequency representation, where $j$ and $k$ denote summation indices for nearest neighboring sites. $G_{jk}^{(0)}$ represents the cavity Green's function, we already know from the discussion of the homogeneous DMFT. These cavity Green's functions are connected to the lattice Green's functions by the relation [149]

$$G_{jk}^{(i)} = G_{jk} - \frac{G_{ji} G_{ik}}{G_{ii}} \; , \tag{4.17}$$

which is also used in the DMFT for homogeneous systems. For general lattices the hybridization function will therefore be an intricate functional of the Green's function

$$\Gamma_i = \Gamma_i[G_{jk}] \tag{4.18}$$

depending on diagonal $(j = k)$ and off-diagonal $(j \neq k)$ terms. Instead of performing the limit of infinite coordination number as in the homogeneous

case, a finite coordination number is considered in the statistical DMFT, which leads to an approximative effective action, since only the quadratic terms are kept. That means also that it becomes exact in infinite dimensions, but since the sum (4.16) extend over an infinite number of terms, CPA would be recovered [83, 84] and localization effects are missed in that case. Hence, the inclusion of a finite coordination number is essential.

In the following, a fixed disorder realization in a finite lattice with a finite coordination number is considered. We already know that the effective action corresponds to an Anderson impurity model, specified by the hybridization. Its solution gives a self-energy, which is identified as the local self-energy of the lattice $\Sigma_{ij} \to \delta_{ij}\Sigma_i$ in the DMFT spirit. Dobrosavljević and Kotliar proposed an exact eigenstate technique [86]

$$G_{ij} = G_{ij}^0[\epsilon_i \to \epsilon_i + \Sigma_i] \,, \tag{4.19}$$

where $G_{ij}^0$ corresponds to the Green's function for the same disorder realization in the non-interacting case. When $G_{ij}$ is calculated, a new hybridization function is obtained via (4.17) and the self-consistency circle is closed. This theory lay the foundations, for the subsequently developed real-space DMFT [142, 255], an extension of DMFT to finite, inhomogeneous lattices. However, Dobrosavljević and Kotliar concentrated on the Bethe lattice, which substantially simplifies the problem as presented in the following.

One of the extraordinary properties of the Bethe lattice is that it is loop-free, which allows for an easy estimation of the hybridization function [2, 14, 85, 86, 90, 168] (see appendix B)

$$\Gamma_i(\omega) \;=\; \sum_{n=1}^{z} t_{in}^2 G_{nn}^{(i)}(\omega) \tag{4.20}$$

$$\Gamma_n^{(i)}(\omega) \;=\; \sum_{m=1}^{K} t_{nm}^2 G_{mm}^{(n)}(\omega) \,. \tag{4.21}$$

We note, that the hybridization function is expressed in terms of local Green's functions only. Following the exact eigenstate concept by Dobrosavljevic and Kotliar [86] and assuming a local self-energy, the local Green' function reads

$$G_{ii}(\omega) = \frac{1}{\omega + \mu - \epsilon_i - \Sigma_i(\omega) - \Gamma_i(\omega) + i\eta} \,. \tag{4.22}$$

Now this equation can be interpreted in a fully stochastic manner, as was first suggested by Abou-Chacra *et al.* [2]. In a disordered system the local

Green's function $G_{ii}(\omega)$ is a random quantity with its distribution described by a PDF. Equations (4.22) and (4.20) state, that this quantity is determined by the random on-site energy $\epsilon_i$ and $z$ random cavity Green's functions. As discussed in detail within the local distribution method (see section 3.3), the equations (4.20) and (4.21) are approximated by the equation [2]

$$\Gamma_i(\omega) = t^2 \sum_{j=1}^{K} G_{jj} . \tag{4.23}$$

These hybridization functions define an impurity Anderson model for every site $i$. The solution of each yields the local self-energy $\Sigma_i$, identified as the local lattice self-energy. In this sense, the statistical DMFT maps the original lattice model onto an ensemble of Anderson impurities, coupled to a stochastic bath of Green's functions (as schematically shown in Fig. 4.3), whose PDF has to be determined self-consistently.

The stochastic equation for the local Green's function is solved by a stochastic sampling method very similar to the local distribution approach (see section 3.3). In practice, the PDF of the Green's function is sampled by an ensemble of $N$ single-particle Green's functions. The starting point is an initial PDF $p[G_{ii}(\omega)]$ and the calculation is performed using the following algorithm:

1. For each sample a random on-site energy $\epsilon_i$ is drawn from the PDF $p_\epsilon(\epsilon_i)$.

2. The hybridization function $\Gamma_i(\omega)$ is determined via equation (4.23) for each sample. The local single-particle Green's function $G_{jj}(\omega)$ of the nearest neighbors are randomly sampled from the PDF $p[G_{ii}(\omega)]$.

3. The local self-energy $\Sigma_i(\omega)$ is calculated from the solution of the local impurity problem by using an impurity solver.

4. The local single-particle Green's function $G_{ii}(\omega)$ is calculated using equation (4.22).

5. Having calculated a completely new ensemble $\{G_{ii}(\omega)\}$, a new PDF $p[G_{ii}(\omega)]$ is obtained by construction of a histogram.

Returning to the first step closes the self-consistency circle. The algorithm is repeated until self-consistency for $p[G_{ii}(\omega)]$ is achieved. Like the local distribution method, the statistical DMFT incorporates spatial fluctuations caused by disorder via step 2.

As statistical DMFT describes a fully interacting problem, different frequencies $\omega$ do not decouple in the self-consistency relations. This is differnet to the
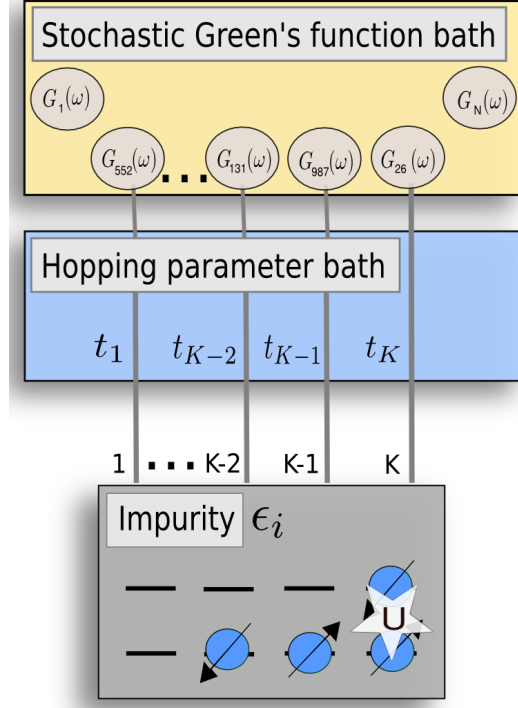
**Figure 4.3.:** Illustration of the statistical DMFT applied in this work. The many-body problem with disorder is mapped onto an ensemble of single impurities, coupled to an ensemble of stochastic Green's functions, which is determined self-consistently. $G_n$ represents the $n$-th sample from the ensemble of Green's functions.

non-interacting case, that is investigated by means of the local distribution approach (see section 3.3), where the self-consistency equations can be solved for each frequency separately. In order to keep the computation time feasible, we need to use a fast impurity solver for determining the self-energy $\Sigma(\omega)$. By using MPT as impurity solver and parallelizing the code, ensembles of the order $10^3$ samples are numerically feasible. The estimation of the PDF typically involves $\sim 10^5$ samples if the histogram is constructed on the basis of $\sim 10^2$ successional update iterations, after self-consistency is obtained. The statistical DMFT reduces to the local distribution method without interaction and to the homogeneous DMFT the absence of disorder.

The statistical DMFT was first developed for application to the Anderson-Hubbard model [85, 86], where a slave-boson approach [123, 169] was used as an impurity solver. In particular, the PDFs of the quasi-particle weight and

density have been calculated. Although the slave boson approach accurately describes the Fermi liquid regime, it fails to capture high energy features and therewith cannot be used for an accurate estimation of the phase diagram.

In addition, the statistical DMFT was used to investigate models of heavy fermion compounds, like Anderson lattices [6, 195, 196]. These works established the existence of a Griffiths phase [136] as a precursor to the Mott-Anderson transition. Moreover, the statistical DMFT has been applied to the Falicov-Kimball model [274], for which the paramagnetic ground state phase diagram has been mapped out. There have been several studies on the Anderson-Hubbard model in the finite lattice version (which we refer to as real-space DMFT) by using the Hubbard-I approximation [257, 258]. This restricts the investigation to certain parameter regimes and is known to give qualitatively incorrect results. Interestingly, it was also applied to disordered electron-phonon systems [52], which demonstrates the wide range of possible applications.

In this work, we will establish the statistical DMFT in its fully stochastic implementation on the infinite Bethe lattice as a suitable method for a comprehensive investigation of disorder and correlation effects on equal footing. For this purpose, we apply the statistical DMFT to the box disordered Anderson-Hubbard Hamiltonian (see chapter 6). In particular, we use the statistical DMFT to investigate disorder models of specific interest for experiments with ultracold atoms: (i) the binary disorder in chapter 7 and (ii) the speckle disorder in chapter 8. Both disorder models will be introduced in detail in the next chapter 5.

### 4.4.1. Off-diagonal disorder within statistical DMFT

In general, the hopping amplitude $t$ between two lattice sites may depend on the disorder potential. The hopping amplitude becomes a random variable [22, 83, 153, 261, 308] distributed by a PDF $p_t(t)$. This type of disorder, also termed off-diagonal disorder, can be incorporated in the statistical DMFT. In detail, equation (4.16) reads

$$\Gamma_i(\omega) = \sum_{j=1}^{K} t_{ij}^2 G_{jj} \; , \tag{4.24}$$

where the hopping amplitude $t_{ij}$ takes on one possible value of the PDF $p_t(t)$. It is reasonable to assume that the PDF is correlated with the difference of the corresponding on-site energies $\Delta\epsilon = |\epsilon_i - \epsilon_j|$. Theoretically this is accounted for by a joint PDF $p_{t,\Delta\epsilon}(t,\Delta\epsilon)$. We will return to this issue in chapter 8, but restrict ourselves to a PDF $p_t(t)$ for the time being. The stochastic self-consistent

calculation scheme is modified to:

1. For each sample, a random on-site energy $\epsilon_i$ is drawn from the PDF $p_\epsilon(\epsilon_i)$.

2. For each sample $i$, random hopping amplitudes $t_{ij}$ are drawn from the PDF $p_t(t)$.

3. The hybridization function $\Gamma_i(\omega)$ is determined via equation. (4.24) for each sample. The local single-particle Green's function $G_{jj}(\omega)$ of the nearest neighbors are randomly sampled from the PDF $p\left[G_{ii}(\omega)\right]$.

4. The local self-energy $\Sigma_i(\omega)$ is calculated from the solution of the local impurity problem by using an impurity solver.

5. The local single-particle Green's function $G_{ii}(\omega)$ is calculated using equation (4.22)

6. Having calculated a completely new ensemble $\{G_{ii}(\omega)\}$, a new PDF $p\left[G_{ii}(\omega)\right]$ is obtained by construction of a histogram.

The inclusion of hopping disorder allows for a more realistic modeling of disorder problems, and is especially important for our later investigation of speckle disordered lattices.

Although the random hopping physics has first been assumed to be equivalent to the physics of pure diagonal disorder types, soon 'unusual' localization effects have been discovered. This effects are referred to as 'unusual' since the behavior of underlying quantities is different from the case of pure diagonal disorder. For instance, it was found that the states at the band center are always extended in case of pure off-diagonal disorder [22, 261], whereas it becomes localized for some particular disorder strength in the case of diagonal disorder. Even more interesting phenomena have been found within systems governed by the interplay between interaction and off-diagonal disorder in infinite dimensions, which were shown to exhibit a diverging specific heat within the metallic phase for example [83]. Such interesting results stimulated recent work on the interplay of interaction and off-diagonal disorder, with the conclusion that correlations are necessary to destabilize the metallic phase [116, 117].

## 4.5. Compendium: Phases of strongly correlated fermions in disordered lattices

In conclusion, we have seen that describing the physics of strongly correlated fermions in a disordered lattice first requires proper a definition of the arising

phases[3]. We first discussed the Mott insulator as a correlation-induced insulating phase, which is incompressible and features a gapped spectrum. The excitation gap is proportional to the interaction strength $U$. Secondly, we discussed the Anderson insulator in the absence of interactions as a disorder-induced, insulating phase. We will characterize it by an extended gap criterion, which is defined as the required energy to create a macroscopically extended charge excitation. A state is localized and consequently not macroscopically extended if its spectrum is point-like. For finite interactions, a pure Anderson insulator is no longer defined, and we will define a many-body state to be many-body localized, if the corresponding single-particle excitation spectrum is point-like. The corresponding phase, defined by the presence of an excitation gap to macroscopically extended single-particle excitations, is called Anderson-Mott insulator. However, no rigorous statement exists so far, that such a point-like spectrum induces insulating behavior, i.e. vanishing DC conductivity. Finally, the paramagnetic disordered metal is compressible and exhibits no gap.

---

[3]Throughout this work, magnetic phases are not considered.

# 5. Ultracold atoms in optical lattices

The invention of laser cooling [24, 71, 225, 298, 299] paved the way to the experimental research field of ultracold atoms. Temperatures lower than $\mu$K became accessible and a route to quantum degenerated gases was provided. A break through was achieved by the realization of the Bose-Einstein condensate [16, 78] and afterwards quantum degeneracy was also achieved for fermions [81]. Later, the experimental technique of loading ultracold atoms into optical lattices [159, 229], acting as artificial crystals for atoms, lead to a new branch of experiments [45, 183, 202]. In a seminal paper, Jaksch *et al.* [154] proposed to simulate the Bose-Hubbard model with ultracold atoms in an optical lattice and predicted a quantum phase transition from a superfluid to a Mott insulator when varying the lattice depth. This was indeed experimentally observed in a optical lattice by Greiner *et al.* in 2002[132].

Thereby, a quantum simulator as proposed by Feynman [108] was achieved to study strongly correlated quantum systems. In general, experiments with ultracold atoms in optical lattices are distinguished by their high control and tunability of the experimental parameters. Hence, theoretical models, which are essential for the understanding of solids are implemented and can be studied with a high accuracy and nearly no approximations.

Nowadays, the diversity of models that can be simulated ranges from Hubbard-type models [155], various spin models [89, 194], to Tonks-Girardeau gases [222]. In particular, the fermionic Hubbard model (2.1) has been realized [166] and the fermionic Mott insulator has been observed [160, 242]. Moreover, ultracold atoms have been successfully exposed to disorder potentials in absence of or in combination with an optical lattices [25, 199, 239]. Within these experiments a milestone was achieved by the observation of localized matter waves [39, 233]. This development is very promising towards gaining a deeper insight in the open issue of the interplay of strong correlations and disorder. An inherent advantage of these experiments is the perfect realization of e.g. the Anderson-Hubbard Hamiltonian[1] among other disorder models. Therefore, they allow a quantitative

---

[1]Recently, the bosonic Anderson-Hubbard Hamiltonian has been studied experimentally [223, 293]. Comparable experiments for fermions are still missing.

comparison of theoretical predictions and experimental observations.

In this chapter we will first shortly review the realization of the Hubbard model in ultracold atoms in optical lattices and focus on how disorder can be added to optical lattices. The chapter concludes with a short discussion of experimental probes.

## 5.1. Simulating the Hubbard model

Alkali atoms[2], such as e.g. $^6$Li, $^7$Li, $^{40}$K, or $^{87}$Rb, interact with an laser field via the AC Stark effect. The electromagnetic field induces an electric dipole moment, given by $\mathbf{d} = \alpha(\omega)\mathbf{E}$ with $\alpha$ being the frequency dependent polarizability of the atom. The corresponding dipole potential is given by [137]

$$V_{\text{dip}} = -\frac{1}{2}\langle \mathbf{dE}\rangle_t, \tag{5.1}$$

where $\langle \dots \rangle_t$ denotes the time average, which is used as the frequency of the electromagnetic field is much higher than the inverse timescale of the center-of-mass motion of the atom. Thus, the light induced potential is proportional to the time averaged intensity $I(\mathbf{x})$ of the laser field.

Typically, the polarizability of the atom is determined by considering a two-level system with transition frequency $\omega_0$ exposed to a classical electromagnetic field. Application of time-dependent perturbation theory to first order, and further using of the rotating wave approximation and considering the finite life time of the excited state[3] yields [137]

$$V_{\text{dip}}(\mathbf{x}) = \frac{3\pi c^2}{2\omega_0^3}\frac{\Gamma_e}{\delta}I(\mathbf{x}) , \tag{5.2}$$

with the detuning $\delta = \omega - \omega_0$ and the decay rate $\Gamma_e$ of the excited state. The structure of equation 5.2 reveals that the induced potential is attractive for red-detuned ($\delta < 0$) and repulsive for blue detuned ($\delta > 0$) light. Specifically for alkali atoms the relevant transition corresponds to the D-line excitation $^n\text{S}_{1/2} \rightarrow{}^n\text{P}_{1/2}, {}^n\text{P}_{3/2}$.

Next we will consider optical lattices. If two counter-propagating laser beams with equal frequency are superimposed, a periodic interference pattern, i.e. a standing wave is realized. Atoms exposed to the beams experience a periodic

---

[2]In experiments usually alkali atoms are used, as they feature a transition spectrum with isolated resonances lying in an experimentally convenient optical range.

[3]Thereby the polarizability becomes a complex number and the dipole potential is given by $V_{\text{dip}} = -\frac{1}{2}\text{Re}(\alpha)I$.

dipole potential $V_{\text{lat,1d}}(z) = s_L \sin^2(\pi z/d)$ with period $d$ equal to half of the wavelength of the laser light [137], a lattice depth $s_L$ which is typically measured in units of the recoil energy $E_R = \hbar k_L^2/2m$, and where $k_L$ is the wave vector of the optical lattice and $m$ is the atomic mass. By using two counter-propagating beams in $x$ direction or additionally also in $y$ and $z$ direction square and cubic lattices

$$V_{\text{lat,1D}}(x,y,z) = s_{L,x} \sin^2(\pi \frac{x}{d}) + s_{L,y} \sin^2(\pi \frac{y}{d}) + s_{L,z} \sin^2(\pi \frac{z}{d}) \,, \tag{5.3}$$

can be realized. An illustration is given in figure 5.1. Different geometries are possible by superimposing laser beams by an angle other than 180° or tuning the polarizations. In particular, triangular optical lattices have been realized recently [30].
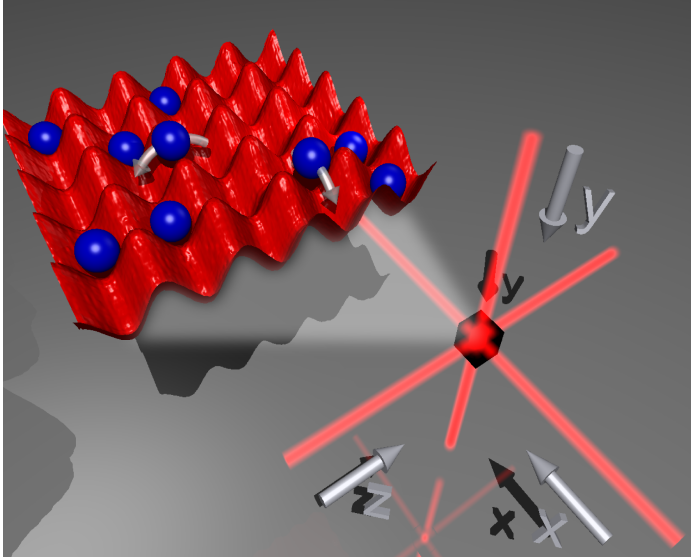


**Figure 5.1.:** Illustration of an optical lattice created by superposition of laser beams.

So far we have discussed single atoms exposed to an external light potential. However, by considering quantum gases, we are faced with a true many-body problem, as the particles are interacting. The physical origin of the interactions between the neutral atoms is given by the short-range van der Waals force, featuring a rapid $1/r^6$ decay at large distances. For dilute gases, two-particle collisions are dominant, which can be theoretically understood by a single-channel scattering process within a first approximation. An expansion in partial waves [238] shows that at sufficiently low temperatures and low energies, the

scattering into higher angular momentum states $l = 1,2,..$ is suppressed due to the centrifugal barrier. Therefore, the scattering process from $l = 0$ into $l = 0$ states, the so-called $s$-wave scattering dominates[4], which is accurately described by a single length scale the so called $s$-wave scattering length $a$ [45, 125, 238]. Since the $s$-wave state is spatially symmetric, only fermions in different spin states can interact in that regime as a consequence of their antisymmetric two-particle state. Typically, the scattering length is two orders of magnitude larger than the size of the atoms.

The $s$-wave scattering length is defined by the low-energy limit of an expansion of the cotangent of the $s$-wave phase shift $\delta_0$ at zero distance [238]

$$\lim_{k \to 0} k \cot(\delta_0) = -\frac{1}{a} \ . \tag{5.4}$$

It is determined theoretically by considering simple model potentials like a hard core potential plus an asymptotic van der Waals decline at long distances or hard-core plus square well potentials [135]. Since the scattering physics only depends on the scattering length, it is convenient to model the interactions via a pseudo potential [125]

$$V(\mathbf{r} - \mathbf{r}') = \frac{2\pi a}{m_r} \delta(\mathbf{r} - \mathbf{r}') \,, \tag{5.5}$$

which reproduces the correct low energy scattering length. Here, $m_r$ denotes the reduced mass of the two particles.

Remarkably, the scattering length, and therewith the strength of the particle interactions, can be tuned [48, 103, 152, 167, 201, 268, 271] via a Feshbach resonance [102, 107]. A more appropriate theoretical investigation of the scattering process accounts for the internal degrees of freedom of the alkali atoms, like the hyperfine structure, thus including multi-channel scattering. The different channels are coupled by the hyperfine interaction. A Feshbach resonance occurs in two-particle collisions, when a diatomic bound state of the two-body system becomes resonant or close to resonant to an open channel, i.e. the continuum threshold of the system. The two atoms form temporarily a bound state, which subsequently decays to an open channel. A multi-channel analysis shows that the resulting scattering length depends on the energies of the various channels (cf. e.g. [267]). These in turn differ in their energy due to different Zeeman shifts corresponding to their spin configurations. Hence, adjusting the magnetic field leads to channel-dependent shifts of the channels'

---

[4]In fact, the ultracold regime of quantum gases is widely defined by the dominating $s$-wave scattering.
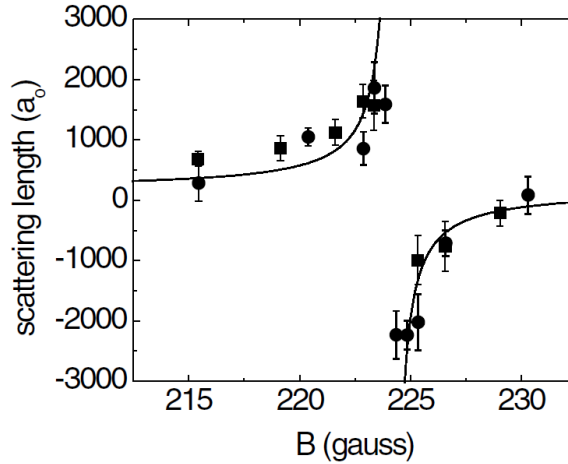
**Figure 5.2.:** Measurement of the *s*-wave scattering length in units of Bohr radii as a function of magnetic field $B$ in a mixture of fermionic $^{40}$K atoms in hyperfine states $|f = 9/2, m_f = -9/2\rangle$ and $|f = 9/2, m_f = -5/2\rangle$. A Feshbach resonance exists at $B_0 = 224.36$G. The solid line corresponds to a fit function of form (5.6). Reprinted from reference [230]

energies and therefore the scattering length is varied. Typically, the relation between the *s*-wave scattering length and the magnetic field can be approximated by [201]

$$a(B) = a_{\mathrm{bg}}\Big(1 - \frac{\Delta B}{B - B_0}\Big) \,, \tag{5.6}$$

with $a_{\mathrm{bg}}$ denoting the background scattering length, $\Delta B$ the width and $B_0$ the magnetic field strength of the resonance. Thereby, it is possible to tune the interaction strength between the particles by changing the external parameter magnetic field. In figure 5.2 the measured *s*-wave scattering length in a mixture of fermionic $|f = 9/2, m_f = -9/2\rangle$ and $|f = 9/2, m_f = -5/2\rangle$ $^{40}$K atoms is plotted as a function of the magnetic field (measurement by Regal *et al.* [230]). Strong repulsive interactions corresponding to large positive scattering lengths are obtained, as well as strong attractive interactions corresponding to negative scattering lengths, by tuning the magnetic field across the Feshbach resonance at $B_0 = 224.36$G [230]. In the experiment, however, fluctuations of the magnetic field hinder an arbitrary adjustment of the scattering length.

Combining the single-particle parts, i.e. the kinetic energy and the external potential, and the two-particle interaction, a two-component mixture of fermions

in an optical lattice is described by the Hamiltonian

$$
\begin{aligned}
H \;=\;& \sum_\sigma \int d\mathbf{x}\, \Psi_\sigma^\dagger(\mathbf{x})\big(-\frac{\nabla^2}{2m_\sigma} + V_{\text{ext},\sigma}(\mathbf{x})\big)\Psi_\sigma(\mathbf{x}) \\
& + \int d\mathbf{x} \int d\mathbf{x}'\, \Psi_\uparrow^\dagger(\mathbf{x})\Psi_\downarrow^\dagger(\mathbf{x}')V(\mathbf{x}-\mathbf{x}')\Psi_\downarrow(\mathbf{x}')\Psi_\uparrow(\mathbf{x})\;.
\end{aligned}
\tag{5.7}
$$

In general, the external potential consists of the lattice potential $V_{\text{lat},\sigma}$ and the trapping potential $V_{\text{trap},\sigma}$. Subsequently, the trapping potential is neglected. In experiments the trapping potential can be compensated by an additional blue-detuned laser (see for example reference [297]). As we considering two hyperfine states, the masses are equal for both components. Moreover, as the AC Stark effect is not sensitive towards the hyperfine state, both components are exposed to the same lattice potential. The fermionic field operator, expanded in the Wannier basis, is given by

$$
\Psi_\sigma^\dagger(\mathbf{x}) = \sum_{i,\nu} w_{\nu,\sigma}^*(\mathbf{x}-\mathbf{R_i})c_{i,\nu,\sigma}^\dagger\;,
\tag{5.8}
$$

where $\nu$ denotes the band index and $c_{i,\nu,\sigma}$ denotes the annihilation operator of the corresponding Wannier state. Within this expansion and under consideration of the pseudo-potential (5.5), the Hamiltonian reads

$$
H = -\sum_{\nu\sigma}\sum_{ij} t_{ij}^{\nu\sigma} c_{i\nu\sigma}^\dagger c_{j\nu\sigma} + \sum_{ijkl}\sum_{\nu_1\nu_2\nu_3\nu_4} U_{ijkl}^{\nu_1\nu_2\nu_3\nu_4} c_{i\nu_1\uparrow}^\dagger c_{j\nu_2\uparrow} c_{k\nu_3\downarrow}^\dagger c_{l\nu_4\downarrow}
\tag{5.9}
$$

with

$$
t_{ij}^{\nu\sigma} \;=\; \int d\mathbf{x}\, w_{i\nu\sigma}^*(\mathbf{x})\big(-\frac{\nabla^2}{2m} + V_{\text{lat}}(\mathbf{x})\big)w_{j\nu\sigma}(\mathbf{x})
\tag{5.10}
$$

$$
U_{ijkl}^{\nu_1\nu_2\nu_3\nu_4} \;=\; \frac{4\pi a}{m} \int d\mathbf{x}\, w_{i\nu_1\uparrow}^*(\mathbf{x})w_{j\nu_2\uparrow}(\mathbf{x})w_{k\nu_3\downarrow}^*(\mathbf{x})w_{l\nu_4\downarrow}(\mathbf{x})
\tag{5.11}
$$

and the short-hand notation $w_{i\nu\sigma}(\mathbf{x}) = w_{\nu\sigma}(\mathbf{x}-\mathbf{R}_i)$. At sufficiently low filling, low temperature, low lattice depth and weak interactions higher bands can be safely neglected, as they will not be populated. This is commonly referred to as single-band approximation[5]. Furthermore, for sufficiently deep lattices the Wannier functions are well localized and all hopping except nearest-neighbor hopping and all interactions except local interactions can be neglected. Thus, the Hubbard model (2.1) is obtained, with local interaction strength $U \equiv U_{0000}^{1111}$, in which the amplitudes $t$ and $U$ can be evaluated numerically for

---

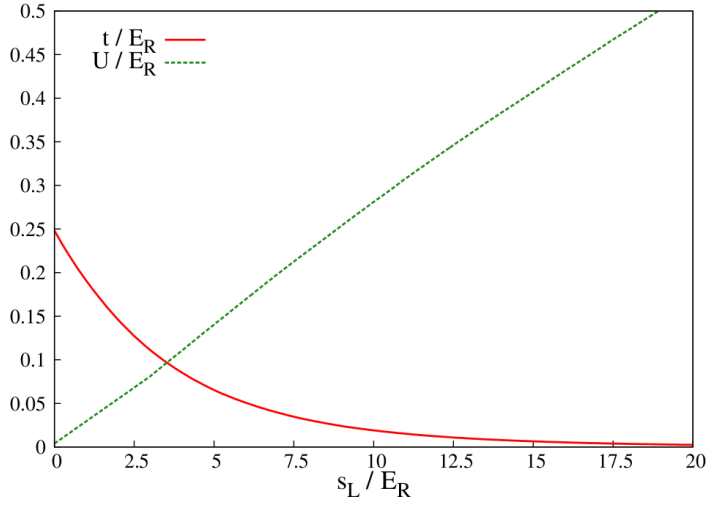[5]For a detailed discussion of the validity see e.g. [292].

**Figure 5.3.:** Local interaction strength $U$ and hopping amplitude $t$ as a function of lattice depth $s_L$ in units of the recoil energy, resulting from band structure calculations performed by Greiner [130]. Here, bosonic $^{87}$Rb atoms in a optical lattice with wavelength $\lambda = 852$nm were considered.

a given optical lattice of strength $s_L$. An analytic expressions for $U$ is obtained by approximating the potential at each lattice site as a harmonic potential [8, 154, 310]. Consequently, the Wannier function takes on the Gaussian ground state wave function of the harmonic potential and the on-site interaction is given by

$$U = \sqrt{\frac{8}{\pi}} a k_L \left( \frac{s_L}{E_R} \right)^{3/4} E_R \ . \tag{5.12}$$

An analytic approximation for the hopping amplitude

$$t = \frac{4}{\sqrt{\pi}} \left( \frac{s_L}{E_R} \right)^{3/4} e^{-2(\frac{s_L}{E_R})^{1/2}} E_R \tag{5.13}$$

can be obtained from the solution of the 1d Mathieu equation [45, 310]. However, especially for comparisons with experimental data, it is necessary to calculate the amplitudes from an exact band structure calculation [130], which involves the numerical solution of a single-particle Schrödinger equation. The resulting parameter of such a evaluation are plotted in figure 5.3. By tuning the lattice potential, the on-site interaction strength $U$ and the hopping parameter $t$ are
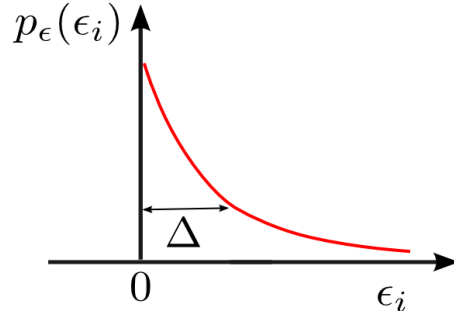
**Figure 5.4.:** Illustration of the probability distribution function of the on-site energies in case of speckle disorder. The standard deviation and the expectation value are given by the disorder strength parameter $\Delta$.

simultaneously changed, but in different fashions. Hence, almost arbitrary ratios $U/t$ can be adjusted.

## 5.2. Adding disorder to optical lattices

Disorder in ultracold gases can be added in different ways: (i) by using an optical speckle laser [39, 223, 293], (ii) by loading two atomic species, where only one is mobile, into an optical lattice [119, 138, 220]. or (iii) by superimposing two laser beams with incommensurate frequencies [101, 233]. All approaches are briefly introduced in the following.

### 5.2.1. Speckle disordered lattices

The speckle disorder potential is created by a coherent laser beam that is scattered by a diffusor plate [39, 73, 191, 223, 293]. A statistical analysis of the light scattering process [126, 127] shows that the PDF of the resulting light intensity pattern obeys $p_I(I) = \Theta(I) \exp(-I/\langle I \rangle)/\langle I \rangle$, where $\langle I \rangle$ is the averaged light intensity and $\Theta(x)$ denotes the Heaviside function. By superimposing the speckle light pattern on the optical lattice, the atoms are subjected to a random optical dipole potential $V_D(\mathbf{r}) \propto I(\mathbf{r})$ [73] as already discussed for the lattice potentials in the preceding section. The potential is attractive for red-detuned laser light or repulsive for blue-detuned laser light. Here and later in chapter 8, we consider the latter, i.e. the repulsive potential. In the tight binding model this random potential gives rise to diagonal disorder, i.e. random on-site
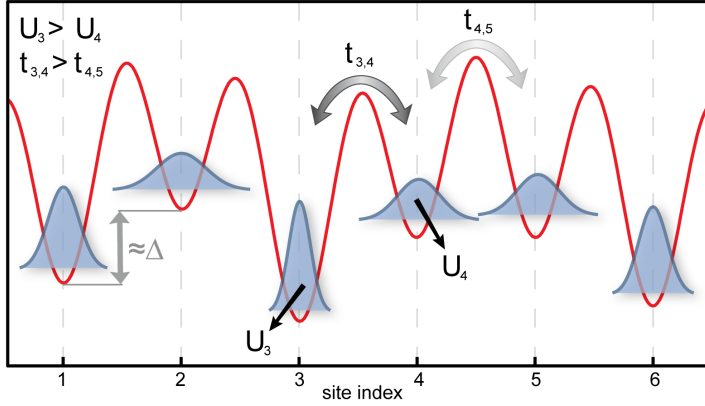
**Figure 5.5.:** One-dimensional illustration of the disordered lattice problem. The speckle field induces random on-site energies given by the PDF $p_\epsilon(\epsilon)$. Hopping amplitudes $t_{ij}$ are random variables, which manifests itself in the PDF $p_{\Delta\epsilon,t}(\Delta\epsilon,t)$. The local interaction strength $U_i$ depends on the extension of the respective Wannier function, which results in a further PDF $p_{\epsilon,U}(\epsilon,U)$.

energies $\epsilon_i$, which are drawn from a PDF $p_\epsilon(\epsilon_i)$ given by

$$p_\epsilon(\epsilon) = \frac{1}{\Delta} \exp(-\frac{\epsilon}{\Delta})\Theta(\epsilon)\,, \tag{5.14}$$

where $\Delta$ denotes the disorder strength. The expectation value $\langle\epsilon\rangle = \int d\epsilon p_\epsilon(\epsilon)\epsilon$ is equal to the disorder strength parameter $\Delta$ and the expectation value of the on-site energy squared is estimated as

$$\langle\epsilon^2\rangle = \int d\epsilon p_\epsilon(\epsilon)\epsilon^2 = \Delta^2\Gamma(3) = 2\Delta^2\,. \tag{5.15}$$

Hence, the standard deviation is given by $\Delta$.

We note that this PDF of the on-site energies is unbounded from above, in contrast to other typically used distributions, such as box or binary disorder. Furthermore, we assume that the on-site energies of all lattice sites are independently and identically distributed. This is valid, if the autocorrelation length of the speckle pattern is smaller than the lattice spacing and was well accomplished in the recent experiments within the DeMarco group [293, 306]. Furthermore, in a tight binding model, the speckle disorder potential leads to a off-diagonal disorder [293, 306]. I.e. disorder in the hopping parameter $t_{ij}$, also referred to as hopping disorder [22, 42, 83, 153, 261, 308]. For a given disorder

distribution, inducing fluctuations in both the hopping and on-site energies, the hopping coefficient $t_{ij}$ at neighboring pair of sites is correlated with the difference in on-site energies $\Delta\epsilon = \epsilon_i - \epsilon_j$ and a realistic description requires the modeling using a joint PDF [306]

$$p_{\Delta\epsilon,t}(\Delta\epsilon,t) \neq p_{\Delta\epsilon}(\Delta\epsilon) \cdot p_t(t) \,. \tag{5.16}$$

Furthermore, for a short-range interaction between particles, the local interaction potential is proportional to the integral over the fourth power of the Wannier function (cf. equation (5.11)), which in turn depends on the random lattice potential. Hence, the on-site interaction potential $U$ is a random variable as well. The joint PDF $p_{\epsilon,U}(\epsilon,U)$ of the on-site interaction strength and the on-site energy also needs to be accounted for. A one-dimensional cartoon illustration of the disordered lattice problem is shown in Fig. 5.5.

Fermionic ultracold atoms in a speckle disordered optical lattice are investigated in chapter 8 by means of the statistical DMFT.

## 5.2.2. Binary disorder

In systems of cold atoms in optical lattices binary disorder can be prepared by adding an additional immobile species of atoms [119, 278]. The atoms of the mobile species experience an on-site energy shift proportional to the interaction strength due to the randomly distributed immobile species. Just two on-site energies are therefore realized, corresponding to either an immobile impurity atom bing present or not at a given lattice site. Hence, the PDF of the on-site
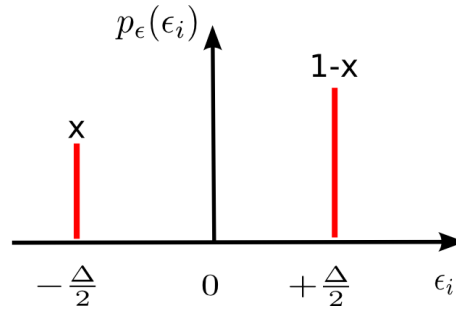


**Figure 5.6.:** Illustration of the probability distribution function of the on-site energies in case of binary disorder. $x$ denotes the impurity concentration and $\Delta$ the on-site energy splitting.

energies is given by the bimodal function

$$p_\epsilon(\epsilon_i) = x\,\delta(\epsilon_i + \frac{\Delta}{2}) + (1-x)\delta(\epsilon_i - \frac{\Delta}{2}),\qquad(5.17)$$

where $x$ and $1-x$ are the fractions[6] of lattice sites with energies $\epsilon_i = -\frac{\Delta}{2}$ and $\epsilon_i = \frac{\Delta}{2}$ respectively. The expectation value of the on-site energy takes on the value $\langle\epsilon\rangle = \int d\epsilon p_\epsilon(\epsilon)\epsilon = \Delta(1/2 - x)$ and the expectation value of the on-site energy squared is given by

$$\langle\epsilon^2\rangle = \int d\epsilon p_\epsilon(\epsilon)\epsilon^2 = \Delta^2 x(1-x)\ .\qquad(5.18)$$

Consequently, the standard deviation is given by $\Delta\sqrt{x(1-x)}$.

Here $\Delta$ describes the on-site energy splitting, which is proportional to the interspecies interaction strength in the weakly interacting, linear regime. The PDF is illustrated in figure 5.6 In general, $\Delta$ and $x$ are independent parameters. However, the cases $x = 0$ or $1$ correspond to non-disordered systems with on-site energy shift $\pm\Delta/2$. Therefore, a natural parameter for measuring the disorder strength in binary alloy systems is $\delta \equiv x(1-x)\Delta$ [303], which is closely connected to the standard deviation. An Illustration of the physical situation is schematically presented in figure 5.7.

It is noticeable, that in contrast to the disorder types discussed so far, the PDF for binary disorder is not continuous, but discrete. A very important difference between the discrete binary-alloy disorder and continuous disorder types, is that in the former case the Bloch band is split if $\Delta > W_0$ in non-interacting systems and in arbitrary lattices [59, 164]. In this limit two alloy subbands are formed and the system is a band insulator if $\nu = 2x$ or $\nu = 2$, where $\nu$ is the number of fermions per site. At other fillings it is a metal. In the presence of interaction a Mott insulator at fractional particle filling $\nu = x$ or $\nu = 1 + x$ is in principle possible [59, 64]. In chapter 7, it is investigated how Anderson localization modifies these predictions by means of the statistical DMFT.

First experimental attempts to realize binary disorder have been performed [138, 220]. However, in such a system care has to be taken that the positions of the immobile atoms are random stationary, i.e. the disorder must be quenched. One possibility to randomly trap the impurity species is to rapidly quench the system from the delocalized state to a localized state, like the Mott insulating state. Also this approach is problematic, since phenomena like collapse and

---

[6]In the context of impurities in solids, $x$ corresponds to the impurity concentration.
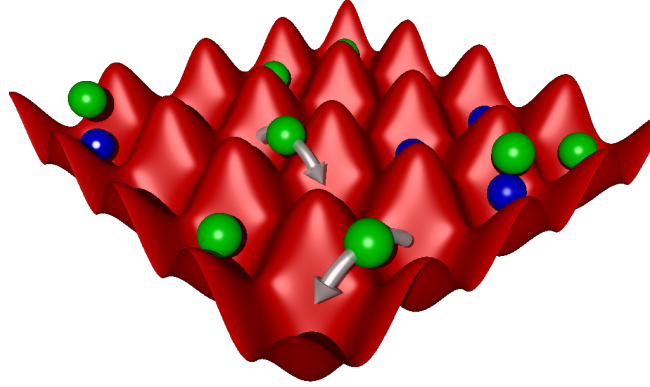
**Figure 5.7.:** Illustration of a given realization of binary disorder in optical lattices. Two atomic species (indicated as green and blue spheres) are loaded into an optical lattice. The hopping amplitude of one species (blue) is strongly suppressed and they are approximated to be immobile. Due to the interatomic interaction, the second species experiences a binary disordered lattice potential, depending on the presence of an atom of the immobile species on the same lattice site, i.e. if there is a blue atom present the on-site energy is $\epsilon_i = +\Delta/2$ otherwise $\epsilon_i = -\Delta/2$.

revival may arise [133].

### 5.2.3. Quasi-periodic lattices

A further approach is based on the superposition of laser beams with incommensurable frequencies [76, 235] that are superimposed on the regular lattice. The resulting potential of two superimposed beams with wave vectors $\mathbf{k_1}$ and $\mathbf{k_2}$ reads [76]

$$V(\mathbf{r}) = V_{\mathrm{lat}}(\mathbf{r}) + V_1(\cos^2(\mathbf{k_1 r}) + \cos^2(\mathbf{k_2 r})) \ . \tag{5.19}$$

In fact, the resulting potential does not represent a true random potential but a quasi-crystal potential [200] and are accurately described by the Harper model [140] or Aubry-André model [26] in one dimension. Within this system the on-site energies are strongly correlated. Nevertheless, it gives rise to similar physics as random potentials as was shown e.g. by theoretical comparisons to speckle disordered potentials [76]. In particular, the system features a sharp transition from extended to localized states [26, 235], hence allowing for glass phases like the Bose glass phase. Since the ratio of $k_1/k_2$ can not be realized as a true irrational number [200], the transition becomes a smooth crossover in

real experiments. On the other hand typical features of disordered systems like Lifshitz tails or mobility edges are missing [200]. The latter are present in the system, if long-range tunneling is taken into account [38, 46]. The distribution of the on-site energies was shown to be well approximated by the shifted $\beta$ distribution [165].

Experimentally, Bose-Einstein condensates in such quasi-periodic potentials have been studied and their excitation spectrum has been measured [101]. In one dimension, localization of non-interacting particles by quasi-disorder has been clearly verified [233].

### 5.2.4. Further approaches

In the context of immobile impurity atoms it was also discussed to tune the interspecies on-site interaction randomly [124]. For this purpose, the strong dependence of the s-wave scattering length on the magnetic field strength near a Feshbach resonance is utilized. Inhomogeneities in the magnetic field tune the interspecies interaction strength locally and these inhomogeneous magnetic fields can be created by the rough surfaces of atom chips [296].

## 5.3. Experimental probing techniques

In this section a brief overview on experimental probing techniques is given.

The time-of-flight measurement has established itself as the most important and common method in the cold atom community [45, 131]. The first step of a time-of-flight measurement is given by suddenly turning-off all trapping potentials, which allows the atoms to expand freely, neglecting the short-range interactions due to their short-range character. The expansion of a Bloch state is governed by its momentum distribution as a superposition of plane waves. After some expansion time the atoms are imaged with a resonant probing laser and a CCD camera. Due to the expansion of time $T_{\mathrm{ToF}}$, the time-of-flight imaged density $n(\mathbf{x}, T_{\mathrm{ToF}})$ is directly proportional to the momentum distribution of the atoms, trapped in the lattice, times the quasi-momentum distribution $n(\mathbf{k}) = \sum_\sigma \langle c_{\mathbf{k}\sigma}^\dagger c_{\mathbf{k}\sigma} \rangle$ [45]. Therefore it gives direct access to first order coherence. This technique is especially useful for bosons, since in case of condensed bosons the lowest Bloch state is populated macroscopically, which results in well defined interference maxima in the time-of-flight image. A further technique, called band mapping is closely connected [45, 166]. If the lattice is ramped down adiabatically, the quasi-momentum of the Bloch state is preserved and finally mapped on to a free particle momentum, which allows the pictorial detection of Brillouin zones [131, 166].

However, in the many particle system nontrivial correlations exist, and it was shown that these correlations are present in the time-of-flight pictures as spatial noise correlations [9]. It has been discussed that signatures of fermionic superfluids, Mott insulating states show up in the noise correlations as well as spin-spin correlations in multi-component systems [9]. Experimentally, such quantum correlations have been probed shortly later in a bosonic system in the Mott insulating phase [114] and in ultracold molecules [134].

For fermions the measurement of double occupancies has been used successfully to obtain signatures of the Mott insulator [160]. The depth of the lattice is rapidly increased to large values, suppressing inter-site tunneling. Afterwards the energy of doubly occupied states is shifted by means of a Feshbach resonance. Thereby only the hyperfine component of the single occupied state can be addressed selectively with a resonant radio frequency pulse to transfer these atoms to a third previously unoccupied hyperfine component. From the time of flight image, where the different components are spatially separated by a magnetic field gradient, the fraction of doubly occupied states can be determined.

Recently, single-site imaging has been established as in-situ technique [27, 28] also with single-atom resolution [252] for two-dimensional optical lattices. Within these experiments, a single two-dimensional optical lattice is prepared and after some time evolution, the lattice is ramped-up suddenly to such high values that the many-particle wave function is projected onto the single-site number states. By turning on an optical molasses system, the atoms are illuminated and time laser cooled at the same. The resulting fluorescent light is collected with a high-resolution optical setup. Besides other results, the shell-structure of a bosonic Mott insulator in a trap was clearly observed [28, 252] and claimed to be expendable in order to investigate quantum critical phenomena that are not accessible within solid state experiments like [252].

In solid state physics, spectroscopic methods such as the angle-resolved photo emission spectroscopy [75] have become established techniques, enabling access to a big variety of relevant information, as for instance the single-particle excitation spectrum. Remarkably, analogous methods giving access to the single-particle excitation spectrum have been developed for experiments with cold atoms. One prominent example is Raman spectroscopy, which enables the probing of the single-particle spectral function, the Fermi surface and the quasi-particle structure of strongly correlated ultracold atoms [77]. In Raman spectroscopy atoms are transferred from a given hyperfine and spatial state into a different hyperfine state via a two-photon process, gaining a momentum transfer $\mathbf{q}$, depending on the setup of the two Raman laser beams. Afterwards, the spectral function can be extracted from the Raman signal by counting the

number of transfered atoms [43, 77]. It was shown that signatures of strongly correlated phases, in particular the Mott insulating phase, are encoded in the Raman signal [35]. Bragg spectroscopy is a very closely related technique [265], which also makes use of a two-photon induced transition but not to a different internal state. Here, the fraction of transferred atoms is determined from the time-of-flight images. Experimentally, it has been successfully applied to bosonic ultracold atoms confined to optical lattices to probe the excitation spectra of the superfluid state [72, 98]. Interestingly, signatures of the glass phases have been recently discussed in the Bragg response in absence of an optical lattice [74].

A further promising spectroscopic technique is the momentum-resolved radio frequency spectroscopy [266], which has been developed in analogy to the angle-resolved photo emission spectroscopy. In the recent experiment [266], a radio frequency field of frequency $\Omega_{\mathrm{RF}}$ was applied to a two-component mixture of fermionic $^{40}$K atoms in hyperfine states $|1\rangle$ and $|2\rangle$ in order to excite the atoms of hyperfine state $|2\rangle$ to hyperfine state $|3\rangle$. Subsequently, the trap is turned off and by counting the number of atoms in state $|3\rangle$ ($N_3$), the dispersion $\epsilon_{\mathbf{k}}$ is obtained [266]. The radio frequency current, defined by $I = \langle \dot{N}_3 \rangle$ is calculated within the linear response theory [141]

$$I(\mathbf{k}, \delta\nu) = \frac{|T_{\mathbf{k}}|^2}{2\pi}\rho(\mathbf{k},\omega)f(\omega)|_{\omega=\xi_{\mathbf{k}}-\delta\nu} \qquad (5.20)$$

for homogeneous systems. $T_{\mathbf{k}}$ denotes the transition matrix, $\delta\nu$ is the RF detuning and $\xi_{\mathbf{k}}$ is equal to $k^2/2m - \mu$, assuming that hyperfine state $|3\rangle$ is not occupied. The photo current within angle-resolved photo emission spectroscopy is given by [75]

$$I_{\mathrm{ph}}(\mathbf{k},\omega) = M(\mathbf{k},\Omega)\rho(\mathbf{k},\omega)f(\omega)\,. \qquad (5.21)$$

Comparing this to equation (5.20) reveals the connection between angle-resolved photo emission spectroscopy and momentum-resolved radio frequency spectroscopy for homogeneous systems. In inhomogeneous systems, such as trapped and/or disordered systems, final state effects have to be taken into account, which can be described by using density functional theory within a local density approximation [69].

Summing up, many powerful probing techniques have been realized or proposed, which allow for a identification on both the experimental and theoretical side to clearly distinguish strongly correlated many-body phases and the investigation of their physical properties. As discussed above, also disorder induced effects and quantum phases are observable within today's available probing tech-

niques. However, further research is required to obtain a clear signature of the fermionic Anderson and Anderson-Mott insulator[7], as so far only compressibility measurements may reveal their existence [80].

---

[7]The measurement of exponential decay of the macroscopically occupied wave-function as done e.g. in [39] is not possible in case of fermionic systems.

# 6. Anderson-Hubbard model with box disorder

Among the investigations of the box disordered Anderson-Hubbard model in $d > 1$ dimensions which are non-perturbative and incorporate localization effects the TMT was used in the most comprehensive way [5, 60–62, 82]. Within these works the ground state phase diagram has been determined for half-filling [5, 60] and the physical two fluid picture of the Anderson-Mott transition has been developed [5, 82]. The statistical DMFT has also been used to study the Anderson-Hubbard model with box disorder [85, 86, 257, 258]. On the one hand, the Anderson-Mott transition has been characterized in detail by an accurate treatment of the low energy excitations [85, 86]. Remarkably, two critical disorder strengths have been found, one corresponding to the entering of a non-Fermi liquid phase and a second one corresponding to the Anderson-Mott transition. On the other hand, a special focus was laid on the zero-bias anomaly [10, 95] in two dimensions [257, 258]. However, partially due to the immense numerical effort and partially due to the restrictions of the used impurity solvers – the slave-boson approach [123, 169] and the Hubbard I approximation [147] – the ground state phase diagram was not determined.

In this chapter we show what kind of knowledge is accessible within statistical DMFT and how this knowledge is gained by revisiting the box disordered (3.27) Anderson-Hubbard model (4.1). Here, the statistical DMFT is consolidated as an appropriate method to investigate the Anderson-Hubbard model in the whole range of disorder and interaction strength. In particular, we are interested in the interplay of both phenomena. We discuss disorder-induced as well as correlation-induced metal insulator transitions and identify two delocalization processes. By studying the PDF of the LDOS, we find that it strongly deviates in the metallic phase from a log-normal distribution as found for the non-interacting case (cf. section 3.3). Moreover, using MPT as impurity solver allows for the determination of the complete paramagnetic ground state phase diagram for the first time by means of the statistical DMFT. Our results are critically discussed with respect to established results obtained within the TMT earlier [60, 82].

We investigate the half-filled system, which is accomplished by $\mu = U/2$ for the box disorder distribution of the on-site energies. Throughout this chapter
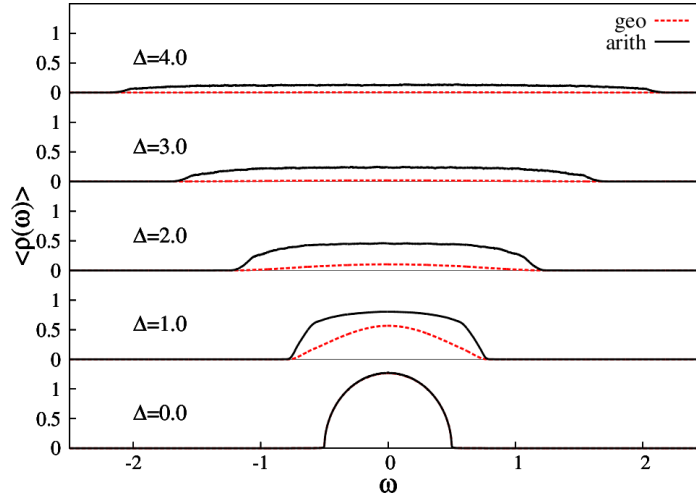
**Figure 6.1.:** Evolution of the arithmetically and geometrically averaged spectral function of the non-interacting system with increasing disorder strength $\Delta$. Parameters are $\eta = 10^{-3}$, $\mu = U/2$ and $K = 6$.

we will measure energies in units of the non-interacting bandwidth of the homogeneous system $W_0 = 1$. Parts of this chapter have been published [249].

## 6.1. Non-interacting system

Since the statistical DMFT reduces to the local distribution approach in the non-interacting system, we already know from section 3.3 and the literature [2, 14] that the Anderson-Hubbard model with box disorder exhibits an Anderson transition on the Bethe lattice when the disorder strength is increased. The disorder causes a broadening of the spectrum as can be clearly seen from figure 6.1, where the geometrically averaged (4.11) and arithmetically averaged spectral functions (3.25) are plotted for selected values of the disorder strength and zero interaction. The broadening is naturally accompanied by a drop-off of the geometric average as well as the arithmetic average. This is because the spectral weight is distributed over a bigger range of energies with increasing disorder strength. As an important feature we note the much stronger decline of the geometric average to zero, as previously described in section 4.3. Since the arithmetically and geometrically averaged spectral function are plotted as a function of the energy, we are also able to note that the decline is not uniform, but rather strongly depends on the energy. For instance, the geometric average of the LDOS remains clearly finite in the band center for $\Delta = 2$, whereas it is

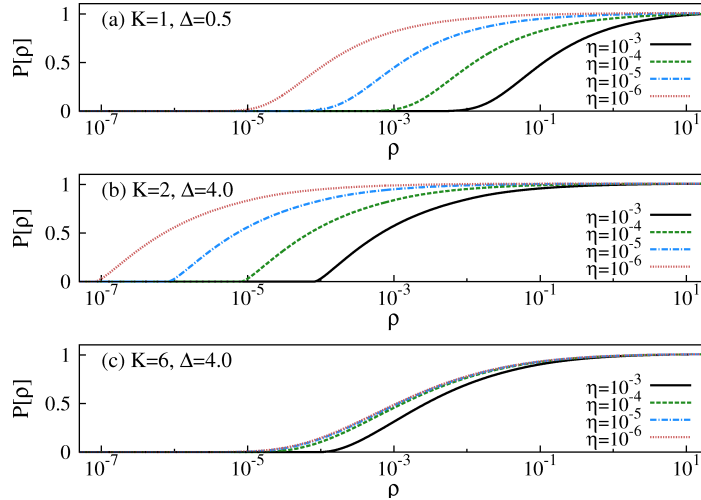close to zero for the states in the outer parts of the spectrum.



**Figure 6.2.:** Evolution of the cumulative PDFs at the Fermi level $P[\rho(0)]$ of the non-interacting system with decreasing $\eta$ in (a) for $K = 2$ and (b) for $K = 6$ at fixed disorder strength $\Delta = 4.0$. Parameters are $U = 0$ and $\mu = 0$.

Compared to CPA and TMT, the connectivity $K$ represents an additional free parameter within statistical DMFT. It is well established that no localization occurs in the limit of infinite spatial dimensions, or for infinite connectivity, respectively. On the other hand, it is known from scaling theory that in one dimension and in two dimensions – i.e. for small connectivities – already arbitrarily small disorder suffices to localize all states in the absence of interactions [3]. Hence, this strong dependence of localization on the connectivity should be captured by statistical DMFT. We would expect that for higher connectivity the tendency towards delocalization is enhanced. Let us, for instance, consider the evolution of the cumulative PDF of the LDOS at the Fermi level defined in equation (3.26) when the broadening $\eta$ approaches zero for several parameter sets as given in figure 6.2. In panel (a) we consider a small disorder strength $\Delta = 0.5$ for connectivity $K = 1$, that means a linear chain. We note that the $\omega = 0$ state is localized according to our discussion in section 3.3. For $K = 2$ (not displayed) our analysis shows that the state is extended and higher disorder strengths are needed to localize the state at the Fermi level, as can be seen for example for $\Delta = 4$ in panel (b). Finally, in panel (c) we investigate the connectivity $K = 6$ for the same disorder strength. In the former case the state at $\omega = 0$ is localized, whereas in the latter case with a larger connectivity the state is extended. We see that our expectation is met.
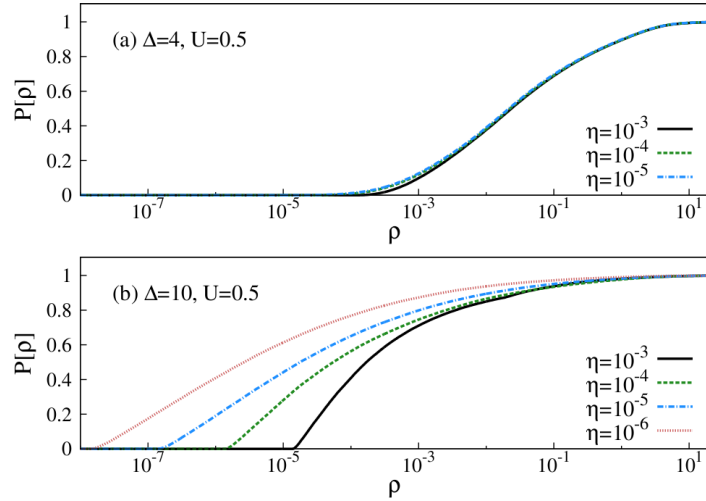
**Figure 6.3.:** Evolution of the cumulative PDFs at the Fermi level $P[\rho(0)]$ with decreasing $\eta$ (a) for $\Delta = 4$ and (b) for $\Delta = 10$ at fixed interaction strength $U = 0.5$. Parameters are $K = 3$, $W_0 = 1.0$, and $\mu = U/2$.

## 6.2. Probability distribution of the local density of states for finite interactions

In this section we will investigate the PDFs of the LDOS for finite interactions. We will first address the question of disorder-induced localization in presence of interactions. The evolution of the cumulative PDF of the LDOS with decreasing broadening is plotted in figure 6.3 for the weakly interacting case $U = 0.5$. In panel (a) the disorder strength is given by $\Delta = 4$ and in panel (b) $\Delta = 10$, corresponding to the strongly disordered regime. We note that the PDF saturates for $\Delta = 4$, when the broadening approaches zero, corresponding to an extended state. In contrast, for very strong disorder strength $\Delta = 10$ the PDF does not saturate. Here, the state is localized within the resolution given by the size of our stochastic Green's function bath. By comparison to figure 6.2, we note that the shape of the PDFs of the interacting system differs from these given in the non-interacting case. In particular, the slope of the cumulative PDFs varies with the broadening, which indicates that significant weight of the PDF is distributed over several orders of magnitude of the LDOS.

The statistical DMFT allows for studying how the PDF of the LDOS evolves, from the non-interacting case and weakly interacting case to the regime of strong correlations. In figure 6.4 the PDFs are plotted for several selected values of the interaction and fixed disorder strength $\Delta = 4$ and connectivity $K = 3$. In
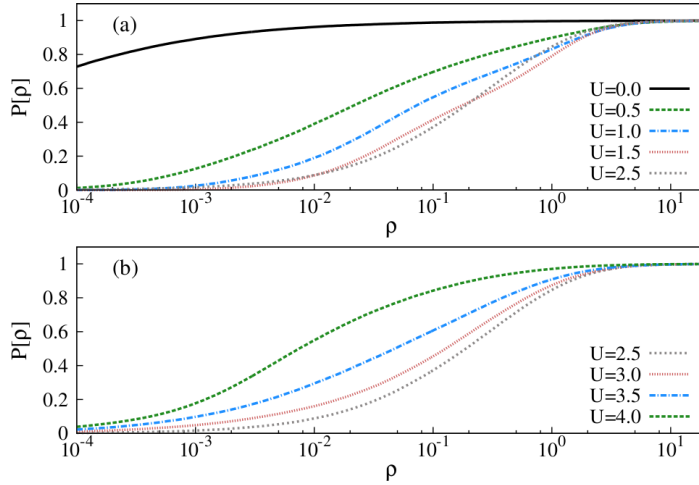
**Figure 6.4.:** Evolution of the cumulative PDFs at the Fermi level $P[\rho(0)]$ with increasing interaction strength $U$ for fixed disorder strength $\Delta = 4$. In panel (a) the PDF of the non-interacting system is compared with the PDFs of the interacting system from weak interactions ($U = 0.5$) to intermediate interactions ($U = 1,1.5,2$). In panel (b) the interaction strength $U$ is further increased stepwise to the strongly interacting regime ($U = 3,3.5,4$). Parameters are $K = 3$, $\eta = 10^{-5}$, $W_0 = 1$, and $\mu = U/2$.

panel (a) weak interactions ($U = 0.5$) are introduced and stepwise increased to the intermediate regime ($U = 2.5$). In comparison to the non-interacting case (corresponding to a localized state as we will see clearly in the next section), we note a striking redistribution already for weak interactions. The PDF is still extended over many decades of values of the LDOS, but a big fraction of the PDF is shifted to much higher values of the LDOS compared to the non-interacting case. We will understand this severe modification later. Further increase of the interaction strength to $U = 1.5$ systematically fortifies this redistribution. More and more sites exhibit comparable values of the LDOS, as can be seen from the larger slope of the cumulative PDF. This behavior contradicts a strong fragmentation of the single-particle excitation spectrum. Moreover, we note that the cumulative PDF gains most of its weight in two regions of a big slope for $U = 1.5$ . This feature erodes for bigger interaction strengths as can be seen from the cumulative PDF for $U = 2.5$. In panel (b) the interaction strength is stepwise increased further to $U = 4$. In contrast to the behavior found in panel (a) it can be clearly seen that opposite behavior is obtained in that case. The PDFs shifts again to smaller and smaller values of the LDOS. Obviously, correlations do not monotonically influence the PDF of
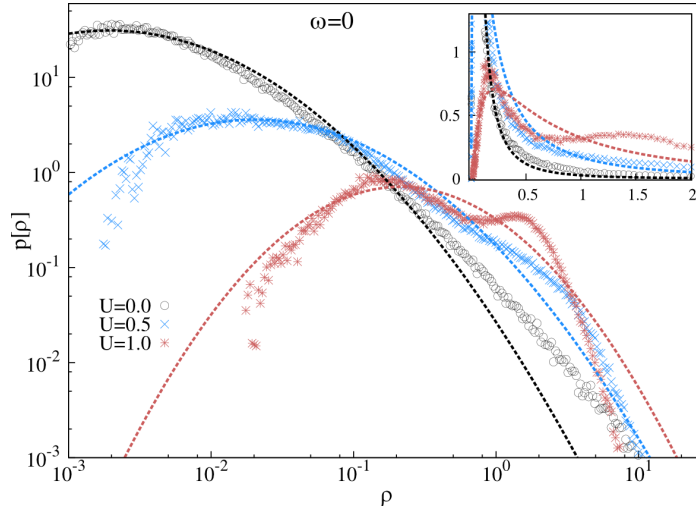
**Figure 6.5.:** Evolution of the PDF of the LDOS at the Fermi level $p[\rho(\omega = 0)]$ for fixed disorder strength $\Delta = 2$ and increasing interaction strength: $U = 0,0.5,1$. The dashed lines correspond to least square fits with a log-normal function. The inset shows the same data on a linear scale. Parameters are $K = 3$, $\eta = 10^{-3}$, $W_0 = 1.0$ and $\mu = U/2$.

the LDOS, but rather lead to two different regimes. We expect this behavior to have a strong influence on the conduction properties of the system, and that it should also be mirrored in other observables.

To understand this behavior the PDF is compared to least square fits with log-normal distributions on a log-log scale for $\Delta = 2$ in figure 6.5. At zero interaction the log-normal distribution represents a good approximation of the PDF of the LDOS, but for increasing interaction strengths $U = 0.5$ and $U = 1$ strong modifications are observed. The weight of the PDF is shifted to higher values of the LDOS and an additional interaction-induced peak is observed. The latter becomes particularly apparent on a linear scale as shown in the inset. From these results it is obvious that the log-normal distribution is not sufficient to approximate the PDF of the LDOS in the interacting case. It is interesting to note that the formation of a second peak is reversed upon further increase of the interaction strength as we learned from the discussion of figure 6.4.

Next we discuss the evolution of the PDF with increasing disorder and for fixed interaction strength $U = 1$ as plotted in figure 6.6. In the homogeneous system the PDF of the LDOS is given by a delta-function at the value $\rho = 1.26$, which corresponds to the value of the non-interacting system due to the Luttinger theorem. Finite disorder strength ($\Delta = 1$) broadens the PDF similar to the
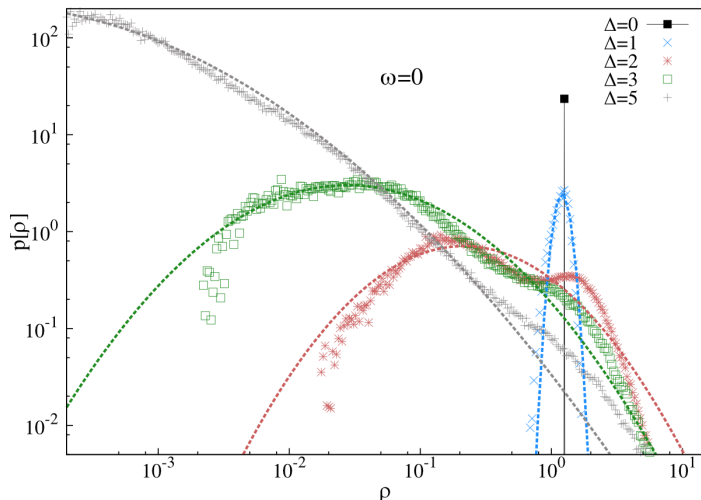
**Figure 6.6.:** Evolution of the PDF of the LDOS at the Fermi level $p[\rho(\omega = 0)]$ for fixed interaction strength $U = 1.0$ with increasing disorder strength: $\Delta = 0,1,2,3,5$. The dashed lines correspond to least square fittings of a log-normal function. Parameters are $K = 3$, $\eta = 10^{-3}$, $W_0 = 1$, and $\mu = U/2$.

behavior found in the non-interacting case as shown in figure 3.4. However, we clearly recognize the two-peak structure of the PDF for $\Delta = 2$ and $\Delta = 3$. This structure is also observable for $\Delta = 5$, but a suitable approximation via the log-normal distribution is clearly restored in the strongly disordered regime.

## 6.3. Paramagnetic ground state phase diagram

An important feature of the system considered here is given by the Mott transition in the homogeneous system as discussed in section 2.6. By construction the statistical DMFT reduces to DMFT in the homogeneous system and therefore a Mott transition is contained in the theory for the half-filled homogeneous system. It is reasonable to expect the Mott transition to be also present in the disordered case at least for moderate disorder strengths, since the box disorder exhibits a bounded range of accessible on-site energies. An example of such a transition is given in figure 6.7, in which the geometrically and arithmetically averaged spectral functions are displayed for fixed disorder strength $\Delta = 3$ and increasing interaction strength. For $U = 2$ we recognize a spectral function corresponding to a disordered metal, as at the same time it was checked that the states at the Fermi level are extended. This means that the system exhibits
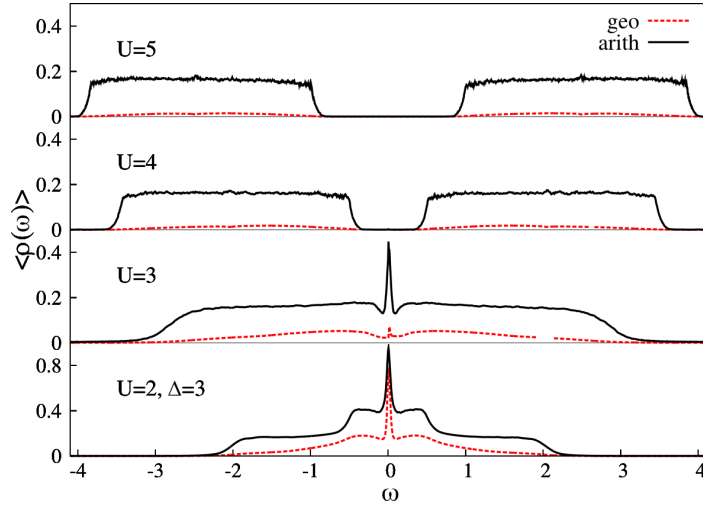
**Figure 6.7.:** Evolution of the arithmetically and geometrically averaged spectral function with increasing interaction strength ($U = 2,3,4,5$) for fixed disorder strength $\Delta = 3$. Parameters are $\eta = 10^{-3}$, $\mu = U/2$, $W_0 = 1$, and $K = 3$.

no excitation gap. When the interaction strength is increased ($U = 3$), the spectrum becomes more and more dominated by incoherent excitations. Finally, the spectra belonging to $U = 4$ and $U = 5$ evidently correspond to Mott insulating states, since $\langle\rho(0)\rangle_{\mathrm{arith}} = 0$. Obviously, a Mott transition takes place between $U = 3$ and $U = 4$.

It is of fundamental interest, how the Anderson transition of the non-interacting system is modified in the presence of interactions and how the Mott transition of the homogeneous system is affected by disorder. The nature of the Anderson-Mott transition has been investigated in detail within TMT [4, 5, 82] and within statistical DMFT [85]. In the latter, also a Griffiths phase was revealed as precursor for the Anderson-Mott transition. However, the extent of the metallic phase has not been systematically discussed within statistical DMFT so far, but only within TMT, which neglects spatial fluctuations [5, 60].

We will discuss how the homogeneous system in the Mott insulating state is affected by disorder and its strength is increased stepwise. In figure 6.8 the evolution of the geometrically and arithmetically averaged spectral function is presented at fixed interaction strength $U = 3$. In the homogeneous system the corresponding state is Mott insulating. The Mott excitation gap persists for small disorder strengths. From the spectrum at $\Delta = 2$ we clearly see that the Mott gap is reduced by disorder. This can be understood by a redistribution
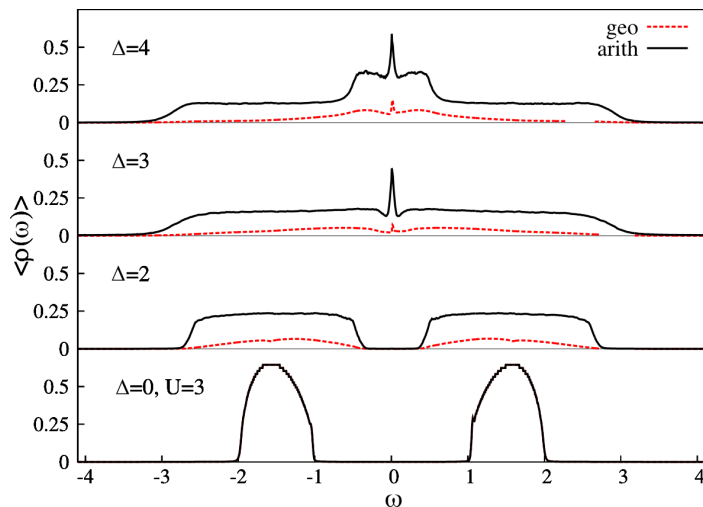
**Figure 6.8.:** Evolution of the arithmetically and geometrically averaged spectral function with increasing disorder strength $\Delta$ ($\Delta = 0,2,3,4$) for fixed interaction strength $U = 3$. Parameters are $\eta = 10^{-3}$, $\mu = U/2$, $W_0 = 1$, and $K = 3$.

of states into the gap. For $\Delta = 3$ the gap is completely filled. The geometric average is finite in the core of the band, but zero in the outer parts of the spectrum. This suggests that a metallic phase is obtained. This is confirmed by a proper investigation (which is not shown here) of the evolution of the PDF of the LDOS in the limit $\eta \to 0$ to rule out localized states at the Fermi level. Hence, the increase of the disorder strength causes a delocalization of the local magnetic moments of the Mott insulator and the system undergoes a transition from the Mott insulator to a disordered metal. This result is in agreement with findings obtained by TMT [60]. Moreover, we note that the Kondo resonance corresponding to coherent quasi-particle excitations is present in the disordered metal.

The question how the correlation-induced metal-insulator transition is affected by randomness arises naturally. In previous TMT studies [60] it was observed that the Luttinger theorem, i.e. the pinning of the LDOS at its non-interacting value [210], is not fulfilled in the presence of randomness. Moreover, it was shown that the metallicity, given by the DOS at the Fermi level, grows with increasing interaction strength so that the Luttinger theorem is nearly fulfilled again [60]. Sufficiently strong interactions hinder a decay of the quasi-particle excitations. Further increase of the interaction strength leads to a rather abrupt transition to the Mott insulating phase. Within statistical DMFT we observe a
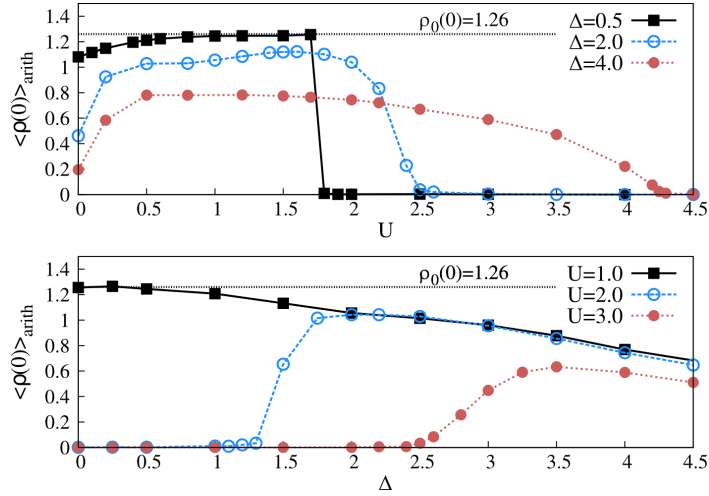
**Figure 6.9.:** Arithmetically averaged LDOS at the Fermi level $\langle \rho(0) \rangle_{\mathrm{arith}}$ for three different values of the disorder strength $\Delta$: $\Delta = 0.5$ (solid squares), $\Delta = 2$ (open circles) and $\Delta = 3$ (solid circles) in the upper panel. In the lower panel the arithmetically averaged LDOS is plotted as a function of the disorder strength for three different values of the interaction strength $U$: $U = 1$ (solid squares), $U = 2$ (open circles) and $U = 3$ (solid circles) in the upper panel. Parameters are $\mu = U/2$, $\eta = 10^{-3}$, $W_0 = 1$, and $K = 3$.

similar behavior as given in the upper panel of figure 6.9, where the arithmetic average of the LDOS at the Fermi level is plotted as a function of the interaction strength for three different disorder strengths. For $U = 0$ the arithmetic average LDOS decreases for higher disorder strengths as expected. As a consequence of increasing interaction we observe an increase of the metallicity for each value of the considered disorder strengths in agreement with the TMT results. For $\Delta = 0.5$ the metallicity increases gradually until it suddenly drops to zero for $U_c = 1.8$. This behavior indicates a first order transition in agreement with the observed hysteresis region within TMT [60]. However, no sudden transition to the Mott insulator occurs for higher interaction strengths as for example displayed for $U = 2$ and $U = 3$ but a rather smooth decline. Our data does not allow for answering the question whether the decline corresponds to second order transition or a crossover, whereas the previous TMT analysis suggests a crossover [60].

The increase of metallicity is conform with the observed influence of the interaction strength on the PDF of the LDOS as discussed in context of figure 6.4 for $\Delta = 4$. The two regimes of distinct behaviors of the PDF upon
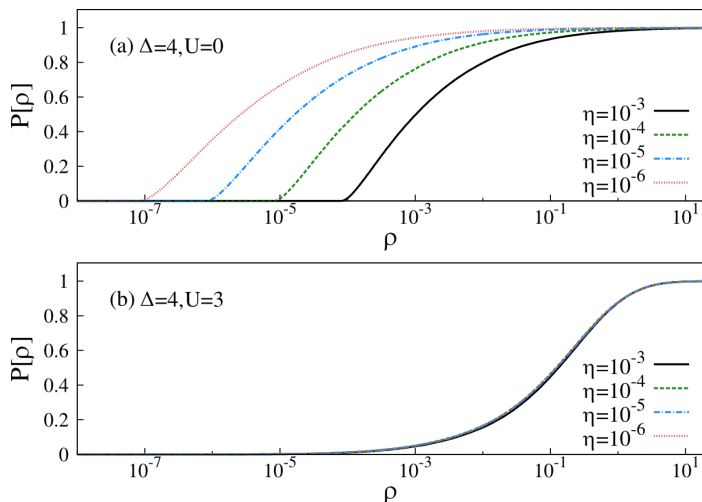
**Figure 6.10.:** Evolution of the cumulative PDFs at the Fermi level $P[\rho(0)]$ with decreasing $\eta$ for the (a) non-interacting system and (b) in presence of interactions, $U = 3$, at fixed disorder strength $\Delta = 4$. Parameters are $\mu = U/2$, $W_0 = 1$, and $K = 3$.

increase of the interaction strength discussed previously are not reflected in the metallicity. The metallic phase obviously features non-trivial properties, which might be associated to the non-Fermi liquid phase representing the precursor of the Anderson-Mott transition [85]. Future research is needed to substantiate this possibility and the additional determination of the PDF of further local observables such as the quasi-particle decay rate might be necessary to properly characterize this phase.

The lower panel of figure 6.9 displays the metallicity as a function of disorder strength for three different values of the interaction strength. The finite metallicity of the homogeneous system found for small interaction remains for increasing disorder strength, but reduces gradually. Starting within the Mott insulating phase of the homogeneous system, an increase of the interaction results in a finite metallicity from some critical value on, which confirms the the disorder-induced delocalization.

Next we discuss how Anderson localized states are influenced by interactions. Panel (a) of figure 6.10 shows the evolution of the PDF of the LDOS at the Fermi level upon $\eta \to 0$ for the non-interacting system with $\Delta = 4$ and $K = 3$. The state is Anderson insulating. In panel (b) the corresponding evolution is shown for finite interactions, namely $U = 3$. Clearly, the PDF saturates corresponding to an extended state. The interaction obviously causes a transition from the
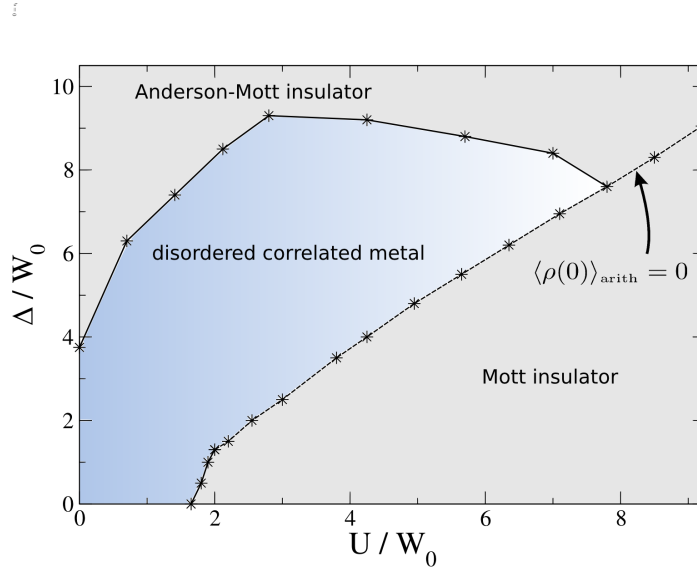
**Figure 6.11.:** Paramagnetic ground state phase diagram of the half-filled Anderson-Hubbard model calculated by means of the statistical DMFT in the $\Delta - U$-plane. It consists of Anderson-Mott insulator, Mott insulator and paramagnetic disordered metal. Parameters are $\mu = U/2$, $W_0 = 1.0$, and $K = 3$.

Anderson insulator to the disordered metal. Thus, a second delocalization transition caused by the increase of the interaction strength is identified, which is in agreement with the corresponding TMT analysis [60]. Now we are also able to understand the dramatic effect of the introduced correlations on the PDF of the LDOS as displayed in panel (a) of figure 6.4, since the system is in the metallic state already for $U = 0.5$.

Our systematic analysis results in the paramagnetic phase diagram depicted in figure 6.11. Both above described delocalization processes are clearly visible, as can be judged from the extent of the metallic phase. For strong interactions a Mott insulator occurs, which is continuously connected to the Anderson-Mott insulator for strong disorder. That means, the Mott insulating state can be continuously tuned into an Anderson-Mott insulating state by changing the disorder and the interaction strength. The dashed line corresponds to a vanishing arithmetic average of the LDOS at the Fermi level, as a reasonable distinction between the Mott insulator and the Anderson-Mott insulator. Within TMT studies a distinction was achieved by the criterion of vanishing Hubbard subbands [60] or whether the quasi-particle weight drops to zero for all on-site

energies or not [5]. Here, we see that the Anderson-Mott insulator and the Mott insulator are separated both by the metallic phase and for strong interactions by a crossover line $\Delta \approx U$. Future research is needed to quantify the critical behavior of the transition from metal to the Mott insulator for higher disorder strengths. Statistical DMFT investigations in combination with more powerful and accurate impurity solvers such as the numerical renormalization group [56, 144, 176] could give valuable insight in this respect.

It is interesting to compare our statistical DMFT phase diagram with the phase diagram obtained by means of the TMT [5, 60] depicted in figure 6.12. The overall structure is reproduced. Within both methods one finds a metallic core for intermediate strengths of both the disorder and the interaction. Also the shape of the metallic core is in agreement. The two delocalization processes are obtained within both methods.
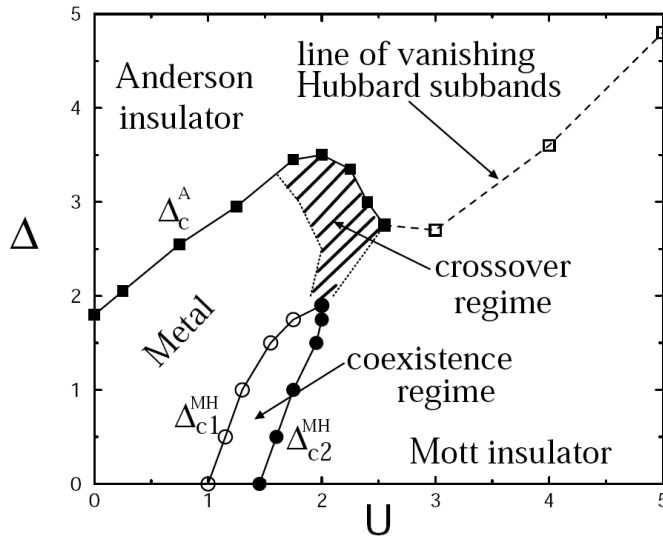


**Figure 6.12.:** Paramagnetic ground state phase diagram of the half-filled Anderson-Hubbard model calculated by means of TMT in the $\Delta - U$-plane. Reprinted from reference [60].

However, on a quantitative level the methods differ substantially. In the non-interacting system, the TMT predicts the Anderson localization to occur at a critical disorder strength $\Delta_c \approx 1.8$ [60]. Within statistical DMFT the transition is found for significant higher disorder strength. For the connectivity $K = 3$ the critical disorder strength $\Delta_c \approx 3.75$ results in a discrepancy of a factor $\sim 2$. We remark that within TMT no fluctuations due to disorder are

incorporated. Furthermore, the choice of the mean, i.e. geometric average, is arbitrary and has a strong influence on the extent of the metallic phase [262]. This discrepancy was already discussed by Alvermann and Fehske for the non-interacting system [13]. Therein it was also shown that TMT misses the re-entrance behavior of the mobility edge that was found by means of the local distribution method. Moreover, our discussion above shows that within statistical DMFT the extent of the metallic phase depends on the connectivity $K$. From a physical reasoning this is an expected and a reasonable feature. For higher connectivities, within the statistical DMFT, this discrepancy to TMT findings will even be consolidated, since the critical disorder strength for Anderson or Anderson-Mott localization will be higher. As a consequence, the crossover line between the metallic phase and the Mott insulating phase exists for much larger disorder strengths than found within TMT.

On the other hand, it should be mentioned that within the TMT investigation the numerical renormalization group was employed as impurity solver. Therewith, the Mott transition is determined essentially numerically exactly. In contrast, within the here presented statistical DMFT approach the approximate MPT was used, which is known to differ from the most accurate values known [57].

To sum up the comparison, our findings indicate that the criticisms regarding the detection of localization within TMT [13, 256, 262] is justified on a quantitative level. However, our investigation supports that the statistical DMFT and the TMT lead to qualitatively agreeing results in general. In this sense, the TMT represents a valuable investigation tool for strongly correlated, disordered systems. An important advantage of the TMT is the considerable smaller computational effort, which enables the use of more powerful impurity solvers than it is feasible to date within statistical DMFT.

## 6.4. Conclusion

The statistical DMFT was applied to the box disordered Anderson-Hubbard Hamiltonian. We have confirmed, that the statistical DMFT is able to describe localization transitions in the presence of interactions and disorder. Localization is judged by the evolution of the PDF of the LDOS in the limit $\eta \to 0$, which enables the investigation of the Anderson-Mott transition.

It was found that the presence of interactions in the Anderson insulating phase causes delocalization for intermediate disorder strengths. On the other hand, also disorder delocalizes the Mott insulating phase by the redistribution of states into the Mott gap. However, if the disorder or respectively the

interaction is strong enough, no metallic phase occurs anymore. Consequently, the Mott insulator and the Anderson-Mott insulator are continuously connected. The resulting paramagnetic ground state phase diagram containing all these results was found to be in qualitative agreement with TMT results. However, considerable quantitative differences between statistical DMFT and TMT were found regarding the extent of the metallic phase.

Our analysis of the probability distribution functions of the LDOS in the interacting case revealed a non monotonic dependence on the interaction strength. The most striking feature is an emerging second peak in the PDF which was not observed before. In particular, the log-normal distribution does not serve as a suitable approximation in the interacting case.

# 7. Binary disordered fermions

In section 5.2.2 it was discussed how a binary disorder distribution of random on-site energies can be realized by ultracold atoms in optical lattices. Beside this interesting realization of quantum simulations of the Anderson-Hubbard model, the binary disorder model is of general interest in solid state theory, where it serves as a basic model of alloys, two-species compounds and doped semiconductors.

Due to its physical significance the binary disorder model was studied since the early stages of disorder physics [163, 164, 263, 277, 307]. By means of CPA disorder-induced band splitting was established [164, 277, 307] and exact diagonalization revealed a rich localization structure as for example bound states have been identified [163], a phenomenon known from percolation theory [99]. In fact, for infinite disorder splitting of the two energy levels a percolation problem is yielded. Recently these rich localization phenomena were confirmed by a local distribution investigation of the binary model [13].

The binary disorder model combined with local interactions, modeled by the Anderson-Hubbard Hamiltonian has been addressed within DMFT on a CPA level to deal with disorder [59, 63, 178, 190, 275]. In particular, it was shown that new types of alloy-Mott or alloy-charge transfer insulators can appear and that the Mott metal-insulator transition can occur at non-integer particle densities [59, 190]. However, CPA is not able to incorporate localization effects and therefore an essential piece of the picture is missing.

In this chapter the statistical DMFT (see section 4.4) is applied to correlated fermions on a lattice with binary type of disorder. Thereby, localization effects are incorporated on the level of full PDFs and it is shown that Anderson localization significantly extends the picture. In particular, we investigate how the predictions from the work Byczuk *et al.* [59] are modified when the Anderson localization is present.

We consider the Anderson-Hubbard model (4.1), in which the PDF of the on-site energies $p_\epsilon(\epsilon)$ is given by the bimodal function (5.17), with disorder energy splitting $\Delta$ and impurity weight $x$. In the following we set the impurity

concentration $x$ and the total particle density

$$\nu = \frac{1}{N} \sum_{i,\sigma} \langle n_{i\sigma} \rangle \tag{7.1}$$

to be equal, i.e. $x = \nu$, by adjusting the chemical potential during the iterative solution of DMFT equations. This choice enables us to study Mott metal-insulator transition at non-integer particle densities [59]. For the calculations presented below, we choose the impurity concentration and the particle density equal to $x = \nu = 0.2$. Furthermore, we set the coordination number $K = 6$ shortly above the classical percolation threshold $x_p = 1/K$ [231], i.e., extended states can exist within both upper and lower alloy bands when they are split due to disorder. We work again in energy units of the non-interacting bandwidth of the homogeneous system. Parts of this chapter are published [248].
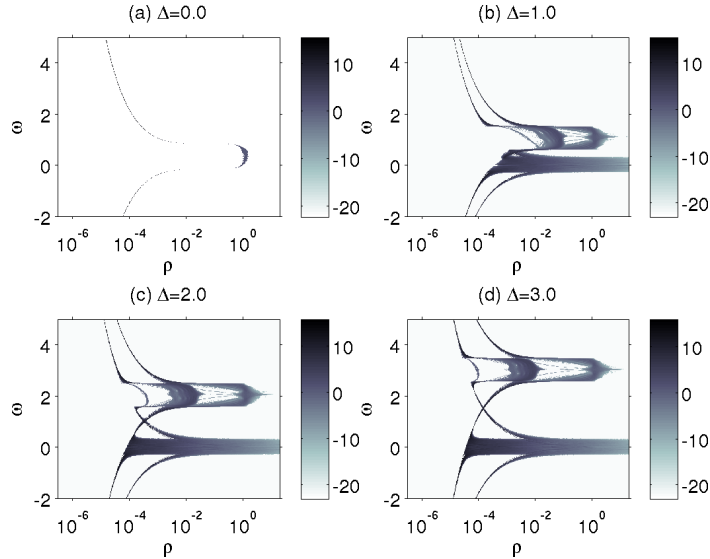


**Figure 7.1.:** Natural logarithm of the PDFs of the non-interacting system $p[\rho]$ plotted color coded for fixed broadening $\eta = 10^{-3}$ and several disorder parameters $\Delta$: (a) $\Delta = 0.0$, (b) $\Delta = 1.0$, (c) $\Delta = 2.0$, (d) $\Delta = 3.0$. Parameters are $K = 6$, $\nu = 0.2$, $W_0 = 1.0$ and $x = 0.2$.

## 7.1. Anderson transition and localization effects in the non-interacting case

First we will concentrate on the various localization phenomenon that are present in the binary disorder model. In particular, it is discussed how to detect localization effects and how to distinguish between extended and localized states in the non-interacting limit.
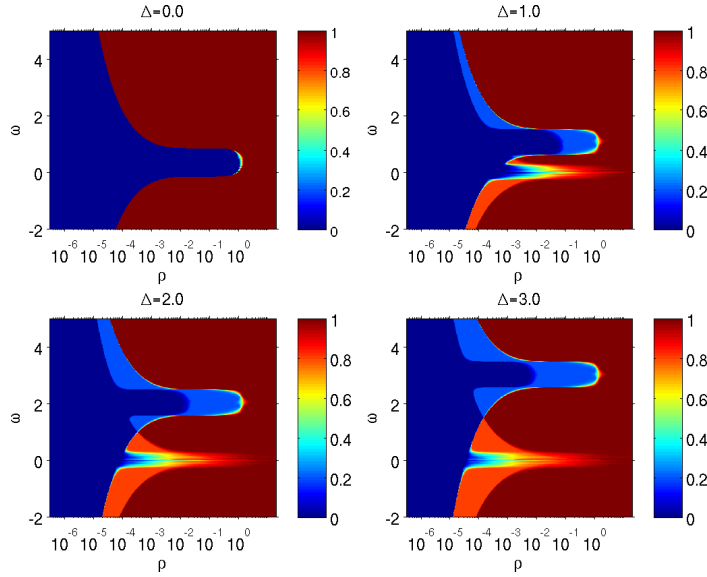


**Figure 7.2.:** Cumulative PDFs of the non-interacting system $P[\rho]$ plotted color coded for fixed broadening $\eta = 10^{-3}$ and several disorder parameters $\Delta$: (a) $\Delta = 0.0$, (b) $\Delta = 1.0$, (c) $\Delta = 2.0$, (d) $\Delta = 3.0$. Parameters are $K = 6$, $\nu = 0.2$ and $x = 0.2$.

In figure 7.1 the PDFs are plotted on a logarithmic scale for different increasing values of the disorder parameter $\Delta$. They are presented as color plot in the plane spanned by the LDOS in $x$-direction and frequency in $y$-direction. In the homogeneous system all PDFs of course correspond to delta functions. For finite disorder the PDFs are broadened over many decades of the LDOS. By comparison with the typical PDFs obtained for box disorder, as for example given in figure 3.6, we note that the PDFs are not smooth for all frequencies, but rather given as a aggregation of different steps for some frequencies.

The step structure becomes especially clear by looking on the corresponding cumulative PDFs $P[\rho(\omega)]$ as defined in equation (3.26) for the same parameters in figure 7.2. Right the PDFs around $\omega \sim \Delta$ exhibit a clear two-step structure.

Coming from small values of the LDOS, the cumulative PDFs finally add up to one, as it is expected. It is remarkable that the value of the discussed cumulative PDFs changes from 0.0 to 0.2 at the first step, which exactly corresponds to the impurity weight.
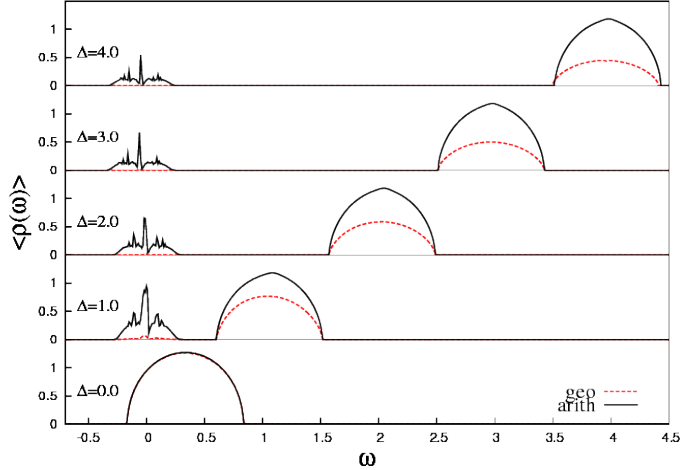


**Figure 7.3.:** Geometrically (dashed red line) and arithmetically averaged (solid black line) spectral functions of the non-interacting system for fixed broadening $\eta = 10^{-3}$ and several disorder parameters ($\Delta = 0.0, 1.0, 2.0, 3.0, 4.0$). Parameters are $K = 6$, $\nu = 0.2$ and $x = 0.2$.

The most intriguing feature is given by the band splitting into an upper and a lower alloy band that occurs with increasing disorder strength. The upper and lower alloy band can be named majority or minority band depending on the concentration $x$. The band splitting can be seen unambiguously by plotting the arithmetically and geometrically averaged density of states as shown in figure 7.3. With increasing disorder strength the majority band is shifted away from the Fermi level. Its band center is exactly dislodged by the disorder parameter $\Delta$. Looking at figure 7.3, we observe a vanishing geometrically averaged LDOS in the minority band with increasing disorder strength. This corresponds to disappearing extended states and is used within TMT-DMFT to identify the Anderson transition [62, 82]. As mentioned before, by using the statistical DMFT we use a more powerful and general approach to detect Anderson localization.

Extended states are characterized by a branch cut on the real axis of the local Green's function, whereas localized states are characterized by a dense distribution of poles in the thermodynamic limit (see section 3.1). As explained

within the local distribution method, this can be used to detect if states are localized or extended by investigating the behavior of the PDFs of the LDOS $p[\rho_i(\omega)]$ shown in figure 7.1 when the broadening $\eta$ tends to 0 [13]. The PDF of the LDOS for extended states saturates at a finite value for $\eta \to 0$, whereas the PDF of the LDOS for localized states decreases to zero for $\eta \to 0$.
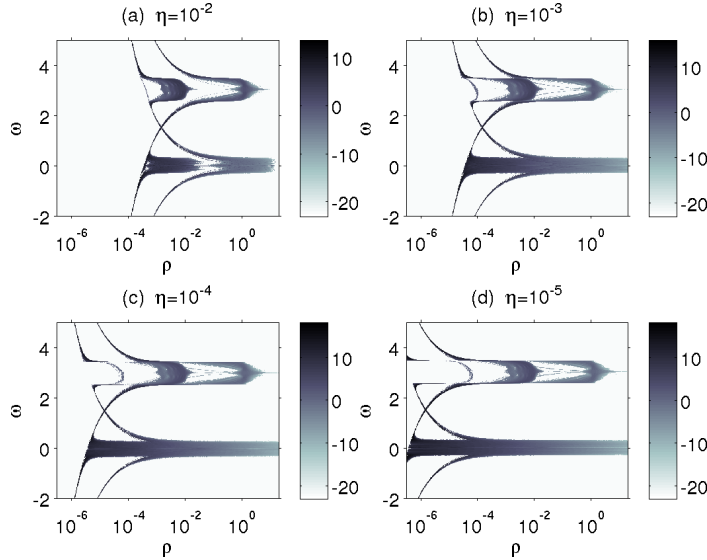


**Figure 7.4.:** Natural logarithm of the PDFs $p[\rho]$ of the non-interacting system plotted color coded for fixed disorder parameter $\Delta = 3.0$ and several broadenings $\eta$: (a) $\eta = 10^{-2}$, (b) $\eta = 10^{-3}$, (c) $\eta = 10^{-4}$, (d) $\eta = 10^{-5}$. Parameters are $K = 6$, $\nu = 0.2$ and $x = 0.2$.

As an example, figure 7.4 shows the behavior of the PDF when decreasing the broadening from $\eta = 10^{-2}$ to $\eta = 10^{-5}$ for a selected value $\Delta = 3.0$. A change is seen for states in the lower alloy band, whereas the PDFs of the upper alloy band remain almost unchanged in this regime of $\eta$. The probability distributions of the LDOS of the lower alloy band – the minority band – are presented in detail for $\Delta = 1.0$ and $\Delta = 4.0$ in figure 7.5. It is clearly visible that the PDFs for small $\Delta = 1.0$, which correspond to the lower alloy band, become $\eta$-independent for $\eta \to 0$. On the contrary, at large $\Delta = 4.0$ the PDFs strongly depend on $\eta$.

In addition to Anderson localization effects we also observe that the spectrum is highly fragmented (cf. figures 7.3 and 7.5), which is due to the presence of states with different physical properties. These states differ in the behavior of the PDF of the LDOS for $\eta \to 0$ (cf. figure 7.5) and are identified either
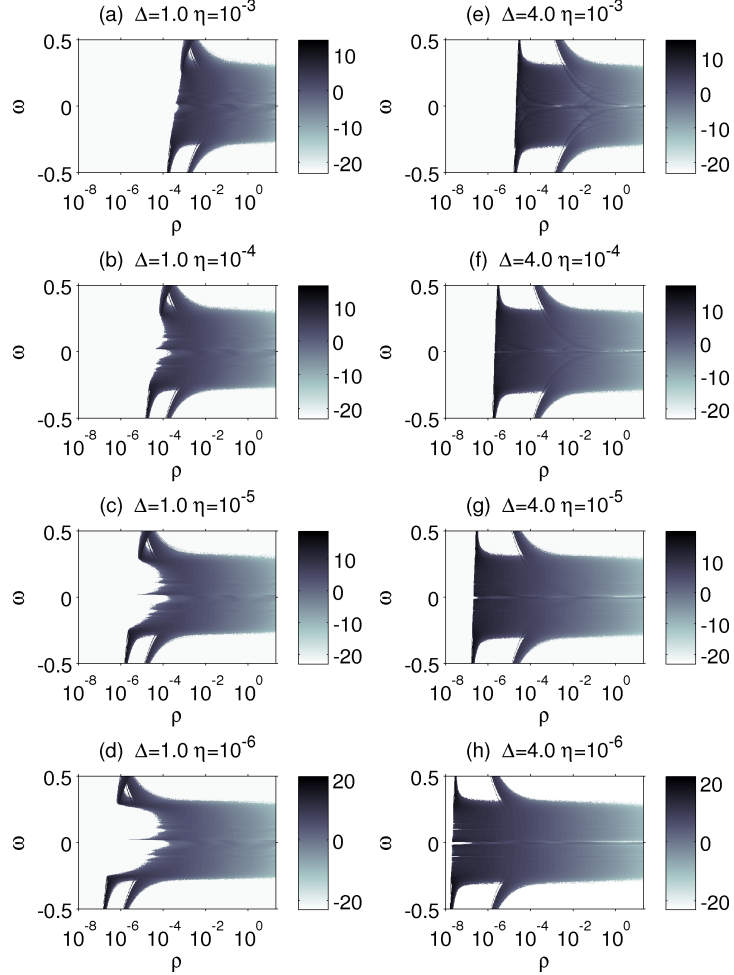
**Figure 7.5.:** Comparison of color coded natural logarithm of PDFs $p[\rho(\omega)]$ of the minority band of the non-interacting system for two different disorder parameters $\Delta = 1.0$ (plots on the left side (a)-(d)), $\Delta = 4.0$ (plots on the right side (e)-(h)) and for several broadenings $\eta$: (a,e) $\eta = 10^{-3}$, (b,f) $\eta = 10^{-4}$, (c,g) $\eta = 10^{-5}$, (d,h) $\eta = 10^{-6}$. Parameters are $K = 6$, $\nu = 0.2$ and $x = 0.2$.

as cluster resonances [13, 163] or as 'anomalous' localized states [244]. The resonance states are similar bound eigenstates but with a finite life-time. They appear because of special geometrical configurations of the impurity atoms [13, 163]. The 'anomalous' localized states are in fact extended states over the whole lattice but they are insulating and do not contribute to the dc conductivity [244]. On a bipartite lattice these states have small wave function amplitudes on one sublattice and large amplitudes on the other sublattice. The typical $\eta$ behaviors of the PDFs for given frequencies are shown in figure 7.6. Panel (a) shows the behavior of an extended state, panel (b) presents the behavior of an Anderson localized state, and panel (c) shows the behavior of an 'anomalous' localized state with its typical bimodal structure [244]. Our exemplary 'anomalous' localized state at $\omega = -0.01$ exhibits a LDOS of $\sim 10^{-4}$ on one sublattice and a LDOS of $\sim 5 \times 10^{-2}$ on the other sublattice.
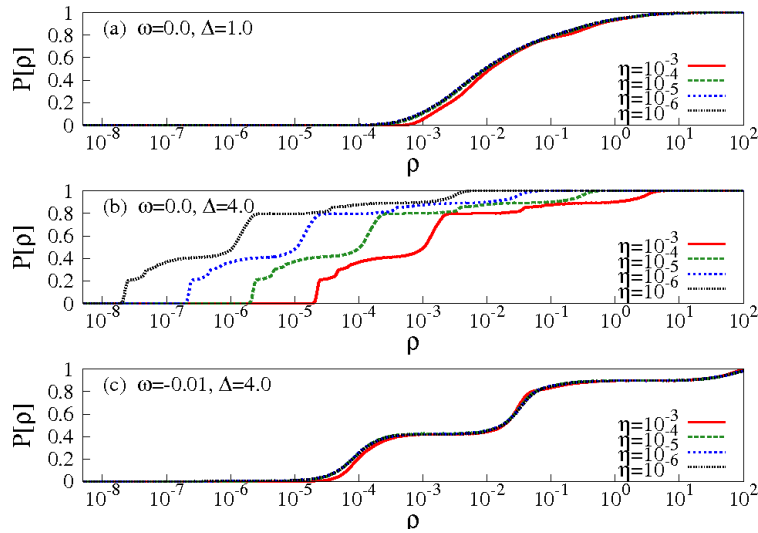


**Figure 7.6.:** Behavior of cumulative PDFs $P[\rho(\omega)]$ of the non-interacting system with decreasing broadening $\eta$ (a) for an extended state at $\Delta = 1.0$ and $\omega = 0.0$, (b) for an Anderson localized state at $\Delta = 4.0$ and $\omega = 0.0$ and (c) for an 'anomalous' localized state at $\Delta = 4.0$ and $\omega = -0.01$. Parameters are $K = 6$, $\nu = 0.2$ and $x = 0.2$.

The fragmentation of the minority is highlighted by plotting the cumulative PDFs of the minority band only in figure 7.7 for decreasing values of the broadening. States exist at many discrete energies corresponding to 'anomalous' localized states and bound states in agreement to previous findings [14, 163]. These states are separated by regions with Anderson localized states. Ac-

**Figure 7.7.:** Color-coded cumulative PDFs $P[\rho]$ of the non-interacting system for fixed disorder parameter $\Delta = 4.0$ and several broadenings $\eta$: (a) $\eta = 10^{-3}$, (b) $\eta = 10^{-4}$ and (c) $\eta = 10^{-5}$. Parameters are $K = 6$ and $x = 0.2$. Here, the filling $\nu$ is not fixed, which explains the offset on the energy axis.
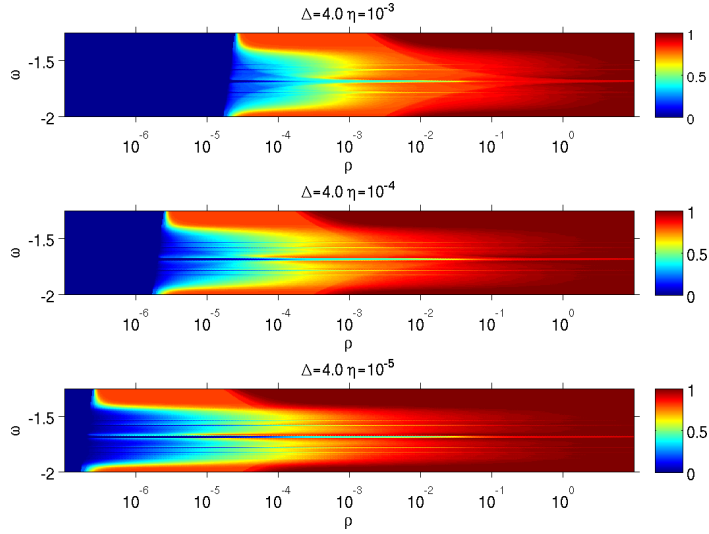
cordingly, many different mobility edges exist. A circumstance that was also found within percolation physics [68, 244]. It should be emphasized that all these phenomena are not present in the usual localization picture based on the continuous box disorder (see section 3.3 and chapter 6). These remarkable features are directly connected to the discrete character of the binary disorder.

It is interesting to study how the arithmetically averaged spectral function evolves under changing of the connectivity $K$ as displayed in figure 7.8. For fixed disorder strength $\Delta = 2.0$ the coordination number is given by $K = 2$ in panel (a) and increased to $K = 4$ in panel (b) and $K = 6$ in panel (c). For lower K resonances corresponding to bound states and 'anomalous localizes states' are more pronounced. For $K = 2$ there are even resonances present in the majority band. In case of higher $K$ the resonances in the majority band are washed out and a smooth band is obtained. Upon increasing of the connectivity a continuous conduction band is formed, where the impurity states are located, as soon as the percolation threshold is exceeded. For the here investigated impurity concentration $x = 0.2$, a connectivity $K > 5$ is needed, which is confirmed by the shape of the minority conduction band in panel (c). Panel (d) displays the result of a CPA calculation. We note that there is no fragmentation left and no localization effects are present. The increase of $K$ can be associated

with an increase of the dimensionality and for bigger and bigger $K$ the spectra converge towards the CPA result. In fact, it is known that CPA is exact in infinite dimensions [84, 275, 279].
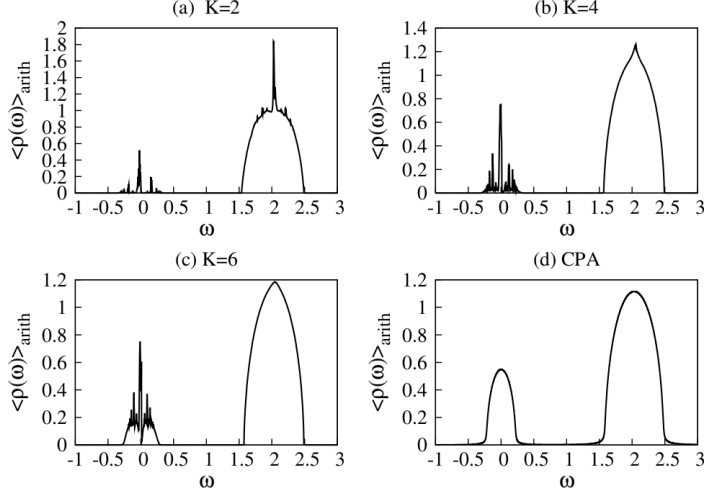


**Figure 7.8.:** Arithmetically averaged spectral functions of the non-interacting states for fixed diorder strength $\Delta = 2.0$ for (a) $K = 2$, (b) $K = 4$, (c) $K = 2$, and the CPA result. Parameters are $\nu = 0.2$ and $x = 0.2$.

## 7.2. Anderson and Mott transitions in the interacting case

In the interacting limit we restrict our investigation of the $\eta$-dependence to the lower limit $\eta = 10^{-5}$, as we use small ensembles due to computational limitations. We also note that the MPT requires a small finite broadening in any case. By considering the binary model in the investigated parameter regime, we also need to distinguish between an Anderson-Mott insulator and a band insulator. The band insulator is characterized by $\langle \rho(\omega = 0) \rangle_{\mathrm{arith}} = 0$, but in contrast to the Mott insulator the excitation gap is determined by the energy distance between the upper edge of the occupied band and the upper alloy band, which in this case is proportional to $\Delta$.

The phase diagram presented in figure 7.9 is the main result of this chapter. The phase diagram consists of three different phases: the disordered metal, the Anderson-Mott insulator and the band insulator. For zero interaction, the above described involved localization process takes place under increase of the disorder strength. For $\Delta \sim 1.75$ the Anderson insulator is obtained. In the homogeneous
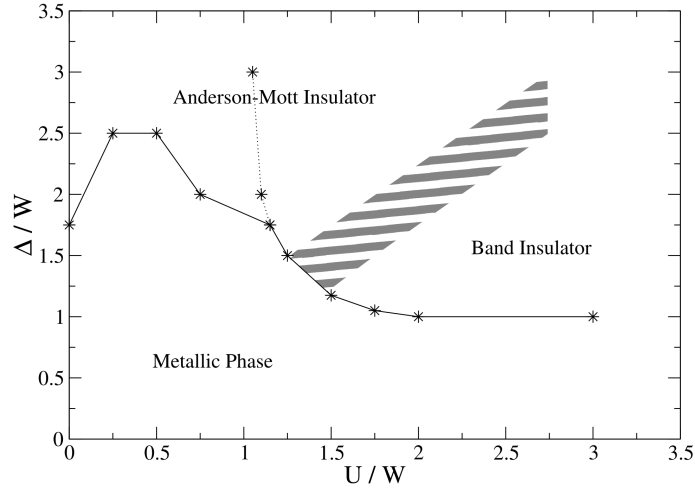
**Figure 7.9.:** Paramagnetic ground state Phase diagram for the interacting and disordered system in $\Delta - U$-plane, showing of Anderson-Mott insulator, paramagnetic metal and band insulator. The solid line corresponds to the transition between insulating phases and the metal, the dotted line corresponds to a vanishing arithmetic average of the LDOS at the Fermi level and the dashed region denotes the crossover between Anderson-Mott insulator and band insulator. Parameters are $K = 6$, $\nu = 0.2$, $x = 0.2$.

case the increase of the interaction does not result into a Mott insulator as the overall filling is not integer, but a paramagnetic metal is obtained for all values of $U$.

In presence of both phenomena the scenario is much more interesting. Let us first consider small disorder strengths. Here, a disordered metallic phase is obtained for any interaction strength. When the disorder is sufficiently strong to induce a band splitting (which corresponds to the intermediate regime) a correlation-induced transition from the disordered metal to a insulator is obtained at non-integer filling. When the interaction is increased further, the half-filled lower alloy band exhibits a Mott transition due to alloy band splitting and the mechanism described earlier in references [59, 64, 190]. However, as the current results prove, this type of Mott-Hubbard metal-insulator transition at non-integer particle densities is also possible, if Anderson localization effects are taken into account.

The CPA phase diagram is depicted in figure 7.10 for comparison. For its estimation MPT was used as impurity solver. The phase diagram was first obtained by Byczuk *et al.* by using numerical renormalization group () as
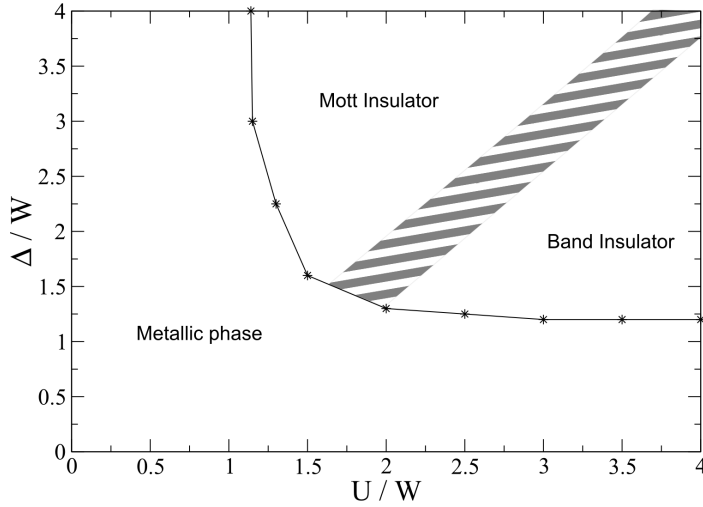
**Figure 7.10.:** CPA+MPT paramagnetic ground state phase diagram for the interacting and disordered system in $\Delta - U$-plane, consisting of Mott insulator, paramagnetic metal and band insulator. The solid line corresponds to the transition between insulating phases and the metal and the dashed region denotes the crossover between Anderson-Mott insulator and band insulator. First obtained by K. Byczuk *et al.* with numerical renormalization group as impurity solver [59]. Parameters are $K = 6$, $\nu = 0.2$ and $x = 0.2$.

impurity solver, which gives a much more accurate estimation of the Mott transition line [57]. Furthermore, in the mentioned work also a hysteresis region was found [59] corresponding to the critical lines $U_{c_1}$ and $U_{c_2}$ [123]. In the here presented work only the $U_{c_2}$ is determined, since it is the relevant transition line for zero temperature [123]. A further difference between the phase diagrams calculated with MPT and with the numerical renormalization group is the missing band insulator in the latter, due to the poor resolution of NRG at higher energies.

By comparison to the phase diagram evaluated by statistical DMFT, we note the missing Anderson localized phase in the CPA phase diagram. In the limit of large disorder parameter $\Delta$ the metallic phase as well as the Mott-Hubbard transition is terminated by Anderson localization. The states in the upper part of the phase diagram in figure 7.9 are localized due to strong disorder.

Spectra corresponding to the Mott-Hubbard transition are displayed in figure 7.11, where the arithmetically averaged LDOS obtained within statistical DMFT is compared to that obtained within a CPA type treatment of disorder.
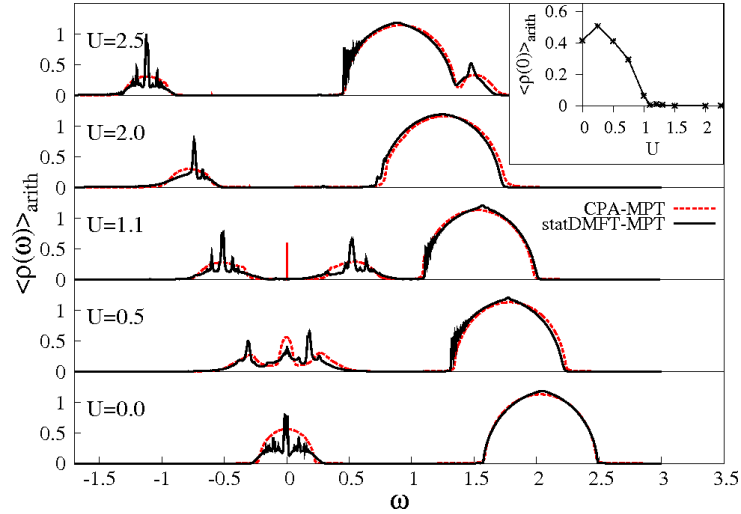
**Figure 7.11.:** Arithmetic average of the LDOS for increasing interaction strength $U$ ($U = 0.0, 0.5, 1.1, 2.0, 2.5$) at fixed disorder parameter $\Delta = 2.0$. The results from statistical DMFT calculations (solid black line) are compared to CPA results (dashed red line). The inset shows the arithmetic mean of the LDOS at the Fermi level with increasing interaction strength. Parameters are $K = 6$, $\nu = 0.2$, $x = 0.2$.

With increasing interaction $U$ at fixed $\Delta$ three peaks emerge because of the Mott-Hubbard and band splitting transitions. Moreover, we observe additional spikes in the LDOS similar to those observed for the non-interacting system [13, 163]. These spikes are not reproduced by a CPA treatment of disorder and we conclude that they are due to local interference effects on clusters of impurity atoms. In the inset of figure 7.11, the arithmetic average of the LDOS at the Fermi level is presented as a function of $U$. The Mott-Hubbard transition appears to take place at $U = 1.1$. However, this is not a true transition point as it corresponds to the regime within the Anderson-Mott insulator where all states are already localized, cf. figure 7.9. We also see in figure 7.11 that by further increasing the interaction to $U = 2.0$ the upper alloy band and the upper Hubbard band are merging. This corresponds to the crossover regime between alloy Anderson-Mott insulator and alloy-charge band insulator indicated by the dashed area in the phase diagram in figure 7.9 [59]. An additional effect is observed in figure 7.11, namely, with increasing $U$ the position of the upper alloy band is shifted with respect to zero on the energy scale, cf. reference [190].

For comparison the LDOS at a selected $U$ value for different disorder parameters $\Delta$ are presented in figure 7.12. As expected, we observe a band splitting
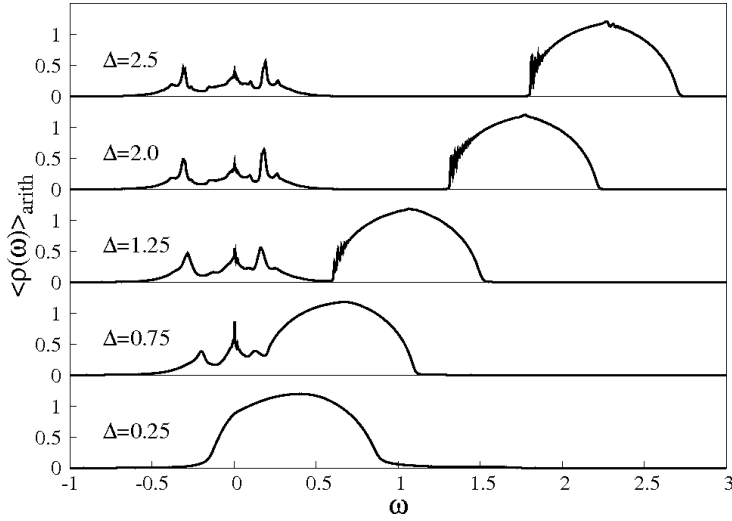
**Figure 7.12.:** Arithmetic average of the LDOS with increasing disorder parameter $\Delta$ ($\Delta = 0.25, 0.75, 1.25, 2.0, 2.5$) for fixed interaction strength $U = 0.5$ and broadening $\eta = 10^{-3}$. Parameters are $K = 6$, $\nu = 0.2$, $x = 0.2$.

with increasing $\Delta$ and the formation of an energy gap proportional to $\Delta$ between the lower and the upper alloy bands. Note that additional peaks appear in the lower band when the disorder parameter $\Delta$ is increased. These peaks do not occur in a CPA treatment of disorder.

Finally, in figure 7.13 we show the evolution of the PDFs across the Mott-Hubbard transitions. The onset of a three peak structure is seen as well as sharp resonances in the LDOS. These resonances are broadened and washed out by increasing the interaction strength $U$.

## 7.3. Conclusion

In this chapter, we have investigated the binary alloy disordered Anderson-Hubbard model within statistical DMFT, using MPT as impurity solver. Applying the statistical DMFT, we were able to compute the full PDF of the LDOS, and therefore, we were able to study localization effects in a more rigorous way and in more detail than in TMT. In contrast to continuous disorder types, the localization process is highly complex. In addition to the Anderson localized states known from the box disorder distribution, bound states and 'anomalous' localized states emerge and give rise to sharp resonances in the LDOS. These resonances are also present in the interacting case, but are broadened due to
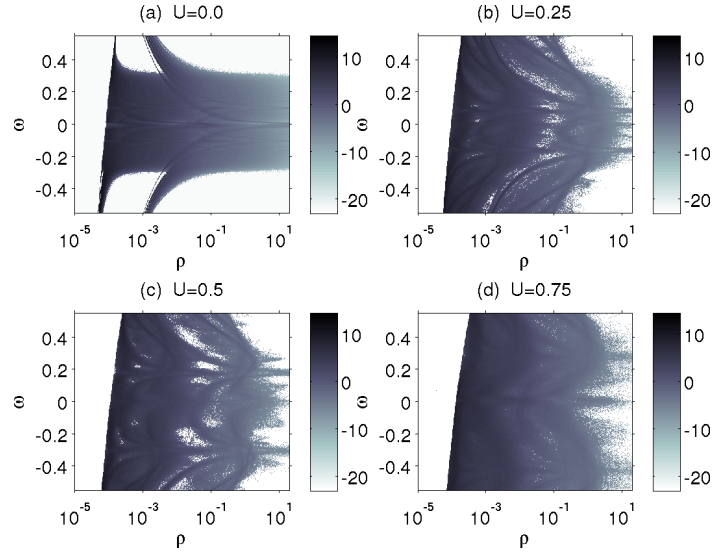
**Figure 7.13.:** Comparison of the color coded natural logarithm of PDFs $p[\rho(\omega)]$ for disorder parameter $\Delta = 2.0$ and several interaction strengths $U$: (a) $U = 0.0$, (b) $U = 0.25$, (c) $U = 0.5$, (d) $U = 0.75$. Parameters are $K = 6$, $\nu = 0.2$, $x = 0.2$.

the interaction. Consequently, many mobility edges are present in the binary disorder model.

As a main result, the paramagnetic ground state phase diagram was obtained. In comparison to the previous calculated phase diagram by means of CPA, the additional presence of the Anderson-Mott insulating phase, as well as the band insulating phase was found. For non-integer particle density $n = x$ a Mott-Hubbard metal-insulator transition is obtained even when Anderson localization effects are taken into account. We conclude that this special Mott transition is accessible within a two-component mixture of ultracold fermions in optical lattices, if it becomes possible to suppress the hopping of one species.

In future work, it is of interest to calculate the finite temperature phase diagram. Furthermore, the estimation of the phase diagram in dependence on the impurity concentration appears useful as this dependence is of relevance for solid state experiments. From the methodical point of view, it would be desirable to use impurity solvers that are superior or at least complementary to MPT.

# 8. Fermions in a speckle disordered optical lattice

Up to know, the most successful realization of disordered potentials for ultracold atoms is given by speckle disorder [73, 223, 233, 293] (see section 5.2.1). In a seminal work Roati *et al.* [233] demonstrated Anderson localization of matter waves by exposing a $^{87}$Rb Bose Einstein condensate to an one-dimensional speckle pattern. Recently, speckle patterns have been superimposed onto an optical lattice [223, 293], by which disordered lattices have been realized for ultracold atoms. Taking care of the experimental geometric setup, the autocorrelation length of the speckle pattern was nearly reduced down to the lattice spacing, so that correlations of the random potential on neighboring sites are negligible [293]. Although so far only bosonic systems have been studied in the experiment, the route is paved towards a quantum simulator of the Anderson-Hubbard model (4.1).

A realistic theoretical description of ultracold atoms in a speckle disordered optical lattice should be capable of describing interaction and disorder on equal footing, preferably non-perturbatively. As a matter of fact, a careful theoretical description necessitates also the incorporation of non-diagonal disorder besides the diagonal disorder[293, 306]. Last but not least the theoretical investigation should be able to treat other experimentally unavoidable features, such as finite temperature and the presence of the harmonic trap. In the case of bosons there have been several theoretical works [41, 177] combining some of these requirements. So far no comparable works have been performed for fermions.

The aim of this chapter – which is partially published [250] – is to close this gap and to provide a realistic description of strongly correlated fermions in an optical lattice. For this purpose, the statistical DMFT (cf. section 4.4) is employed to solve the Anderson-Hubbard Hamiltonian numerically. The main finding is that the paramagnetic ground state phase diagram differs strongly from the phase diagram found for pure diagonal box disorder (cf. section 8.3) The latter has been calculated within TMT [5, 60, 62] or as presented in chapter 6 also within statistical DMFT. In particular, the Mott insulator and the Anderson-Mott insulator are not continuously connected in case of speckle disorder. The results are reappraised in section 8.4 by a complementary

investigation of the two-dimensional square lattice by means of the real-space DMFT [86, 142, 255]. The influence of temperature on the spectral function is discussed in section 8.5. Before the results are presented, it is explained in more detail how the speckle disorder is modeled and how the necessary PDFs are incorporated.

## 8.1. Model and joint probability distribution functions for the Hubbard parameters

The PDF for the on-site energies was already introduced in equation (5.14). In experimental realizations, the disorder strength $\Delta$ is proportional to the speckle field strength $s_D = \langle V_D(\mathbf{r}) \rangle$ [306] with $V_D$ the optical dipole potential (see section 5.2.1). Hence, the disorder strength can be tuned by the speckle field strength. The proportionality constant scales monotonically with the ratio of the speckle field autocorrelation length to the typical spatial extend of the Wannier function. Thus, the proportionality constant depends in particular on the experimental optical setup. In the setup of the experiment by White *et al.* [293], the relation $\Delta = 0.97 s_D$ was found [306]. As usually in optical lattice experiments, the mean value of the interaction strength $U$ can be tuned by adjusting the $s$-wave scattering length $a$ between the two fermionic components by means of the Feshbach resonance or by varying the lattice depth $s_L$, which in turn also influences the hopping amplitude (cf. section 5.1). Keeping the lattice depth fixed, the disorder strength and the interaction strength can be tuned independently by varying the speckle field strength and the magnetic field. Hence, experimentally full control of the strength of the interaction as well as of the disorder is given. The relevant energy scale for the lattice depth $s_L$ and the speckle field strength $s_D$ is the recoil energy $E_R$. Throughout this chapter we work in units of the non-interacting bandwidth $W_0 = 4t\sqrt{K}$ of the homogeneous system, where the hopping amplitude $t$ can be related to the lattice depth $s_l$ by an exact band structure calculation, as for instance performed by M. Greiner [130]. The $s$-wave scattering length $a$ is given in units of the Bohr radius $a_0$.

In our calculations we consider ultracold $^{40}$K atoms in two hyperfine states in an optical lattice generated by a laser with a wavelength $\lambda_L = 738nm$. The lattice depth is fixed to $s_L = 10E_R$. Moreover, we consider the half-filled case, i.e. the band filling $\nu = \frac{1}{N}\sum_{i\sigma}\langle n_{i\sigma}\rangle = 1$, which is accomplished by adjusting the chemical potential $\mu$. The connectivity $K = 6$ was chosen for the statistical DMFT calculations.

As already pointed out in section 5.2.1, the realistic description of speckle disordered lattices necessitates the incorporation of the joint PDFs $p_{\Delta\epsilon,t}(\Delta\epsilon,t)$
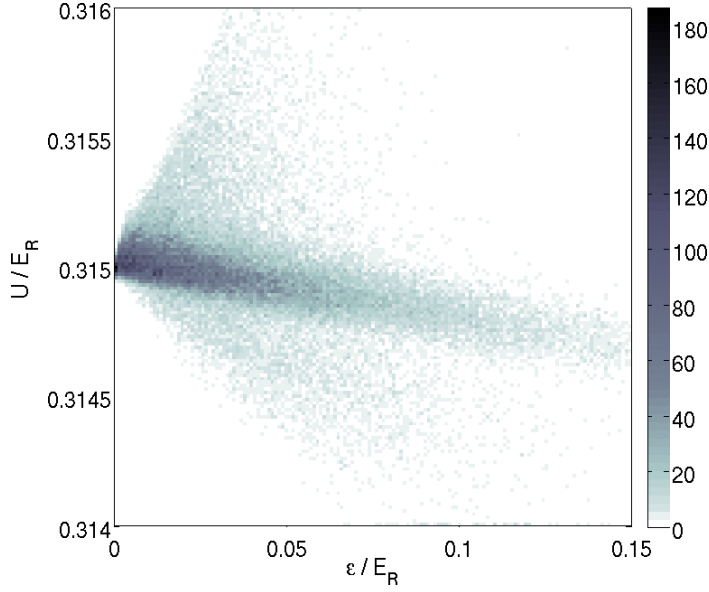
**Figure 8.1.:** Color coded probability distribution function (histogram) $p_{\epsilon,U}(\epsilon,U)$ of the on-site energies and the on-site interaction for speckle field strength $s_D = 0.05 E_R$ and $s$-wave scattering length $a = 100 a_0$. The lattice depth is given by $s_L = 10 E_R$.

and $p_{\epsilon,U}(\epsilon,U)$. This is done on basis of data calculated by Zhou and Ceperley [306], who calculated the distributions of the Hubbard parameters within an imaginary time evolution approach for the Wannier functions. The calculations were performed at fixed disorder strength $s_D = 1 E_R$ and lattice intensity $s_L = 14 E_R$. The parameters local interaction strength $U$, on-site energy $\epsilon$ and hopping amplitude $t$ were determined for 1222 disorder realizations on a three dimensional $6 \times 6 \times 6$ lattice. Based on these data, PDFs for the various parameters were constructed, inherently containing correlations as for example shown in figure 8.1. Up to a very good approximation, the on-site energies $\epsilon_i$ and tunneling parameters $t_{ij}$ are independent. However, there is a significant correlation between the difference in on-site energies $\Delta\epsilon_{ij} = \epsilon_i - \epsilon_j$ and the tunneling parameter $t_{ij}$, as is shown in figure 8.2.

Although these calculations were originally performed for bosonic $^{87}$Rb, the random parameters $\epsilon_i, U_i, t_{ij}$ depend only on the structure of the single particle states and can thus also be used for fermionic system after an appropriate rescaling.

Being bounded from below the most likely value and lower bound for the on-site energy corresponds to regions of low intensity, where we set $\epsilon = 0$, thus
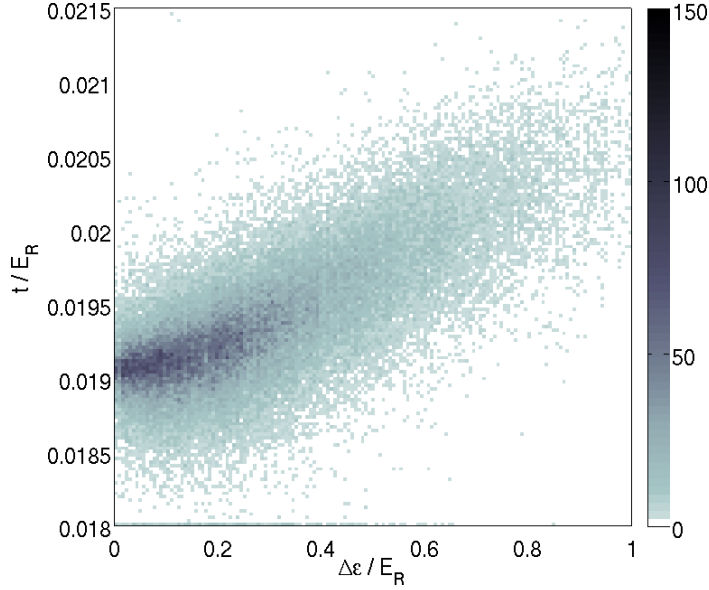
**Figure 8.2.:** Color coded joint probability distribution function (histogram) $p_{\Delta\epsilon,t}(\Delta\epsilon,t)$ of the difference in on-site energies and the respective hopping amplitudes for a speckle field strength $s_D = 0.4E_R$ and lattice depth $s_L = 10E_R$. Due to the reflectional symmetry of the disorder-averaged system, the distribution only depends on $|\Delta\epsilon|$.

recovering the usual energy scale in the absence of the disorder speckle laser. It was found in reference [293], that the disorder strength $\Delta$ (i.e. the standard deviation of $p_\epsilon(\epsilon)$) scales linearly with the speckle intensity $s_D$, as is to be expected in the perturbative limit. Thus, after an on-site energy is drawn from the distribution, it is simply scaled by multiplication with the respective $s_D$. An affine shift is not required due to the bound discussed above.

The on-site energy $\epsilon$ and on-site interaction strength $U$ are sampled from a two-dimensional joint PDF, which is equivalent to first sampling $\epsilon$ from the marginal PDF $p_{epsilon}(\epsilon)$ and subsequently $U$ from the conditional PDF $p_U(U|\epsilon)$. The standard deviation of the on-site interaction parameter $U$ (i.e. the marginal distribution $p_U(U) \equiv \int d\epsilon\, p_{\epsilon,U}(\epsilon,U)$) scales linearly with $s_D$, while the most probable value of $U$ remains unaffected by a variation in $s_D$ up to a good approximation. Therefore, the variation in $U$ in the two-dimensional distribution $p_{\epsilon,U}(\epsilon,U)$ is scaled by $s_D$ while the most likely value is set to the value of $U$ determined from a band-structure calculation of the Wannier functions in the pure case without disorder, as performed in reference [130] for instance.

*8.1. Model and joint probability distribution functions for the Hubbard parameters*

In contrast to the local interaction parameter $U$, the nearest neighbor tunneling amplitude $t_{ij}$ exhibits only very weak correlation with the respective on-site energy while the correlation with the energy difference between the two sites $\Delta\epsilon \equiv \epsilon_i - \epsilon_j$ is significant. Hence, the distribution for $\Delta\epsilon$ and $t$ cannot be sampled independently (i.e. $p_{\Delta\epsilon,t}(\Delta\epsilon, t) \neq p_{\Delta\epsilon}(\Delta\epsilon)\, p_t(t)$) and a conditional distribution function $p_t(t|\Delta\epsilon)$ for $t$, given a fixed value of $\Delta\epsilon$, was constructed from the data in [306]: For 200 discrete values of $\Delta\epsilon$ a histogram approximating $p_t(t|\Delta\epsilon)$ was extracted, approximating the PDF. This PDF is integrated with respect to $t$, yielding the conditional PDF $F_t(t|\Delta\epsilon)$ and subsequently normalized for each fixed $\Delta\epsilon$, such that $\lim_{t\to\infty} F_t(t|\Delta\epsilon) = 1$. To randomly sample values in a numerically efficient manner from $p_t(t|\Delta\epsilon)$, the conditional cumulative PDF $F_t(t|\Delta\epsilon)$ is inverted with respect to $t$ on a linearly interpolated grid on [0,1], consisting of 800 points. Given a fixed $\Delta\epsilon$, a randomly drawn value of the inverted cumulative distribution is thus distributed according to the initial conditional PDF $p_t(t|\Delta\epsilon)$, leading to the sought-after sampling routine. This routine was implemented by Ulf Bissbort.

As now has become clear the three sets of the parameters for the Hubbard model underly statistical fluctuations. For the three-dimensional case with equal laser intensity along each of the three axes, all parameters are unique functions of $s_L$ and $s_D$ for a given atomic species, when expressed in units of $E_R$. However, this is not the case in the two-dimensional lattice, which is investigated by means of real-space DMFT. Here, the interaction parameter $U$ depends on the shape and strength of the axial trapping potential, which may vary significantly in different experiments. In this anisotropic case with fixed $a_s$, the lattice depth $s_L$ does not uniquely characterize the point in the phase diagram and, therefore, we work in units of the non-interacting bandwidth $W_0$ of the homogeneous system.

In order to incorporate the disorder in the on-site interactions, the stochastic self-consistent calculation scheme presented in section 4.4.1 is modified slightly by an additional step:

1. For each sample a random on-site energy $\epsilon_i$ is drawn from the PDF $p_\epsilon(\epsilon_i)$ given in equation (5.14).

2. For each sample a random on-site interaction $U_i$ is drawn from the conditional PDF $p_U(U|\epsilon)$.

3. For each sample random hopping amplitudes $t_{ij}$ are drawn from the conditional PDF $p_t(t|\Delta\epsilon)$ depending on the difference $\Delta\epsilon = \epsilon_i - \epsilon_j$ of the on-site energies $\epsilon_i$ and $\epsilon_j$ of the randomly determined nearest neighbor $j$.
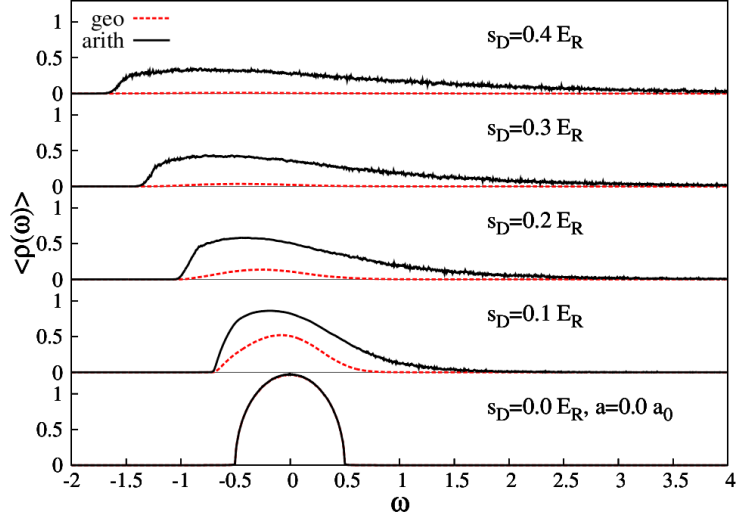
**Figure 8.3.:** Comparison of arithmetically (black solid lines) and geometrically (red dashed lines) averaged spectral functions with increasing speckle field strength $s_D$ ($s_D = 0.0E_R, 0.1E_R, 0.2E_R, 0.3E_R, 0.4E_R$) in the non-interacting limit $a = 0$. Parameters are $\nu = 1.0$, $s_L = 10E_R$, and $\eta = 10^{-3}$.

4. The hybridization function $\Gamma_i(\omega)$, with the local single-particle Green's function $G_{jj}(\omega)$ of the nearest neighbors randomly sampled from the PDF $p[G_{ii}(\omega)]$, is determined via equation (4.24) for each sample.

5. The local self-energy $\Sigma_i(\omega)$ is calculated from the solution of the local impurity problem by using an impurity solver.

6. The local single-particle Green's function $G_{ii}(\omega)$ is calculated using equation (4.22)

7. Having calculated a completely new ensemble $\{G_{ii}(\omega)\}$, a new PDF $p[G_{ii}(\omega)]$ is obtained by construction of a histogram.

## 8.2. Anderson localization in the non-interacting case

The arithmetic and geometric average of the LDOS obtained within statistical DMFT, which for the non-interacting case reduces to the local distribution approach [2, 13], exhibit different behavior with increasing disorder strength

$\Delta$. Figure 8.3 displays the evolution of the arithmetically and geometrically averaged LDOS in the non-interacting case, when the speckle field strength is increased from $0E_R$ to $0.4E_R$.

First of all, we note that with an increase in the speckle field strength, the spectra are broadened and long tails emerge at positive energies. A noticeable difference between the geometric mean and the arithmetic mean, is that the geometric mean of the LDOS converges to zero with increasing $\Delta$. This can be attributed to the transition from extended states to localized states, which is
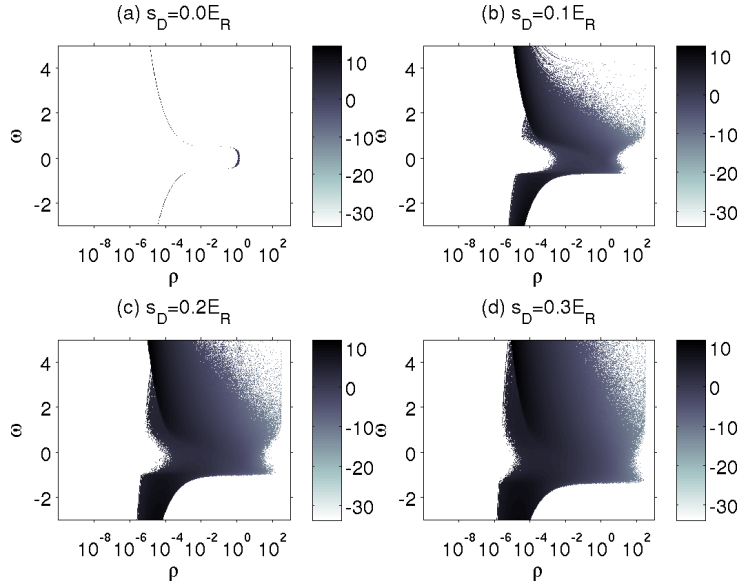


**Figure 8.4.:** Color coded natural logarithm of PDF $p[\rho]$ for increasing speckle field strength $s_D$: (a) $s_D = 0.0E_R$, (b) $s_D = 0.1E_R$, (c) $s_D = 0.2E_R$, and (d) $s_D = 0.3E_R$. Parameters are $a_s = 0$, $\eta = 10^{-3}$, $\nu = 1.0$, and $s_L = 10E_R$.

used within the TMT [5, 60–62, 82, 87]. However, not only averages, but also the full PDF $p[\rho(\omega)]$ is accessible within the statistical DMFT. This enables a more powerful and clearer distinction between localized states and extended states as already explained in chapters 6 and 7. The PDFs $p[\rho(\omega)]$ associated with the data shown in figure 8.3, are plotted in figure 8.4. As expected in the homogeneous case (cf. panel (a)), the PDF for each frequency is given by a delta function. For finite disorder strength, the PDFs spread out over several orders of magnitude.

Within the statistical DMFT, extended and localized states are characterized by different behavior of the PDF $p[\rho(\omega)]$ in the limit of vanishing broadening $\eta \to 0$ [13]. The PDF of an extended state saturates at a finite value for $\eta \to 0$,
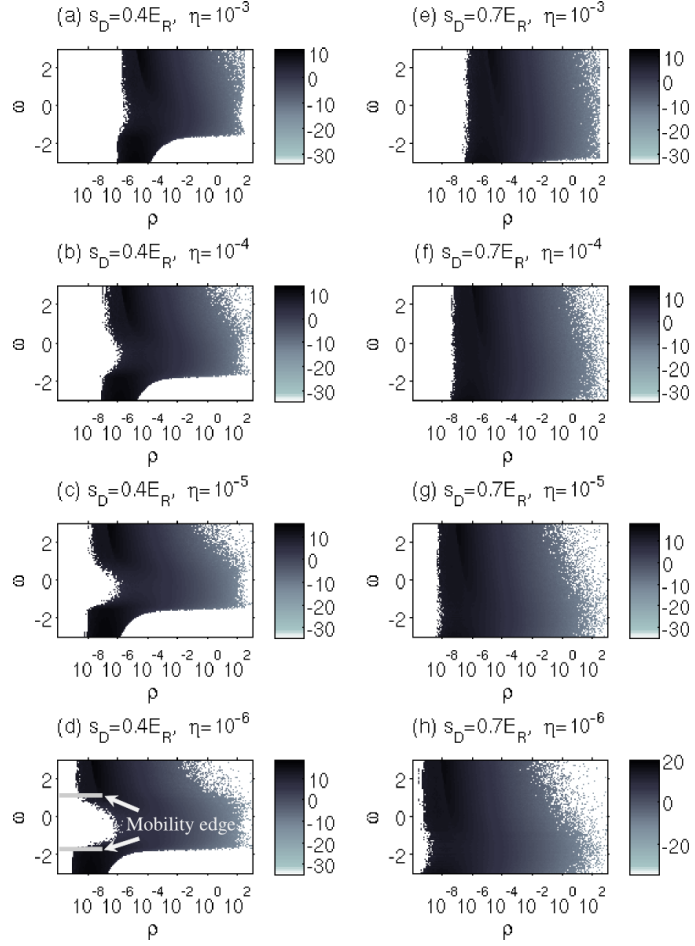
**Figure 8.5.:** Color coded natural logarithm of PDFs $p[\rho(\omega)]$ for decreasing broadening $\eta$ and speckle field strength $s_D = 0.4E_R$ (panels (a)-(d)) and $s_D = 0.7E_R$ (panels (e)-(h)) of non-interacting fermions. Parameters are $\nu = 1.0$ and $s_L = 10E_R$.

while more and more weight of the PDF shifts towards zero in the case of localized states. In figure 8.5 the behavior of the PDFs at two speckle field
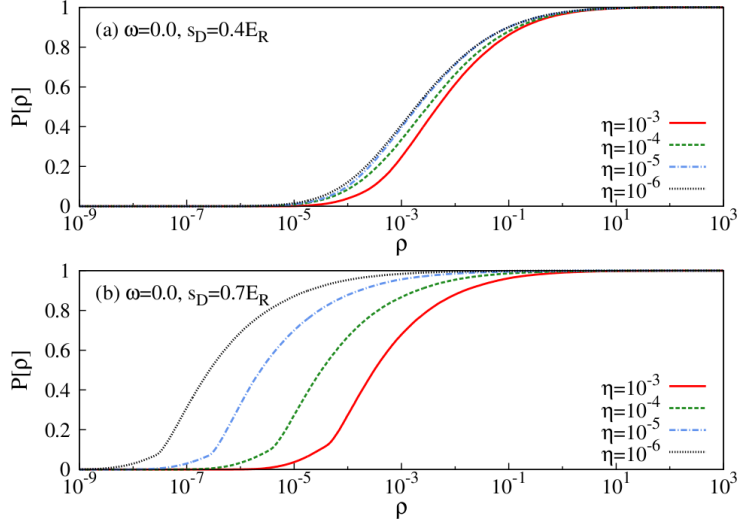


**Figure 8.6.:** Behavior of the cumulative PDFs $P[\rho(\omega = 0.0)]$ as the broadening $\eta$ is decreased from $10^{-3}$ to $10^{-6}$ for (a) speckle field strength $s_D = 0.4E_R$ and (b) speckle field strength $s_D = 0.7E_R$ without interaction. Parameters are $a = 0$, $\nu = 1.0$, and $s_L = 10E_R$.

strengths $s_D = 0.4E_R$ and $s_D = 0.7E_R$ are plotted as a series of vanishing broadening $\eta \to 0$. The different behavior of the extended and localized states allows us to distinguish between them and the mobility edges can be identified as shown in panel (d) for $s_D = 0.4E_R$. Here, we find a similar behavior as in the box disorder case. Mobility edges are identified clearly and the states between the mobility edges are extended, whereas the states outside are localized. As soon as the Fermi level is passed, the system becomes Anderson insulating. We observe that the states at the Fermi level are extended for speckle field strength $s_D = 0.4$ - therefore it is metallic whereas for speckle field strength $s_D = 0.7E_R$ the states at the Fermi level are localized. This can also be seen from the 2D-plots of the corresponding cumulative PDFs at the Fermi level for the two speckle field strengths in figure 8.6. These localization phenomena differ strongly from the involved localization physics investigated in the last chapter 7.

## 8.3. Paramagnetic ground state phase diagram of the interacting system

Now we will discuss the main result of our investigation, i.e. the paramagnetic ground state phase diagram of interacting fermions exposed to speckle disorder (in the $s$-wave scattering length $a$ and speckle field strength $s_D$ plane), as displayed in figure 8.7.
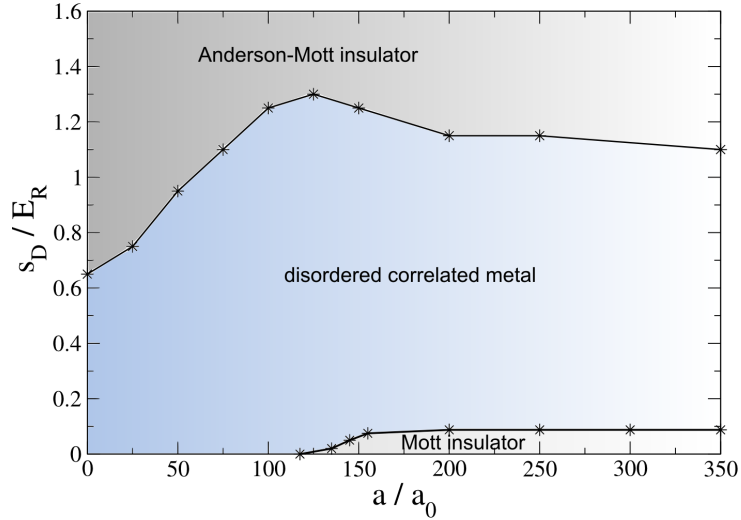


**Figure 8.7.:** Paramagnetic ground state phase diagram of fermions in a speckle disordered optical lattice in the $s_D$-$a$-Plane. Parameters are $\nu = 1.0$ and $s_L = 10E_R$. In the Munich experiment [242] - so far without disorder - scattering lengths up to $a = 300a_0$ can be achieved.

In the absence of disorder ($s_D = 0$), a Mott metal insulator transition is found at intermediate interaction strength. For the system considered here, we found the critical s-wave scattering length for Mott transition $a_c = 117.5a_0$. In the absence of interactions ($a = 0$), the Anderson transition is found at $s_D = 0.66$. In a system with both speckle disorder and interactions, three separate phases exist: Mott insulator, disordered correlated metal, and Anderson-Mott insulator.

In figure 8.8 the arithmetically averaged spectral functions are given for two different speckle field strengths $s_D$: in panel (a) for $s_D = 0.05E_R$ and in panel (b) for $s_D = 0.1E_R$. In both cases the interaction strength is increased from the bottom to the top. Remarkably, the spectral functions evolve very differently for the two disorder strengths. For speckle field strength $s_D = 0.05E_R$ a correlation-induced metal-insulator transition takes place at finite $a$. For $s_D = 0.1E_R$ in the

**Figure 8.8.:** Arithmetically (black solid) and geometrically (red dashed) averaged spectral function with increasing $s$-wave scattering length $a$ for speckle field strength $s_D = 0.05E_R$ in panel (a) and for speckle field strength $s_D = 0.1E_R$ in panel (b). Parameters are $\nu = 1.0$ and $s_L = 10E_R$.

investigated regime up to $a = 350a_0$, no metal-insulator transition was found. Instead, the Kondo peak, i.e. the coherent low-energy excitations, are stabilized for higher interaction values, whereas the lower Hubbard band is shifted away from the Fermi level.

This behavior is caused by the redistribution of the states into the Mott-Hubbard gap due to disorder. For sufficiently strong disorder, the gap is closed. The unbounded nature of the speckle disorder at any finite $\Delta$ gives rise to states with very high energies, although their ratio is exponentially suppressed in $\Delta^{-1}$. This means that the Mott transition at finite disorder strength, which is described here, might even be an artifact of the finite size $N$ in the stochastic Green's function ensemble. If this is the case, it would be an intrinsic feature of finite size optical lattice as well.

To gain further insight, we plotted the arithmetically averaged LDOS at the Fermi level as a function of the s-wave scattering length $a$ in figure 8.9 for three different speckle field strengths. Due to the finite disorder strength, the arithmetically averaged LDOS at zero interaction is reduced, which means that the Luttinger theorem is not fulfilled in presence of disorder. By increasing the interaction strength, the metallicity is improved for all three disorder strengths. At low disorder strength ($s_D = 0.05E_R$), the Luttinger theorem is asymptotically
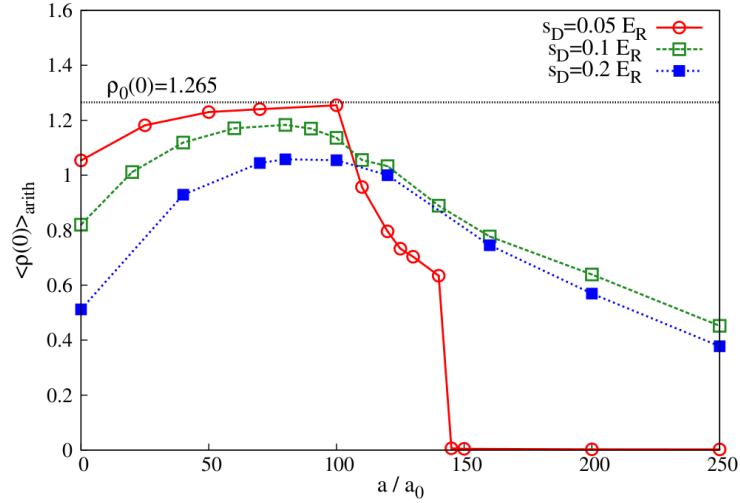
**Figure 8.9.:** Arithmetically averaged local density of states at the Fermi level $\langle\rho(0)\rangle_{\text{arith}}$ for three different values of the speckle field strength $s_D$: $s_D = 0.05E_R$ (red solid line), $s_D = 0.2E_R$ (green dashed line) and $s_D = 0.2E_R$ (blue dotted line). For comparison the local density of states at the Fermi level of the homogeneous, non-interacting system $\rho_0(0) = 1.265$ is included. Parameters are $\nu = 1.0$ and $s_L = 10E_R$.

fulfilled for $a \sim 100a_0$. This is in agreement with results for the Anderson-Hubbard model with box disorder [5, 60, 62]. The metallicity is suddenly reduced for stronger interactions and finally a Mott-Hubbard transition takes place at $a_c = 145a_0$ for $s_D = 0.05E_R$. For higher disorder strengths ($s_D = 0.1E_R$ and $s_D = 0.2E_R$), no Mott transition is found for scattering lengths up to $a = 350a_0$.

It is interesting to compare the qualitative structure of the phase diagram in Fig. 8.7 with the counterpart of ultracold bosonic atoms in speckle disordered lattices [41]. In the latter case, an arbitrarily weak speckle field leads to a vanishing of the excitation gap and the Mott insulator only exists in the homogeneous system without disorder, in contrast to the fermionic case where a Mott insulator may exist at $\Delta > 0$. Furthermore, the results presented here differ from the results obtained within TMT [5, 60, 62] for fermions with bounded box disorder. Although a delocalization tendency was found for box disorder, a correlation-induced metal-insulator transition takes place at intermediate disorder strengths. The critical interaction strength is shifted to higher values proportional to the disorder strength. Thus, the Anderson-Mott insulator and the Mott insulator were found to be continuously connected [60]. All important differences between the paramagnetic ground state phase diagrams for box

disorder and speckle disorder can be attributed to the unbounded nature of the speckle distribution.

## 8.4. Speckle disordered square lattice

Fermions with a semi-elliptic density of states are assumed to qualitatively exhibit the same physics as fermions in three-dimensional lattices. It is important to note, that the physics may differ in a two-dimensional system. For this reason fermions on a square lattice were investigated within real-space DMFT [86, 142, 255] in collaboration with Julia Wernsdorfer.

As already indicated in section 4.4 the statistical DMFT [85] was originally introduced in two implementations, on the infinite Bethe lattice as well as a computation scheme for finite lattices. A terminological distinction by referring to the first implementation by statistical DMFT and to the latter as real-space DMFT is justified and helpful[1]. Real-space DMFT is applicable to any lattice structure and incorporates present disorder or inhomogeneities non-perturbatively. For an initial disorder realization the self-consistency of the whole system is guaranteed by the converged solution for each local Green's function of the coupled sites. It represents a system of self-consistency equations for each disorder realization and, hence, it is a deterministic approach. In contrast, statistical DMFT investigates the loop-free Bethe lattice on an infinite system and the self-consistency is aimed on a level of PDFs for the Green's function. The statistical DMFT is a statistical approach from the beginning and investigates a random disordered system on a fully stochastic level.

In some more detail, within real-space DMFT each lattice site is mapped onto a single-impurity Anderson Hamiltonian. The hybridization function has to be determined self-consistently for each lattice site. Starting with an arbitrary hybridization function, the solution of each impurity problem is provided by MPT, as in statistical DMFT, and leads to a set of local self-energy functions $\Sigma^i \delta_{ij}(i\omega_n)$. They determine the self-energy matrix in the real-space representation

$$(\boldsymbol{\Sigma})_{ij} = \Sigma^i \delta_{ij} \,. \tag{8.1}$$

Following the Dyson equation, the interacting lattice Green's function is given by

$$\mathbf{G}(i\omega_n)^{-1} = \mathbf{G}_0(i\omega_n)^{-1} - \boldsymbol{\Sigma}(i\omega_n) \,, \tag{8.2}$$

---

[1]In the literature real-space DMFT is also referred to as statistical DMFT at times, e.g. in [258].

**Figure 8.10.:** Arithmetically averaged spectral function with increasing interaction strength $U$ for fixed speckle field strength $s_D = 0.05E_R$ obtained via statistical DMFT with $K = 4$ (black solid line) and real-space DMFT (red dashed line). The spin-summed filling is given by $\nu = 1.0$ and the lattice size within the RDMFT calculations was $24 \times 24$.

where $\omega_n$ are the Matsubara frequencies. The non-interacting Green's function $\mathbf{G}_0(i\omega_n)$ in real-space representation is given by

$$\mathbf{G}_0(i\omega_n)^{-1} = (\mu + i\omega_n)\mathbf{1} - \mathbf{t} - \mathbf{V}\,, \tag{8.3}$$

where $\mathbf{1}$ is the unity matrix, $\mathbf{t}$ is the matrix of hopping amplitudes, and $(\mathbf{V})_{ij} = \varepsilon_i \delta_{ij}$ denotes the matrix of random on-site energies. Together with equation (4.22) and the diagonal elements from the inverted relation (8.2) a set of local hybridization functions $\Gamma^{(i)}(\omega)$ is extracted, which closes the self-consistency loop. Besides describing the Mott-Hubbard metal-insulator transition and magnetic order, real-space DMFT is capable of treating spatial inhomogeneities such as disorder. For more details the reader is referred to the literature [142, 255].

In order to investigate the speckle disordered square lattice and to assess our results obtained within statistical DMFT for fermions with a semi-elliptical density of states, Julia Wernsdorfer performed real-space DMFT calculations. An exemplary comparison of the arithmetically averaged spectral functions obtained by the two methods for identical parameters is given in figure 8.10. In these statistical DMFT calculations the connectivity $K = 4$ is chosen to obtain
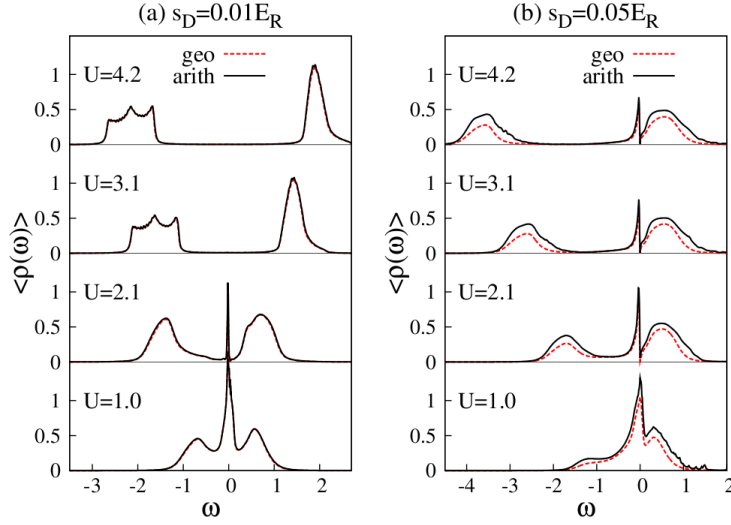
**Figure 8.11.:** Arithmetically (black solid) and geometrically (red dashed) averaged
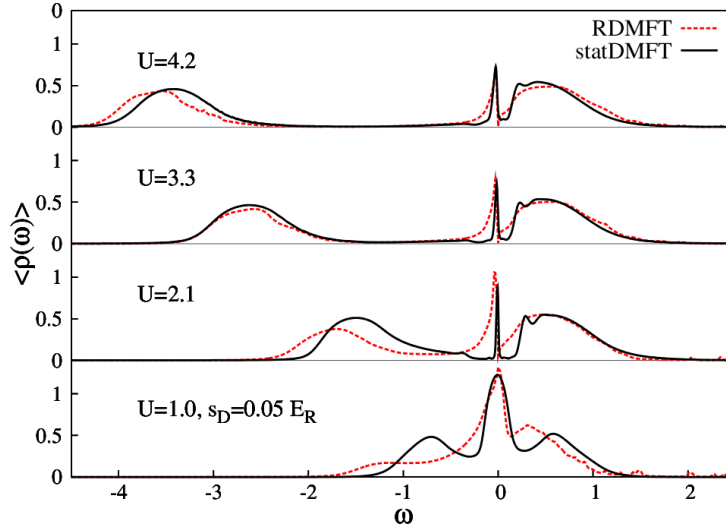spectral function with increasing interaction strength $U$ for speckle
field strength $s_D = 0.01 E_R$ in panel (a) and $s_D = 0.05 E_R$ in panel (b)
obtained by RDMFT on a $24 \times 24$ square lattice. The spin-summed
filling is given by $\nu = 1.0$.

the same bandwidth.

Both methods lead to qualitatively identical results. The differences in
the spectral functions can be traced back to the differences of the simulated
models. The statistical DMFT is employed for particles with a semi-elliptical
density of states, whereas real-space DMFT was used for particles on the square
lattice. Since the kinetic energy is connected to the lattice structure, the
observed differences are pronounced when the kinetic energy dominates over
the interaction energy. Consequently, deviations in the distributions of the
spectral weights are larger for low and intermediate interaction strengths (figure
8.10 $U = 1.0$ and $U = 2.1$). On the other hand, the agreement is good for the
strongly interacting case (figure 8.10 $U = 3.3$ and $U = 4.2$).

Interestingly, a pseudo-gap at the Fermi level in the LDOS on the square
lattice is found within real-space DMFT. This pseudo-gap arises for intermediate
and strong interactions in the presence of disorder and is stable under variation
of the system size. The pseudo-gap anomalies, also called zero bias anomalies,
are a common feature in two-dimensional strongly correlated systems with
disorder [10, 95]. A pseudo-gap anomaly was for instance found within a
quantum Monte Carlo investigation of the Anderson-Hubbard Hamiltonian with
box disorder [70, 257]. Our results suggest, that the physics of the pseudo-gap
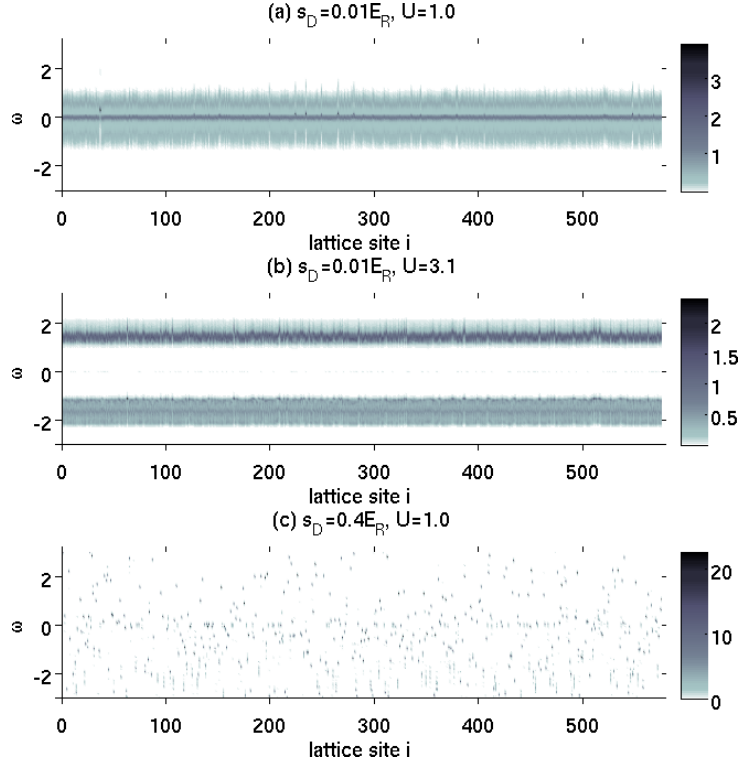
**Figure 8.12.:** Color coded local density of states $\rho_i(\omega)$ as a function of frequency $\omega$ and lattice site index $i$ for three different parameter sets: (a) $U = 1.0$ and $s_D = 0.01E_R$, (b) $U = 3.1$ and $s_D = 0.01E_R$ and (a) $U = 1.0$ and $s_D = 0.04E_R$. Parameters are $\nu = 1.0$ and the lattice size was $24 \times 24$.

anomaly could be studied with ultracold atoms in speckle disordered optical lattices in the future. A detailed theoretical investigation of the pseudo-gap is under current ongoing research.

Arithmetically and geometrically averaged spectral functions calculated by real-space DMFT for two different disorder strengths, namely $s_D = 0.01E_R$ and $s_D = 0.05E_R$, are displayed in figure 8.11. Qualitatively, the spectral functions show similar behavior as obtained within statistical DMFT, cf. figure 8.8. For weak disorder ($s_D = 0.01E_R$), metallic solutions are obtained for weak interactions. Raising the interaction, a Mott insulating phase is obtained, analogous to the case of a homogeneous system. On the contrary, for larger speckle disorder ($s_D = 0.05E_R$) the LDOS remains finite at the Fermi level $\omega = 0$, even at strong interaction $U = 4.2$.

We note that within real-space DMFT for $U = 3.1$ and $U = 4.2$, the lower
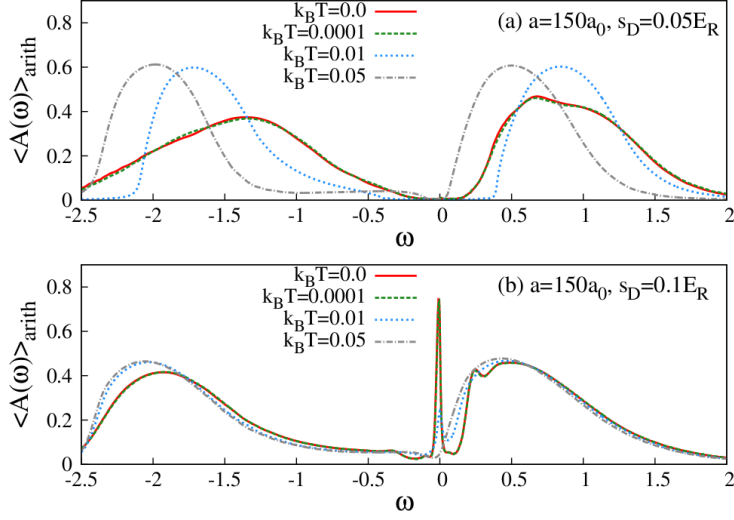
**Figure 8.13.:** Evolution of the arithmetically averaged spectral function with increasing temperature for two parameter sets: (a) $s_D = 0.05E_R$, $a = 150a_0$ and (b) $s_D = 0.1E_R$, $a = 150a_0$. Parameters are $\nu = 1.0$ and $s_L = 10E_R$.

Hubbard-band shows a peaked structure at low disorder. This feature cannot be exclusively identified with physical properties of the system because of numerical uncertainties. Within real-space DMFT, a artificial broadening $\eta$ is applied to obtain an spectrum comparable to the infinite system. The broadening is scaled proportionally to the system size, i.e. $\eta \propto 1/L^2$[2]. Since the peaks are not fully recovered for other lattice sizes, we conclude that they are finite size effects. Nevertheless, despite possible finite size effects within the real-space DMFT calculations and differences due to different underlying lattice structure both methods result in qualitatively agreeing results.

The real space resolution of the LDOS gives us insight into localization effects of the system. In figure 8.12 the LDOS $\rho_i(\omega)$ is plotted for a $24 \times 24$ lattice and different interaction strengths, each for a different disorder realization. At $U = 1.0$ and weak disorder $s_D = 0.01E_R$ (figure 8.12 panel (a)) the spectral weight around the Fermi level $\omega = 0$ remains at each lattice site. The vast majority of single particle states are extended and the system is in the metallic phase. At $U = 3.1$ (figure 8.12 panel (b)) the Hubbard bands are formed and the

---

[2]Compared to the values used in statistical DMFT, the broadening is large, which is rather problematic for the investigation of localization phenomena within real-space DMFT. This issue was recently addressed in a preprint for the non-interacting case [211]. Moreover, it is also under current investigation for the interacting case within our group.
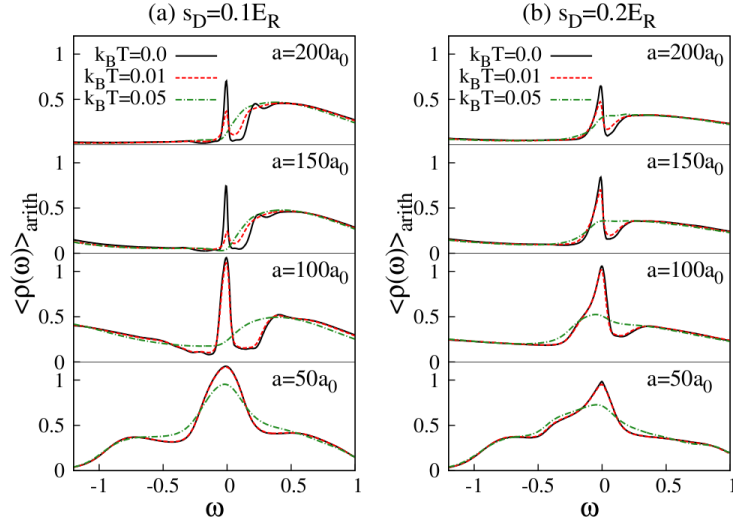
**Figure 8.14.:** Evolution of the arithmetically averaged spectral function with increasing $s$-wave scattering length ($a = 50a_0, 100a_0, 150a_0, 200a_0$) for two disorder strengths (a) $s_D = 0.1E_R$ and (b) $s_D = 0.2E_R$. For each parameter the spectral function is compared at three different temperatures, namely $k_bT = 0.0$ (black solid line), $k_bT = 0.01$ (red dashed line) and $k_bT = 0.05$ (green dash-dotted line). Parameters are $\nu = 1.0$ and $s_L = 10E_R$.

spectrum exhibits a gap proportional to the interaction strength for all lattice sites, indicating that the system is in a Mott insulating state. However, as the speckle field strength is increased to $s_D = 0.4E_R$, the states with spectral weight at the same frequency are separated. In other words, the spectrum is highly fragmented and each local spectrum consists of isolated delta peaks, consistent with Anderson localized states in the infinitely large system (cf. figure 8.12 panel (c)).

## 8.5. Finite temperature effects

Here, we investigated a system of fermions with a semi-elliptic density of states at finite temperature. The spectral functions are plotted in figure 8.13 for two parameter sets. Panel (a) displays the arithmetically averaged spectral functions for speckle disorder strength $s_D = 0.05$ and scattering length $a = 150a_0$ for various increasing temperatures. At zero temperature, this parameter set would correspond to the Mott insulator. In figure 8.13 we note that with increasing temperature, the gap initially grows and the incoherent excitations reveal a

significant redistribution of the spectral weight, which is shifted away from the Fermi level. This is not observed in the homogeneous case, where the spectral transfer is weak. Panel (b) shows the corresponding behavior for different parameters, namely $s_D = 0.1$ and $a = 150a_0$, which corresponds to the disordered strongly correlated metal at zero temperature. With increasing temperature, the low energy excitations are reduced, and for $k_B T = 0.05$ the system enters a Mott insulating state.

In figure 8.14, the evolution of the arithmetically averaged spectral function with increasing temperature is displayed for two values of the speckle field strength ($s_D = 0.1 E_R$ in panel (a) and $s_D = 0.2 E_R$ in panel (b)) and three different temperatures: $k_B T = 0$, $k_B T = 0.01$ and $k_B T = 0.05$. We note the reduction of the spectral weight at the Fermi level due to finite temperatures. This leads to an enlargement of the Mott insulating phase. However, as can be seen in panel (b) of figure 8.14, a metal without a resonant peak at the Fermi level is stabilized a higher disorder strength. In this respect, our central finding at $T = 0$, that the Mott and the Anderson-Mott insulators are not continuously connected in presence of the speckle disorder, also holds at finite temperature.

## 8.6. Conclusion

In this chapter we have investigated a gas of ultracold fermions in optical lattices subjected to an additional speckle disorder field using statistical DMFT and real-space DMFT. The presented statistical DMFT schemes include off-diagonal disorder as described in section 4.4.1. This allows for a systematic inclusion of joint PDFs for the difference in the on-site energies and the hopping amplitudes as well as the on-site energies and the local interaction strength, which are present in experiments and were calculated by Zhou and Ceperley [306].

The complete paramagnetic ground state phase diagram was determined. It consists of a disordered metallic phase, as well as Mott insulating and Anderson-Mott insulating phases. A strong suppression of the correlation-induced metal insulator-transition is observed and a finite metallic phase is found, even in the strongly interacting regime. Hence, the Mott and the Anderson-Mott insulators are not continuously connected. This contrasts with predictions for bounded box disorder by TMT and our investigation within statistical DMFT in chapter 6. This, of course, puts the feasibility of simulating the Anderson-Hubbard model for relevant disorder types in solids by using the speckle disorder into question. Obviously, the unbounded nature of speckle disorder on-site energies is quite specific and in particular not realized in solids. From this point of view, we can conclude that there is a need for future research to develop ways of

introducing box disorder to optical lattices.

Speckle disordered fermions on a square lattice were also investigated by means of the real-space DMFT. Our main finding for the case of high-dimensional systems also holds in the two-dimensional case. A pseudo-gap was found, which should be investigated in detail in the future. Finally, we investigated the high-dimensional system at finite temperature, where the Mott insulating region is enlarged but the separation of the Mott and the Anderson-Mott insulators persists.

# 9. Disordered Bose-Fermi mixtures

In optical lattices systems of mixed quantum statistics, Bose-Fermi mixtures have been realized [36, 138, 220]. These systems represent first-time realizations of systems with mixed quantum statistics. Exotic physics have been predicted to occur, such as the supersolid phase [54, 219, 272, 273], phase separation [54, 234, 273] or composite fermions [184, 226].

On the other hand, we have already discussed the possibility of introducing disorder to these systems (cf. section 5.2). Hence, a route to exciting physics is available by bringing together these two developments, the disordered lattice with mixed quantum statistics. Such a system may give rise to new effects of the interplay between interaction and disorder, which is under intense investigation. Phases which have their origin in the interaction, such as the Mott insulator [206] or the charge density wave compete with disorder-induced phases, the Anderson insulator [17, 172] for fermions and the Bose glass phase [111] for bosons. Theoretically these systems have been studied in the strongly interacting limit within an effective Hamiltonian approach [7, 240]. It was shown that within certain parameter regimes the Ising-spin glass model and the Edwards-Anderson model can be realized [240].

In this chapter, we investigate mixtures of strongly correlated bosons and spin-polarized fermions non-perturbatively, in the whole regime from weak interactions to strong interactions. For this purpose, a recently developed calculation scheme for Bose-Fermi mixtures extended from the DMFT (cf. section 2.3), called the generalized DMFT [188, 272, 273], is used for solving the many-body problem numerically. The corresponding impurity problems that result from the generalized DMFT are solved with the numerical renormalization group [144, 176]. In previous studies [272, 273] the fermionic subsystem was considered to be half-filled and also the bosonic subsystem was also considered to have fixed filling $1/2$ and $3/2$. Here, we will investigate complementary systems by allowing for arbitrary bosonic filling and work for fixed bosonic chemical potential.

The second focus of this chapter is to study, how weak correlated on-site disorder modifies the behavior in the homogeneous system. This is done by employing the recently developed TMT (cf. section 4.3) to the Bose-Fermi system. The TMT allows for the description of disorder-induced and correlation-

induced metal-insulator transitions within a unified framework.

In particular, we find that introducing weak diagonal disorder to the system has a dramatic influence on the ground state phase diagram, in particular a supersolid is induced already for very small disorder strengths, which is stable over a relatively large range of values of the bosonic chemical potential.

Finally, we study mixture of two-component fermions and bosons in disordered lattices. We focus on the evolution of the bosonic ground state phase diagram when the interspecies interaction strength, as well as the disorder strength, is varied.

## 9.1. Disordered Bose-Fermi Hubbard Hamiltonian

Mixtures of spin-polarized fermions and bosons in an optical lattice with diagonal disorder are well described by the disordered Bose-Fermi Hubbard Hamiltonian

$$H = H_{bf} + H_{\text{dis}}^{\text{corr}} \tag{9.1}$$

consisting of two parts, the Bose-Fermi Hubbard Hamiltonian [8, 54]

$$
\begin{aligned}
H_{bf} &= -t_f \sum_{<i,j>} c_i^\dagger c_j - t_b \sum_{<i,j>} b_i^\dagger b_j - \mu_f \sum_i c_i^\dagger c_i - \mu_b \sum_i b_i^\dagger b_i \\
&\quad + \frac{U_b}{2} \sum_i n_i^b (n_i^b - 1) + U_{fb} \sum_i n_i^b n_i^f
\end{aligned}
\tag{9.2}
$$

and the correlated diagonal disorder part

$$H_{\text{dis}}^{\text{corr}} = \sum_i \epsilon_i (c_i^\dagger c_i + \alpha_i b_i^\dagger b_i) \ , \tag{9.3}$$

where $c_i^\dagger$ and $b_i^\dagger$ denote the fermionic and bosonic creation operator at site $i$ respectively. The fermionic and bosonic number operator are given by $n_i^f = c_i^\dagger c_i$ and $n_i^b = b_i^\dagger b_i$. The fermionic and bosonic hopping amplitude is denoted by $t_f$ and $t_b$. $U_b$ and $U_{fb}$ denote boson-boson and fermion-boson interaction strength and $\mu_f$ and $\mu_b$ stand for the fermionic and bosonic chemical potential. Summations in the hopping terms are restricted to the $z$ nearest neighbors indicated by the brackets $<\cdot,\cdot>$, all other hopping processes are excluded.

The diagonal disorder manifests itself in the on-site energies $\epsilon_i$. We assume that all on-site energies are identically and independently distributed via the PDF $p_\epsilon(\epsilon)$ as already done in the preceding chapters. In the following we will consider the common box distribution (defined in equation 3.27) with disorder

strength $\Delta$ for the on-site energies. We only consider correlated disorder with $\alpha_i = 1$ for all sites $i$, which is reasonable for ${}^6\text{Li-}{}^7\text{Li}$ mixtures. Coincidentally, this also represents a valid approximation for ${}^{40}\text{Ka-}{}^{87}\text{Rb}$ mixtures, if a light of wavelength $\lambda = 1064nm$ is used to create a random optical dipole potential.

## 9.2. Method

As discussed in detail in chapters 3 and 4 disordered systems are most accurately investigated by focusing on PDFs of observables. Nevertheless, we already argued that calculating the full PDFs is laborious and becomes in many cases numerically infeasible depending on the desired accuracy of the theoretical tool. This is in particular true for the here considered Bose-Fermi mixtures. For this reason the investigation based on full distributions is not performed and instead only single moments of the distributions that are informative regarding the disorder physics are considered, which is the general spirit of the TMT (see section 4.3). In this chapter, we will employ the TMT for the disordered systems. In particular, we will calculate the geometric disorder average of the fermionic LDOS as defined in equation (4.12) to account for localization effects. The geometric average is incorporated in the DMFT calculation circle as described in section 4.3, leading to en ensemble of single-impurity Anderson models, that has to be solved self-consistently.

However, here we are interested in Bose-Fermi mixtures and considering single-impurity Anderson models is obviously not sufficient. To accomplish a TMT for Bose-Fermi mixtures we follow the lines of the recently developed generalized DMFT [272, 273]. Therein, the bosons are investigated within the Gutzwiller approximation [253], which is given as a decomposition of the bosonic hopping operator. The bosonic annihilation operator is written as sum of its expectation value $\Psi_i = \langle \text{gs}|b_i|\text{gs}\rangle$ representing the superfluid order parameter and its fluctuating part $\delta b_i$. Here, $|\text{gs}\rangle$ is the ground state of the system. Accordingly, the operators appearing in the hopping term of the Hamiltonian decouple

$$
\begin{align}
b_i^\dagger b_j &= (\Psi_i^* + \delta b_i^\dagger)(\Psi_j + \delta b_j) \tag{9.4}\\
&= \Psi_i^* \Psi_j + \Psi_i^*(b_j - \Psi_j) + \Psi_j(b_i^\dagger - \Psi_i^*) + \delta b_i^\dagger \delta b_j \tag{9.5}\\
&\approx \Psi_i^* b_j + \Psi_j b_i^\dagger - \Psi_i^* \Psi_j . \tag{9.6}
\end{align}
$$

In the final step, fluctuations in quadratic order have been neglected.

The disorder gives rise to PDFs of the superfluid order parameter $p_\Psi$, which have been investigated by means of the stochastic mean-field theory [40, 41]. In

general, it was found that finite disorder strength broadens the PDF, which can be approximated by a log-normal PDF. At the transition from the superfluid to the Bose glass phase the typical value of PDF is zero. Similar to the case of the LDOS, we calculate the geometric average of the superfluid order parameter

$$\langle \Psi \rangle_{\mathrm{geo}} = \exp \int\limits_{-\infty}^{\infty} d\epsilon \ln \Psi(\epsilon) p_\epsilon(\epsilon) \tag{9.7}$$

as approximation for the typical value, which enables accounting for localization effects for the bosons. In particular, it allows for the description of the Bose glass phase[1].

By applying the generalized DMFT for the disordered system, we are left with a much simpler problem than the original disordered Bose-Fermi-Hubbard Hamiltonian, namely an ensemble of generalized Anderson impurity models

$$H_{\mathrm{imp},\epsilon} = H_f^{\mathrm{imp},\epsilon} + H_b^{\mathrm{imp},\epsilon} + H_{fb}^{\mathrm{imp}} \, , \tag{9.8}$$

with

$$H_f^{\mathrm{imp},\epsilon} = -\sum(\mu_f - \epsilon)n_f + \sum_k \epsilon_k a_k^\dagger a_k + \sum_k V_k(c^\dagger a_k + h.c.) \tag{9.9}$$

$$H_b^{\mathrm{imp},\epsilon} = -zt_b(\Psi_{\mathrm{typ}}b^\dagger + \Psi_{\mathrm{typ}}^* b) + \frac{U_b}{2}n_b(n_b - 1) - (\mu_b - \alpha\epsilon)n_b \tag{9.10}$$

$$H_{fb}^{\mathrm{imp}} = U_{fb}n_f n_b \, . \tag{9.11}$$

The bath electron annihilation operator is given by $a_k$ with energy $\epsilon_k$ and the bath couplings by $V_k$, which are calculated from the hybridization function [56]. In this work the impurity models are solved by means of the numerical renormalization group [144, 176], which is a non-perturbative method. The main idea of this method is to discretize the fermionic bath band logarithmically. By a unitary transformation the Hamiltonian can be mapped onto a semi-infinite linear chain, which then can be diagonalized iteratively. The solution of the impurity models yields the fermionic Green's function $G_{\mathrm{imp}}(\omega,\epsilon)$ and the superfluid order parameter $\Psi(\epsilon)$ [272].

The ensemble of impurity models is supplemented by the self-consistency conditions

$$-\operatorname{Im}(\Gamma(\omega)) = \pi t_f^2 \langle \rho_{\mathrm{imp}}(\omega) \rangle_{\mathrm{geo}} \, , \tag{9.12}$$

$$\Psi_{\mathrm{typ}} = \langle \Psi \rangle_{\mathrm{geo}} \tag{9.13}$$

---

[1]U. Bissbort, unpublished.

for the Bethe lattice, where the necessary Hilbert transform equation (4.9) simplifies considerably [123]. In the homogeneous system the self-consistency conditions reduce to $\Psi = \langle \text{gs}|b|\text{gs}\rangle$ and $\text{Im}\Gamma(\omega) = -\pi t_f^2 \rho(\omega)$.

The fermionic states on the impurity are coupled to a non-interacting fermionic bath via the hybridization function $\Gamma(\omega)$, whereas the bosonic states are coupled to a bosonic bath via the geometric disorder average of the superfluid order parameter $\langle\Psi\rangle_{\text{geo}}$. This situation is illustrated in figure 9.1. In the homogeneous system the calculation scheme is exact in infinite dimensions under suitable scaling of the hopping amplitudes [272] and known to be a good approximation in three dimensions. Moreover, it captures the physics over the whole range of interaction strength, from weak to strong interactions, as the local correlations are calculated without approximations.
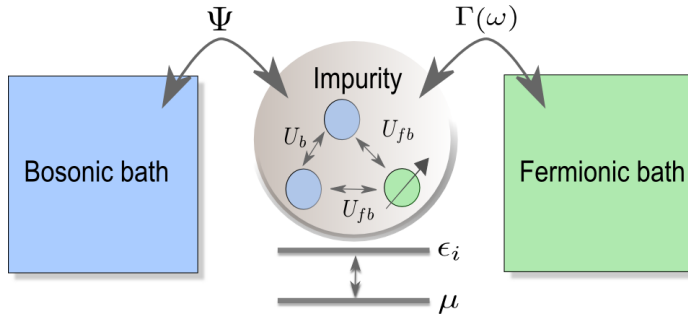


**Figure 9.1.:** Illustration of the impurity problem that is solved for several on-site energies $\epsilon_i$ with the help of the Numerical Renormalization group. The impurity is coupled to a bosonic bath via the geometric average of the superfluid order parameter $\langle\Psi\rangle_{\text{geo}}$ and to a fermionic bath via the hybridization function $\Gamma(\omega)$.

The presentation of the obtained results is divided into four sections. In section 9.3 we begin with results for the homogeneous system of bosons and spin-polarized fermions which are complementary to the results of references [272, 273]. We also investigate the system when the fermions are in the atomic limit to gain a better understanding of the fermionic excitation spectrum (section 9.4). The uniformly disordered system of bosons and spin-polarized fermions is addressed subsequently in section 9.5. Finally, mixtures of two-component fermions and bosons in disordered optical lattices are studied in section 9.6.

In general, we observe the following bosonic phases: (i) the superfluid phase (SF), which is compressible, defined by a non-zero geometric average of the bosonic superfluid order parameter $\langle\Psi\rangle_{\text{geo}}$. (ii) The bosonic Mott insulator (BMI), which is incompressible and $\langle\Psi\rangle_{\text{geo}}$ equal to zero. (iii) The alternating

Mott insulator (AMI), which is also incompressible and has a zero superfluid order parameter, but is characterized by a charge density wave within the two sublattices of the investigated bipartite lattice. (iv) The Bose glass phase (BG), which is also characterized by a zero bosonic superfluid order parameter, but which is compressible in contrast to the Mott insulator. Finally, (v) we observe a supersolid phase (SS), defined by a non-zero bosonic superfluid order parameter and a charge density wave.

As fermionic phases we obtain the following phases: (i) The Fermi liquid (FL) and disordered Fermi liquid (DFL) which were already discussed extensively. (ii) The charge density wave (CDW), which is incompressible, i.e. the fermionic spectral function shows an excitation gap and has alternating spectral weight on the two sublattices of the bipartite lattice. In our calculations we did not find the fermionic Anderson insulator due to the investigated parameter regime. The same is true for the fermionic Mott insulator in section 9.6.

In all calculations presented in the following, the fermionic system will be half-filled, that is $\nu_f \equiv \frac{1}{N} \sum_i \langle n_i^f \rangle = 0.5$ for spin-polarized fermions. In this chapter, we work in units of half of the bandwidth of the non-interacting fermionic spectral function of the homogeneous system $D = \frac{1}{2} W_0 = 1.0$.

This work was done in collaboration with Irakli Titvinidze, who in particular provided the numerical renormalization group routine.

## 9.3. Mixtures of spin-polarized fermions and bosons: homogeneous system

In previous studies, the bosonic filling was equal to 1/2 [273] and 3/2 [272] respectively. Here, we present the results of complementary calculations for fixed bosonic chemical potential, which later are used as starting point of the investigation of disorder effects.

In figure 9.2 the obtained ground state phase diagram in the $\mu_b$-$zt_b$-plane is shown, where the bosonic interaction strength $U_b = 5.0$, and the interspecies interaction strength $U_{fb} = 2.5$. We note that bosonic Mott insulator phases and alternating Mott insulator phases occur in turns while increasing the chemical potential, i.e. pushing more bosons into the systems for small bosonic hopping amplitude. The direct transition between the alternating Mott insulator and the bosonic Mott insulator for small bosonic hopping amplitudes is an artifact of the limited resolution of our calculation. To be more precise, we consider a transect in the phase diagram for small bosonic hopping, e.g. $zt_b = 0.05$. Increasing the bosonic chemical potential to a value bigger than 0.25 the alternating Mott insulator phase with filling $\nu_b \equiv \frac{1}{N} \sum_i \langle n_i^b \rangle = 0.5$ is found, which means that

**Figure 9.2.:** Ground state phase diagram of spin-polarized Fermions and Bosons mixture in the $\mu_b$-$t_b$-plane. Parameters are $U_{fb} = 2.5$, $U_b = 5.0$ and $\nu_f = 0.5$.

on one sublattice of the bipartite lattice the expectation value of the bosonic number operator $\langle n_b \rangle$ is equal to 0, whereas on the other sublattice it is equal to 1. Further increase of the bosonic chemical potential leads subsequently to the bosonic Mott insulator with filling $\nu_b = 1$, where we found the expectation value $\langle n_b \rangle = 1$ on both sublattices, followed by the alternating Mott insulator ($\nu_b = 3/2$) and finally the bosonic Mott insulator ($\nu_b = 2$).

At the same time the fermionic spectral function $\rho(\omega)$ changes dramatically: For all bosonic Mott insulating phases with integer filling we find a particle-hole symmetric Fermi liquid phase, characterized by a finite density of states at the Fermi level, whereas for all bosonic alternating Mott insulators the spectral function is gaped. In other words a metal-insulator transition in the fermionic spectrum is recurrently triggered by the increasing bosonic chemical potential.

In figure 9.3 several characteristic fermionic spectral functions are shown for a fixed interspecies interaction strength. In panel (a) the spectral functions of both sublattices are plotted for the bosonic chemical potential $\mu_b = 1.0$, which corresponds to a fermionic charge density wave that coincides with a bosonic alternating Mott insulator. For $\mu_b = 3.5$ a particle-hole symmetric fermionic spectral function is obtained, that always occurs together with the bosonic Mott insulator. Finally, panels (c) and (d) correspond to fermionic spectral functions that are given when the bosonic system is in the superfluid phase. We note a characteristic three-peak structure with two incoherent single-particle
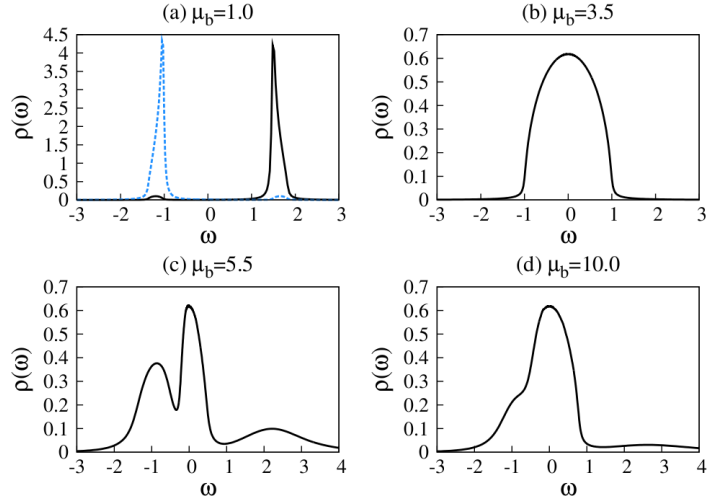
**Figure 9.3.:** Fermionic spectral function $\rho(\omega)$ for several bosonic chemical potentials $\mu_b$: (a) $\mu_b = 1.0$ (b) $\mu_b = 3.5$ (c) $\mu_b = 5.5$ and (d) $\mu_b = 10.0$ and fixed bosonic hopping amplitude $zt_b = 0.3$. In panel (a) the spectral functions for sublattice A and B are plotted. Parameters are $U_{fb} = 2.5$, $U_b = 5.0$, and $\nu_f = 0.5$.

excitations in the fermionic spectrum.

To understand the properties of the fermionic single-particle excitation spectrum, the development of the fermionic spectral function is investigated for $U_b = 5.0$ and $\mu_b = 5.5$ in two cases in figure 9.4: in panel (a) the bosonic hopping is fixed to $zt_b = 0.4$ while the interspecies interaction strength $U_{fb}$ is increased stepwise from 1.0 to 4.0, whereas in (b) the interspecies interaction strength $U_{fb}$ is fixed, while the bosonic hopping is increased. With increasing $U_{fb}$ the incoherent excitation peak at positive energy is shifted from the Fermi level and its maximum position is dislodged approximately by the value of $U_{fb}$.

Due to the relatively high bosonic interaction strength $U_b$ the bosonic system tries to minimize its energy by avoiding as many multiple bosons on-site occupations as possible. Therefore, in a simple picture the system will exhibit a localized uniform distributions of bosons with integer filling. The remaining bosons can be thought of being mobile giving rise to the fermionic excitation peak at positive frequency, when interacting with a fermion on a site. Increasing repulsive interspecies interaction strength $U_{fb}$ leads to an effectively smaller filling of the bosonic subsystem. Hence, the positive excitation peak loses spectral weight. Furthermore, we note that the peak position of the negative energy excitation gap is not affected by increasing interspecies interaction

**Figure 9.4.:** Fermionic spectral function $\rho(\omega)$ (a) for several interspecies interaction strengths $U_{fb}$ and fixed bosonic hopping $zt_b = 0.4$ and (b) for several bosonic hopping parameters $t_b$ and fixed interspecies interaction strength $U_f b$. Parameters are $\mu_b = 5.5$, $U_b = 5.0$, and $\nu_f = 0.5$.

strength, but shifts to lower values with increasing bosonic hopping amplitude. We will gain a more detailed understanding of the excitation spectrum and in particular of its origin, in the next section, where spin-polarized fermions in the atomic limit are considered.

## 9.4. Mixtures of bosons and spin-polarized fermions: fermionic atomic limit

In order to gain further insight into the physics of the homogeneous system we have performed self-consistent Gutzwiller calculations for the system, where the fermions are in the atomic limit, i.e. $t_f = 0$. In this subsection we introduce the energy $\tau = 1.0$ as an energy unit to allow for an easy comparison with the results of the full DMFT calculations of the previous section.

We incorporate the Gutzwiller approximation (9.6) and are therefore left with a local Hamiltonian

$$H_{\text{atom}} = -\mu_f n_f - \mu_b n_b - zt_b \Psi^* b - zt_b \Psi b^\dagger + \frac{U_b}{2} n_b(n_b - 1) + U_{fb} n_f n_b .$$

(9.14)

Diagonalizing the Hamiltonian given in the Fock space basis spanned by the
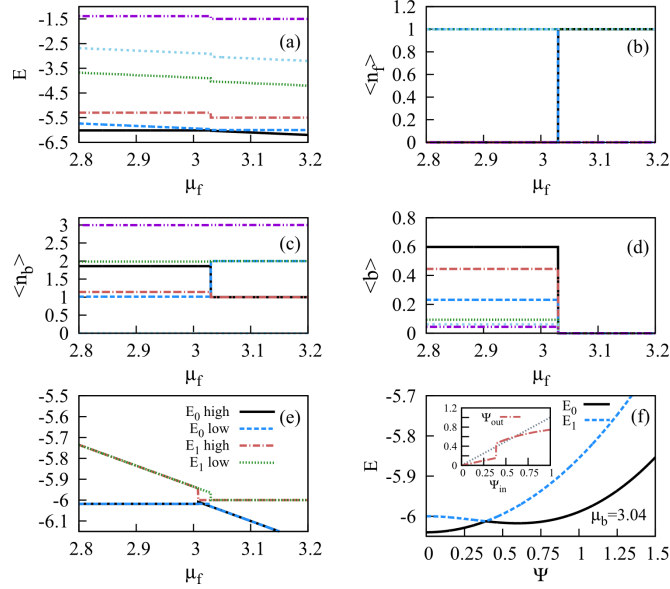
**Figure 9.5.:** Results of a Gutzwiller mean-field calculation of a mixture of bosons and spin-polarized fermions in the fermionic atomic limit as a function of the fermionic chemical potential $\mu_f$. In panel (a) the six energetically lowest eigenenergies are plotted, the ground state is given by the black solid line. The to the Eigenstates corresponding expectation values of the occupation numbers $n_f$, $n_b$ and the bosonic annihilation operator $b$ are given in panels (b-d). In panel (e) the eigenenergies of the ground state and the first excited state are plotted for a low and a high initial superfluid order parameter $\Psi$. Panel (f) displays the eigenenergies of the Hamiltonian as a function of $\Psi$ and in the inset the resulting superfluid order parameter is plotted. Parameters are $U_{fb} = 2.5$, $U_b = 5.0$, $\mu_b = 5.5$ and $zt_b = 0.3$.

Fock states $|n,m\rangle$ with $n$ fermions and $m$ bosons yields the eigenstates and the eigenenergies. The necessary cutoff in the bosonic number was placed to be high enough to have no influence on the results. After determining the ground state, the superfluid order parameter $\Psi$ can be calculated and a self-consistent calculation cycle is closed by demanding $\Psi = \langle gs|b|gs\rangle$.

In figure 9.5 the six lowest eigenenergies are displayed in panel (a) as a function of $\mu_f$ for $U_{fb} = 2.5$, $U_b = 5.0$, $\mu_b = 5.5$ and $zt_b = 0.3$. The panels (b), (c) and (d) display the corresponding expectation values of the fermionic number operator, the bosonic number operator and the bosonic annihilation parameter, respectively. For low fermionic chemical potentials the ground state is given by a fermionic filling exactly equal to zero, i.e. $|0\rangle = \sum_m b_m|0,m\rangle$. Increasing

the fermionic chemical potential leads to a degeneracy point of the ground state and the first excited state which in turn is given as $|1\rangle = \sum_m a_m |1,m\rangle$. At this point the fermionic density exhibits a step from one to zero and after the degeneracy point the fermionic filling of the ground state is equal to one. We note that in order to fix the fermionic filling $\nu_f = 0.5$ the system must be exactly at the degeneracy point in the fermionic atomic limit and the ground state of the system will be given by the superposition

$$|\text{gs}\rangle = \frac{1}{\sqrt{2}}\left(|0\rangle_f |\psi_0\rangle_b + |1\rangle_f |\psi_1\rangle_b\right), \tag{9.15}$$

with $|\psi_0\rangle_b$ and $|\psi_1\rangle_b$ being the associated states of the bosonic subsystem.

It is interesting to note that the physics of the bosonic system differs drastically at both sides of the degeneracy point. In the absence of fermions the bosonic system behaves as a superfluid (i.e. $|\psi_0\rangle_b$ is a coherent superposition of bosonic Fock states), whereas as soon as one fermion enters the system the bosonic subsystem experiences a phase transition to a Mott insulator (i.e. $|\psi_0\rangle_b = |n_b = 1\rangle_b$, cf. panels (c) and (d)). This fact is attributed to the parameter choice and depends in particular on the ratio of $U_{fb}/U_b$. Our calculations show that an increasing ratio leads to a system where on both sides of the degeneracy point the bosonic system is in the superfluid state.

Furthermore, we observe a small kink in the eigenenergies when the fermionic chemical potential arrives at the value of the degeneracy point. To elucidate this further we compare the resulting two lowest eigenenergies of two calculations in panel (e). One is performed with a relatively high initial value of the superfluid order parameter $\Psi$ in the self-consistent cycle and the second is performed with a relatively small superfluid order parameter. The figure shows that a region exists around the degeneracy point, where metastable solutions are present. To substantiate this result, we plot the ground state energy and the energy of the first excited state as a function of the superfluid order parameter $\Psi$ in panel (f) for $\mu_f = 3.04$. Two minima are observed, one at $\Psi = 0$, that is global and corresponds to a bosonic Mott insulator and one at finite $\Psi$, that is local and corresponds to a superfluid. The inset shows the corresponding superfluid order parameter as function of the input superfluid order parameter. The two fix points are clearly visible.

We have calculated the fermionic single-particle Green's function in the atomic limit

$$G(\omega) = \sum_{|k\rangle} \left(\frac{|\langle k|c^\dagger|\text{gs}\rangle|^2}{\omega + E_k - E_0 + i\eta} + \frac{|\langle k|c|\text{gs}\rangle|^2}{\omega - (E_k - E_0) + i\eta}\right), \tag{9.16}$$
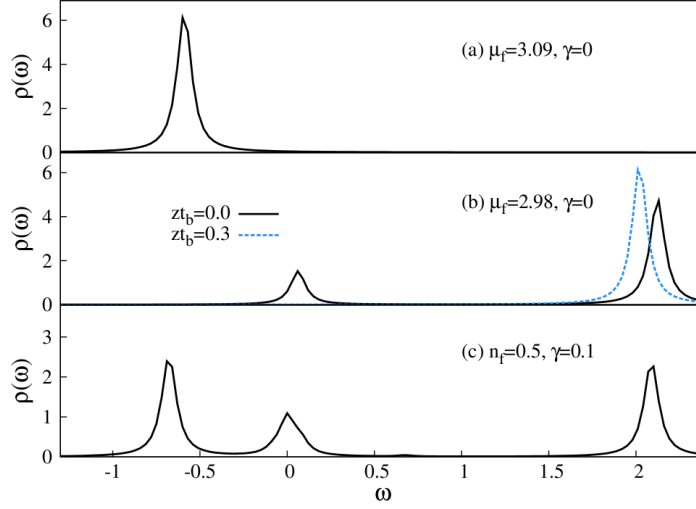
**Figure 9.6.:** Fermionic spectral functions in the fermionic atomic limit for (a) a chemical potential $\mu_f = 3.09$ slightly after the degeneracy point of the ground state and the first excited state, for (b) a chemical potential $\mu_f = 2.98$ slightly before and (c) at the degeneracy point for fermionic density $n_f = 0.5$, where a small coupling $\gamma = 0.1$ between the Fock states $|n_f = 0\rangle$ and $|n_f = 1\rangle$ has been introduced. The blue dashed line in panel (b) shows the corresponding spectral function, when also the bosons are in the atomic limit. Parameters are $U_{fb} = 2.5$, $U_b = 5.0$, $\mu_b = 5.5$ and $zt_b = 0.3$. For all spectra a broadening $\eta = 0.05$ has been used.

where $|k\rangle$ corresponds to the $k$th eigenstate with eigenenergy $E_k$.

Panel (a) of figure 9.6 shows the excitation spectrum for a fermionic chemical potential $\mu_f = 3.09$ slightly greater than that at the degeneracy point. Since the fermionic filling is equal to one, only hole excitations are possible. We note one incoherent peak stemming from the overlap to the eigenstate $|0,1\rangle$, where the fermion is removed. The particle excitation spectra is shown for a fermionic chemical potential $\mu_f = 2.98$ at the other side of the degeneracy point in panel (b). In this case the ground state is a bosonic coherent superposition of states $\sim |n_f = 0,n_b >$ as can be seen from figure 9.5. We note two excitation peaks: an incoherent peak and a nearly coherent peak. The incoherent peak has its origin in the overlap of adding a fermion to the ground state and eigenstate $|3\rangle \sim |1,2\rangle$. The coherent excitation is created by adding a fermion and at the same time effectively removing a boson from the ground state. The corresponding overlap is given to the first excited state. This is an analogous excitation to the well-known Kondo resonance in two-component fermion systems, where a fermion with spin $\sigma$ is exchanged by a fermion with opposite spin $\bar{\sigma}$.

The blue dashed line in panel (b) corresponds to the fermionic spectral function of the double atomic limit, i.e. with the additional constraint $t_b = 0$. The nearly coherent excitation peak is absent, which confirms the necessity for its existence of a ground state being a coherent superposition of bosonic number states. This is a remarkable feature, since the coherent fermionic excitation originates from the interaction with a bosonic coherent superfluid state. In conclusion, the characteristic fermionic three-peak excitation spectrum of the lattice system can be traced back to excitations already present in the fermionic atomic limit.

Neither the hole excitation nor the particle excitation spectrum are sufficient on their own to explain the excitation spectrum of the lattice system for fixed fermionic filling $\nu_f = 0.5$. For that purpose we introduce a small coupling $\gamma = 0.1$ between the Fock states $|0,m\rangle$ and $|1,m\rangle$, corresponding to an additional term $\gamma(c + c^\dagger)$ in the Hamiltonian (9.14). This effectively smooths the step behavior of the bosonic and fermionic filling as a function of $\mu_f$, which allows for the adjusting of the fermionic filling $\nu_f$ to 0.5. The corresponding single-particle spectrum is plotted in panel (c). We note the existence of all three described peaks. However, since the ground state as well as the first excited state are coherent superpositions of Fock states $|n_f = 0,m>$ and $|n_f = 1,m>$ in this case, the coherent peak has a more complex origin. It consists of the processes as described above and their opposite, i.e. removing a fermion and effectively adding a boson, as well as coherent processes originating to the significant overlap with themselves when a fermion is removed or added.

## 9.5. Mixtures of spin-polarized fermions and bosons: weakly disordered system

In this section we study how the disorder potential modifies the physics of the homogeneous system discussed in the two previous sections.

In figure 9.7 the homogeneous, i.e. $\Delta = 0$, fermionic spectral functions at bosonic hopping $zt_b = 0.4$ and four different bosonic chemical potentials are compared to the fermionic spectral functions at two finite disorder strengths $\Delta = 0.5$ and $\Delta = 1.0$. At $\mu_b = 1.5$ we know that for zero disorder the system is given by a bosonic alternating Mott insulator and a fermionic charge density wave (cf. panel (a)). By increasing the disorder strength the fermionic spectrum broadens, but the charge density waves remain stable for small disorder strength. By increasing the bosonic chemical potential to $\mu_b = 3.5$ (cf. panel(b)) a bosonic Mott insulator in combination with a disordered Fermi liquid is obtained. The fermionic spectrum decreases and becomes broadened with increasing disorder
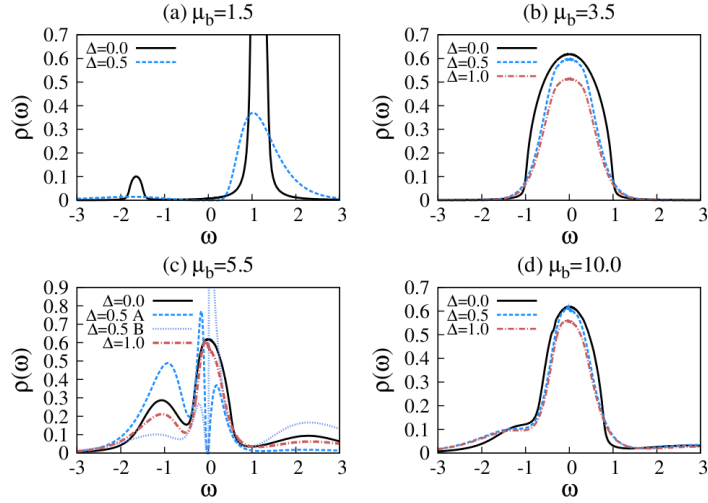
**Figure 9.7.:** Fermionic spectral function $\rho(\omega)$ for several bosonic chemical potentials $\mu_b$: (a) $\mu_b = 1.5$ (b) $\mu_b = 3.5$ (c) $\mu_b = 7.0$ and (d) $\mu_b = 10.0$ and fixed bosonic hopping amplitude $zt_b = 0.4$. The development of the fermionic spectral function is displayed for three different disorder strengths: The solid black lines corresponds to the homogeneous case $\Delta = 0.0$, the blue dotted line corresponds to $\Delta = 0.5$ and the red dashed-dotted line to disorder strength $\Delta = 1.0$. Parameters are $U_{fb} = 2.5$, $U_b = 5.0$, and $\nu_f = 0.5$.

strength, which corresponds to insetting localization effects in TMT [62, 82]. Similar behavior is obtained for the Fermi liquid and superfluid phase at $\mu_b = 10.0$ in panel (d). However, a dramatic change of the fermionic spectral function triggered by the disorder is obtained for $\mu_b = 5.5$. The Fermi liquid spectrum of the homogeneous case develops a gap at small disorder strengths, e.g. $\Delta = 0.5$. With further increase of the disorder strength the gap is lost again. In other words a fermionic metal insulator transition is induced by weak disorder.

To elucidate this phenomenon further, the bosonic density $\langle n_b \rangle$, the fermionic density $\langle n_f \rangle$ and the superfluid order parameter $\langle \Psi \rangle_{\text{geo}}$ are plotted for the two sublattices of the bipartite lattice for bosonic hopping amplitude $zt_b = 0.4$ and disorder strength $\Delta = 0.5$ in figure 9.8 as a function of the bosonic chemical potential. Various phases are arising subsequently accounting for the rich physics of the system. For small chemical potentials a charge density wave can be clearly identified for both subsystems. The underlying bosonic phase is either a supersolid or an alternating Mott insulator, depending on whether the superfluid order parameter $\langle \Psi \rangle_{\text{geo}}$ is finite or zero, respectively. By increasing the
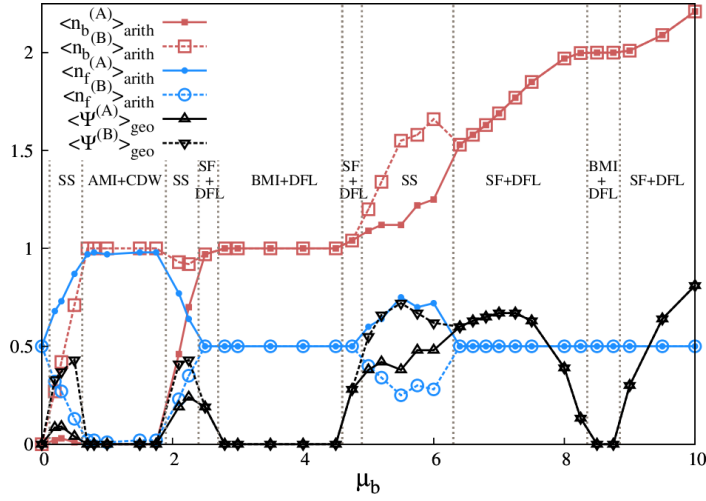
**Figure 9.8.:** Evolution of the fermionic density $\langle n_f \rangle$, the bosonic density $\langle n_b \rangle$ and the superfluid order parameter $\langle \Psi \rangle_{geo}$ on the sublattices A (solid) and B (dashed) of the bipartite lattice with increasing bosonic chemical potential $\mu_b$. Parameters are $U_{fb} = 2.5$, $U_b = 5.0$, $zt_b = 0.4$, $\Delta = 0.5$ and $\nu_f = 0.5$.

bosonic chemical potential the charge density wave dies away and a tiny bosonic superfluid and disordered Fermi liquid region is entered, followed by a bosonic Mott insulator combined with a disordered Fermi liquid. Around $\mu_b \sim 4.7$ density waves are induced again in both subsystems. However, in contrast to the charge density waves for smaller chemical potentials, the occurring supersolid is not intercepted by a bosonic alternating Mott insulator, but is extended over a relatively large set of values for the chemical potential.

It is interesting to note that this behavior differs strongly from the physics found for the homogeneous case as discussed in the preceding section. The disorder-induced supersolid is relatively robust towards fluctuations of the bosonic filling. Experiments within a optical lattice setup are almost always realized in presence of a harmonic trap, resulting for example in the famous wedding cake structure [115] within the Mott insulating regime. Theoretically, this can be accounted for by a local density approximation, with a radially decreasing local chemical potential. From our finding that small disorder induces a supersolid which is extended over a large interval of bosonic chemical potentials we conclude that the observation of a supersolid in Bose-Fermi mixtures might be favored by the presence of weak disorder.

The results of our investigation of mixtures of spin-polarized fermions and bosons in the presence of weak disorder are summed up in the ground state
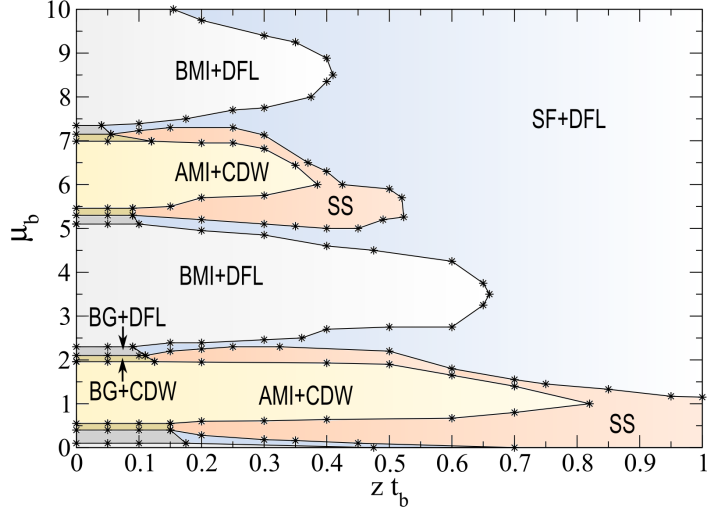
**Figure 9.9.:** Ground state phase diagram of spin-polarized fermions and bosons mixture in the $\mu_b$-$t_b$-plane at weak disorder strength $\Delta = 0.5$. Parameters are $U_{fb} = 2.5$, $U_b = 5.0$ and $\nu_f = 0.5$.

phase diagram in the $\mu_b$-$zt_b$ plane for disorder strength $\Delta = 0.5$, which is displayed in figure 9.9. Checking the phase diagram for weak disorder to the homogeneous phase diagram in figure 9.2 we note that the overall structure is reproduced as the disorder energy scale is small compared to the other energy scales of the system. However, a major difference is given by the the largely extended supersolid region in presence of weak disorder. We note that the disorder phase is not extended symmetrically on both sides of the half-filled case.

In panel (a) of figure 9.10 we consider a different slit in the phase diagram for fixed bosonic chemical potential $\mu_b = 5.5$. For small hopping amplitudes the alternating Mott insulator combined with a fermionic charge density wave is obtained. Increasing the hopping amplitude induces a transition to a supersolid phase which can be clearly seen by the finite superfluid order parameter $\langle \Psi \rangle_{\text{geo}}$, while the charge density wave is still present in the system. This is recognizable from the charge density wave order parameters $\Delta n_f \equiv |\langle n_f^{(A)} \rangle - \langle n_f^{(B)} \rangle|$ and $\Delta n_b \equiv |\langle n_b^{(A)} \rangle - \langle n_b^{(B)} \rangle|$. Upon further increase of the bosonic hopping amplitude the charge density wave dies away and a bosonic superfluid combined with a disordered Fermi liquid is obtained. We also note the extension of the supersolid phase over a large interval of bosonic hopping amplitudes, which suggest that the disorder-induced supersolid is present for a big set of field strengths of the

optical lattice.
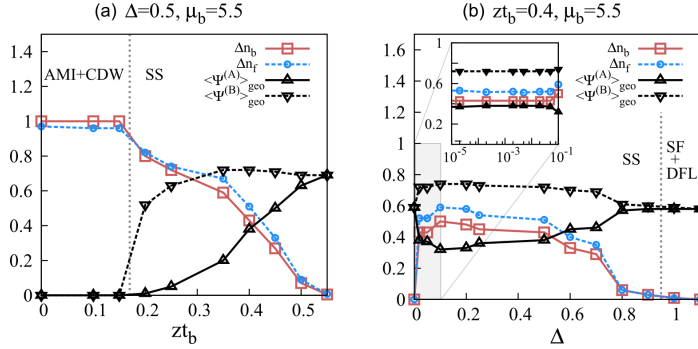


**Figure 9.10.:** Evolution of the fermionic and bosonic charge density wave order parameter $(\Delta n_f, \Delta n_b)$ and and the superfluid order parameter $\langle \Psi \rangle_{geo}$ on the sublattices A (solid) and B (dashed) of the bipartite lattice with (a) increasing bosonic hopping $t_b$ for $\Delta = 0.5$ and increasing disorder strength $\Delta$ for $zt_b = 0.4$. Parameters are $U_{fb} = 2.5$, $U_b = 5.0$ and $\nu_f = 0.5$.

In panel (b) we plotted the the superfluid order parameter and the charge density order parameter as a function of the disorder strength for $zt_b = 0.4$ and $\mu_b = 5.5$. The inset shows the data on a logarithmic scale for very weak disorder strengths. We note that the supersolid order arises already for very weak disorder strengths and remains stable until intermediate disorder destroys the long-range order. We conclude that the disorder-induced supersolid is obtained by a first order transition already at very weak disorder strengths triggered by metastable states, which are at least present in the fermionic atomic limit. It is reasonable that a breaking of the translational invariance as given by a finite disorder benefits the occurring of the supersolid phase which is characterized by two broken symmetries: the $U(1)$-symmetry and the translational symmetry.

Furthermore, we obtained strong evidence that the reiteratively occurring bosonic Mott insulator and alternating Mott insulator lobes are separated by two different Bose glass phases at small bosonic hopping amplitudes. Both bosonic glasses exhibit a superfluid order parameter equal to zero, and are compressible, but one is also characterized by a charge density wave, while the other does not exhibit long-range order. However, a clear proof of the existence and a more detailed study of these phases necessitate a higher resolution than numerical feasible within the here employed TMT. In particular, methods that give access to the full PDF of the superfluid order parameter might give an insight into the physics of these phases.

## 9.6. Disordered mixtures of two-component fermions and bosons

Finally, we will consider mixtures of two-component fermions and bosons in an optical lattice with diagonal disorder. Now the disordered Bose-Fermi Hubbard Hamiltonian is given by

$$H = H_{bf} + H_{\text{dis}}^{\text{corr}} \tag{9.17}$$

consisting of two parts, the Bose-Fermi Hubbard Hamiltonian [8, 54]

$$
\begin{aligned}
H_{bf} &= -t_f \sum_{<i,j>,\sigma} c_{i\sigma}^{\dagger} c_{j\sigma} - t_b \sum_{<i,j>} b_i^{\dagger} b_j - \mu_f \sum_{i\sigma} c_{i\sigma}^{\dagger} c_{i\sigma} - \mu_b \sum_i b_i^{\dagger} b_i \\
&\quad + \frac{U_b}{2} \sum_i n_i^b (n_i^b - 1) + U_f \sum_i n_{i\uparrow}^f n_{i\downarrow}^f + U_{fb} \sum_{i\sigma} n_i^b n_{i\sigma}^f
\end{aligned} \tag{9.18}
$$

and the correlated diagonal disorder part

$$H_{\text{dis}}^{\text{corr}} = \sum_i \epsilon_i (c_i^{\dagger} c_i + \alpha_i b_i^{\dagger} b_i) \ . \tag{9.19}$$

The fermionic on-site interaction strength is denoted by $U_f$. As for the spin-polarized fermions, we study the half-filled fermionic system, i.e. $\nu_f \equiv \frac{1}{N} \sum_{i\sigma} \langle n_{i\sigma}^f \rangle = 1.0$. Furthermore, the fermionic interaction strength $U_f$ as well as the bosonic interaction strength $U_b$ are fixed to 1.0. In our calculations neither the fermionic Anderson insulator nor the fermionic Mott insulator were observed due to the investigated parameter regime.

In figure 9.11 the bosonic ground state phase diagrams in the $\mu_b$-$zt_b$-plane are shown for fixed Bose-Fermi interaction strength $U_{fb} = 0.5$ and several disorder strengths $\Delta$. In subplot (a) the disorder strength amounts to 0.25 and is increased to 0.5 in subplot (b) and 1.0 in subplot (c). For zero disorder strength the phase diagram consists of bosonic Mott insulator and superfluid phase only. For finite disorder strength the Bose glass phase appears between the different Mott lobes for small bosonic hopping $t_b$. With increasing disorder strength the Bose glass phase grows and finally for $\Delta = 1.0$ no bosonic Mott insulating phase is left and the phase diagram is constituted by the Bose glass phase and for larger hopping amplitudes $t_b$ the superfluid phase only. For a more detailed comparison the superfluid-insulator transition lines are summarized in the lower right subplot of figure 9.11. Here, the growing of the Bose glass phase becomes especially apparent, by the modification of the metal-insulator transition line near $\mu_b \sim 0.5$ and $\mu_b \sim 1.5$.
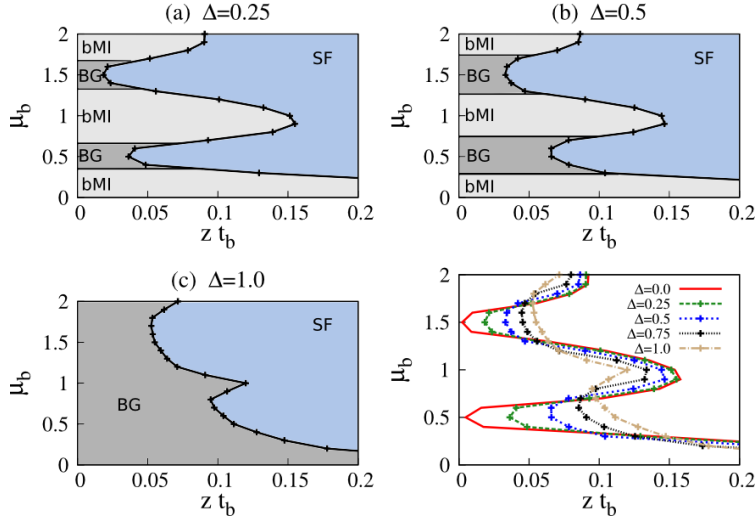
**Figure 9.11.:** Bosonic phase diagrams in the $\mu_b$-$t_b$-plane for fixed interspecies interaction strength $U_{fb} = 0.5$ and several disorder strengths $\Delta$: (a) $\Delta = 0.25$, (b) $\Delta = 0.5$, (c) $\Delta = 1.0$. In the lower right subplot the superfluid-insulator transition lines are summarized for $\Delta = 0.0, 0.25, 0.5, 0.75, 1.0$. Parameters are $\nu_f = 1.0$, $U_f = 1.0$ and $U_b = 1.0$.

At the same time when the Bose glass phase is growing we also note a drastic shrinking of the Mott lobes: with increasing disorder strength the transition from the bosonic Mott insulator to the superfluid phase takes place a smaller values of $t_b$. We conclude a delocalization tendency with increasing disorder strength from the correlation-induced insulating phase. A similar behavior is found for pure fermionic systems [60], where for intermediate repulsive interaction strengths that result in a fermionic Mott insulator a transition to a metallic phase, the disordered Fermi liquid, is found with increasing disorder strength. Similar results are also established for pure bosonic systems [41].

So far we did not comment on the corresponding fermionic phases. For all investigated parameter regimes the fermions are in the disordered Fermi liquid phase. Corresponding fermionic spectra are given in figure 9.12 for fixed bosonic chemical potential $\mu_b = 0.8$ and bosonic hopping $t_b = 0.004$. In subplot (a) the development of the geometrically averaged fermionic spectral function with increasing disorder strength is displayed for $U_{fb} = 0.5$. The Kondo peak broadens and at the same time the spectral weight within the Hubbard subbands decreases, corresponding to insetting localization effects [62, 82]. Within TMT Anderson localization of fermionic states is characterized by the decline of the geometrically averaged LDOS to zero. Therefore, in the investigated parameter
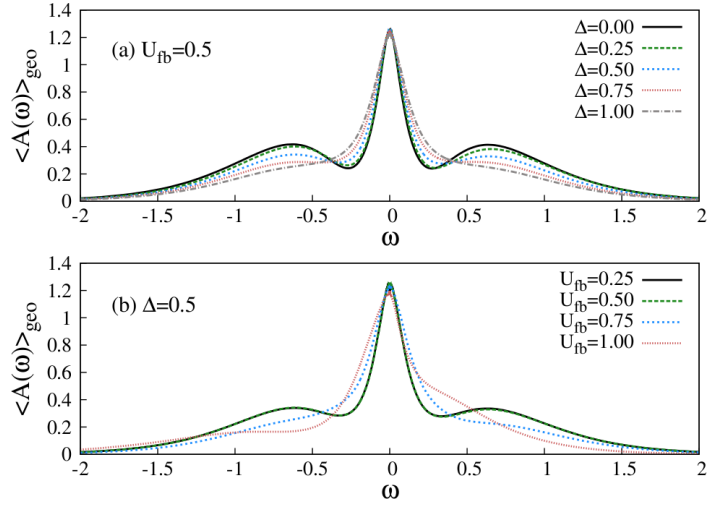
**Figure 9.12.:** Geometric averaged fermionic spectral functions for (a) several disorder strengths ($\Delta = 0.0,0.25,0.5,0.75,1.0$ and $U_{fb} = 0.5$) and (b) several interspecies interaction strengths ($U_{fb} = 0.25,0.5,0.75,1.0$ and $\Delta = 0.5$). Parameters are $\nu_f = 1.0$, $U_f = 1.0$, $U_b = 1.0$, $\mu_b = 0.8$ and $t_b = 0.004$.

regime our fermionic system is far from being Anderson localized. In subplot (b) the disorder strength is fixed to 0.5 and the Bose-Fermi interaction strength $U_{fb}$ is increased from 0.25 to 1.0. Clearly, all spectra correspond to the disordered Fermi liquid phase.

In figure 9.13 the bosonic ground state phase diagrams in the $\mu_b$-$zt_b$-plane are shown for fixed disorder strength $\Delta = 0.5$ and several interspecies interaction strengths $U_{fb}$. In subplot (a) the interspecies interaction strength is zero, i.e. the fermionic and the bosonic system are decoupled. In this case the displayed result stems from a standard Gutzwiller calculation, in which the superfluid order parameter $\Psi$ is averaged geometrically over the disorder. We note a superfluid-insulator transition line, as well as alternatingly occurring regions of the bosonic Mott insulator and the Bose glass phase. It is not our aim to discuss the question, whether a direct transition from the bosonic Mott insulator to the superfluid phase is present in the pure bosonic case or if always a transition to the Bose glass phase lies in between. The direct transition results from the theory we applied. More advanced techniques were applied for the pure bosonic case [40, 41, 227] tackling the mentioned question. By now it is established that there is no direct transition from the bosonic Mott insulator to the superfluid phase, but always intersected by the Bose glass. In subplot (b) the interspecies interaction is added, $U_{fb} = 0.25$, and raised to
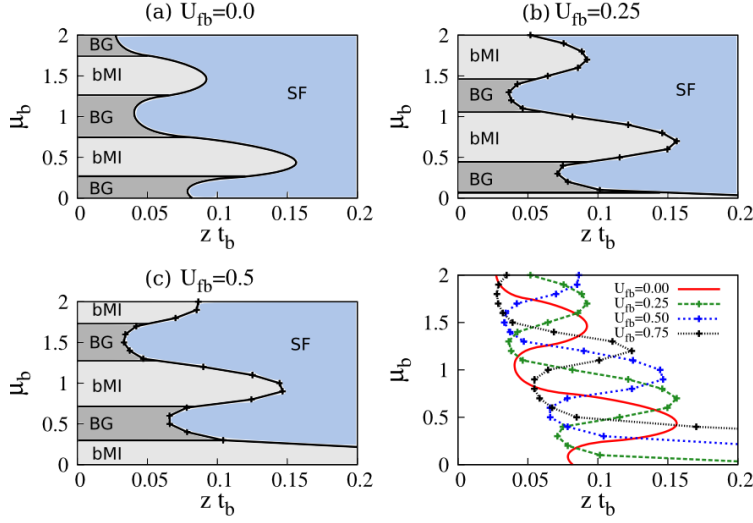
**Figure 9.13.:** Bosonic phase diagrams in the $\mu_b$-$t_b$-plane for fixed disorder strength $\Delta = 0.5$ and several interspecies interaction strengths $U_{fb}$: (a) $U_{fb} = 0.0$, (b) $U_{fb} = 0.25$, (c) $U_{fb} = 0.5$. In case of zero interspecies interaction strength $U_{fb}$ the calculation of the bosonic phase diagram reduces to a Gutzwiller calculation. In the lower right subplot the superfluid-insulator transition lines are summarized for $U_{fb} = 0.0, 0.25, 0.5, 0.75$. Parameters are $\nu_f = 1.0$, $U_f = 1.0$ and $U_b = 1.0$.

$U_{fb} = 0.5$ in subplot (c). For a better comparison of our results, the obtained superfluid-insulator transition lines are summarized in the lower right subplot. A main effect of the interspecies interaction strength is obviously an overall shift of the transition lines. This can be easily explained by a Hartree decoupling of the Bose-Fermi interaction. Moreover, we note that the Mott lobe shrinks with increasing interspecies interaction strength. In other words, if the bosonic hopping amplitude is increased the transition to the superfluid sets in earlier for higher values of the interspecies interaction strength. Similar results were obtained within other theoretical investigations [226], but contrasts the findings of recent experiments [36, 138, 220] without disorder. This discrepancy was recently shown to be a matter of the used parameters and explained by a strong dependence on the bosonic density [276]. Furthermore, the summarized superfluid-insulator transition lines show that also the transition from the Bose glass phase to the superfluid phase sets in earlier.

## 9.7. Conclusion

We have investigated mixtures of bosons and spin-polarized fermions in a homogeneous optical lattice by generalized DMFT, and the influence of weak disorder on this system by means of a TMT. We calculated the ground state phase diagram of the homogeneous system. It consists of lobes of the alternating Mott insulator with a fermionic charge density wave, lobes of the bosonic Mott insulator combined with the Fermi liquid, and a superfluid phase combined with a Fermi liquid. In the latter the fermionic single-particle excitation spectrum exhibits a characteristic three-peak structure, which can be traced back to elementary excitations also present in the fermionic atomic limit. The supersolid turned out to be very sensitive towards fluctuations of the bosonic filling.

The presence of weak disorder induces a supersolid that is comparably stable for a large set of bosonic fillings. Therefore, the observation of a supersolid phase within Bose-Fermi mixtures in optical lattices is favored if weak disorder is added to the system. Intermediate disorder, however, destroys the long-range order.

In future, it might be interesting to develop further impurity solvers for the generalized Anderson impurity problems. Therewith higher energy excitations might be considered in a more accurate extend than this is possible within numerical renormalization group. This might complete the results obtained in this work. Furthermore, fast impurity solvers might pave the way to a statistical Bose-Fermi dynamical mean-field theory of the disordered mixed quantum statistics system in which the full distributions of physical observables are accessible. Such a method would constitute a perfectly suitable method to study the Bose glass phase in more detail.

Finally, mixtures of two-component fermions and bosons have been investigated. The evolution of the bosonic phase diagram has been studied in detail in two cases: On the one hand when the interspecies interaction strength and on the other hand when the disorder strength is varied. Disorder causes the occurrence of the Bose glass phase and a shrinking of the Mott lobe. The interspecies interaction strength induces a delocalization tendency, so that the superfluid phase grows at the expense of the Bose glass phase as well as the Mott insulator.

# 10. Conclusion and outlook

The central subject of investigation in this dissertation is the physics of degenerate quantum gases in disordered optical lattices. As the focus of the thesis lies on strongly correlated fermionic systems, the study of which is notoriously difficult even in the absence of disorder, a powerful numerical method, namely the statistical dynamical mean-field theory [85, 86, 196] has been adapted for this purpose. This method is capable of simultaneously treating disorder as well as local correlations on a non-perturbative level. The most intriguing feature of the statistical dynamical mean-field theory is that it gives access to the full probability distribution function of local observables. Within this approach the Mott insulator and Anderson-Mott transition are described on equal footing, as it is intrinsically constructed in terms of the probability distribution function of the local density of states.

In preparation for the investigation of experimentally relevant disorder types in optical lattices, the statistical dynamical mean-field theory has been applied to fermions with box-type disorder [249], which is the most prominent type of disorder addressed in solid state physics to date. Therein, two localization mechanisms have been identified, one due to correlations and a second due to disorder. The complete paramagnetic ground state phase diagram of the Anderson-Hubbard model has been calculated within statistical dynamical mean-field theory for the first time. Qualitative agreement with the predictions by typical medium theory [5, 60] is found. Within both approaches the Anderson-Mott insulator is found to be continuously connected to the Mott insulator, enclosing a metallic core. Furthermore, this has allowed for the systematic investigation of the probability distributions of the local density of states in explicit form which was implicitly assumed within the construction of typical medium theory. For the non-interacting case, a detailed numerical investigation was recently performed [243] and good agreement with the analytical prediction of a log-normal distribution [197, 198] was found. Here, this finding was confirmed, but in the interacting case it was found that a log-normal distribution does not serve as a suitable approximation.

The main part of this work is dedicated to the investigation of ultracold fermions in disordered optical lattices, where the disorder can be tuned experimentally [25, 199, 239]. These systems have continuously gained significance

with the experimental progress in recent years. The two experimentally most relevant cases have been analyzed: firstly, binary disorder [248] and secondly speckle disorder [250].

The preceding theoretical understanding of strongly interacting systems in binary disordered lattices [59] has been significantly extended by allowing the system to enter the Anderson localized phase. As a main result, the paramagnetic ground state phase diagram was determined and elaborate localization phenomena have been revealed. The presence of Anderson localized states and 'anomalous' localized states [243], as well as the appearance of bound states has been established, not only in the non-interacting [13], but also in the interacting system. Furthermore, a Mott insulator transition has been found to take place at non-integer filling, when fluctuations due to disorder are taken into account. Moreover, these results are of high significance for the solid state community, since binary disordered fermions serve as a constitutive model system for alloys and doped semiconductors. Here, it is of great future interest to investigate the phase diagrams and its dependence on the impurity concentration, as well as to also consider the generalization to finite temperature.

A further central topic of investigation within this thesis was the behavior of interacting speckle disordered fermions. For this purpose a method was constructed, fundamentally relying on the non-separability of the true joint probability distribution functions for the Hubbard model parameters, as was calculated by Zhou and Ceperley [306]. Ultracold bosons in such disordered optical lattices have recently been investigated with great success in experiments [223, 293].

In the fermionic case, the paramagnetic ground state phase diagram has been calculated for the first time within this work. The most striking feature is the strong suppression of the Mott insulator by the unbounded nature of the probability distribution function of the on-site energies. This result is in accordance with similar investigations for bosons in speckle disordered optical lattices [41]. Compared to the phase diagrams for box disorder obtained either by typical medium theory [60] or statistical dynamical mean-field theory [249], a crucial difference arises in the topology of the phase diagram: the Anderson-Mott insulator and the Mott insulator are not continuously connected, but separated by a metallic phase, both at zero and finite temperature. This important qualitative difference limits the direct comparability to Anderson-Hubbard Hamiltonians which commonly appear in the context of solid state physics and where the distribution of the on-site energies is intrinsically bounded.

As statistical DMFT is known to provide an accurate description in high dimensions, further focus was cast on the deviations arising from a lower coordination number. For this purpose, speckle disordered square lattices

162

were investigated by means of the real-space dynamical mean-field theory and the obtained results support the previously found suppression of the Mott insulator. Remarkably, a zero-bias anomaly [10, 95] was observed, which does not appear within the statistical dynamical mean-field theory. A detailed investigation of this physical effect is beyond the scope of this work and should be conducted in greater detail in future to clarify the exact behavior and also addressing the aspect of its experimental observability. The incorporation of the Hubbard parameters with their statistical correlations was achieved within a generalization of the statistical dynamical mean-field theory to include off-diagonal disorder. Moreover, it would be interesting to perform an analysis of the effects arising from pure hopping disorder. It should be verified that the states at the band center are indeed extended for all disorder strengths [261] and how this property is modified in presence of interactions. Concerning the interplay of off-diagonal disorder and interactions, diverging thermodynamic properties have been predicted [83], but so far only on the level of the coherent potential approximation.

In this part of the thesis, we studied mixtures of bosons and fermions by a generalized typical medium theory, where localization effects for fermions are treated within the framework of a geometrically averaged local density of states [82, 82, 87]. The geometrically averaged superfluid order parameter, on the other hand, was determined self-consistently for the bosons. The disordered Bose-Fermi Hamiltonian is thereby mapped onto an ensemble of generalized single-impurity Anderson Hamiltonians, which were solved by means of the numerical renormalization group. The investigation of spin-polarized fermion and boson mixtures lies at the heart of this chapter. The homogeneous ground state phase diagram contains both conventional, as well as alternating Mott insulating lobes in the bosonic chemical potential and hopping parameter plane, surrounded by a superfluid phase. At small values of the bosonic hopping amplitude it was shown that the change of the bosonic chemical potential induces a transition from a Fermi liquid occurring in coexistence with a bosonic Mott insulator to a fermionic charge density wave characterized by an excitation gap occurring together with the alternating Mott insulator. The fermionic spectral function in conjunction with the bosonic superfluid phase exhibits a characteristic three-peak structure and we clarified the origin of these excitations in the fermionic atomic limit. In the presence of weak disorder, the phase diagram is drastically modified: the most prominent feature is the emergence of a supersolid phase, which is robust for a wide range of bosonic hopping amplitudes as well as bosonic chemical potentials. This observation indicates the remarkable fact that the experimental observation of the supersolid phase is favored by the introduction of a small amount of disorder.

Moreover, mixtures of bosons and two-component fermions in disordered optical lattices have been studied with an emphasis on the effects induced by disorder and the fermions on the bosonic subsystem. With an increase of the disorder strength we found that the Bose glass phase grows and the Mott lobe shrinks. Moreover, a delocalization tendency, mediated by the interspecies interaction strength, was found.

Our investigation of Bose-Fermi mixtures opens up a vast number of interesting branches of future research. One of the most prominent is to study the influence of bosons on the various fermionic Anderson-Hubbard model phase diagrams. Furthermore, the investigation of disordered spin-polarized fermion and boson mixtures was given for the weakly disordered case. A complementary investigation of the strongly disordered case is needed to gain further insight into the localization physics of the mixed quantum statistics system. From the theoretical point of view, it is desirable to go beyond the typical medium level by employing a statistical theory that gives access to the probability distribution function of local observables. One way to accomplish this was recently paved by the development of the bosonic dynamical mean-field theory [65, 150] and the subsequent generalization to Bose-Fermi mixtures [61]. A statistical generalization to disordered systems seems to be possible in a fashion along the lines of the in this thesis established fermionic statistical dynamical mean-field theory. However, the numerical effort of such a method is enormous if exact diagonalization is used as a generalized impurity solver, emphasizing the requirement of a fast impurity solver for Bose-Fermi impurity problems. The development of a purely bosonic statistical dynamical mean-field theory is a convenient first step. This theory also allows for a valuable insight into the physics of quantum magnetism in disordered lattices, in analogy to a recent investigation of the fermionic pendant [62].

The results of this thesis demonstrate the unrivaled power of the statistical DMFT allowing for the only detailed investigation of high-dimensional strongly correlated fermions in disordered lattices to date. On the other hand, from a methodical point of view, one of the most appealing features of real-space dynamical mean-field theory is the possibility to easily incorporate any specific lattice structure. Also in the context of optical lattices, this is particularly favorable, as it directly allows for the inclusion of a spatial harmonic trapping potential. However, real-space dynamical mean-field theory is restricted to finite lattices whereas statistical dynamical mean-field theory naturally recovers the physical behavior in the thermodynamic limit. Moreover, further theoretical progress is needed on the question of detecting localization within real-space dynamical mean-field theory in a finite lattice. It needs to be clarified which observables are useful to consider and which system sizes are necessary to

achieve a conclusive finite-size scaling. First studies in that direction were performed recently [211, 243]. As long as these issues are open, statistical dynamical mean-field theory remains the only method of choice for investigating high-dimensional, strongly correlated disordered systems as shown in detail and studied comprehensively in this thesis.

# 11. Zusammenfassung

Seit Anbeginn der Festkörperphysik ist die Frage, warum manche Materialien metallisch sind, andere dagegen isolierend, von zentraler Bedeutung. Eine erste Erklärung wurde durch die Bändertheorie [23, 44] gegeben. Die Elektronen sind dem periodischen Potential der Rumpfatome ausgesetzt, wodurch ein Energiespektrum bestehend aus Bändern erzeugt wird und die Füllung dieser Bänder bestimmt die Leitungseigenschaften des Festkörpers.

In Experimenten wurde festgestellt, dass Übergänge zwischen metallischen und isolierenden Phasen stattfinden, falls externe Parameter wie die Temperatur oder der Druck geändert werden [151, 206]. Die Modellierung und Erklärung dieser sogenannten Metall-Isolator-Übergänge sind zentale Forschungsgegenstände der Festkörperphysik [120, 151, 205]. Metall-Isolator-Übergänge werden wie alle Phasenübergänge in zwei Klassen unterteilt [120]: Zum einen thermodynamische Phasenübergänge [264, 304], die aus der Konkurrenz zwischen Entropie und innerer Energie des Systems resultieren; zum anderen Quantenphasenübergänge [280], die ihren Ursprung in der Konkurrenz verschiedener Beiträge zur inneren Energie des Systems haben. Zwei Quantenphasenübergänge von Metallen zu Isolatoren fanden besondere Beachtung: der Anderson-Übergang aufgrund von Unordnung in Festkörpern [17, 172, 204, 270] und der Mott-Übergang hervorgerufen durch starke Korrelationen innerhalb des Vielteilchensystems [151, 206].

Korrelationsinduzierte Phasenübergängen wurden seit der Beobachtung von Isolatoren, die nicht in Einklang mit der Bändertheorie stehen, zu einem zentralen Forschungsgegenstand [79]. Erste theoretische Untersuchungen kamen zu dem Schluss, dass das isolierende Verhalten auf die Wechselwirkung zwischen den Elektronen zurückzuführen ist [203, 205, 206, 295]. Im Verlauf der weiteren Forschung wurde das berühmte Hubbard-Modell zur Standardmodellierung eingeführt [139, 147, 162], indem Elektronen ausschliesslich am selben Gitterplatz wechselwirken. Trotz dieser fundamentalen Vereinfachung ist das Hubbard-Modell – abgesehen vom eindimensionalen System [186] – bis heute nicht exakt gelöst. Erste starke Näherungen zeigten, dass der Mott-Übergang ein intrinsisches Merkmal des Hubbard-Modells ist [147, 149]. Die Entdeckung der Hochtemperatursupraleitung im Jahre 1986 [31] und die deutlichen Hinweise auf einen rein elektronischen Ursprung dieser, rückten das Hubbard-Modell

abermals in den Fokus der theoretischen Festkörperphysik [21]. Kurz darauf gelangen entscheidende theoretische Fortschritte im Limes hoher Dimensionen [193], die schliesslich zur Entwicklung der dynamischen Molekularfeldtheorie führten [122, 123, 171]. Diese stellt eine nicht-perturbative Beschreibung der lokalen Wechselwirkung dar und ermöglichte erstmals ein nicht-triviales Verständnis des Mott-Übergangs, welches auf lokalen Quantenfluktuationen beruht [55, 57, 121, 236, 305].

Parallel zu dem Forschungszweig der korrelationsinduzierten Phasenübergänge entwickelte sich die Untersuchung von Unordnung, wie Fehlstellen oder Verunreinigungen, in Festkörpern [172, 204, 270] zu einem aktiven Forschungsfeld. Im Jahre 1958 modellierte Anderson die Unordnung durch lokal fluktuierende Potenialenergien in einem *tight-binding-Modell* – das Anderson-Modell – und zeigte, dass eine hinreichend starke Unordnung isolierendes Verhalten hervorruft [17]. Kohärente Streuprozesse führen zu einer räumlichen Lokalisierung der Elektronen und unterdrücken deren Diffusion. Der Zufallscharakter der Unordnung benötigt statistische Methoden zur theoretischen Beschreibung und erschwert exakte Lösungen, wodurch numerische Untersuchungen dieser Einteilchenprobleme unumgänglich sind.

Sowohl Unordnung als auch starke Korrelationen für sich genommen sind noch immer Gegenstand aktueller Forschung. Jedoch erfordert die realistische Beschreibung von Materialien die gleichzeitige Inbetrachtnahme beider Phänomene. Daher ist das gleichzeitige und wechselseitige Wirken beider Phänomene von zentraler Bedeutung innerhalb der modernen Festkörperphysik [32, 174, 182, 196]. Die theoretische Beschreibung solcher Systeme, zum Beispiel durch das Anderson-Hubbard-Modell, ist offenkundig schwierig, da die wichtigsten Phänomene auf intermediären Größenordnungen der Wechselwirkungstärke und Unordnungsstärke stattfinden. Dadurch erlauben störungstheoretische Methoden nur einen geringfügigen Einblick in die Physik dieser Systeme. Erweiterungen der dynamischen Molekularfeldtheorie zur Beschreibung von ungeordneten Systemen sind hierfür besonders geeignet, da die Wechselwirkung nicht-perturbativ beschrieben wird. Solche wurden in Analogie zur *coherent potential approximation* [275, 279] und auf dem Level eines typischen Mediums durchgeführt [5, 58, 60–62, 82]. Letzterer Ansatz erlaubt die Beschreibung von Lokalisierungseffekten, jedoch vernachlässigen beide Methoden räumliche Fluktuationen, die durch die Unordnung hervorgerufen werden. Die Unordnungsphysik wird daher lediglich rudimentär beschrieben. Dobrosavljević und Kotliar entwickelten mit der statistischen dynamischen Molekularfeltheorie eine fundamental stochastische Theorie [85, 86], die es ermöglicht unordnungisinduzierte Fluktuationen einzubeziehen und sowohl die Wechselwirkung als auch die Unordnung nicht-perturbativ zu beschreiben. Jedoch erfordert diese Theo-

168

rie einen erheblichen numerischen Aufwand, was den Mangel an umfassenden Untersuchungen des Anderson-Hubbard-Modells mittels dieser Theorie erklären könnte.

Auf der experimentellen Seite ist die systematische Untersuchung von starkkorrelierten und ungeordneten Festkörpern problematisch, da weder die Stärke der Unordnung noch die Wechselwirkungsstärke wohldefiniert und präzise kontrollierbar sind. Insbesondere ist es nicht möglich ein Phänomen zu isolieren. Dadurch können diese Experimente nur in begrenzten Maßen Aufschluss liefern, inwiefern theoretische Näherungen berechtigt und zutreffend sind. Diesbezüglich sind die in jüngster Vergangenheit entwickelten Experimente mit ultrakalten Atomen in optischen Gittern [45, 183, 202] vielversprechend diese Schwierigkeiten zu beheben und einen entscheidenden Beitrag zum Verständnis dieser Systeme zu gewinnen.

Möglich wurden diese Experimente durch die Erfindung der Laserkühlung von Atomen [24, 71, 225, 298, 299], die es erlaubte quantenentartete Bose-, Fermi- und Bose-Fermi-Gase zu erzeugen [16, 78, 81]. Darüberhinaus ist es möglich solche entarteten Quantengase in optische Gitter zu laden [45, 132, 138, 159, 166, 220, 229], wodurch unter anderem Systeme realisiert werden, die sich zur Quantensimulation von Vielteilchenmodellen eignen [108, 145, 154, 155, 183]. Beispielsweise wird das Bose-Hubbard-Modell sehr präzise realisiert [154] und wurde 2002 erstmals erfolgreich im Experiment simuliert [132]. Die experimentelle Kontrolle über fast alle relevanten Parameter ist charakteristisch für diese Experimente, insbesondere können Parameter, wie die Wechselwirkungsstärke zwischen den Teilchen, präzise und weitestgehend unabhängig von anderen Parametern eingestellt werden. In festkörperrelevanter Hinsicht wurde zudem das fermionische Hubbard-Modell erfolgreich simuliert [166] und der fermionische Mott-Isolator experimentell nachgewiesen [160, 242]. Darüberhinaus ist es gelungen ultrakalte Atome mittels verschiedener Methoden ungeordneten Potentialen auszusetzen [25, 199, 239]. Zum Beispiel werden Speckle-Felder verwendet, die durch die Streuung eines kohärenten Laserstrahls an einer Difussorplatte entstehen und durch den AC-Stark-Effekt ein ungeordnetes Potential für die ultrakalten Atome darstellen [39, 73, 191]. Solche Speckle-Felder wurden zudem erfolgreich mit optischen Gittern kombiniert [223, 293], so dass ungeordnete Gitterpotentiale realisiert werden konnten. Ein weiterer Ansatz besteht in der Überlagerung von zwei Laserstrahlen mit inkommensurabler Frequenz, wodurch ein quasiperiodisches Potential erzeugt wird, dessen Physik weitreichende Analogien zu ungeordneten Systemen zulässt [76, 101, 235]. Mittels beider Methoden wurde die Lokalisierung von Materiewellen jüngst nachgewiesen [39, 233]. Eine weitere Herangehensweise ermöglicht prinzipiell die Realisierung einer binären Unordnung. Darin werden zwei Arten Atome in das optische Gitter geladen

und die Mobilität einer Sorte wird derart unterdrückt, dass die Atome auf der relevanten Zeitskala praktisch eine stationäre Verteilung im Gitter annehmen. Die Wechselwirkung zwischen den beiden Atomsorten erzeugt ein binäres Unordnungspotential für die mobile Atomsorte, je nachdem ob an dem entsprechenden Gitterplatz ein immobiles Atom anwesend ist. Erste Experimente in dieser Richtung wurden bereits vollzogen [138, 220].

Zusammenfassend erlauben diese neuen experimentellen Möglichkeiten die Quantensimulation von starkkorellierten, ungeordneten Systemen. Insbesondere ist es möglich, das Anderson-Hubbard-Modell mit bisher unübertroffener experimenteller Kontrolle zu untersuchen. Besonders reizvoll und vielversprechend an diesen Experimenten ist die Möglichkeit, sowohl Unordnungsstärke als auch Wechselwirkungsstärke präzise innerhalb mehrerer Größenordnungen einzustellen. Die theoretische Untersuchung dieser Systeme im Falle hoher Dimensionen ist das zentrale Anliegen der vorliegenden Dissertation. Insbesondere liegt der Fokus dieser Forschungsarbeit auf fermionischen Systemen, zu deren Beschreibung die statistische Molekularfeldtheorie verwendet wird.

Zunächst werden die notwendigen theoretischen Grundlagen gelegt. In Kapitel 2 werden das Hubbard-Modell, Vielteilchen-Greensche Funktionen und die dynamische Molekularfeldtheorie eingeführt. Darauffolgend werden in Kapitel 3 nichtwechselwirkende Teilchen in ungeordneten Gitterpotentialen betrachtet. Ein besonderer Fokus liegt hier auf der Charakterisierung von lokalisierten Zuständen mittels Greenscher Funktionen. Die Ergebnisse werden mittels einer numerischen Methode, der lokalen Verteilungsmethode, verdeutlicht. Die Einführung dieser Methode erleichtert den späteren Zugang zur statistischen Molekularfeldtheorie, da sie den nichtwechselwirkenden Grenzfall der statistischen dynamischen Molekularfeldtheoreie darstellt. Diese wiederum wird in Kapitel 4 detailliert als Untersuchungsmethode starkkorrelierter, ungeordeneter, fermionischer Systeme vorgestellt. Zudem werden die weiteren Erweiterungen der dynamischen Molekularfeldtheorie auf ungeordnete Systeme sowohl auf dem Level der *coherent potential approximation* als auch auf dem Level des typischen Mediums eingeführt. Anschliessend werden in Kapitel 5 ultrakalte Atome in optischen Gittern diskutiert, wobei besonderes Augenmerk auf die Realisierung von ungeordneten Potentialen gelegt wird.

Nachdem alle notwendigen Grundlagen dieser Dissertation erarbeitet sind, wird in Kapitel 6 die statistische dynamische Molekularfeldtheorie umfassend zur Untersuchung der Kastenunordnung, welche die Standardunordnungsverteilung innerhalb der Festkörperphysik darstellt, für das halbgefüllte System angewendet [249]. Es wird gezeigt, dass die statistische dynamische Molekularfeldtheorie sowohl die Beschreibung des Mott-Übergangs im ungeordneten System, als auch die Beschreibung des Anderson-Mott-Überganges ermöglicht. Ins-

besondere werden zwei Delokalisierungsprozesse herausgearbeitet. Zum einen sind umso größere kritische Wechselwirkungsstärken für den Mott-Übergang nötig, je grösser die Unordnungsstärke ist; zum anderen tritt ausgehend vom Anderson-Isolator ein Wiedereintritt in die metallische Phase auf, falls die Wechselwirkungsstärke stetig erhöht wird und die Unordnung nicht zu stark ist. Diese Prozesse führen zu einem Phasendiagramm, welches durch ein weit ausgedehntes, stark-korreliertes Metall charakterisiert ist. Für starke Unordnung findet man einen Anderson-Mott-Isolator, der kontinuierlich mit dem Mott-Isolator für große Wechselwirkungsstärken verbunden ist. Dieses Resultat stimmt qualitativ mit Ergebnissen aus Untersuchungen mittels der Theorie des typischen Mediums überein [5, 60]. Quantitativ ergeben sich allerdings bezüglich der Ausdehnung der metallischen Phase erhebliche Unterschiede, insbesondere ergeben sich innerhalb der Theorie des typischen Medium geringere kritische Unordnungsstärken. Dieser Effekt ist bereits aus Vergleichsrechnungen für den nichtwechselwirkenden Fall bekannt [13].

Der Hauptteil dieser Dissertation widmet sich der Untersuchung zweier spezieller Unordnungsverteilungen die in Experimenten mit ultrakalten, fermionischen Atomen realisiert werden können: In Kapitel 7 wird die binäre Unordnungsverteilung [248] und in Kapitel 8 wird die Speckle-Unordnung [250] untersucht. Im Falle der binären Unordnung wird das bis dato erarbeitete theoretische Bild [59] durch die Beschreibung von Lokalisierungsphänomenen signifikant erweitert. Es wird gezeigt, dass der Lokalsierungsprozess in diesem System einen komplexen Charakter aufweist und sich erheblich von den üblichen Lokalisierungphänomenen unterscheidet, die man für kontinuierliche Verteilungen findet. Zusätzlich zu Anderson-lokalisierten Zuständen findet man 'anormal' lokalisierte Zustände und gebundene Zustände, sowie eine Vielzahl an Mobilitätsgrenzen. Es stellt sich heraus, dass das System den unkonventionellen Mott-Übergang für nichtintegere Füllung auch in Inbetrachtnahme von bisher vernachlässigten Lokalisierungseffeken aufweist. Das resultiernde paramagnetische Phasendiagramm besteht aus dem Anderson-Mott-Isolator, Band-Isolator und einer metallischen Phase. Diese Ergebnisse sind von grosser Relevanz für die Festkörperphysik, in welcher die binäre Unordnungsverteilung als Grundlagenmodell für Zweikomponentenlegierungen oder dotierte Halbleiter dient.

Zur Untersuchung der Speckle-Unordnung werden gemeinsame Wahrscheinlichkeitsverteilungen der Hubbardparameter herangezogen, die für Experimente realistisch sind und kürzlich von Zhou und Ceperley errechnet wurden [306]. Das Hauptresultat ist das erstmalig berechnete Phasendiagramm für speckleungeordnete, fermionische Systeme. Als hervorstechendes Merkmal findet man die starke Unterdrückung des korrelations-induzierten Metall-Isolator-Übergangs, welche auf die unbeschränkte Verteilung der Gitterplatzenergien

zurückzuführen ist. Dadurch sind der Mott-Isolator und der Anderson-Mott-Isolator im Gegensatz zur Kastenverteilung nicht kontinuierlich verbunden, sondern durch eine metallische Phase getrennt. Darüberhinaus wurden Fermionen auf dem speckle-ungeordneten Quadratgitter mittels ortsraumaufgelöster dynamischer Molekularfeldtheorie untersucht. Die Unterdrückung des Mott-Übergangs wird qualitativ übereinstimmend mit der statistischen dynamischen Molekularfeldtheorie bestätigt. Zudem wird die Anwesenheit einer Zero-Bias-Anomalie nachgewiesen, die in Zukunft näher untersucht werden sollte.

In Kapitel 9 werden kastenungeordnete Bose-Fermi-Mischungen mittels der Theorie des typischen Mediums untersucht. Dazu wird zusätzlich zu der geometrisch gemittelten fermionischen Zustandsdichte der geometrisch gemittelte bosonische Superfluidordnungsparameter berechnet, um Lokalsierungseffekte sowohl für das fermionische als auch das bosonische Untersystem beschreiben zu können. Zunächst werden Mischungen bestehend aus spin-ploarisierten Fermionen betrachtet. Im homogenen System besteht das berechnete Phasendiagramm aus sich als Funktion des bosonischen chemischen Potentials abwechselnden Regionen des bosnische alternierenden und konventionellen Mott-Isolators, die für größere werdende bosonisches Hüpfamplituden einen Phasenübergang zu der superfluiden Phase aufweisen. Der bosonische, alternierende Mott-Isolator geht mit einer fermionsichen Dichtewelle einher, die eine Anregungslücke am Fermilevel aufweist, während der bosonische Mott-Isolator mit einem Fermiliquid einhergeht. Letztgenanntes trifft auch auf die bosonische Superfluidphase zu und das entsprechende Fermiliquid ist durch eine charakteristisches Anregungspektrum bestehend aus drei Peaks gekennzeichnet. Der Ursprung dieser Anregungen wird im fermionischen, atomaren Limes geklärt. Schwache Unordnung führt zu erheblichen Konsequenzen für das System. Am auffälligsten ist das Auftreten einer supersoliden Phase, die für ein großes Werteintervall des bosonischen chemischen Potentials stabil ist. Daher könnte schwache Unordnung einen experimentellen Nachweis der supersoliden Phase in Bose-Fermi-Mischungen begünstigen. Darüberhinaus werden starke Indizien für die Existenz von zwei Boseglas-Phasen, von denen eine durch Dichtewellen in beiden Untersystemen gekennzeichnet ist, gefunden. Eine detaillierte Untersuchung dieser Phasen erfordert jedoch aufwendigere Untersuchungsmethoden, die dem statistischen Charakter der Unordnung gerecht werden. Abschliessend werden Bose-Fermi-Mischungen bestehend aus zwei Spin-Komponenten-Fermionen untersucht. Darin stehen Konsequenzen auf das bosonische Phasendiagramm im Fokus, die aus dem Variieren der Wechselwirkung zwischen Bosonen und Fermionen und der Unordnungsstärke resultieren. Der Übergang zwischen bosonischem Mott-Isolator und bosonischem Superfluid findet für immer geringere bosonische Hüpfamplituden statt je stärker die Unordnung ist. Gleichzeitig entwickelt sich

172

eine Boseglass-Phase, die ab einer genügend grossen Unordnungsstärke die einzig lokalisierte bosonische Phase darstellt. Darüberhinaus zeigt die Untersuchung, das eine stärkere Wechsewirkung zwischen den Bosonen und den Fermionen generell zu einer Delokalisierung führt, die sich in geringeren Ausdehnungen sowohl der Boseglas-Phase als auch des Mott-Isolators äußert.

# A. Particles in a periodic potential

In this appendix, a brief overview on non-interacting particles in a periodic potential – i.e a system obeying discrete translational invariance – is given, which applies to e.g. electrons in a crystal as well as ultracold atoms in an optical lattice. The periodic potential is given by

$$V(\mathbf{x}) = \sum_n V_{\text{atom}}(\mathbf{x} - \mathbf{R_n}) \,, \tag{A.1}$$

with the atomic potential $V_{\text{atom}}$ and lattice vectors $\mathbf{R_n}$ ($n \in \{1, \ldots, N\}$). The periodicity is defined by $V(\mathbf{x}) = V(\mathbf{x} + \mathbf{R_n})$. The Schrödinger equation reads

$$(\frac{\mathbf{p}^2}{2m} + V(\mathbf{x}))\Psi_{\mathbf{k}}(\mathbf{x}) = \epsilon_{\mathbf{k}}\Psi_{\mathbf{k}}(\mathbf{x}) \tag{A.2}$$

with the eigenfunction $\Psi_{\mathbf{k}}(\mathbf{x})$[1], the so-called Bloch function and eigenenergy $\epsilon_k$. The explicit expression depends on the underlying potential structure and must be calculated numerically. Bloch's theorem states that the wave function is given as [23, 44]

$$\Psi_{\mathbf{k}}(\mathbf{x} + \mathbf{R_n}) = e^{i\mathbf{k}\cdot\mathbf{R_n}}\Psi_{\mathbf{k}}(\mathbf{x}) \,, \tag{A.3}$$

which means that the wave function is a periodic function up to a phase. In general several eigenenergies exist for a given wave vector $\mathbf{k}$, which necessitates the introduction of the so-called band index $n$. The set of all $\epsilon_{\mathbf{k},n}$ constitutes the band structure. In the following we suppress the band index and just consider a single band. The ansatz $\Psi_{\mathbf{k}}(\mathbf{x}) = u_{\mathbf{k}}(\mathbf{x})\exp(i\mathbf{k}\cdot\mathbf{R_n})$ results in a periodic amplitude function

$$u_{\mathbf{k}}(\mathbf{x} + \mathbf{R_n}) = u_{\mathbf{k}}(\mathbf{x}) \,. \tag{A.4}$$

The wave vector $\mathbf{k}$ can be restricted to the first Brillouin zone due to the $2\pi$ periodicity of the complex exponential function. It is further known that the Bloch functions constitute a complete orthonormal set of functions. The creation operator that creates a particle in a Bloch eigenstate is denoted by $a_{\mathbf{k}}^{\dagger}$.

---

[1]Spin indices or other internal degrees of freedom are omitted for simplicity reasons.

*A. Particles in a periodic potential*

A further important basis set in periodic lattices is given by the so-called Wannier functions. They are defined via the Fourier transform of the Bloch functions

$$w(\mathbf{x} - \mathbf{R_n}) = \frac{1}{\sqrt{N}} \sum_{\mathbf{k}\text{in 1.BZ}} e^{-\mathbf{k}\cdot\mathbf{R_n}} \Psi_{\mathbf{k}}(\mathbf{x}) \ . \tag{A.5}$$

The Wannier function are highly localized on a single lattice site. The operator $c_n^{\dagger} \equiv c_{\mathbf{R_n}}^{\dagger}$ creates a particle in a Wannier state on lattice site $\mathbf{R_n}$.

# B. Renormalized perturbation expansion

The renormalized perturbation expansion [17, 91] is an expansion in the hopping amplitude to calculate the Green's function of a tight-binding Hamiltonian. The Hamiltonian is constituted of two parts

$$H = H_0 + H_1 \tag{B.1}$$

one is the atomic orbital term

$$H_0 = \sum_i \epsilon_i |i\rangle\langle i| \tag{B.2}$$

and the second is the hopping term

$$H_1 = \sum_{i \neq j} t_{ij} |i\rangle\langle j| \tag{B.3}$$

connecting the sites with each other. $H_0$ is considered as the unperturbed Hamiltonian and $H_1$ represents a perturbation. The resolvent operator is given by

$$G(z) \equiv \frac{1}{z - H} = \frac{1}{z - H_0 - H_1} = \frac{1}{(z - H_0)(1 - H_1(z - H_0)^{-1})} \tag{B.4}$$

$$= \frac{G_0(z)}{1 - H_1 G_0(z)} \tag{B.5}$$

with $G_0(z) \equiv (z - H_0)^{-1}$. Applying the geometric series

$$\frac{1}{1 - x} = 1 + x + x^2 + x^3 + \ldots \tag{B.6}$$

we find the expansion

$$G(z) = G_0 + G_0 H_1 G_0 + G_0 H_1 G_0 H_1 G_0 + \ldots \tag{B.7}$$

$$= G_0 + G_0 H_1 G . \tag{B.8}$$

## B. Renormalized perturbation expansion

The series can be rewritten in terms of matrix elements

$$
\begin{aligned}
\langle k|G|l\rangle &\equiv G_{kl} && \text{(B.9)} \\
&= (G_0)_{kl} + \sum_{nm} (G_0)_{kn}(H_1)_{nm}(G_0)_{ml} \\
&\quad + \sum_{nmop} (G_0)_{kn}(H_1)_{nm}(G_0)_{mo}(H_1)_{op}(G_0)_{pl} + \dots && \text{(B.10)} \\
&= \frac{\delta_{k,l}}{z-\epsilon_k} + \frac{1}{z-\epsilon_k}(H_1)_{kl}\frac{1}{z-\epsilon_l} \\
&\quad + \sum_n \frac{1}{z-\epsilon_k}(H_1)_{kn}\frac{1}{z-\epsilon_n}(H_1)_{nl}\frac{1}{z-\epsilon_l} + \dots \;, && \text{(B.11)}
\end{aligned}
$$

where in the last step it was incorporated that $G_0$ is diagonal. To proceed, we assume that only nearest neighbor hopping is of interest and that each hopping process is attributed with a factor of $t$. Obviously, the terms appearing in the expansion (B.11) can be identified with all possible paths connecting the lattice sites $k$ and $l$. Each hopping process contributes a factor of $t$ and at each time, when a lattice site $q$ is arrived, a factor $(z-\epsilon_q)^{-1}$ must be taken into account. The terms can be resummed in so-called skeleton paths, when each hopping process is decorated with additional factors. A path represents a skeleton path, if it is self-avoiding, i.e. that no site of the path is visited twice. The correct decorations are identified easily: the path $k \to n \to m \to \dots \to l$ corresponds to all terms connecting the sites $k$ and $l$ and all possible loop corrections at every visited lattice site. The later is given by all intermediate paths starting at a visited lattice site and returning to it. Let us consider the starting site $k$. All loop corrections summed up clearly correspond to the full diagonal Green's function $G_{kk}$, which represents the right decorating factor. At the next site $n$, the same reasoning is true, but all loop corrections visiting site $k$ have to be omitted as they are already incorporated. Hence, the right decoration consists of the full diagonal cavity Green's function $G_{nn}^{(k)}$ of the lattice where site $k$ has been removed. This procedure continues so that the correct decoration factors are given by multi cavity Green's functions $G_{qq}^{(k,n,\dots)}$. The full partial summation leads to [91]

$$
G_{kl} = \sum_{\text{all skeleton paths } k\to l} G_{kk}t_{kn}G_{nn}^{(k)}t_{nm}G_{mm}^{(k,n)}t_{mo}\dots .G_{ll}^{(k,n,m,\dots)} \quad \text{(B.12)}
$$

In particular, the diagonal Green's function is found to be

$$
G_{kk} = (G_0)_{kk} + \sum_{\text{all skeleton paths } k\to k} G_{kk}t_{kn}G_{nn}^{(k)}t_{nm}\dots(G_0)_{kk} \;, \quad \text{(B.13)}
$$

178

which we can rewrite as

$$G_{kk} = (G_0)_{kk} + G_{kk}\Gamma_k(G_0)_{kk} \, , \tag{B.14}$$

with the already introduced 'self-energy' $\Gamma_k$ (cf. chapter 3 equation 3.11). The self-energy is given as

$$\Gamma_k = \sum_{\text{all skeleton paths } k \to k} t_{kn} G_{nn}^{(k)} t_{nm} G_{mm}^{(k,n)} \ldots t \tag{B.15}$$

and the Green's function reads

$$G_{kk}(z) = \frac{(G_0)_{kk}(z)}{1 - (G_0)_{kk}(z)\Gamma_k(z)} = \frac{1}{z - \epsilon_k - \Gamma_k(z)} \, . \tag{B.16}$$

The above expansion for the Green's function and the 'self-energy' over skeleton paths is called renormalized perturbation expansion. The decorating factors are given by intricate quantities, namely matrix elements of the cavity Green's functions. Clearly, a hierarchy of equations needs to be solved to determine all lattice Green's functions and cavity Green's functions. On a finite lattice the hierarchy terminates, since there is one finite degree of cavity, when all sites have been removed. For infinite lattices an hierarchy of infinitely many equations [185]

$$\begin{aligned}
\Gamma_k(z) &= \sum_{n \neq k} t_{kn} \frac{1}{z - \epsilon_n - \Gamma_n^{(k)}} t_{nk} \\
&\quad + \sum_{n,m \neq k; m \neq n} t_{k,n} \frac{1}{z - \epsilon_n - \Gamma_n^{(k)}} t_{nm} \frac{1}{z - \epsilon_m - \Gamma_m^{(k,n)}} t_{mk} + \ldots
\end{aligned} \tag{B.17}$$

$$\Gamma_n^{(k)}(z) = \sum_{m \neq k,n} t_{nm} \frac{1}{z - \epsilon_m - \Gamma_m^{(k,n)}} t_{mn} + \ldots \tag{B.18}$$

$$\Gamma_m^{(k,n)}(z) = \ldots \tag{B.19}$$

has to be considered.

However, the renormalized perturbation expansion is used very effectively on the Bethe lattice due to its special structure. It is loop-free and therefore the only non-intersecting paths are given by first terms in the above series. The only path that contributes to $\Gamma_k$, for example, is $k \to n \to k$. Hence, on the

## B. Renormalized perturbation expansion

Bethe Lattice, we find [2]

$$\Gamma_k(z) = \sum_{n \text{ N.N. of } k} t_{kn} \frac{1}{z - \epsilon_n - \Gamma_n^{(k)}} t_{nk} \tag{B.20}$$

$$\Gamma_n^{(k)}(z) = \sum_{m \text{ N.N. of } n} t_{nm} \frac{1}{z - \epsilon_m - \Gamma_m^{(k,n)}} t_{mn} \tag{B.21}$$

$$\Gamma_m^{(k,n)}(z) = \sum_{o \text{ N.N. of } m} t_{mo} \frac{1}{z - \epsilon_o - \Gamma_o^{(k,n,m)}} t_{om} \tag{B.22}$$

$$\cdots \tag{B.23}$$

which, remarkably, is exact. The second equation is given on the Bethe lattice, where site $k$ has been remove, the third on the Bethe lattice, where sites $k$ and $n$ have been removed, and so forth. The cavity Green's functions of lattices with several sites removed are also simplified due to the absence of loops on the Bethe lattice. The equation (B.21) involves $\Gamma_m^{(k,n)}$, which for all possible $m$ reduces to $\Gamma_m^{(n)}$, as no path can visit site $k$. So finally, on the Bethe lattice just two instances of 'self-energies' are relevant, namely $\Gamma_k$ and $\Gamma_n^{(k)}$. Correspondingly just two Green's functions $G_k$ and $G_n^{(k)}$. All higher multi cavity Green's function reproduce the structure of the latter. Our hierarchy of equations reduces exactly to two equations:

$$\Gamma_k = \sum_{n=1}^{z} t_{kn}^2 G_{nn}^{(k)} \tag{B.24}$$

$$\Gamma_n^{(k)} = \sum_{m=1}^{K} t_{mn}^2 G_{mm}^{(n)} \,. \tag{B.25}$$

Here, both sums extend over the nearest neighbors. The prior equation is given on the Bethe lattice, whereas the latter equation is defined on the cavity lattice.

# Bibliography

[1] ABOU-CHACRA, R., AND THOULESS, D. Self-consistent theory of local-ization. II. Localization near the band edges. *Journal of Physics C 7* (1974), 65.

[2] ABOU-CHACRA, R., THOULESS, D. J., AND ANDERSON, P. W. A self-consistent theory of localization. *Journal of Physics C 6* (1973), 1734.

[3] ABRAHAMS, E. Scaling theory of localization: Absence of quantum diffusion in two dimensions. *Physical Review Letters 42* (1979), 673.

[4] AGUIAR, M. C. O., DOBROSAVLJEVIĆ, V., ABRAHAMS, E., AND KOTLIAR, G. Scaling behavior of an Anderson impurity close to the Mott-Anderson transition. *Physical Review B 73* (2006), 115117.

[5] AGUIAR, M. C. O., DOBROSAVLJEVIĆ, V., ABRAHAMS, E., AND KOTLIAR, G. Critical behavior at Mott-Anderson transition: a TMT-DMFT perspective. *Physical Review Letters 102* (2009), 156402.

[6] AGUIAR, M. C. O., MIRANDA, E., AND DOBROSAVLJEVIĆ, V. Localiza-tion effects and inelastic scattering in disordered heavy electrons. *Physical Review B 68* (2003), 125104.

[7] AHUFINGER, V., SANCHEZ-PALENCIA, L., KANTIAN, A., SANPERA, A., AND LEWENSTEIN, M. Disordered ultracold atomic gases in optical lattices: A case study of Fermi-Bose mixtures. *Physical Review A 72* (2005), 063616.

[8] ALBUS, A., ILLUMINATI, F., AND EISERT, J. Mixtures of bosonic and fermionic atoms in optical lattices. *Physical Review A 68* (2003), 023606.

[9] ALTMAN, E., DEMLER, E., AND LUKIN, M. D. Probing many-body states of ultracold atoms via noise correlations. *Physical Review A 70* (2004), 013603.

[10] ALTSHULER, B. Zero bias anomaly in tunnel resistance and electron-electron interaction. *Solid State Communications 30* (1979), 115.

[11] ALTSHULER, B. L., GEFEN, Y., KAMENEV, A., AND LEVITOV, L. S. Quasiparticle lifetime in a finite system: A nonperturbative approach. *Physical Review Letters 78* (1997), 2803.

[12] ALTSHULER, B. L., ZHAREKESHEV, I. K., KOTOCHIGOVA, S. A., AND SHKLOVSKII, B. I. Energy-level repulsion and the metal-insulator-transition. *Soviet Physics JETP 67* (1988), 625.

[13] ALVERMANN, A., AND FEHSKE, H. Local distribution approach to disordered binary alloys. *The European Physical Journal B 48* (2005), 295.

[14] ALVERMANN, A., AND FEHSKE, H. Stochastic Green's function approach to disordered systems. *Journal of Physics: Conference Series 35* (2006), 145.

[15] ALVERMANN, A., AND FEHSKE, H. Local distribution approach. In *Computational Many-Particle Physics* (2008), H. Fehske, R. Schneider, & A. Weiße, Ed., vol. 739 of *Lecture Notes in Physics, Springer Verlag.*

[16] ANDERSON, M. H., ENSHER, J. R., MATTHEWS, M. R., WIEMAN, C. E., AND CORNELL, E. A. Observation of Bose-Einstein condensation in a dilute atomic vapor. *Science 269* (1995), 198.

[17] ANDERSON, P. W. Absence of diffusion in certain random lattices. *Physical Review 109* (1958), 1492.

[18] ANDERSON, P. W. New Approach to the Theory of Superexchange Interactions. *Physical Review 115* (1959), 2.

[19] ANDERSON, P. W. Localized magnetic states in metals. *Physical Review 124* (1961), 41.

[20] ANDERSON, P. W. Local moments and localized states. *Reviews of Modern Physics 50* (1978), 191.

[21] ANDERSON, P. W. The resonating valence bond state in $La_2CuO_4$ and superconductivity. *Science 235* (1987), 1196.

[22] ANTONIOU, P. D., AND ECONOMOU, E. N. Absence of Anderson's transition in random lattices with off-diagonal disorder. *Physical Review B 16* (1977), 3768.

[23] ASHCROFT, N., AND MERMIN, D. *Festkörperphysik*, 3rd. ed. Oldenbourg Wissenschaftsverlag, 2007.

[24] ASPECT, A., ARIMONDO, E., KAISER, R., VANSTEENKISTE, N., AND COHEN-TANNOUDJI, C. Laser cooling below the one-photon recoil energy by velocity-selective coherent population trapping. *Physical Review Letters 61* (1988), 826.

[25] ASPECT, A., AND INGUSCIO, M. Anderson localization of ultracold atoms. *Physics Today 62* (2009), 30.

[26] AUBRY, S., AND ANDRÉ, G. Analyticity breaking and Anderson localization in incommensurate lattices. *Ann. Israel Phys. Soc 3* (1980), 133.

[27] BAKR, W. S., GILLEN, J. I., PENG, A., FÖLLING, S., AND GREINER, M. A quantum gas microscope for detecting single atoms in a Hubbard-regime optical lattice. *Nature 462* (2009), 74.

[28] BAKR, W. S., PENG, A., TAI, M. E., MA, R., SIMON, J., GILLEN, J. I., FÖLLING, S., POLLET, L., AND GREINER, M. Probing the Superfluid-to-Mott Insulator Transition at the Single-Atom Level. *Science 329* (2010), 547.

[29] BASKO, D., ALEINER, I., AND ALTSHULER, B. Metal–insulator transition in a weakly interacting many-electron system with localized single-particle states. *Annals of Physics 321* (2006), 1126.

[30] BECKER, C., SOLTAN-PANAHI, P., KRONJÄGER, J., DÖRSCHER, S., BONGS, K., AND SENGSTOCK, K. Ultracold quantum gases in triangular optical lattices. *New Journal of Physics 12* (2010), 065025.

[31] BEDNORZ, J., AND MÜLLER, K. Possible high-$T_c$ superconductivity in the Ba-La-Cu-O system. *Zeitschrift für Physik B 64* (1986), 189.

[32] BELITZ, D., AND KIRKPATRICK, T. The anderson-mott transition. *Reviews of modern physics 66* (1994), 261.

[33] BERGMANN, G. Weak localization in thin films: a time-of-flight experiment with conduction electrons. *Physics Reports 107* (1984), 1.

[34] BERKOVITS, R., AND AVISHAI, Y. Localization in Fock space: a finite-energy scaling hypothesis for many-particle excitation statistics. *Physical Review Letters 80* (1998), 568.

[35] BERNIER, J.-S., DAO, T.-L., KOLLATH, C., GEORGES, A., AND CORNAGLIA, P. S. Thermometry and signatures of strong correlations from

Raman spectroscopy of fermionic atoms in optical lattices. *Physical Review A 81* (2010), 063618.

[36] BEST, T., WILL, S., SCHNEIDER, U., HACKERMÜLLER, L., VAN OOSTEN, D., AND BLOCH, I. Role of interactions in $^{87}$Rb-$^{40}$K Bose-Fermi mixtures in a 3D optical lattice. *Physical Review Letters 102* (2009), 030408.

[37] BHATT, R. N., AND FISHER, D. S. Absence of spin diffusion in most random lattices. *Physical Review Letters 68* (May 1992), 3072.

[38] BIDDLE, J., WANG, B., PRIOUR, D. J., AND DAS SARMA, S. Localization in one-dimensional incommensurate lattices beyond the aubry-andré model. *Physical Review A 80* (2009), 021603.

[39] BILLY, J., JOSSE, V., ZUO, Z., BERNARD, A., HAMBRECHT, B., LUGAN, P., CLÉMENT, D., SANCHEZ-PALENCIA, L., BOUYER, P., AND ASPECT, A. Direct observation of Anderson localization of matter waves in a controlled disorder. *Nature 453* (2008), 891.

[40] BISSBORT, U., AND HOFSTETTER, W. Stochastic mean-field theory for the disordered Bose-Hubbard model. *Europhysics Letters 86* (2009), 50007.

[41] BISSBORT, U., THOMALE, R., AND HOFSTETTER, W. Stochastic mean-field theory: Method and application to the disordered Bose-Hubbard model at finite temperature and speckle disorder. *Physical Review A 81* (2010), 063643.

[42] BISWAS, P., CAIN, P., RÖMER, R., AND SCHREIBER, M. Off-diagonal disorder in the Anderson model of localization. *Physica Status Solidi (b) 218* (2000), 205.

[43] BLAKIE, P. Raman spectroscopy of Mott insulator states in optical lattices. *New Journal of Physics 8* (2006), 157.

[44] BLOCH, F. Über die Quantenmechanik der Elektronen in Kristallgittern. *Zeitschrift für Physik A 52* (1929), 555.

[45] BLOCH, I., DALIBARD, J., AND ZWERGER, W. Many-body physics with ultracold gases. *Reviews of Modern Physics 80* (2008), 885.

[46] BOERS, D. J., GOEDEKE, B., HINRICHS, D., AND HOLTHAUS, M. Mobility edges in bichromatic optical lattices. *Physical Review A 75* (2007), 063404.

[47] BORLAND, R. The nature of the electronic states in disordered one-dimensional systems. *Proceedings of the Royal Society of London. Series A, Mathematical and Physical Sciences 274* (1963), 529.

[48] BOURDEL, T., CUBIZOLLES, J., KHAYKOVICH, L., MAGALHAES, K. M. F., KOKKELMANS, S. J., SHLYAPNIKOV, G. V., AND SALOMON, C. Measurement of the interaction energy near a Feshbach resonance in a $^6Li$ Fermi Gas. *Physical Review Letters 91* (2003), 020402.

[49] BRANDT, U., AND MIELSCH, C. Thermodynamics and correlation functions of the Falicov-Kimball model in large dimensions. *Zeitschrift für Physik B 75* (1989), 365.

[50] BRANDT, U., AND MIELSCH, C. Thermodynamics of the Falicov-Kimball model in large dimensions II. *Zeitschrift für Physik B 79* (1990), 295.

[51] BRANDT, U., AND MIELSCH, C. Free energy of the Falicov-Kimball model in large dimensions. *Zeitschrift für Physik B 82* (1991), 37.

[52] BRONOLD, F. X., ALVERMANN, A., AND FEHSKE, H. Anderson localization in strongly coupled disordered electron-phonon systems. *Philosophical Magazine B 84* (2004), 673.

[53] BROUERS, N., ET AL. On the theory of localization in disordered systems. *Solid State Communications 17* (1975), 1453.

[54] BÜCHLER, H. P., AND BLATTER, G. Supersolid versus Phase Separation in Atomic Bose-Fermi Mixtures. *Physical Review Letters 91* (2003), 130404.

[55] BULLA, R. Zero Temperature Metal-Insulator Transition in the Infinite-Dimensional Hubbard Model. *Physical Review Letters 83* (1999), 136.

[56] BULLA, R., COSTI, T., AND PRUSCHKE, T. The numerical renormalization group method for quantum impurity systems. *Reviews of Modern Physics 80* (2008), 395.

[57] BULLA, R., COSTI, T. A., AND VOLLHARDT, D. Finite-temperature numerical renormalization group study of the Mott transition. *Physical Review B 64* (2001), 045103.

[58] BYCZUK, K. Metal-insulator transitions in the Falicov-Kimball model with disorder. *Physical Review B 71* (2005), 205105.

[59] Byczuk, K., Hofstetter, W., and Vollhardt, D. Mott-Hubbard metal-insulator transition at non-integer filling. *Physical Review B 69* (2004), 045112.

[60] Byczuk, K., Hofstetter, W., and Vollhardt, D. Mott-Hubbard transition vs. Anderson localization of correlated, disordered electrons. *Physical Review Letters 94* (2005), 056404.

[61] Byczuk, K., Hofstetter, W., and Vollhardt, D. Competition between Anderson Localization and Antiferromagnetism in Correlated Lattice Fermion Systems with Disorder. *Physical Review Letters 102* (2009), 146403.

[62] Byczuk, K., Hofstetter, W., and Vollhardt, D. Anderson Localization VS. Mott-Hubbard Metal-Insulator Transition in Disordered, Interacting Lattice Fermion Systems. *International Journal of Modern Physics B 24* (2010), 1727.

[63] Byczuk, K., and Ulmke, M. Curie temperature in the Hubbard model with alloy disorder. *The European Physical Journal B 45* (2005), 449.

[64] Byczuk, K., Ulmke, M., and Vollhardt, D. Ferromagnetism and Metal-Insulator Transition in the Disordered Hubbard Model. *Physical Review Letters 90* (2003), 196403.

[65] Byczuk, K., and Vollhardt, D. Correlated bosons on a lattice: Dynamical mean-field theory for Bose-Einstein condensed and normal phases. *Physical Review B 77* (2008), 235106.

[66] Castellani, C., Di Castro, C., Lee, P. A., and Ma, M. Interaction-driven metal-insulator transitions in disordered fermion systems. *Physical Review B 30* (1984), 527.

[67] Castellani, C., Kotliar, G., and Lee, P. Fermi-liquid theory of interacting disordered systems and the scaling theory of the metal-insulator transition. *Physical Review Letters 59* (1987), 323.

[68] Chayes, J. T., Chayes, L., Franz, J. R., Sethna, J. P., and Trugman, S. A. On the density of states for the quantum percolation problem. *Journal of Physics A 19* (1986), L1173.

[69] Chen, Q., and Levin, K. Momentum Resolved Radio Frequency Spectroscopy in Trapped Fermi Gases. *Physical Review Letters 102* (2009), 190402.

[70] CHIESA, S., CHAKRABORTY, P., PICKETT, W., AND SCALETTAR, R. Disorder-induced stabilization of the pseudogap in strongly correlated systems. *Physical Review Letters 101* (2008), 86401.

[71] CHU, S., HOLLBERG, L., BJORKHOLM, J. E., CABLE, A., AND ASHKIN, A. Three-dimensional viscous confinement and cooling of atoms by resonance radiation pressure. *Physical Review Letters 55* (1985), 48.

[72] CLÉMENT, D., FABBRI, N., FALLANI, L., FORT, C., AND INGUSCIO, M. Exploring Correlated 1D Bose Gases from the Superfluid to the Mott-Insulator State by Inelastic Light Scattering. *Physical Review Letters 102* (2009), 155301.

[73] CLÉMENT, D., VARÓN, A., RETTER, J., SANCHEZ-PALENCIA, L., ASPECT, A., AND BOUYER, P. Experimental study of the transport of coherent interacting matter-waves in a 1D random potential induced by laser speckle. *New Journal of Physics 8* (2006), 165.

[74] CRÉPIN, F. M. C., ZARÁND, G., AND SIMON, P. Disordered One-Dimensional Bose-Fermi Mixtures: The Bose-Fermi Glass. *Physical Review Letters 105* (2010), 115301.

[75] DAMASCELLI, A., AND SHEN, Z.-X. Angle-resolved photoemission studies of the cuprate superconductors. *Reviews of Modern Physics 75* (2003), 473.

[76] DAMSKI, B., ZAKRZEWSKI, J., SANTOS, L., ZOLLER, P., AND LEWENSTEIN, M. Atomic Bose and Anderson glasses in optical lattices. *Physical Review Letters 91* (2003).

[77] DAO, T.-L., GEORGES, A., DALIBARD, J., SALOMON, C., AND CARUSOTTO, I. Measuring the One-Particle Excitations of Ultracold Fermionic Atoms by Stimulated Raman Spectroscopy. *Physical Review Letters 98* (2007), 240402.

[78] DAVIS, K., MEWES, M., ANDREWS, M., VAN DRUTEN, N., DURFEE, D., KURN, D., AND KETTERLE, W. Bose-Einstein condensation in a gas of sodium atoms. *Physical Review Letters 75* (1995), 3969.

[79] DE BOER, J., AND VERWEY, E. Semi-conductors with partially and with completely filled 3d-lattice bands. *Proceedings of the Physical Society 49* (1937), 59.

[80] DELANDE, D., AND ZAKRZEWSKI, J. Compression as a Tool to Detect Bose Glass in a Cold Atomic Gas. *Physical Review Letters 102* (2009), 085301.

[81] DEMARCO, B., AND JIN, D. Onset of Fermi degeneracy in a trapped atomic gas. *Science 285* (1999), 1703.

[82] DOBROSAVLJEVIĆ, V. Typical-Medium Theory of Mott-Anderson Localization. *International Journal of Modern Physics B 24* (2010), 1680.

[83] DOBROSAVLJEVIĆ, V., AND KOTLIAR, G. Hubbard models with random hopping in d=∞. *Physical Review Letters 71* (1993), 3218.

[84] DOBROSAVLJEVIĆ, V., AND KOTLIAR, G. Strong correlations and disorder in d=∞ and beyond. *Physical Review B 50* (1994), 1430.

[85] DOBROSAVLJEVIĆ, V., AND KOTLIAR, G. Mean Field Theory of the Mott-Anderson Transition. *Physical Review Letters 78* (1997), 3943.

[86] DOBROSAVLJEVIĆ, V., AND KOTLIAR, G. Dynamical mean-field studies of metal-insulator transitions. *Philosophical Transactions: Mathematical, Physical and Engineering Sciences 356* (1998), 57.

[87] DOBROSAVLJEVIĆ, V., PASTOR, A. A., AND NIKOLIC, B. K. Typical medium theory of Anderson localization: A local order parameter approach to strong disorder effects. *Europhysics Letters 62* (2003), 76.

[88] DONGEN, P. G. J., GEBHARD, F., AND VOLLHARDT, D. Variational evaluation of correlation functions for lattice electrons in high dimensions. *Zeitschrift für Physik B 76* (1989), 199.

[89] DUAN, L.-M., DEMLER, E., AND LUKIN, M. D. Controlling spin exchange interactions of ultracold atoms in optical lattices. *Physical Review Letters 91* (2003), 090402.

[90] ECKSTEIN, M., KOLLAR, M., BYCZUK, K., AND VOLLHARDT, D. Hopping on the bethe lattice: Exact results for densities of states and dynamical mean-field theory. *Physical Review B 71* (2005), 235119.

[91] ECONOMOU, E. N. *Greens Functions in Quantum Physics*, 3rd. ed. Springer Verlag, 2006.

[92] ECONOMOU, E. N., AND COHEN, M. H. Existence of Mobility Edges in Anderson's Model for Random Lattices. *Physical Review B 5* (1972), 2931.

[93] Economou, E. N., Kirkpatrick, S., Cohen, M. H., and Eggarter, T. P. Localization in Disordered Materials: Binary Alloys. *Physical Review Letters 25* (1970), 520.

[94] Edwards, J., and Thouless, D. Numerical studies of localization in disordered systems. *Journal of Physics C 5* (1972), 807.

[95] Efros, A., and Shklovskii, B. Coulomb gap and low temperature conductivity of disordered systems. *Journal of Physics C 8* (1975), L49.

[96] Elliott, R. J., Krumhansl, J. A., and Leath, P. L. The theory and properties of randomly disordered crystals and related physical systems. *Reviews of Modern Physics 46* (1974), 465.

[97] Epperlein, F., Kilina, S., Schreiber, M., Uldanov, S., and Vojta, T. Fock space localization, return probability, and conductance of disordered interacting electrons. *Physica B 296* (2001), 52.

[98] Ernst, P., Götze, S., Krauser, J., Pyka, K., Lühmann, D., Pfannkuche, D., and Sengstock, K. Probing superfluids in optical lattices by momentum-resolved Bragg spectroscopy. *Nature Physics 6* (2009), 56.

[99] Essam, J. W. Percolation theory. *Reports on Progress in Physics 43* (1980), 833.

[100] Evers, F., and Mirlin, A. D. Anderson transitions. *Review of Modern Physics 80* (2008), 1355.

[101] Fallani, L., Lye, J. E., Guarrera, V., Fort, C., and Inguscio, M. Ultracold atoms in a disordered crystal of light: Towards a Bose glass. *Physical Review Letters 98* (2007), 130404.

[102] Fano, U. Effects of configuration interaction on intensities and phase shifts. *Physical Review 124* (1961), 1866.

[103] Fedichev, P. O., Kagan, Y., Shlyapnikov, G. V., and Walraven, J. T. M. Influence of Nearly Resonant Light on the Scattering Length in Low-Temperature Atomic Gases. *Physical Review Letters 77* (1996), 2913.

[104] Feher, G. Electron Spin Resonance Experiments on Donors in Silicon. I. Electronic Structure of Donors by the Electron Nuclear Double Resonance Technique. *Physical Review 114* (1959), 1219.

[105] FEHER, G., FLETCHER, R. C., AND GERE, E. A. Exchange Effects in Spin Resonance of Impurity Atoms in Silicon. *Physical Review 100* (1955), 1784.

[106] FEHER, G., AND GERE, E. A. Electron Spin Resonance Experiments on Donors in Silicon. II. Electron Spin Relaxation Effects. *Physical Review 114* (1959), 1245.

[107] FESHBACH, H. Unified theory of nuclear reactions. *Annals of Physics 5* (1958), 357.

[108] FEYNMAN, R. P. Simulating physics with computers. *International Journal of Theoretical Physics 21* (1982), 467.

[109] FINKELSHTEIN, A. Influence of Coulomb interaction on the properties of disordered metals. *Soviet Physics JETP 57* (1983), 97.

[110] FINKELSHTEIN, A. M. Weak localization and Coulomb interaction in disordered systems. *Zeitschrift für Physik B 56* (1984), 189.

[111] FISHER, M. P. A., GRINSTEIN, G., AND FISHER, D. S. Boson localization and the superfluid-insulator transition. *Physical Review B 40* (1989), 546.

[112] FLEISHMAN, L., AND ANDERSON, P. Interactions and the Anderson transition. *Physical Review B 21* (1980), 2366.

[113] FLEISHMAN, L., LICCIARDELLO, D., AND ANDERSON, P. Elementary Excitations in the Fermi Glass. *Physical Review Letters 40* (1978), 1340.

[114] FÖLLING, S., GERBIER, F., WIDERA, A., MANDEL, O., GERICKE, T., AND BLOCH, I. Spatial quantum noise interferometry in expanding ultracold atom clouds. *Nature 434* (2005), 481.

[115] FÖLLING, S., WIDERA, A., MÜLLER, T., GERBIER, F., AND BLOCH, I. Formation of Spatial Shell Structure in the Superfluid to Mott Insulator Transition. *Physical Review Letters 97* (2006), 060403.

[116] FOSTER, M. S., AND LUDWIG, A. W. W. Metal-insulator transition in Hubbard-like models with random hopping. *Physical Review B 74* (2006), 241102.

[117] FOSTER, M. S., AND LUDWIG, A. W. W. Metal-insulator transition from combined disorder and interaction effects in Hubbard-like electronic lattice models with random hopping. *Physical Review B 77* (2008), 165108.

[118] FREED, K. Electron Localization in Disordered Systems. *Physical Review B 5* (1972), 4802.

[119] GAVISH, U., AND CASTIN, Y. Matter-Wave Localization in Disordered Cold Atom Lattices. *Physical Review Letters 95* (2005), 020401.

[120] GEBHARD, F. *The mott metal-insulator transition: models and methods*, 1st. ed. Springer Verlag, 1997.

[121] GEORGES, A. Physical properties of the half-filled Hubbard model in infinite dimensions. *Physical Review B 48* (1993), 7167.

[122] GEORGES, A., AND KOTLIAR, G. Hubbard model in infinite dimensions. *Physical Review B 45* (1992), 6479.

[123] GEORGES, A., KRAUTH, W., AND ROZENBERG, M. J. Dynamical mean-field theory of strongly correlated fermion systems and the limit of infinite dimensions. *Reviews of Modern Physics 68* (1996), 13.

[124] GIMPERLEIN, H., WESSEL, S., SCHMIEDMAYER, J., AND SANTOS, L. Ultracold Atoms in Optical Lattices with Random On-Site Interactions. *Physical Review Letters 95* (2005), 170401.

[125] GIORGINI, S., AND STRINGARI, S. Theory of ultracold atomic Fermi gases. *Reviews of Modern Physics 80* (2008), 1215.

[126] GOODMAN, J. Some fundamental properties of speckle. *Journal of the Optical Society of America 66* (1976), 1145.

[127] GOODMAN, J. *Speckle phenomena in optics: theory and applications*, 1st. ed. Roberts & Co, 2007.

[128] GOR'KOV, L., LARKIN, A., AND KHMEL'NITSKII, D. Particle conductivity in a two-dimensional random potential. *JETP Letters 30* (1979), 248.

[129] GORNYI, I. V., MIRLIN, A. D., AND POLYAKOV, D. G. Interacting Electrons in Disordered Wires: Anderson Localization and Low-$T$ Transport. *Physical Review Letters 95* (2005), 206603.

[130] GREINER, M. *Ultracold quantum gases in three-dimensional optical lattice potentials*. PhD thesis, Ludwig-Maximilians-Universität München, 2003.

[131] GREINER, M., BLOCH, I., MANDEL, O., HÄNSCH, T. W., AND ESSLINGER, T. Exploring phase coherence in a 2d lattice of bose-einstein condensates. *Physical Review Letters 87* (2001), 160405.

[132] GREINER, M., MANDEL, O., ESSLINGER, T., HÄNSCH, T. W., AND BLOCH, I. Quantum phase transition from a superfluid to a Mott insulator in a gas of ultracold atoms. *Nature 415* (2002), 39.

[133] GREINER, M., MANDEL, O., HÄNSCH, T., AND BLOCH, I. Collapse and revival of the matter wave field of a Bose-Einstein condensate. *Nature 419* (2002), 51.

[134] GREINER, M., REGAL, C., STEWART, J., AND JIN, D. Probing pair-correlated fermionic atoms through correlations in atom shot noise. *Physical review letters 94* (2005), 110401.

[135] GRIBAKIN, G. F., AND FLAMBAUM, V. V. Calculation of the scattering length in atomic collisions using the semiclassical approximation. *Physical Review A 48* (1993), 546.

[136] GRIFFITHS, R. B. Nonanalytic Behavior Above the Critical Point in a Random Ising Ferromagnet. *Physical Review Letters 23* (1969), 17.

[137] GRIMM, R., WEIDEMÜLLER, M., AND OVCHINNIKOV, Y. Optical dipole traps for neutral atoms. *Advances in atomic, molecular, and optical physics 42* (2000), 95.

[138] GÜNTER, K., STÖFERLE, T., MORITZ, H., KÖHL, M., AND ESSLINGER, T. Bose-Fermi Mixtures in a Three-Dimensional Optical Lattice. *Physical Review Letters 96* (2006), 180402.

[139] GUTZWILLER, M. C. Effect of Correlation on the Ferromagnetism of Transition Metals. *Physical Review Letters 10* (1963), 159.

[140] HARPER, P. G. Single band motion of conduction electrons in a uniform magnetic field. *Proceedings of the Physical Society. Section A 68* (1955), 874.

[141] HE, Y., CHEN, Q., AND LEVIN, K. Radio-frequency spectroscopy and the pairing gap in trapped Fermi gases. *Physical Review A 72* (2005), 011602.

[142] HELMES, R. W., COSTI, T. A., AND ROSCH, A. Mott transition of fermionic atoms in a three-dimensional optical trap. *Physical Review Letters 100* (2008), 056403.

[143] HOFSTETTER, E., AND SCHREIBER, M. Relation between energy-level statistics and phase transition and its application to the Anderson model. *Physical Review B 49* (1994), 14726.

[144] HOFSTETTER, W. Generalized Numerical Renormalization Group for Dynamical Quantities. *Physical Review Letters 85* (2000), 1508.

[145] HOFSTETTER, W., CIRAC, J. I., ZOLLER, P., DEMLER, E., AND LUKIN, M. D. High-temperature superfluidity of fermionic atoms in optical lattices. *Physical Review Letters 89* (2002), 220407.

[146] HU, C., IZMAILIAN, N., AND OGANESYAN, K. Exact phase diagrams for an Ising model on a two-layer Bethe lattice. *Physical Review E 59* (1999), 6489.

[147] HUBBARD, J. Electron Correlations in narrow energy bands. *Proceedings ot the Royal Society of London. Series A, Mathematical and physical sciences 276* (1963), 238.

[148] HUBBARD, J. Electron correlations in narrow energy bands. II. The degenerate band case. *Proceedings of the Royal Society of London. Series A, Mathematical and Physical Sciences 277* (1964), 237.

[149] HUBBARD, J. Electron Correlations in Narrow Energy Bands. III. An Improved Solution. *Proceedings of the Royal Society of London. Series A, Mathematical and Physical Sciences 281* (1964), 401.

[150] HUBENER, A., SNOEK, M., AND HOFSTETTER, W. Magnetic phases of two-component ultracold bosons in an optical lattice. *Physical Review B 80* (2009), 245109.

[151] IMADA, M., AND TOKURA, Y. Metal-insulator transitions. *Reviews of Modern Physics 70* (1998), 1039.

[152] INOUYE, S., ANDREWS, M., STENGER, J., MIESNER, H., STAMPER-KURN, D., AND KETTERLE, W. Observation of Feshbach resonances in a Bose–Einstein condensate. *Nature 392* (1998), 151.

[153] INUI, M., TRUGMAN, S., AND ABRAHAMS, E. Unusual properties of midband states in systems with off-diagonal disorder. *Physical Review B 49* (1994), 3190.

[154] JAKSCH, D., BRUDER, C., CIRAC, J. I., GARDINER, C. W., AND ZOLLER, P. Cold Bosonic Atoms in Optical Lattices. *Physical Review Letters 81* (1998), 3108.

[155] JAKSCH, D., AND ZOLLER, P. The cold atom Hubbard toolbox. *Annals of physics 315* (2005), 52.

[156] JANIŠ, V., AND VOLLHARDT, D. Coupling of quantum degrees of freedom in strongly interacting disordered electron systems. *Physical Review B 46* (1992), 15712.

[157] JANIŠ, V. A new construction of thermodynamic mean-field theories of itinerant fermions: application to the Falicov-Kimball model. *Zeitschrift für Physik B 83* (1991), 227.

[158] JARRELL, M. Hubbard model in infinite dimensions: A quantum Monte Carlo study. *Physical Review Letters 69* (1992), 168.

[159] JESSEN, P. S., AND DEUTSCH, I. H. Optical lattices. *Advances in atomic, molecular, and optical physics 37* (1996), 95.

[160] JOERDENS, R., STROHMAIER, N., GUENTHER, K., MORITZ, H., AND ESSLINGER, T. A Mott insulator of fermionic atoms in an optical lattice. *Nature 455* (2008), 204.

[161] KAJUETER, H., AND KOTLIAR, G. New Iterative Perturbation Scheme for Lattice Models with Arbitrary Filling. *Physical Review Letters 77* (1996), 131.

[162] KANAMORI, J. Electron Correlation and Ferromagnetism of Transition Metals. *Progress of Theoretical Physics 30* (1963), 275.

[163] KIRKPATRICK, S., AND EGGARTER, T. P. Localized States of a Binary Alloy. *Physical Review B 6* (1972), 3598.

[164] KIRKPATRICK, S., VELICKÝ, B., AND EHRENREICH, H. Paramagnetic NiCu Alloys: Electronic Density of States in the Coherent-Potential Approximation. *Physical Review B 1* (1970), 3250.

[165] KNAP, M., ARRIGONI, E., AND VON DER LINDEN, W. Excitations in disordered bosonic optical lattices. *Physical Review A 82* (2010), 053628.

[166] KÖHL, M., MORITZ, H., STÖFERLE, T., GÜNTER, K., AND ESSLINGER, T. Fermionic Atoms in a Three Dimensional Optical Lattice: Observing Fermi Surfaces, Dynamics, and Interactions. *Physical Review Letters 94* (2005), 080403.

[167] KÖHLER, T., GÓRAL, K., AND JULIENNE, P. S. Production of cold molecules via magnetically tunable Feshbach resonances. *Reviews of Modern Physics 78* (2006), 1311.

[168] Kollar, M., Eckstein, M., Byczuk, K., Blumer, N., Dongen, P. v., Cuba, M. H. R. d., Metzner, W., Tanaskovic, D., Dobrosavljević, V., Kotliar, G., and Vollhardt, D. Green functions for nearest- and next-nearest-neighbor hopping on the Bethe lattice. *Annalen der Physik 14* (2005), 642.

[169] Kotliar, G., and Ruckenstein, A. E. New Functional Integral Approach to Strongly Correlated Fermi Systems: The Gutzwiller Approximation as a Saddle Point. *Physical Review Letters 57* (1986), 1362.

[170] Kotliar, G., Savrasov, S. Y., Haule, K., Oudovenko, V. S., Parcollet, O., and Marianetti, C. A. Electronic structure calculations with dynamical mean-field theory. *Reviews of Modern Physics 78* (2006), 865.

[171] Kotliar, G., and Vollhardt, D. Strongly Correlated Materials: Insights From Dynamical Mean-Field Theory. *Physics Today 57* (2004), 53.

[172] Kramer, B., and MacKinnon, A. Localization: theory and experiment. *Reports on Progress in Physics 56* (1993), 1469.

[173] Kravchenko, S., Mason, W., Bowker, G., Furneaux, J., Pudalov, V., and D'Iorio, M. Scaling of an anomalous metal-insulator transition in a two-dimensional system in silicon at $B = 0$. *Physical Review B 51* (1995), 7038.

[174] Kravchenko, S., and Sarachik, M. Metal–insulator transition in two-dimensional electron systems. *Reports on Progress in Physics 67* (2004), 1.

[175] Kravchenko, S., Simonian, D., Sarachik, M., Mason, W., and Furneaux, J. Electric field scaling at a $B = 0$ metal-insulator transition in two dimensions. *Physical Review Letters 77* (1996), 4938.

[176] Krishna-Murthy, H. R., Wilkins, J. W., and Wilson, K. G. Renormalization-group approach to the Anderson model of dilute magnetic alloys. I. Static properties for the symmetric case. *Physical Review B 21* (1980), 1003.

[177] Kruger, F., Wu, J., and Phillips, P. Anomalous suppression of the Bose glass at commensurate fillings in the disordered Bose-Hubbard model. *Physical Review B 80* (2009), 094526.

[178] LAAD, M. S., CRACO, L., AND MÜLLER-HARTMANN, E. Effect of strong correlations and static diagonal disorder in the d=∞ Hubbard model. *Physical Review B 64* (2001), 195114.

[179] LAGENDIJK, A., VAN TIGGELEN, B., AND WIERSMA, D. Fifty years of Anderson localization. *Physics Today 62* (2009), 24.

[180] LANDAU, L. The theory of a Fermi liquid. *Soviet Physics JETP 3* (1957), 920.

[181] LANGER, J., AND NEAL, T. Breakdown of the concentration expansion for the impurity resistivity of metals. *Physical Review Letters 16* (1966), 984.

[182] LEE, P. A. Disordered electronic systems. *Reviews of Modern Physics 57* (1985), 287.

[183] LEWENSTEIN, M., SANPERA, A., AHUFINGER, V., AND DAMSKI, B. Ultracold atomic gases in optical lattices: mimicking condensed matter physics and beyond. *Advances in Physics 56* (2007), 243.

[184] LEWENSTEIN, M., SANTOS, L., BARANOV, M., AND FEHRMANN, H. Atomic Bose-Fermi Mixtures in an Optical Lattice. *Physical Review Letters 92* (2004), 050401.

[185] LICCIARDELLO, D. C., AND ECONOMOU, E. N. Study of localization in Anderson's model for random lattices. *Physical Review B 11* (1975), 3697.

[186] LIEB, E. H., AND WU, F. Y. Absence of Mott Transition in an Exact Solution of the Short-Range, One-Band Model in One Dimension. *Physical Review Letters 20* (1968), 1445.

[187] LIFSHITZ, I. Energy spectrum structure and quantum states of disordered condensed systems. *Physics-Uspekhi 7* (1965), 549.

[188] LIU, Q.-M., DAI, X., FANG, Z., ZHUANG, J.-N., AND ZHAO, Y. Bose-fermi mixtures in a three-dimensional optical lattice. *Applied Physics B: Lasers and Optics 99* (2010), 639.

[189] LLOYD, P. Exactly solvable model of electronic states in a three-dimensional disordered Hamiltonian: non-existence of localized states. *Journal of Physics C 2* (1969), 1717.

[190] LOMBARDO, P., HAYN, R., AND JAPARIDZE, G. I. Insulator-metal-insulator transition and selective spectral weight transfer in a disordered strongly correlated system. *Physical Review B 74* (2006), 085116.

[191] LYE, J. E., FALLANI, L., MODUGNO, M., WIERSMA, D. S., FORT, C., AND INGUSCIO, M. Bose-Einstein Condensate in a Random Potential. *Physical Review Letters 95* (2005), 070401.

[192] MACKINNON, A., AND KRAMER, B. One-Parameter Scaling of Localization Length and Conductance in Disordered Systems. *Physical Review Letters 47* (1981), 1546.

[193] METZNER, W., AND VOLLHARDT, D. Correlated lattice fermions in d=∞ dimensions. *Physical Review Letters 62* (1989), 324.

[194] MICHELI, A., BRENNEN, G., AND ZOLLER, P. A toolbox for lattice-spin models with polar molecules. *Nature Physics 2* (2006), 341.

[195] MIRANDA, E. Griffiths phase of the Kondo insulator fixed point. *Journal of Magnetism and Magnetic Materials 226-230* (2001), 110.

[196] MIRANDA, E., AND DOBROSAVLJEVIĆ, V. Disorder-driven non-Fermi liquid behaviour of correlated electrons. *Reports on Progress in Physics 68* (2005), 2337.

[197] MIRLIN, A. Statistics of energy levels and eigenfunctions in disordered systems. *Physics Reports 326* (2000), 259.

[198] MIRLIN, A. D. Distribution of local density of states in disordered metallic samples: Logarithmically normal asymptotics. *Physical Review B 53* (1996), 1186.

[199] MODUGNO, G. Anderson localization in Bose–Einstein condensates. *Reports on Progress in Physics 73* (2010), 102401.

[200] MODUGNO, M. Exponential localization in one-dimensional quasi-periodic optical lattices. *New Journal of Physics 11* (2009), 033023.

[201] MOERDIJK, A. J., VERHAAR, B. J., AND AXELSSON, A. Resonances in ultracold collisions of $^6Li$, $^7Li$, and $^{23}Na$. *Physical Review A 51* (1995), 4852.

[202] MORSCH, O., AND OBERTHALER, M. Dynamics of Bose-Einstein condensates in optical lattices. *Reviews of Modern Physics 78* (2006), 179.

[203] MOTT, N. The basis of the electron theory of metals, with special reference to the transition metals. *Proceedings of the Physical Society. Section A 62* (1949), 416.

[204] MOTT, N. Electrons in Disordered Structures. *Advances in Physics 16* (1967), 49.

[205] MOTT, N. Metal-Insulator Transition. *Reviews of Modern Physics 40* (1968), 677.

[206] MOTT, N. *Metal-Insulator transitions*, 2nd. ed. Taylor & Francis, 1990.

[207] MOTT, N., AND TWOSE, W. The theory of impurity conduction. *Advances in Physics 10* (1961), 107.

[208] MOTT, N., AND ZINAMON, Z. The metal-nonmetal transition. *Reports on Progress in Physics 33* (1970), 881.

[209] MÜLLER-HARTMANN, E. Correlated fermions on a lattice in high dimensions. *Zeitschrift für Physik B 74* (1989), 507.

[210] MÜLLER-HARTMANN, E. The Hubbard model at high dimensions: some exact results and weak coupling theory. *Zeitschrift für Physik B 76* (1989), 211.

[211] MURPHY, N., WORTIS, R., AND ATKINSON, W. Generalized inverse participation ratio as a possible measure of localization for interacting systems. *Physical Review B 83* (2011), 184206.

[212] NAGAOKA, Y. Ferromagnetism in a narrow, almost half-filled s-band. *Physical Review 147* (1966), 392.

[213] NATTERMANN, T., GIAMARCHI, T., AND LE DOUSSAL, P. Variable-Range Hopping and Quantum Creep in One Dimension. *Physical Review Letters 91* (2003), 056603.

[214] NEGELE, J., AND ORLAND, H. *Quantum many-particle systems*, 1st. ed. Westview Press, 1998.

[215] NOLTING, W. *Grundkurs Theoretische Physik 7: Viel-Teilchen-Theorie*, 6th. ed. Springer Verlag, 2005.

[216] NOLTING, W., AND BORGIEL, W. Band magnetism in the Hubbard model. *Physical Review B 39* (1989), 6962.

[217] Nozières, P., and Pines, D. *The theory of quantum liquids*, 1st. ed. Westview Press, 1999.

[218] Oganesyan, V., and Huse, D. Localization of interacting fermions at high temperature. *Physical Review B 75* (2007), 155111.

[219] Orth, P., Bergman, D., and Le Hur, K. Supersolidity of cold-atom Bose-Fermi mixtures in optical lattices. *Physical Review A 80* (2009), 23624.

[220] Ospelkaus, S., Ospelkaus, C., Wille, O., Succo, M., Ernst, P., Sengstock, K., and Bongs, K. Localization of Bosonic Atoms by Fermionic Impurities in a Three-Dimensional Optical Lattice. *Physical Review Letters 96* (2006), 180403.

[221] Paalanen, M., and Bhatt, R. Transport and thermodynamic properties across the metal-insulator transition. *Physica B 169* (1991), 223–230.

[222] Paredes, B., Widera, A., Murg, V., Mandel, O., Fölling, S., Cirac, I., Shlyapnikov, G., Hänsch, T., and Bloch, I. Tonks-Girardeau gas of ultracold atoms in an optical lattice. *Nature 429* (2004), 277.

[223] Pasienski, M., McKay, D., White, M., and DeMarco, B. A disordered insulator in an optical lattice. *Nature Physics 6* (2010), 677.

[224] Phillips, P. Anderson localization and the exceptions. *Annual Review of Physical Chemistry 44* (1993), 115.

[225] Phillips, W. D. Nobel lecture: Laser cooling and trapping of neutral atoms. *Reviews of Modern Physics 70* (1998), 721.

[226] Pollet, L., Kollath, C., Schollwoeck, U., and Troyer, M. Mixture of bosonic and spin-polarized fermionic atoms in an optical lattice. *Physical Review A 77* (2008), 23608.

[227] Pollet, L., Prokof'ev, N. V., Svistunov, B. V., and Troyer, M. Absence of a Direct Superfluid to Mott Insulator Transition in Disordered Bose Systems. *Physical Review Letters 103* (2009), 140402.

[228] Potthoff, M., Wegner, T., and Nolting, W. Interpolating self-energy of the infinite-dimensional Hubbard model: Modifying the iterative perturbation theory. *Physical Review B 55* (1997), 16132.

199

[229] RAIZEN, M., SALOMON, C., AND NIU, Q. New light on quantum transport. *Physics Today 50* (1997), 30.

[230] REGAL, C., AND JIN, D. Measurement of Positive and Negative Scattering Lengths in a Fermi Gas of Atoms. *Physical Review Letters 90* (2003), 230404.

[231] REICH, G. R., AND LEATH, P. L. High-density percolation: Exact solution on a Bethe lattice. *Journal of Statistical Physics 19* (1978), 611.

[232] RICHARDELLA, A., ROUSHAN, P., MACK, S., ZHOU, B., HUSE, D., AWSCHALOM, D., AND YAZDANI, A. Visualizing Critical Correlations Near the Metal-Insulator Transition in $Ga_{1-x}Mn_xAs$. *Science 327* (2010), 665.

[233] ROATI, G., D'ERRICO, C., FALLANI, L., FATTORI, M., FORT, C., ZACCANTI, M., MODUGNO, G., MODUGNO, M., AND INGUSCIO, M. Anderson localization of a non-interacting Bose-Einstein condensate. *Nature 453* (2008), 895.

[234] ROTH, R. Structure and stability of trapped atomic boson-fermion mixtures. *Physical Review A 66* (2002), 013614.

[235] ROTH, R., AND BURNETT, K. Phase diagram of bosonic atoms in two-color superlattices. *Physical Review A 68* (2003), 023604.

[236] ROZENBERG, M. J., KOTLIAR, G., KAJUETER, H., HONIG, J. M., AND METCALF, P. Optical Conductivity in Mott-Hubbard Systems. *Physical Review Letters 75* (1995), 105.

[237] ROZENBERG, M. J., KOTLIAR, G., AND ZHANG, X. Y. Mott-Hubbard transition in infinite dimensions. II. *Physical Review B 49* (1994), 10181.

[238] SAKURAI, J., AND TUAN, S. *Modern quantum mechanics*, 2nd. ed. Addison-Wesley, 1994.

[239] SANCHEZ-PALENCIA, L., AND LEWENSTEIN, M. Disordered quantum gases under control. *Nature Physics 6* (2010), 87.

[240] SANPERA, A., KANTIAN, A., SANCHEZ-PALENCIA, L., ZAKRZEWSKI, J., AND LEWENSTEIN, M. Atomic Fermi-Bose Mixtures in Inhomogeneous and Random Lattices: From Fermi Glass to Quantum Spin Glass and Quantum Percolation. *Physical Review Letters 93* (2004), 040401.

[241] SCHÄFER, L., AND WEGNER, F. Disordered system with n orbitals per site: Lagrange formulation, hyperbolic symmetry, and goldstone modes. *Zeitschrift für Physik B 38* (1980), 113.

[242] SCHNEIDER, U., HACKERMÜLLER, L., WILL, S., BEST, T., BLOCH, I., COSTI, T. A., HELMES, R. W., RASCH, D., AND ROSCH, A. Metallic and insulating phases of repulsively interacting fermions in a 3D optical lattice. *Science 322* (2008), 1520.

[243] SCHUBERT, G., SCHLEEDE, J., BYCZUK, K., FEHSKE, H., AND VOLL-HARDT, D. Distribution of the local density of states as a criterion for Anderson localization: Numerically exact results for various lattices in two and three dimensions. *Physical Review B 81* (2010), 155106.

[244] SCHUBERT, G., WEISSE, A., AND FEHSKE, H. Unusual localisation effects in quantum percolation. *Physical Review B 71* (2005), 045126.

[245] SCHWEITZER, H., AND CZYCHOLL, G. Second order U-perturbation approach to the Anderson lattice model in high dimensions. *Solid State Communications 69* (1989), 171.

[246] SCHWEITZER, H., AND CZYCHOLL, G. Selfconsistent perturbational approach to the heavy fermion problem in high dimensions. *Zeitschrift für Physik B 79* (1990), 377.

[247] SCHWEITZER, H., AND CZYCHOLL, G. Weak-coupling treatment of the Hubbard model in one, two and three dimensions. *Zeitschrift für Physik B 83* (1991), 93.

[248] SEMMLER, D., BYCZUK, K., AND HOFSTETTER, W. Mott-Hubbard and Anderson metal-insulator transitions in correlated lattice fermions with binary disorder. *Physical Review B 81* (2010), 115111.

[249] SEMMLER, D., BYCZUK, K., AND HOFSTETTER, W. Anderson-Hubbard model with box disorder: Statistical dynamical mean-field theory investigation. *preprint, submitted to Physical Review B, arXiv:1106.4028* (2011).

[250] SEMMLER, D., WERNSDORFER, J., BISSBORT, U., BYCZUK, K., AND HOFSTETTER, W. Localization of correlated fermions in optical lattices with speckle disorder. *Physical Review B 82* (2010), 235115.

[251] SHEPELYANSKY, D. L. Coherent Propagation of Two Interacting Particles in a Random Potential. *Physical Review Letters 73* (1994), 2607.

[252] Sherson, J., Weitenberg, C., Endres, M., Cheneau, M., Bloch, I., and Kuhr, S. Single-atom-resolved fluorescence imaging of an atomic Mott insulator. *Nature 467* (2010), 68.

[253] Sheshadri, K., Krishna-Murthy, H. R., Pandit, R., and Ramakrishnan, T. V. Superfluid and insulating phases in an interacting-boson model: mean-field theory and the RPA. *Europhysics Letters 22* (1993), 257.

[254] Shklovskii, B., Shapiro, B., Sears, B., Lambrianides, P., and Shore, H. Statistics of spectra of disordered systems near the metal-insulator transition. *Physical Review B 47* (1993), 11487.

[255] Snoek, M., Titvinidze, I., Töke, C., Byczuk, K., and Hofstetter, W. Antiferromagnetic order of strongly interacting fermions in a trap: real-space dynamical mean-field analysis. *New Journal of Physics 10* (2008), 093008.

[256] Song, Y., Atkinson, W. A., and Wortis, R. Geometrically averaged density of states as a measure of localization. *Physical Review B 76* (2007), 045105.

[257] Song, Y., Bulut, S., Wortis, R., and Atkinson, W. A. Effects of strong correlations on the disorder-induced zero-bias anomaly in the extended Anderson–Hubbard model. *Journal of Physics: Condensed Matter 21* (2009), 385601.

[258] Song, Y., Wortis, R., and Atkinson, W. A. Dynamical Mean Field Study of the Two-Dimensional Disordered Hubbard Model. *Physical Review B 77* (2008), 054202.

[259] Soukoulis, C. M., and Economou, E. N. Fractal Character of Eigenstates in Disordered Systems. *Physical Review Letters 52* (1984), 565.

[260] Soukoulis, C. M., Economou, E. N., and Grest, G. S. Localization in quantum percolation: Transfer-matrix calculations in three dimensions. *Physical Review B 36* (1987), 8649.

[261] Soukoulis, C. M., Webman, I., Grest, G. S., and Economou, E. N. Study of electronic states with off-diagonal disorder in two dimensions. *Physical Review B 26* (1982), 1838.

[262] SOUZA, A., MAIONCHI, D., AND HERRMANN, H. Hölder mean applied to Anderson localization. *Physical Review B 76* (2007), 35111.

[263] SOVEN, P. Coherent-Potential Model of Substitutional Disordered Alloys. *Physical Review 156* (1967), 809.

[264] STANLEY, H. E. *Introduction to Phase Transitions and Critical Phenomena*, 1st. ed. Oxford University Press, 1987.

[265] STENGER, J., INOUYE, S., CHIKKATUR, A. P., STAMPER-KURN, D. M., PRITCHARD, D. E., AND KETTERLE, W. Bragg Spectroscopy of a Bose-Einstein Condensate. *Physical Review Letters 82* (1999), 4569.

[266] STEWART, J. T., GAEBLER, J. P., AND JIN, D. S. Using photoemission spectroscopy to probe a strongly interacting Fermi gas. *Nature 454* (2008), 744.

[267] STOOF, H., GUBBELS, K., AND DICKERSCHEID, D. *Ultracold quantum fields*, 1st. ed. Springer Verlag, 2009.

[268] THEIS, M., THALHAMMER, G., WINKLER, K., HELLWIG, M., RUFF, G., GRIMM, R., AND DENSCHLAG, J. H. Tuning the Scattering Length with an Optically Induced Feshbach Resonance. *Physical Review Letters 93* (2004), 123001.

[269] THOULESS, D. Anderson's theory of localized states. *Journal of Physics C 3* (1970), 1559.

[270] THOULESS, D. Electrons in disordered systems and the theory of localization. *Physics Reports 13* (1974), 93.

[271] TIESINGA, E., VERHAAR, B. J., AND STOOF, H. T. C. Threshold and resonance phenomena in ultracold ground-state collisions. *Physical Review A 47* (1993), 4114.

[272] TITVINIDZE, I., SNOEK, M., AND HOFSTETTER, W. Generalized Dynamical Mean-Field Theory for Bose-Fermi Mixtures in Optical Lattices. *Physical Review B 79* (2008), 144506.

[273] TITVINIDZE, I., SNOEK, M., AND HOFSTETTER, W. Supersolid Bose-Fermi Mixtures in Optical Lattices. *Physical Review Letters 100* (2008), 100401.

[274] TRAN, M.-T. Statistics of local density of states in the Falicov-Kimball model with local disorder. *Physical Review B 76* (2007), 245122.

[275] ULMKE, M. Anderson-Hubbard model in infinite dimensions. *Physical Review B 51* (1995), 10411.

[276] VARNEY, C., ROUSSEAU, V., AND SCALETTAR, R. Quantum Monte Carlo study of the visibility of one-dimensional Bose-Fermi mixtures. *Physical Review A 77* (2008), 41608.

[277] VELICKỲ, B., KIRKPATRICK, S., AND EHRENREICH, H. Single-site approximations in the electronic theory of simple binary alloys. *Physical Review 175* (1968), 747.

[278] VIGNOLO, P., AKDENIZ, Z., AND TOSI, M. The transmittivity of a Bose–Einstein condensate on a lattice: interference from period doubling and the effect of disorder. *Journal of Physics B 36* (2003), 4535.

[279] VLAMING, R., AND VOLLHARDT, D. Controlled mean-field theory for disordered electronic systems: Single-particle properties. *Physical Review B 45* (1992), 4637.

[280] VOJTA, M. Quantum phase transitions. *Reports on Progress in Physics 66* (2003), 2069.

[281] VOJTA, T., EPPERLEIN, F., AND SCHREIBER, M. Do interactions increase or reduce the conductance of disordered electrons? It depends! *Physical Review Letters 81* (1998), 4212.

[282] VOJTA, T., EPPERLEIN, F., AND SCHREIBER, M. Quantum Coulomb Glass: Anderson Localization in an Interacting System. *Physica Status Solidi B 205* (1998), 53.

[283] VOLLHARDT, D. Dynamical Mean-Field Theory of Electronic Correlations in Models and Materials. *AIP Conference Proceedings 1297* (2010), 339.

[284] VOLLHARDT, D., AND WÖLFLE, P. Anderson localization in $d < 2$ Dimensions: A self-consistent diagrammatic theory. *Physical Review Letters 45* (1980), 842.

[285] VOLLHARDT, D., AND WÖLFLE, P. Diagrammatic, self-consistent treatment of the Anderson localization problem in $d \leq 2$ dimensions. *Physical Review B 22* (1980), 4666.

[286] VOLLHARDT, D., AND WÖLFLE, P. Scaling equations from a self-consistent theory of Anderson localization. *Physical Review Letters 48* (1982), 699.

[287] WEGNER, F. Inverse participation ratio in 2+$\epsilon$ dimensions. *Zeitschrift für Physik B 36* (1980), 209.

[288] WEGNER, F. Bounds on the density of states in disordered systems. *Zeitschrift für Physik B 44* (1981), 9.

[289] WEGNER, F. J. Electrons in disordered systems: Scaling near the mobility edge. *Zeitschrift für Physik B 25* (1976), 327.

[290] WEGNER, F. J. Disordered system with n orbitals per site: n=$\infty$ limit. *Physical Review B 19* (1979), 783.

[291] WEISSE, A., WELLEIN, G., ALVERMANN, A., AND FEHSKE, H. The kernel polynomial method. *Reviews of Modern Physics 78* (2006), 275.

[292] WERNER, F., PARCOLLET, O., GEORGES, A., AND HASSAN, S. R. Interaction-Induced Adiabatic Cooling and Antiferromagnetism of Cold Fermions in Optical Lattices. *Physical Review Letters 95* (2005), 056401.

[293] WHITE, M., PASIENSKI, M., MCKAY, D., ZHOU, S. Q., CEPERLEY, D., AND DEMARCO, B. Strongly Interacting Bosons in a Disordered Optical Lattice. *Physical Review Letters 102* (2009), 055301.

[294] WIERSMA, D., BARTOLINI, P., LAGENDIJK, A., AND RIGHINI, R. Localization of light in a disordered medium. *Nature 390* (1997), 671.

[295] WIGNER, P. Effects of the electron interaction on the energy levels of electrons in metals. *Transactions of the Faraday Society 34* (1938), 678.

[296] WILDERMUTH, S., HOFFERBERTH, S., LESANOVSKY, I., HALLER, E., ANDERSSON, L., GROTH, S., BAR-JOSEPH, I., KRÜGER, P., AND SCHMIEDMAYER, J. Bose-Einstein condensates: microscopic magnetic-field imaging. *Nature 435* (2005), 440.

[297] WILL, S., BEST, T., SCHNEIDER, U., HACKERMÜLLER, L., LÜHMANN, D., AND BLOCH, I. Time-resolved observation of coherent multi-body interactions in quantum phase revivals. *Nature 465* (2010), 197.

[298] WINELAND, D. J., DRULLINGER, R. E., AND WALLS, F. L. Radiation-pressure cooling of bound resonant absorbers. *Physical Review Letters 40* (1978), 1639.

[299] WINELAND, D. J., AND ITANO, W. M. Laser cooling of atoms. *Physical Review A 20* (1979), 1521.

[300] WISEMAN, S., AND DOMANY, E. Self-averaging, distribution of pseudo-critical temperatures, and finite size scaling in critical disordered systems. *Phys. Rev. E 58* (1998), 2938.

[301] YAMADA, K. Perturbation expansion for the Anderson Hamiltonian. II. *Progress of Theoretical Physics 53* (1975), 970.

[302] YAMADA, K., AND YOSIDA, K. Ground state of the periodic Anderson Hamiltonian. *Journal of Magnetism and Magnetic Materials 31* (1983), 461.

[303] YU, U., BYCZUK, K., AND VOLLHARDT, D. Ferromagnetism and Kondo insulator behavior in the disordered periodic Anderson model. *Physical Review Letters 100* (2008), 246401.

[304] YUKALOV, V., AND SHUMOVSKY, A. *Lectures on phase transitions*, 1st. ed. World Scientific, 1990.

[305] ZHANG, X. Y., ROZENBERG, M. J., AND KOTLIAR, G. Mott transition in the d=$\infty$ Hubbard model at zero temperature. *Physical Review Letters 70* (1993), 1666.

[306] ZHOU, S. Q., AND CEPERLEY, D. M. Construction of localized wave functions for a disordered optical lattice and analysis of the resulting Hubbard model parameters. *Physical Review A 81* (2010), 013402.

[307] ZIMAN, J. Localization of electrons in ordered and disordered systems II. Bound bands. *Journal of Physics C 2* (1969), 1230.

[308] ZIMAN, T. Localization with off-diagonal disorder: A qualitative theory. *Physical Review B 26* (1982), 7066.

[309] ZUBAREV, D. Double-time Green functions in statistical physics. *Physics-Uspekhi 3* (1960), 320.

[310] ZWERGER, W. Mott-Hubbard transition of cold atoms in optical lattices. *Journal of Optics B 5* (2003), S9.

# Acknowledgments

My gratitude goes to my supervisor Prof. Dr. Walter Hofstetter who made this thesis possible by setting up the research projects. He has always been available for productive discussions. Sincere thanks go to Prof. Dr. Roser Valenti who was so kind to referee this thesis.

The collaboration with Prof. Dr. Krzysztof Byczuk gave me valuable insight into disorder physics. It was always a great pleasure discussing physics with him. Without his input this thesis would not have been possible.

Furthermore, it is important for me to point out Daniela Wirth-Pagano's contribution. Her imperturbable optimism was more than one time infectious and helped me a lot. I enjoyed all our discussion about politics, family and life in general.

My special thanks go to Ulf Bissbort who had the dubious pleasure to share the office with me for more than three years. He never – or at least not in my presence – complained, but instead was responsible for the always welcoming atmosphere of my office. I want to thank him not only for all the inspiring discussions about physics we had, but also for all these conversations that went far beyond our shared scholarly interests - ranging from peak oil to the apparent need to use my bicycle to come to the Riedberg. I will definitely miss sitting vis-à-vis with him. Not at least because of the constant sweets and coffee supply. I will also miss looking at the lion skin in our room, especially since it stopped smelling after one year.

Many thanks to Julia Wernsdorfer who made physics much more lively. She is also responsible for some major insights and contributed to the pleasant working atmosphere.

I also have to thank David Roosen for his invaluable help and his never ending willingness to help me with all my computing and compiling problems. But this is only the least important reason that our group felt incomplete after he has left.

Further thanks go to Irakli Titvinidze who is one of the most unselfish person I have ever met. It was really exciting to learn the many hidden aspects of DMFT from him.

I am really thankful to all people who proof read my thesis: Ulf Bissbort, Julia Wernsdorfer, Irakli Titvinidze, Daniel Cocks, Thorsten Thiel, Michael

Buchhold, and Daniela Wirth-Pagano. Without their help this thesis would still be an offense for all friends of the English language.

It is always difficult to express one's gratitude for something which is taken for granted. For this reason I would like to point out my sincere gratitude to my parents and my sister for all their support – not only during the last years – but ever since I can think of.

# Curriculum vitae

### Personal information

| | |
|---|---|
| Name | Denis Semmler |
| Date of birth | 25th of February, 1980 |
| Place of birth | Fulda |
| Nationality | German |
| Address | Dorfelder Strasse 2, 60385 Frankfurt a. M. |
| E-mail | semmler@itp.uni-frankfurt.de |

### Education

| | |
|---|---|
| 08/90 – 06/1999 | Secondary school, Wigbert Gymnasium, Hünfeld |
| 06/1999 | Abitur (German A level), grade 1.4 |

### civilian service

| | |
|---|---|
| 07/1999 – 08/2000 | Medic, German Red Cross, Kreisverband Fulda |

### Studies

| | |
|---|---|
| 10/2000 – 09/2002 | Basic studies of physics, Marburg University |
| 09/2002 | University intermediate examination, grade 1.0 |
| 10/2002 – 09/2006 | Main studies of physics, Heidelberg University |
| 09/2006 | Diploma in physics, grade 1.1<br>diploma thesis: *Competetive phases in the Hubbard model on the square lattice*<br>Supervisor Prof. em. Dr. Wegner |
| 08/2003 – 02/2004 | Studies abroad, Uppsala University, Sweden |

## Postgraduate work

| | |
|---|---|
| 03/2007 – 05/2007 | Research staff member, Heidelberg University, Kirchhoff Institute for Physics, group of Prof. Dr. Pucci |
| 07/2007 – 10/2010 | Research staff member, Frankfurt University, Institute of Theoretical Physics, group of Prof. Dr. Hofstetter |

## Languages

- English (C1)

- Swedish (B2)

- Spanish (A1)

- French (A1)

## Publications

- Denis Semmler, Krzysztof Byczuk, and Walter Hofstetter
  *Mott-Hubbard and Anderson metal-insulator transitions in correlated lattice fermions with binary disorder*
  Phys. Rev. B 81, 115111 (2010)

- Denis Semmler, Julia Wernsdorfer, Ulf Bissbort, Krzysztof Byczuk, and Walter Hofstetter
  *Localization of correlated fermions in optical lattices with speckle disorder*
  Phys. Rev. B 82, 235115 (2010)

- Denis Semmler, Krzysztof Byczuk, and Walter Hofstetter
  *Anderson-Hubbard model with box disorder: Statistical dynamical mean-field theory investigation*
  preprint, arXiv:1106.4028, submitted to Phys. Rev. B